Exploratory routes to reinforce boron carbides using high pressure syntheses

Amrita Chakraborti

INSTITUT POLYTECHNIQUE DE PARIS

NNT : 2020IPPAX095

Thèse de doctorat

Exploratory routes to reinforce boron carbides using high pressure syntheses

Thèse de doctorat de l'Institut Polytechnique de Paris
préparée à l'École Polytechnique

École doctorale n°626 École doctorale de l'Institut Polytechnique de Paris (EDIPP)
Spécialité de doctorat : Physique

Thèse présentée et soutenue à Paris, le 19/11/2020, par

AMRITA CHAKRABORTI

Composition du Jury :

Prof. Domingo Martinez Directeur, Université de Valencia, Espagne (Physique)	Président
Dr Alain Largeteau Ingénieur de recherche, Université de Bordeaux (ICMCB)	Rapporteur
Dr Laetitia Laversenne Chargé de recherche CNRS, Institut Néel (PLUM)	Examinatrice
Dr Gunnar Weck Ingénieur chercheur, CEA	Examinateur
Dr Nathalie Vast CEA-E6, l'École Polytechnique (LSI)	Directrice de thèse
Dr Yann Le Godec Directeur de recherche CNRS, Sorbonne Université (IMPMC)	Directeur de thèse
Dr Guido Roma Ingénieur chercheur, CEA (Saclay)	Invité
Dr Eric Lafontaine Responsable du domaine scientifique MCE, DGA (Direction de la Stratégie)	Invité

Acknowledgements

The work done in this thesis has been performed with the support of the PhD grant of the Ecole Doctorale of the Institut Polytechnique de Paris. I also express my gratitude for the financial support provided by *Le Direction Generale de L'Armament* (DGA) and from the program NEEDS - Matériaux. I would also like to thank Prof. Domingo Martinez and Dr. Alain Largeteau for having graciously agreed to be the reporters for my thesis. I also thank the members of the other members of the jury Dr. Laetitia Laversenne, Dr. Gunnar Weck and Dr. Guido Roma for their support and advice.

I cannot thank the directors of my thesis Dr. Nathalie Vast and Dr. Yann Le Godec enough for the unwavering support and guidance they have provided me during the last three years: I have never walked out of their office doors without feeling freshly motivated about my work.

I would also like to thank IMPMC Sorbonne Université for allowing me access to the experimental facilities and helping me every step of the way. Moreover, I would like to thank the researchers and the administration at LSI, Ecole Polytechnique and

IMPMC, Sorbonne Université for all their suggestions and guidances over the last three years.

I am also grateful to all the friends I made at LSI and IMPMC, who stood beside me during all the ups and downs that inevitably accompany a PhD thesis, and who helped me find a second home in a new country and a new culture. I will forever remember the spontaneous French lessons, coffee breaks and scientific beers (of course, before Covid put a stop to all of it).

From the bottom of my heart, I would like to thank my family for encouraging me to chase my dreams no matter what : my parents, grandparents, my sister, sensei and my practice are the wind to my wings.

Contents

Introduction

Boron carbide is a compound made of boron and carbon, which has a grey-black colour. Even though the carbon content can wary widely, boron carbide is generally considered to have around 20% of carbon atoms, giving rise to the commonly used B_4C formula. It is not widely found in nature, and was first synthesised in the 19th century as a by-product of reactions involving metal borides. However, the elements forming boron carbide, boron and carbon, are some of the most commonly found elements in the earth, mostly in the form of borax and graphite respectively.

This material is well-known for its remarkable properties such as its hardness and incompressibility. It is one of the hardest materials that can be produced industrially in tonnage, earning it the epithet of 'black diamond'. It also has a very low density. The combination of all these properties makes boron carbide an ideal candidate for making light-weight protective and shielding materials. In the domain of defence, it is mostly used as a bulletproof plates to be used on armoured vehicles and military aircrafts. For example, boron carbide and Kevlar composite armours have been widely used in Black Hawk helicopter passenger seats in the United States. It is also used in bulletproof vests

for personnel (Figure 1).

Helicopter (Black hawk)

Tank (MIA2)

Bullet-proof jacket [1]

Figure 1: Examples of use of boron carbide for military purposes

Boron carbide is relatively easy to synthesise and stable at high temperatures. This renders it very useful for a number of uses in industries in the civil domain as well, particularly as cutting and abrasive tools (Figure 2).

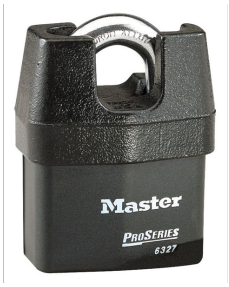

Padlock (Masterlock)

Nozzles [2]

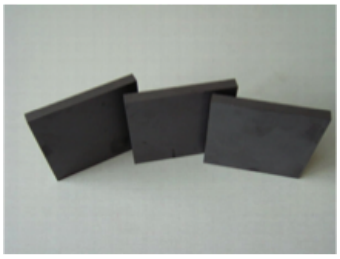

Plates (SCERAM)

Figure 2: Examples of use of boron carbide for civil purposes

Apart from its exceptional mechanical properties, boron carbide is also relevant in the nuclear industry. This is largely because of its nature richness of the ^{10}B isotope, its

resilience against irradiation and thermal stability. It is, therefore, used as control rods in reactions. Boron carbide has also been considered as a potential candidate for an inner protective wall in Tokamaks (Figure 3).

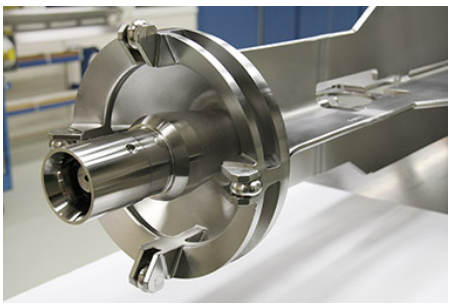

Control rod (BWR CR99)

Faraday screen with B_4C layer [3]

Figure 3: Examples of use of boron carbide for nuclear purposes

However, in spite of its many great qualities, boron carbide suffers from a critical setback. When faced with an impact that goes beyond its Hugoniot Elastic LImit (HEL), the material gradually starts losing its mechanical strength. Much work has been done through the decades to identify the cause of its mechanical failure and to remedy it.

In fact, the plethora of properties that boron carbide has makes it a worthwhile candidate for further research and development. This is evident through the extensive research that is being done on this material world-wide. In fact, during the three years of my thesis, more than 750 scientific articles were published with the name 'boron carbide' in their titles (Source: Google Scholar).

The work done in this PhD work is exploratory and aims to pursue and develop different techniques for the mechanical strengthening of boron carbide. With this main principle in

mind, my work can be described to have three different objectives, which are enumerated below.

1. Experiments using torsion to study the formation of vacancies under non-hydrostatic conditions, which can explain the reasons behind the observed mechanical failure of the material.

2. Synthesis under High Pressure High Temperature (HPHT) conditions to find C-C chains that have been predicted theoretically to stabilise the boron carbon structure.

3. Synthesis of boron carbide with silicon under pressure to reinforce the bonds, and thus prevent mechanical failure.

These objectives have been followed through in seven chapters.

- In the first chapter, I have explained the state of the art on the improved mechanical strength of boron carbide at the time of the beginning of my thesis. I have then justified, with the help of the literature survey, the different routes of synthesis that I have chosen to follow in this work. I have also introduced the reader to the various experimental and theoretical techniques I have used to pursue the goals state above.

- In the second chapter, I have documented the optimum synthesis parameters of pure boron carbide from its elements under moderate pressures up to 5 GPa. The work in this chapter is related to the second objective stated above.

- In the third chapter, I have investigated the synthesis parameters at a high pressure value of 13 GPa. The work in this chapter is related to the second objective stated above.

- In the fourth chapter, I have worked in the very high pressure range between 20 - 50 GPa to find experimental evidence of a theoretically predicted boron carbide phase. This phase with C-C chains is even predicted to be thermodynamically stable at the very high pressure ranges investigated in this chapter.

- In the fifth chapter, I have used the rotational tomography Paris-Edinburgh Cell (RoToPEC) to subject boron carbide to torsion under pressure. Then I used different techniques and studied the vacancies hence formed. This chapter concerns itself with the first objective stated above.

- In the sixth chapter, I have undertaken both theoretical studies of formation energy and used high pressure high temperature synthesis to advance towards the formation of a ternary boron, carbon and silicon compound which would have improved mechanical properties compared to boron carbide. The work in this chapter was done in pursuit of the third objective stated above.

- In the seventh chapter, I have described the formation of an intermediate alpha boron phase during the synthesis of boron carbide under high pressure and high temperature conditions and explained the reasons behind its formation. This was unprecedented in literature and has resulted in the deposition of a patent. This chapter also gives us insights of the mechanism of formation of boron carbide from

its elements under HPHT conditions.

It is perhaps also pertinent to mention here that my work was strongly affected by the epidemic of Covid 19 and the resulting lock-down of three months. The achievement of the objectives of this project depended heavily on experimental resources to which I had no access to during the lockdown and limited access afterwards, during the slow revival of activities post-lockdown on the experimental and characterisation platforms.. Several essential projects, like the allocation of beamtime at Soleil synchrotron was postponed from April 2020 to December 2020, after the date of the defense. Hence, some of the work that is scheduled to be done later and therefore, could not be presented here would be presented later, in conferences and in the form of articles.

Chapter 1

State of the art

In this chapter, I have presented the state of the art of the thesis subject at the beginning of this work. The presentation is in two parts. In the first part, I have discussed the structures of boron carbides and the problems with its utilisation as a protective material, then, I have talked briefly about the explanations found in literature for the origins of these problems and, then, exposed the rationale behind the various exploratory strategies I have used during my thesis to tackle these problems. In the second step, I have provided brief introduction to the various high pressure synthesis techniques, characterisation methods and theoretical techniques that I have used to bring these strategies into action.

1.1 Boron carbide based materials for protective uses: State of the knowledge

1.1.1 Boron carbide

1. Atomic structure

The atomic structure of boron carbide consists of icosahedra and triatomic chains. Though boron carbides have a huge variation in structure and stoichiometry [4], the elemental crystallographic unit cell is believed to have the $R\ \overline{3}m$ space group and to contain 15 atoms per unit cell. The most common structure, B_4C, contains 20 % of atomic carbon concentration and is noted as $(B_{11}C^p)$C-B-C. $(B_{11}C^p)$ refers to the icosahedron which is formed of twelve atoms - eleven atoms of boron and one atom of carbon. C-B-C refers to the triatomic chain which consists of two carbon atoms at the chain ends and one boron atom at the chain centre. Figure 1.1 shows this structure of boron carbide. Perfect icosahedra have five fold rotation axes, that are not compatible with the three dimensional periodic translations defined by the Bravais lattice vectors of the crystal. Thus, icosahedra are distorted and present two crystallographic sites: the polar site (white balls in Figure 1.1) and the equatorial site (grey balls in Figure 1.1). Icosahedra are interconnected directly through covalent bonds between the six atoms in the polar sites and six polar atoms of the six neighbouring icosahedra, and indirectly via the chains through covalent bonds between the six atoms in the equatorial sites.

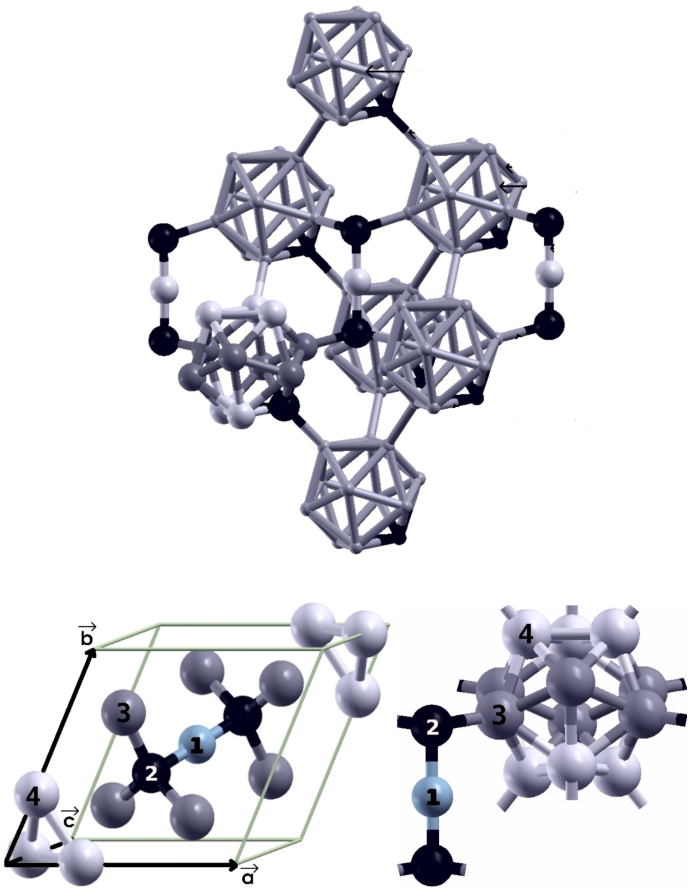

Figure 1.1: Atomic structure of boron carbide (B_4C) (top image). The black balls represent the carbon atoms, the grey balls represent the boron atoms at equatorial sites and the white balls represent the boron atoms at the polar sites and chain centers. The bottom image shows the unit cell of boron carbide. Blue ball (1): atom in the chain centre, Black ball (2): atom in the chain extremity, Grey ball (3): equatorial ball, White ball (4): polar atom. The origin (0,0,0) of the Bravais lattice vectors in the image is the center of the icosahedron. The pictures have been taken from Ref. [5].

Experimentally, the stoichiometry of carbon in boron carbides has been observed to vary between around 9 % to 18.8 % at ambient pressure using techniques like chemical anal-

ysis, X-ray diffraction and electron probe microanalysis [6–9]. The atomic structure is similar to the one described in Figure 1.1. Above 18.8 % of atomic carbon concentration, boron carbide is believed to be obtained with excess carbon deposited at the grain boundaries. Similarly, for less than 9 % carbon concentration, the excess boron is found to be deposited at the grain boundaries [10]. In some cases, it can also form carbon doped boron [11]. The atomic structure presented in Figure 1.1 is for 20 % atomic concentration only, while experimentally the highest concentration is 18.8 %. There is still widespread agreement that for all the different concentrations between 9 % and 18.8 % , the observed atomic structure remains similar, with a rhombohedral space group n°166 : $R\ \bar{3}m$. This conclusion is based on numerous experimental studies through X-ray diffraction and elastic neutron scattering [7, 12, 13].

Reaching thermodynamic equilibrium seems to be difficult in boron carbides. All the observations reported in the literature have been made on samples synthesized at elevated temperatures. Disorders in boron carbides have been considered as 'constitutive' or 'intrinsic'. However, *ab initio* calculations based on density functional theory (DFT) reveal a different picture [6]. For the atomic carbon concentrations of 8.7 % and 13.04 %, the crystal unit cell that leads to the smallest total energy is a $3 \times 3 \times 3$ supercell of the 15-atom unit cell presented in Figure 1.1. With respect to the $3 \times 3 \times 3 \times 15 = 405$ atoms, additional boron atoms are introduced in the atomic structure to satisfy the electron counting rule (Wade's rule, see Appendix). The saturation of electronic bonds by nine such additional boron atoms leads to a smaller energy than that of the $(B_{11}C)$C-B-C 15-atom structure. Keeping icosahedra as (B_{12}) ones, the energy minimum has been

obtained when $\frac{1}{3}$ of the C-B-C chains were replaced with B-C-B-C chains, leading to the concentration of 13.04 % - this was named as OPO_2 by the authors. Here, OPO stood for "ordered partial occupation". They can also be replaced with B_4 blocks, leading to 8.7 %, which was named as OPO_1. Thus, in DFT calculations, boron-rich boron carbides have a complex unit cell containing 414 atoms in a quasi-trigonal structure. In an average trigonal structure, the extra boron atoms occupy either an extra 2c Wyckoff's site (13.04 %) or an extra 6g Wyckoff's site (8.7 %), as seen in Table 1.1.

Name		$B_{2.5}C$	B_4C	OPO_2	OPO_1
Polar.	*6h*	4B + 2C	5B + 1C	6B	6B
Equatorial.	*6h*	6B	6B	6B	6B
Chain-end.	*2c*	2C	2C	2C	$\frac{4}{3}$C + $\frac{2}{3}$B
Chain-center.	*1b*		1B	1B	$\frac{2}{3}B^{\dagger}$ + $\frac{1}{3}\square^{\dagger}$
EIWS ... B	*2c*			$\frac{1}{3}B^{\dagger}$	
EIWS....$\langle \begin{matrix} B \\ \\ B \end{matrix} \rangle$...	*6g*				$\frac{2}{3}B^{\dagger}$

[a] Definition of the □...C-B-C...B block

[b] Definition of the B$\langle \begin{matrix} B \\ \\ B \end{matrix} \rangle$B block

Table 1.1: Occupation of Wyckoff's sites (WS) of the $R\bar{3}m$ average structure for thermodynamically stable icosahedral boron carbides. The last two rows are extrainterstitial Wyckoff's sites (EIWS). WS marked with a dagger (†) have an ordered partial occupation. The square symbol stands for vacancy. In OPO_2, only one additional B is present in the extra 2c WS, yielding the C-B-C...B block or the B...C-B-C one. In OPO_1, two out of four B atoms of the B_4 block occupy the extra 6g positions, the two remaining B atoms being in the 2c chain-end WS. In OPO_2 and OPO_1, only $\frac{1}{3}$ of the chains are replaced with C-B-C...B blocks or with B_4 ones. The table has been taken from Ref. [6].

2. Properties and uses

Boron carbide is a widely known industrial ceramic, thanks to its extreme hardness (Vickers hardness of 38 GPa [14]) , low density (2520 kg/m^3 [15]) and very high incompressibility (adiabatic bulk modulus of 241 GPa [16]). In fact, at ambient pressure, it is the third hardest industrially produced ceramic material in the world, after diamond and cubic boron nitride [17, 18]. This combination of high hardness and low density makes boron carbide an ideal candidate for protective uses for both systems and people, in the civil as well as defense domains. Moreover, boron carbide maintains its extremely high hardness at temperatures quite close to its melting point, under ambient pressure conditions [19]. Applications range from lightweight bullet-proof jackets, safety armours to shielding of engines and cockpits of military aircrafts [18, 20].

Among applications other than shielding ones, and since boron carbide is also fairly easy to synthesize [4, 15, 21] and very stable [18] , it finds several uses in industry as well, such as in cutting and abrasive tools, and wear-resistant components.

Apart from its remarkable mechanical properties, boron carbide is also efficient as neutron absorbers [18, 22]. This is because it is naturally rich in the ^{10}B isotope ($\geqslant$ 19% [23]), and is highly stable under both irradiation [24] and high temperatures [18]. Therefore, it can be effectively used in control rods for nuclear reactors and was expected to be the potential neutron absorber material in the possible French generation IV reactors [25].

Boron carbide has also been studied for its potential as a protective inner wall of Toka-

maks to avoid plasma contamination. This is because of the low atomic number of the elements forming it (boron and carbon), its strong chemical stability and its resistance against damages caused by high temperature exposures [26].

3. Use of boron carbide as protective material: Pros and cons

The goal of a protective shielding system is to prevent damage to people or structures when faced with impacts of very high velocity. Therefore, the protective system used should be able to stop fast projectiles such as bullets before it comes into contact with the target. Generally, this is done in two steps. In the first step, the bullet is broken through contact with a hard ceramic material. After the bullet is broken, the shock generated is then absorbed in the second step by a more ductile material such as an alloy of steel or aluminum alloy, or even a fibrous composite such as glass or polyethylene [27]. Therefore, a protective system is generally composite. The material of the first step is henceforth called the protective material, and likewise, the material of the second step is called the absorbing material. Moreover, the manner in which these two layers are held together is equally important. Boron carbide is a protective material of choice in such composites.

Indeed, the ceramic chosen to stop the projectile has to be naturally much harder than the projectile itself. Projectiles are generally made of a very dense core of lead [28] (or even uranium, in some cases [29]) surrounded by a protective hard casing. The hardest of these casings are made of tungsten carbide with cobalt being used as a binder (91.5% WC - 8.5% Co). These materials have Vickers hardness of around 17 GPa [27]. If the

shielding material has a hardness higher than this value, it will succeed in breaking the projectile. Boron carbide has a recorded Vickers hardness as high as 38 GPa [14]. Thus, boron carbide splendidly satisfies the hardness requirement of a protective material. Moreover, even though a good number of super hard materials have been produced in laboratories around the world in recent years, they are not yet feasible industrially because of difficult synthesis conditions [30]. A super hard material is defined as a material that has a Vickers hardness of above 40 GPa [31, 32]. Thus, boron carbide remains an attractive candidate as protective material, even with the discovery of these new ultra-hard materials.

The density of a shielding material is also a very important consideration, since it directly affects the weight of the shielding system. Ideally, the weight of the shielding system should be kept to the minimum possible for the comfort and ease of movement of the users. Boron carbide has a low density of 2520 kg/m^3 [15] which ensures light-weight shielding systems.

Another requirement of a shielding material is to have very high stiffness. This would prevent the protective structure from getting deformed during a high velocity impact. To ensure that the shielding material deforms less than a steel plate, a Young's modulus of more than 200 GPa is required [33]. Boron carbide performs very well on this metric as well, with a Young's modulus of 472 GPa [34].

It is also important for a shielding material to be very stable and to not become reactive under pressure and/or temperature. Boron carbide fulfills this criterion as well. The

congruent melting point of boron carbide under ambient pressure is 2720 ± 50 K [8,35]. In fact, its hardness even exceeds that of diamond above 1200 K [36–38]. It does not oxidise at temperatures below 773 K, and even beyond this temperature, a thin layer of B_2O_3 forms at the surface, which protects the material inside from further oxidation [18].

Another essential requirement for a shielding material is that the value of the Hugoniot Elastic Limit (HEL) should be as high as possible. HEL corresponds to the maximum stress a material can undergo during an impact or a dynamical loading before it reaches its elastic limit. Therefore, the higher the HEL of a material, the higher the impact velocity of the projectile that it can resist. Boron carbide seems to fare well in this parameter as well, as it is known to have one of the highest values of HEL among ceramics (17-20 GPa) [39].

But in spite of all these excellent properties, boron carbide suffers from a major drawback. If the projectile striking the ceramic creates a shock wave with a very high velocity that goes beyond its Hugoniot limit, boron carbide gradually loses its mechanical strength and shows fractures. This gradual loss lasts till about 40 GPa. Beyond 40 GPa, this ceramic loses its mechanical strength completely [40].

4. Literature review on the loss of mechanical strength of boron carbide

The loss of mechanical strength in boron carbide when impacted beyond its Hugoniot elastic limit has been explored at length in literature. The consequences of an impact on boron carbide depends heavily on the type of impact.

• Dynamical loading and shear bands as a cause of mechanical failure

When exposed to dynamic loading such as during a ballistic impact [41], or during decompression after pressure was increased non-hydrostatically above 25 GPa [42], shear bands appear in boron carbide. These shear bands are amorphous, although it is still not established whether they consist of amorphous boron carbide or amorphous carbon. The origin of these shear bands (also called deformation bands) are still unexplained. However, the experiments that studied the ballistic impact on boron carbide [41] noted that the amorphous zones were extremely localised, with a size no greater than 1 - 3 nm. This size is too small to create a loss of mechanical strength on the macro-scale. Thus, amorphisation does not seem to adequately explain the reason behind the loss of mechanical strength in boron carbide.

In experiments with hydrostatic loading, no shear bands are observed up to pressure values of 50 GPa [42]. However, the debate about a possible phase transition remains in this case.

For experiments incorporating contact mechanics, such as during nano-indentation [43], shear bands have also been observed.

The amorphous shear bands in boron carbide concern a problem of microstructure, which can hardly be investigated by *ab initio* calculations. However, experiments that were performed with reversible experimental parameters, such as by applying pressure with the Paris-Edinburgh cell (PEC) or the diamond anvil cell (DAC), can be approached by *ab initio* calculations under finite pressure. Therefore, a lot of work has already been

done trying to explain the behaviours of boron carbide under such reversible conditions, which will be touched on in the following part of this section.

• Phase transition as a cause of mechanical failure

The loss of mechanical strength in this case has also been attributed to a possible phase transformation under uniaxial compression into an amorphous state with highly distorted yet still identifiable B_{12} and $B_{11}C$ icosahedra by Aryal *et al.* [44]. Phase transitions can be looked for by calculations done on the quantum level. However, these claims have been contested by Betranhandy *et al.* [45] as the energy barrier for the proposed phase transition is very high. The transition is also supposed to take place around 168 GPa, which is much higher than the HEL value of 17-20 GPa beyond which we see the loss of mechanical strength. Moreover, there is no experimental proof of this phase transition up to the pressure value of 110 GPa. But phase transitions can still be induced by point defects.

• Occurrence of point defects as a cause of mechanical failure

Raucoules *et al.* studied defective boron carbide under moderate pressure and have suggested the loss of mechanical strength beyond HEL is the result of the formation of vacancies under dynamic loading [46]. They have calculated the formation energies of vacancies inside boron carbide and have concluded that the boron at the centre of the chain is the most vulnerable to become a vacancy site. This is coherent with an earlier study that showed that the boron atom at the chain centre is bonded weakly with the atoms at the chain ends, since their shorter C-B distance (1.44 Å) points towards

substantial π-bonding [38].

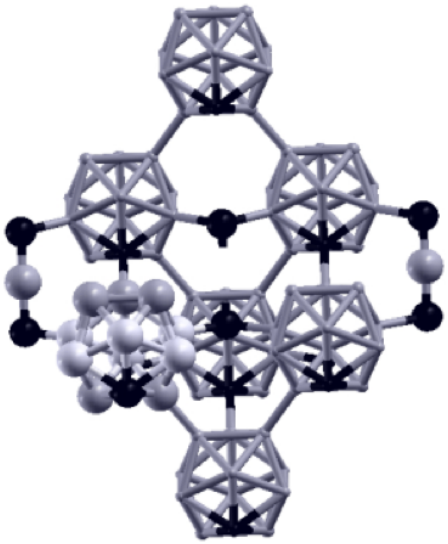

Figure 1.2: Atomic structure of boron carbide with the chain center vacancy as well as two other intact C-B-C chains. The black balls represent the carbon atoms, the grey balls represent the boron atoms at equatorial sites, while the white balls represent the boron atoms at polar sites and chain centers.The figure has been extracted from Ref. [46].

In the absence of the boron atom, the chain becomes C□C (□ represents the vacancy), as shown in Figure 1.2, and dangling bonds are present. Under pressure, the chain becomes unstable as the carbon atoms at the extremities approach each other and form a bond, as shown in Figure 1.3. The theoretical volume change associated with this formation of C-C bonds under pressure, is as high as 4 $Å^3$ /vacancy. The computed pressure needed for this discontinuous change of volume is 28 GPa, which can be attained during a ballistic impact. It is this discontinuous change of volume that leads to the loss of mechanical strength.

However, the concentration of these defects naturally found in boron carbide is too small

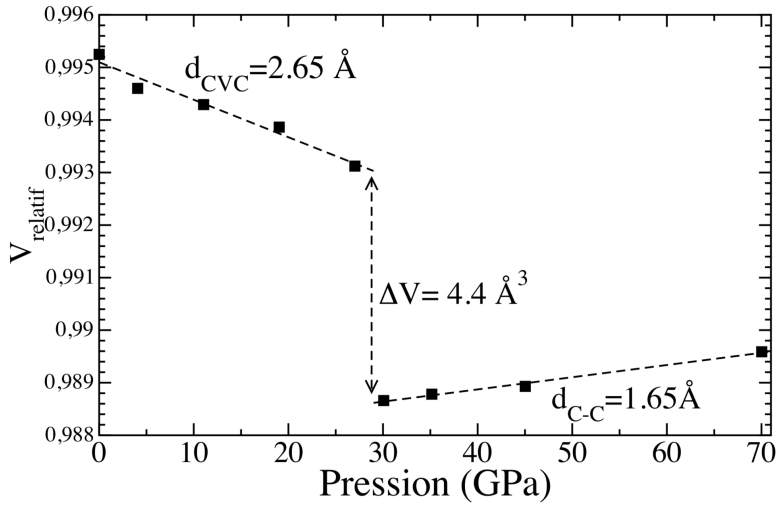

Figure 1.3: DFT-LDA calculations. The curve shows the discontinuous reduction of volume relative to a chain center vacancy as function of pressure. $V_{relatif}$ *is defined by the volume of the defective unit cell divided by the volume of an unit cell of* $(B_{11}C^{p})$*C-B-C* ($V_{relatif} = \frac{V}{V_{B_4C^p}}$). *The figure has been extracted from Ref. [46].*

by itself to lead to mechanical failure. This is coherent with the fact that boron carbide does not lose its mechanical strength even under high temperature conditions [18]. But, the defect concentration can increase dramatically under certain experimental conditions. For example, when the ceramic is impacted beyond its Hugoniot limit, the plastic regime is reached and a high number of dislocations and twinning occurs in the crystal structure. These dislocations do displace rapidly. However, when dislocations are bent because of the intersection of two such dislocations, their movement is only possible through the creation of vacancies [47]. Thus, a great number of vacancies can be formed when the material is under pressure [48]. Therefore, Raucoules *et al.* have hypothesised that above the Hugoniot limit, it is possible that a sufficient concentration of vacancies appear in

the ceramic to diminish the mechanical strength of boron carbide. Even though C-C chains in boron carbide has not been reported experimentally, C□C remains the most observed vacancy in boron carbide [49].

5. A first route to reinforce boron carbide

Jay *et al.* have studied defect free boron carbide at high pressures through *ab initio* calculations and have proposed a solution to address the loss of mechanical strength due to the discontinuous collapse of the C□C chains into C-C chains [5], [6]. They have suggested a new phase of boron carbide $(B_{10}C_2)$C-C or $B_{2.5}C$. This new phase has C-C chains instead of the C-B-C chain - therefore it is not susceptible to the formation of vacancies through the creation of C□C chain under shock. Moreover, this new phase is the thermodynamically stable phase beyond 60 GPa, as shown in figure 1.4. Ektarawong *et al.* has also independently confirmed the stability of the $(B_{10}C_2)$C-C phase [50].

Jay *et al.* have calculated the active modes of Raman spectroscopy of these proposed phases, as shown in Table 1.2 and Table 1.3. Moreover, the XRD spectra of these phases have also been simulated in Ref. [5]. This can help us to identify both the C□C defects and the proposed $(B_{10}C_2)$C-C phase if we succeed in producing them using High Pressure High Temperature (HPHT) techniques.

Experimentally, C-C chains in boron carbides have not yet been reported in literature. Preliminary experiments done at IMPMC before this PhD work have shown traces of C-C chains during high pressure synthesis [51]. These preliminary experiments need to be validated with further syntheses and characterisations. The present work aims to find

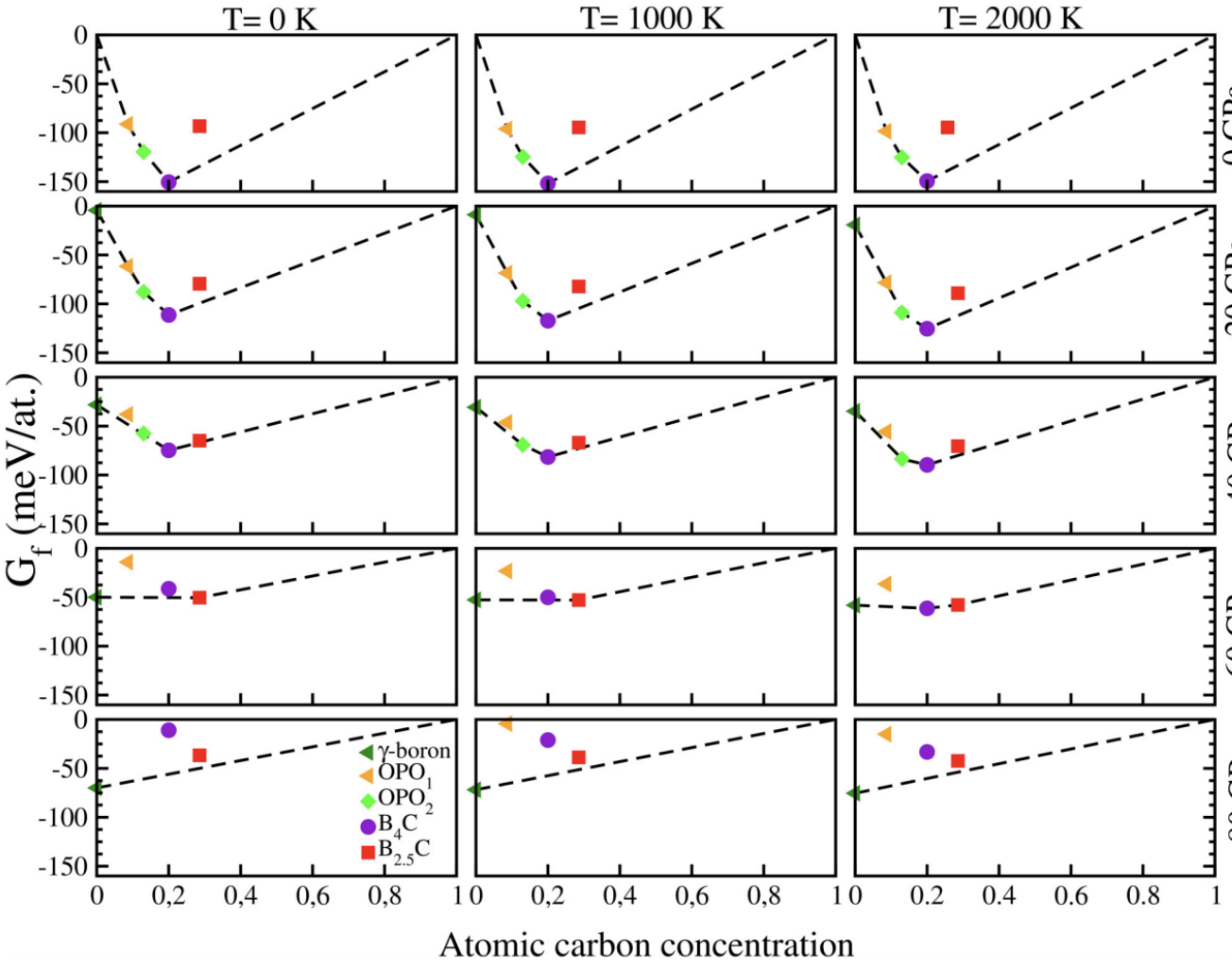

Figure 1.4: DFT-GGA-PW91 calculations. The figure shows the P-T evolution of the theoretical convex hull of boron carbide. The purple circle is B_4C, whereas the red square is $B_{2.5}C$. $B_{2.5}C$ is on the convex hull at 60 GPa, thus showing its thermodynamic stability under these conditions. The figure has been extracted from Ref. [6].

the evidence of the C-C chains in boron carbides, which can lead to the synthesis of the theoretically predicted $B_{2.5}C$ phase with increased mechanical properties. A possible way to do this synthesis, as explained in Ref. [6], is to put boron carbide under a pressure

Material	*Ico*9	*Ico*17	*Ico*21	*Ico*24	*Ch*5
α-B_{12}	707	815	945	1192	-
$(B_{11}C^p)$C-B-C	719	699	994	1069	1095
(B_{12})C-C	729	673	998	1078	573
$(B_{11}C^p)$C-C	805	692	984	1120	570
$(B_{11}C)_{dif}$C-C	842	702	1053	1204	581
(B_{12})C□C	804	624	959	1090	475
$(B_{11}C^p)$C□C	795	713	1057	1133	398

Table 1.2: DFT-LDA calculations. Frequency values in cm^{-1} of A_{1g} active modes of Raman frequency for some materials. The table has been taken from Ref. [5].

between 57-69 GPa using a diamond anvil cell (see Sec 1.3.1.3), and then increase the temperature to 1800- 2000 K in order to overcome the kinetic barrier. A carbon concentration slightly above 28.6 % is also required to avoid formation of B_4C. Since $B_{2.5}C$ is the thermodynamically stable phase predicted under these conditions, it can be expected to form independently of the kind of precursor . Then, the sample has to be quenched and brought back to room temperature and pressure so as to preserve the $B_{2.5}C$ phase under ambient conditions, and prevent it from decomposing into B_4C and carbon.

Also, though the stability of boron carbide under hydrostatic stress has been well-documented in literature [42, 52], there have not been many studies on the defects pro-

Material	*Ico*5	*Ico*7	*Ico*11	*Ico*13	*Ico*20	*Ico*23	*Ch*3
α-B_{12}	528	608	729	790	890	1137	-
$(B_{11}C^p)$C-B-C	549 536	488 479	768 737	841 840	815 808	1052 1056	1139 1098
(B_{12})C-C	389	583	709	646	862	957	1056
$(B_{11}C^p)$C-C	491 410	621 592	770 726	708 692	918 876	1184 885	1048 1059
$(B_{11}C)_{dif}$C-C	527 538	562 NA	NA NA	NA NA	NA NA	1233 1225	1118 1138
(B_{12})C□C	427	507	670	808	759	890	1208
$(B_{11}C^p)$C□C	481 488	533 529	754 730	831 819	827 801	1108 1096	1218 1223

Table 1.3: DFT-LDA calculations. Frequency values in cm^{-1} of E_g active modes of Raman frequency for some materials. NA signifies that the symmetry of the computed mode could not be attributed to E_g symmetry solely (there was also some remnant infrared activity, for instance) and means "Not Attributed". The table has been taken from Ref. [5].

duced in boron carbide under non-hydrostatic pressure. However, as discussed above, defects can play a defining role in diminishing the mechanical strength of boron carbide. Therefore, studying the defects formed in the ceramic under a non-hydrostatic load is fundamental to understand how they can impact boron carbide beyond the Hugoniot limit. However, these defects need to be created in a controlled manner in order to help us quantify the deformation produced and its effect on boron carbide. This objective has been explored in the present work by putting boron carbide under pressure, subjected to a torsional (therefore, non-hydrostatic) force using the Rotational Tomography Paris-Edinburgh Press (RoToPEC) (See Sec 1.3.1.4) and then analysing the spectroscopy and

diffraction of the resulting defects.

1.1.2 Ternary phase(s) with boron, carbon and silicon

Another idea for reinforcing the triatomic C-B-C chains in boron carbide that has been designed in the present work is to insert chains containing silicon atoms between the ($B_{11}C$) icosahedrons using moderate pressures and high temperatures. This is expected to form (a) ternary phase(s) of boron, silicon and carbon with potentially enhanced mechanical properties since the silicon atom containing chains would prevent the central vacancies formed in the C-B-C chains. The larger size of the silicon atom with respect to the boron or carbon atom would decrease the atomic mobility that is necessary for the formation of vacancies. The formation of this ternary phase is made possible by the isovalence of silicon and carbon atoms, with both having four atoms in their outermost shell of their electronic configuration. In fact, a binary phase $B_{2.5}Si$ has been calculated by Bullett *et al.* [53] and the phase $B_{2.5}C$ predicted by the DFT calculations [6] turns out to be isostructural to the $B_{2.5}Si$ phase. Magnusson *et al.* [54] has also reported the existence of an isomorphic binary phase with Si-Si chains and icosahedra in the boron-silicon system ($B_{2.89}Si$).

1. Atomic structure of silicon doped boron carbide

Although a ternary phase containing boron, silicon and carbon has yet to be reported in literature, there have been some examples of silicon doping in boron carbide [55–57]. The atomic structure of these silicon doped boron carbides, as reported in literature, is

useful to obtain a preliminary idea of the preferred location of silicon atoms in the boron carbide crystal structure under different experimental conditions.

Khan *et al.* [55] have reported an overall concentration of silicon of 1.2 % ± 0.1% in samples obtained by mixing boron carbide and SiB_6 powders subjected to spark plasma sintering. They have performed DFT calculations to understand the localisation of silicon atoms in the atomic structure. It turned out that the silicon atom occupies an interstitial position between the icosahedron and the chain. This results in a kinked C-Si-C chain, rather than a straight C-B-C chain, as shown in Figure 1.5. Thus, silicon does not actually occupy the place of the central boron atom in the chain, but an interstitial crystallographic site. The possible silicon atom positions do not lie in the same plane in the horizontal setting, with half of them slightly above the z/c = $\frac{1}{3}$ plane, while the other half slightly below the z/c = $\frac{1}{3}$ plane. This change in z/c = $\frac{1}{3}$ position corresponds to the weak bond between the silicon atoms and the nearby icosahedral boron atoms. However, no evidence of Si-Si chain formation was found which could replace the existing C-B-C chains. Interestingly, the silicon partially occupies the 6*h* Wyckoff positions of the $R\ \overline{3}m$ system - the partial occupation is small and around 0.3055 (see table 1.1). [1].

Finally, Morosin *et al.* [56] also report the same position of the silicon atom in boron-rich silicon doped boron carbide through structure refinement. However, in this case, the silicon atom does not come out of the z/c = $\frac{1}{3}$ plane to weakly bond with icosahedral

[1] In Ref. [55], crystallographic data are expressed in the conventional hexagonal unit cell than in the trigonal elementary unit cell. The Wyckoff site is then 18h and the partial occupation ratio is 0.55/18.

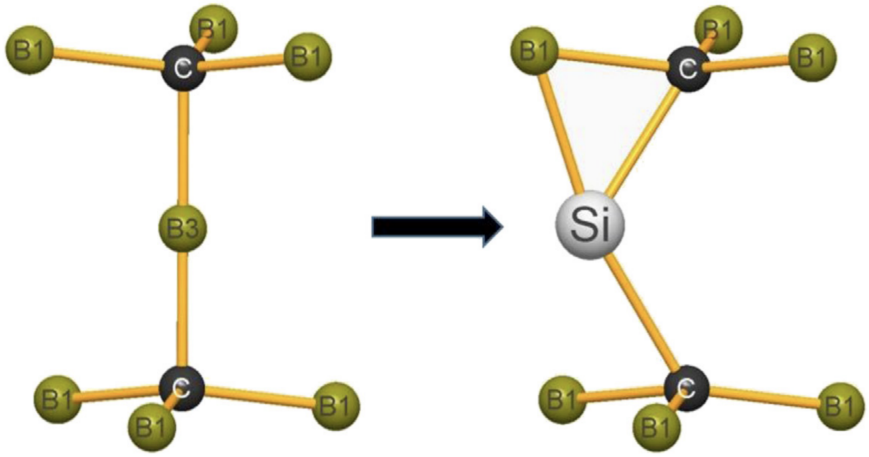

Figure 1.5: Rietveld refinement, guided by DFT calculations, shows the position of Si atom inside a kinked C-Si-C chain, instead of the usual C-B-C chain of boron carbide. The figures have been extracted from Ref. [55].

boron atoms. This discrepancy could be attributed to the fact that Morosin *et al.* had carried out only free atom refinements for the crystal structure. Thus, their structure models were not attempts to completely fit the residual electron density, particularly that due to bonding, which might have led them to overlook the weak bonding between the silicon atom and the icosahedral boron atoms.

	Position of Si atoms in atomic structure
Khan *et al* [55]	half of Si atoms slightly above the z/c = $\frac{1}{3}$ plane (z/c = 0.33860), the other half slightly below the z/c = $\frac{1}{3}$ plane (z/c = =0.32803)
Morosin *et al* [56]	z/c = $\frac{1}{3}$ plane

Table 1.4: Position of Si atoms in Si doped boron carbide found in literature.

2. Description of the synthesis routes

The introduction of silicon in boron carbide is an experimental challenge. Firstly, because the solubility of silicon in boron carbide turns out to be rather low and amounts, for instance, to 2.5 at. % at a temperature of 2323 K [58,59]. Secondly, according to my calculations in Chapter 6, it is difficult to ensure the formation of the desired ternary phase(s) instead of the energetically more favourable silicon carbide with elemental boron or boron carbide with elemental silicon. Even though there are no mentions of a successfully synthesized ternary phase, some reports of doping silicon into the boron carbide crystal structure has been found in the literature, and they are discussed below.

• Doping boron carbide with silicon

Silicon has been incorporated marginally in boron carbide during its growth from molten copper, as a by-product of the main chemical reaction [56].

Proctor *et al.* [57] have doped boron carbide nanowires with silicon using the solid-liquid-solid method with a starting mixture of submicron boron powder, activated carbon in 1:1 ratio and 2% by weight of silicon powder. A catalyst mixture (1% by weight) of nickel boride, nickel diboride and cobalt was used to facilitate the formation of nanowires. The mixture was then heated in a clam shell furnace at 1423 K under argon atmosphere for 1 hour. The nanowires were then ball-milled for 1 hour in an argon atmosphere and then consolidated by spark plasma sintering (SPS) at 2373 K under 50 MPa pressure for 20 minutes. The silicon content was between 0.8 and 1.6 % at. Si, with an average of 1.2 $\pm$ 0.4 % at. Si.

Khan *et al.* [55] have reported the synthesis of silicon doped boron carbide from a starting mixture of boron carbide and SiB_6 powders in various ratios. The mixtures were then densified using a spark plasma sintering furnace at temperatures ranging from 1873 K to 2123 K. The authors report the formation of kinked C-Si-C chains, as described above.

3. Effect on the mechanical properties

The silicon doped boron carbide synthesized by Proctor *et al.* [57] showed no amorphisation under a non hydrostatic pressure of 50 GPa applied in a diamond anvil cell, unlike conventional boron carbide. The authors have attributed it to the reduction of the concentration of the (B_{12})C-C-C polytype of boron carbide under silicon doping. They hypothesized that since the (B_{12})C-C-C polytype is more prone to amorphisation, a reduction in its concentration will deter amorphisation in boron carbide. However, since the position of silicon in the boron carbide structure has not been determined in the study, it is not possible to conclude whether this protects boron carbide from mechanical failure generated through the chain vacancies, as discussed in Sec 1.1.1. We also note that the (B_{12})C-C-C polytype is not the expected thermodynamically stable structure at 20 % atomic carbon concentration [9, 60, 61] (see description in Sec 1.1.1).

Khan *et al.* [55] claim that, in the silicon doped boron carbide they have synthesised, the kinked C-Si-C chain can provide some protection against amorphisation (described in Sec 1.1.1) by stabilising the structure of the boron carbide crystal through its bonds with the icosahedra. Moreover, the silicon atoms can also fill pre-existing boron vacancies in

the centre [46], which sounds promising for protection against mechanical failure due to vacancies, if the viewpoint studied by Raucoules *et al.* [46] and Jay *et al.* [6] is adopted. However, so far, the solubility of silicon in boron carbide is only 2.5% at 2323 K, which is not enough to fortify all the chains in the materials. Therefore, under dynamic shock, this silicon doped boron carbide would not be able to protect against a dramatic increase of vacancies in the remaining C-B-C chains. Hence, this leads to the need to explore other routes of reinforcement as well.

Indeed, the idea of the present PhD work is to use pressure to achieve the synthesis of a ternary phase and overcome the problem of silicon solubility in boron carbide observed at low pressure. High pressure has previously been reported to dramatically increase the stability of the boron-rich phase BC_5 (16.67 at.% of B), whereas, previously, only $\sim$ 2 at.% of B could be incorporated in carbon without subsequent decomposition [62]. Even though silicon atoms are bigger than carbon or boron atoms, a combination of high pressure and high temperature can work together to raise the silicon solubility in boron carbide seen under ambient conditions.

To this end, I have performed Density Functional Theory (DFT) calculations to verify the feasibility of the formation of such a phase with the application of high pressure. Then, experimental attempts were made to synthesize such a phase using the Paris-Edinburgh press (see Sec 1.3.1). Such an attempt to incorporate silicon into the boron carbide structure under elevated pressures has not been reported so far.

1.2 Objectives of the thesis

As explained before, boron carbide is a widely known ceramic with many industrial and defense uses. It has a plethora of useful properties, such as high hardness, chemical stability etc. However, it suffers from the gradual loss of its hardness beyond the Hugoniot Elastic Limit. Therefore, reinforcing boron carbide in order to avoid this pitfall is needed to harness its advantages to their fullest capacity (see Sec 1.1.1. This has led to the main guiding principle of this PhD thesis - to explore different ways to strengthen boron carbide.

Ab initio calculations [46], [63], [6] have already been done which attempt to explain the reasons behind this loss of strength in boron carbide, as described in Sec 1.1.1. These studies have argued that the reason behind the loss of strength could be the formation of vacances, leading to C□C arrangements in boron carbide under dynamic stress, and a possible way to reinforce the material is to avoid the formation of these vacancies.

Towards this goal, many different routes of reinforcement have been followed simultaneously during the last three years, with very fruitful results, which have deepened our knowledge of this compound. The work has been divided into three main objectives.

1. **Experiments using torsion to study the formation of vacancies under non-hydrostatic conditions**

   Ab initio calculations [46], [63], [6] have suggested the formation of C□C chains

in boron carbide under dynamic loading, but there has not been any experimental efforts to verify the existence of these defects or to study them. Even though local amorphisation has been reported in boron carbide after it has been subjected to non-hydrostatic stress [42], [41], the defects created in the crystal structure of boron carbide during such manipulations have not been studied in detail.

In order to bridge this gap, I have used a RoToPEC (Rotating Tomography Paris Edinburgh Cell, see Sec 1.3.1) to create torsion in boron carbide under a pressure of 5 GPa. This dynamic stress was expected to create point defects and vacancies in boron carbide. These defects could then be studied and the presence of C□C chains could be verified using X-ray diffraction and Raman spectroscopy.

2. **Synthesis under High Pressure High Temperature (HPHT) conditions to find C-C chains**

As explained in Sec 1.1.1, the discontinuous volume change because of the C□C vacancies in boron carbide collapsing into C-C chains under dynamic loading can lead to the loss of mechanical strength. To prevent this phenomenon, I have sought to synthesise a new phase of boron carbide with predominantly C-C chains which would be resistant to the formation of the chain centre vacancies. For this purpose, both large volume presses (the Paris-Edinburgh press and multi-anvil press, see Sec 1.3.1) and diamond anvil cells have been used.

The large volume presses can both attain pressure scales up to 20 GPa and contain large volume samples which leads to better uniformity and crystallinity of the

synthesized product. In fact, from DFT calculations, Betranhandy *et al.* [45] have suggested that C-C chains can form from pressures starting at 5-7 GPa, and thus, a large volume cell would be sufficient. However, these chains are part of a metastable phase (($B_{11}C^{p}$) C-C) of boron carbide at this pressure range [5, 63], and the thermodynamically stable state is not expected at moderate pressures [6].

Diamond anvil cells can attain pressures up to hundreds of GPa, which makes it possible to search for the thermodynamically favourable phase with C-C chains ($B_{10}C_2$)C-C at above 55 GPa [6]. I have used laser heating to attain the required high temperatures in this system. However, the samples used in diamond anvil cells are very small, of the order of microns, which makes it difficult to characterise the samples after *ex situ* synthesis.

Considering the relative advantages and disadvantages of the large volume presses and the diamond anvil cell, I have used the Paris-Edinburgh and multi-anvil cells for syntheses up to 20 GPa, and the diamond anvil cell thereafter.

Moreover, in order to study the formation of C-C chains in boron carbide synthesised under HPHT conditions, the synthesised product would need to be very pure - this would make characterisations of the chains simpler as there will be no impurities that can interfere with signals from the synthesised boron carbide. Producing boron carbide from ultra-pure elements, boron and carbon, would result in products of the highest purity [4], which is essential for the objectives of the current work. However, so far, no study has recorded the synthesis parameters of boron

carbide from its elemental components at high pressure. So, I have performed a series of syntheses to fill this gap in the scientific literature and thereby, to find out the optimal parameters of temperature and pressure for the synthesis of boron carbide. This has also led to some interesting revelations about the mechanism of formation of boron carbide from its elements, including the formation of an intermediate phase of α boron at moderate pressure.

3. **Synthesis of boron carbide with silicon under pressure to reinforce the bonds**

   Another route to avoid the formation of the C□C chains in boron carbide is to engineer a process to insert a bigger atom, like silicon, in the interstitial spaces near the chain center and thus reduce the vulnerability of the C-B-C chains to chain centre defects. As discussed in the preceding section, a ternary phase containing boron, carbon and silicon can fulfill this criterion and thereby increase the mechanical strength of boron carbide. Such a phase has not yet been reported in the literature and neither has there been any studies on how high pressure might affect this system.

   Therefore, as a primary step, I have used DFT calculations to gauge the feasibility of a ternary phase containing boron, silicon and carbon under pressure. Based on the parameters of the calculation, I have then used the large volume Paris-Edinburgh press to attempt the syntheses both *ex situ* and *in situ* in the Soleil synchrotron.

Syntheses were begun with starting mixtures of boron, silicon and carbon and the evolution of the system with mounting pressure and temperature was studied.

1.3 State of the art: experimental and theoretical techniques

1.3.1 Experimental techniques: High Pressure High Temperature (HPHT) synthesis

High pressure is a very useful synthesis parameter which brings up an additional element in the thermodynamic phase space. This leads to the synthesis of solid state compounds that would have otherwise been inaccessible with traditional solid state chemistry [64]. This has led to the discovery of many new compounds [62, 65].

The majority of experimental syntheses in this thesis took advantage of various high pressure (HP) devices. The rapid advancement in the technology of these devices in recent years allows us to reach temperatures of around 3000 K and pressures of more than 100 GPa. High pressure devices can be divided broadly into two types: large volume presses (Paris-Edinburgh press, multi-anvil press) and cells with μm^3 sample volume (diamond anvil cells). The large volume presses can be further divided into opposed anvils type (Paris-Edinburgh press, diamond anvil cell, toroid type press etc) and types with 4-8 anvils (multi-anvil press).

The large number of high pressure devices in the modern day can be traced back to the

work of P.W. Bridgman who was awarded the Nobel Prize in 1946 for his work on high pressure physics [66]. The main principle proposed by Bridgman is the massive support principle which states that the press anvils should have truncated forms. The bigger anvil side is called the support while the smaller side is called the tip, or the pressing side. Even a comparatively small force on support can thus generate very high pressures on the pressing side. This can be expressed in the following form

$$\frac{P_{max}}{S} \sim \ln\left(\frac{R}{r}\right)^2 \tag{1.1}$$

where S is yield stress, R is radius of support side, r is radius of pressing side.

From Eq 1.1, we can see that the higher the difference in the sizes of the support and pressing side, the higher is the maximum pressure attained. P_{max} also depends on the hardness of the anvil materials - several known hard materials such as steel, tungsten carbide, cubic zirconia, sintered diamond and single crystal diamond have been used over time. The choice of the anvil material also depends on the parameters of the experiments, such as pressures and temperatures that need to be attained and characterisations that need to be performed.

In the current section, I will discuss the various high pressure synthesis techniques that I have used during my thesis. The devices were chosen based on a few considerations: the pressure and temperature range required for the particular syntheses, the minimum sample volume required for characterisations after the syntheses as well as the availability of the device.

1. The Paris-Edinburgh press (PEP)

The Paris-Edinburgh press is a popular large volume device, with two opposed anvils acting to create the desired pressure. As seen in figure 1.6, the press is pretty compact and its weight does not exceed 50-60 kgs, making it relatively easy to handle.

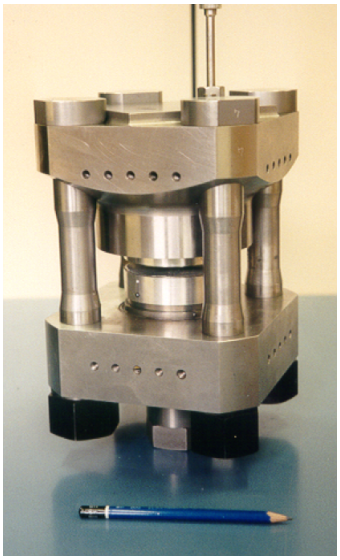

Figure 1.6: Four column Paris-Edinburgh Press. The comparison with the pencil highlights the compactness of the device. Photo taken in the laboratory at IMPMC.

The anvils

The most crucial components of the PEP are the anvils, which can be chosen depending on the pressure range that is targeted. The anvils have a circular base with a quasi-conical shape . The outer rim of the anvils are made of hard steel, while the core is usually made of the hard WC with Co or Ni binders. However, using a sintered diamond core can allow much higher pressures. The anvil consists of a special cavity in the centre,

which allows for sample assembly, as seen in figure 1.7.

Sample assembly

The sample assembly usually consists of a gasket, heater, sample capsule and electrical connection providers.

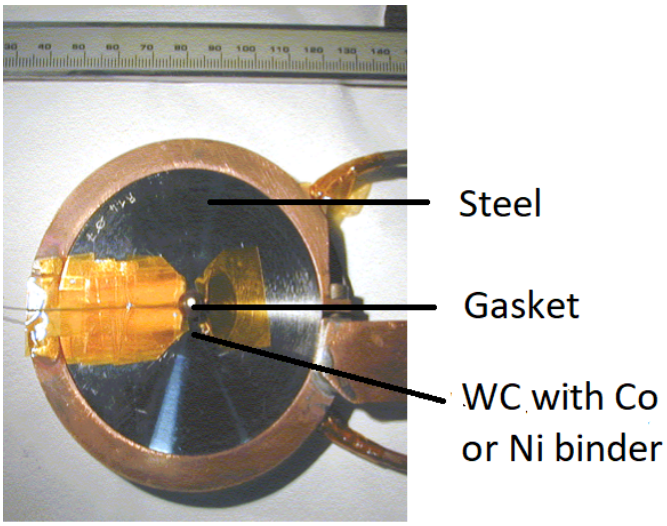

Figure 1.7: An anvil of a Paris-Edinburgh Press made of outer steel rim and inner WC with Co or Ni binder. The sample assembly is placed in its place at the centre of the anvil in the picture.

The gasket is usually made of pyrophillite or boron epoxy ceramics. Pyrophillite ($Al_2Si_4O_{10}(OH)_2$) has a low coefficient of internal friction, high melting point, low thermal conductivity which makes it a good pressure transmitting medium for HPHT experiments. However, it can be cumbersome for *in-situ* X-ray diffraction (XRD) experiments in synchrotrons. As it is a 'heavy' compound with regards to X-ray diffraction, it absorbs too much X-rays and thus produce a low signal strength to background ratio. In such cases, an amorphous boron and epoxy mixture is preferred, as its low Z value does not interfere

with the signal strength of the sample during XRD. Teflon or PEEK rings are often used around the gasket to maintain its form during compression.

The gasket assembly for the experiments performed during this work is discussed next (see Figure 1.8). The sample is placed in a hexagonal boron nitride (h-BN) capsule which acts as the sample capsule. The primary purpose of the sample capsule is to prevent direct contact between the sample and the furnace, and thus, it prevents undesirable chemical reactions between them. In our experiments, the sample capsule is crucial since boron present in the mixture as an initial reactant might react with the graphite of the heater instead of the carbon present in the reacting mixture. We chose h-BN for the capsule material as numerous studies have shown that it does not react with either boron or carbon in the (P, T) ranges of our studies [67, 68]. It is also a good thermal conductor and a good electrical insulator, which are important pre-requisites for the capsule material. The h-BN capsule is then put inside a high resistivity graphite heater. Other heaters can also be used, such as rhenium foil, or $LaCrO_3$. For the graphite heater, it can be heated through resistive heating up to 2300 K by injecting controlled electrical current from the anvils through the assembly. The graphite heater is covered at the two vertical ends with molybdenum discs to enable good electrical conduction . Finally, ceramic discs of Macor ® inside steel rings were placed over the molybdenum discs to increase the stability of the assembly and to ensure thermal insulation of the anvil. Figure 1.8 shows a schema of this gasket assembly.

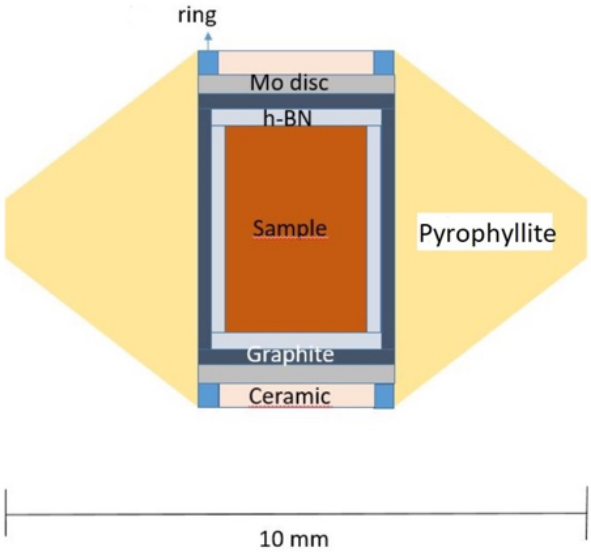

Figure 1.8: Schema of the set-up assembly used in the Paris-Edinburgh press. It shows the fired pyrophyllite gasket, the graphite heater, the hexagonal boron nitride capsule with the sample inside. The heater is covered by molybdenum rings and steel rings filled with ceramic (Macor®). The Teflon ring is not represented in the figure.

Determination of the pressure

A pressure value of up to 7 GPa can be attained by this sample assembly (for a gasket of 10mm). For *in-situ* experiments at synchrotrons, pressure calibrants with well-known equation of states are used like NaCl [69] and gold [70]. In our case, we used h-BN as pressure marker for our *in-situ* experiments [71] - this was done in order to avoid introducing other materials as pressure markers into the assembly as they might react with the carbon or boron of the sample. For *ex situ* experiments, the pressure value on the sample was determined by the value of the primary pressure on the press, using

a calibration curve that had been obtained beforehand with *in situ* experiments at the synchrotrons with pressure calibrants.

Determination of the temperature

The temperature during the synthesis was measured using a calibration curve that was obtained in an earlier work [72]. The calibration curve was obtained using the neutron radiography technique, which gives a precision under pressure of ±20 K [72]. It was then verified at the synchrotrons SOLEIL (Gif-sur-Yvette, France) and ESRF (Grenoble, France) using thermocouples. At the synchrotrons, the thermocouple was inserted coaxially and the synchrotron beam had been used to measure the exact position of the thermocouple inside the sample (with radiography). The results were coherent with the neutron radiography calibration curve.

2. The multi-anvil press (MAP)

The second kind of large volume device is the multi-anvil press. As the name suggests, this press uses several equivalent anvils which can be divided into two stages: 6 steel anvils of the first stage (primary anvils) and 8 cubes of the second stage (secondary anvils). As a result of these stages, the uniaxial compression of the hydraulic ram transforms to almost homogenous compression by the anvils of the second stage. This renders the hydostaticity of the compression generated significantly higher than that of other high pressure devices like the Paris-Edinburgh press or the diamond anvil cell. The multi-anvil press has two main designs: Walker's and DIA modules, as shown in

Figure 1.9.

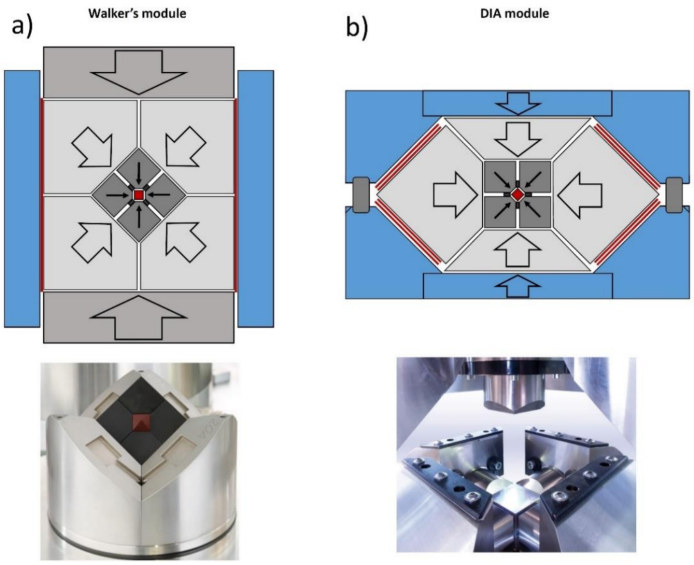

Figure 1.9: Schematic view of the multi-anvil press module types: a) Walker's module; b) DIA module. The arrows show the transformation of the uniaxial hydraulic ram compression to homogeneous hydrostatic one. The photos of the modules were taken from Ref. [73]

Walker's module

The Walker's module starts with a cylindrical cavity, filled with the six primary anvils. Kapton sheets are used to cover these primary anvils, in order to reduce friction between the metallic parts. Three of these anvils face up, while the rest face down, thus creating a new cubic cavity in the centre. This cubic cavity is where the secondary anvils are placed. The DIA module, on the other hand, consists of four independent moveable equatorial anvils and fixed bottom and top anvils as the first stage. These differences in the set up of the primary anvils leads to different geometries for the second stage anvils in the two modules - it can be taken as (111) and (100) for Walker's module and DIA

module respectively.

The DIA module

The DIA module is better suited for *in-situ* synchrotron experiments as the four equatorial primary anvils can have a horizontal groove that permits incoming and outgoing X-ray beams. Consequently, we used the DIA module for the experiments at the Synchrotron SOLEIL and the Walker's module for experiments at IMPMC, with *ex situ* characterisation.

The secondary anvils

In the next stage, the secondary anvils consist of eight cubes with truncated interior corners, as seen in Figure 1.10. These truncations facilitate the insertion of an octahedral sample assembly at the centre. The cubes of the secondary anvils themselves are made of a hard WC with Co or Ni binder. Similar to the Paris-Edinburgh cell, a sintered diamond or a cubic BN material can also be used to reach higher pressures, but they are much more expensive.

Sample assembly

As mentioned above, inside the secondary anvils, the octahedral sample assembly is placed. The octahedral material is usually MgO, with doped Cr. Figure 1.11 shows the schema of a typical sample assembly for a MAP experiment. An isolating ZrO_2 sleeve is used to separate the MgO octahedron from the heater in order to prevent overheating

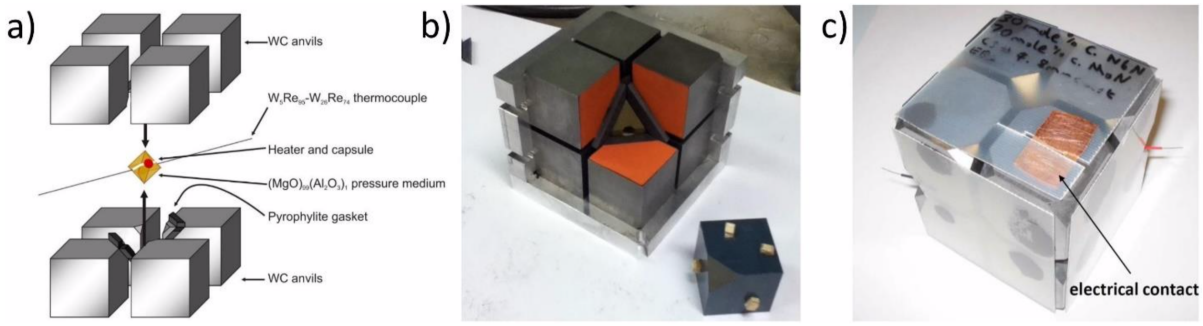

Figure 1.10: Secondary anvils used in the multi-anvil press. a) schema of the secondary anvils; b) arrangement of the secondary anvils set; c) cube made of the eight smaller components fixed by plastic-glass sheets, one of the two copper electrical contacts is marked.

of the octahedron and eventual blowout. The heater can be graphite, rhenium foil or $LaCrO_3$, similar to the Paris-Edinburgh press. The heater is chosen according to the maximum temperature that needs to be reached. Graphite heater is generally a popular choice because of its low cost, transparence to X-rays and ability to attain high temperatures. The sample capsule is placed between the top and bottom ZrO_2 plugs to restrict the heating to a small area, as well as to protect the secondary anvils from overheating.

Transmission of pressure

The gaskets which are made of pyrophillite or sometimes, boron epoxy, are glued around the truncations on four out of the eight secondary anvils. Thus, they are present along the edges of the octahedron. These gaskets, together with the MgO octahedron, serve as the pressure transmitting medium (PTM). During compression, the PTM squeezes out into the spaces between the anvils, thus maintaining the hydrostaticity of the pressure.

They also provide additional insulation between the sample assembly and the secondary anvils.

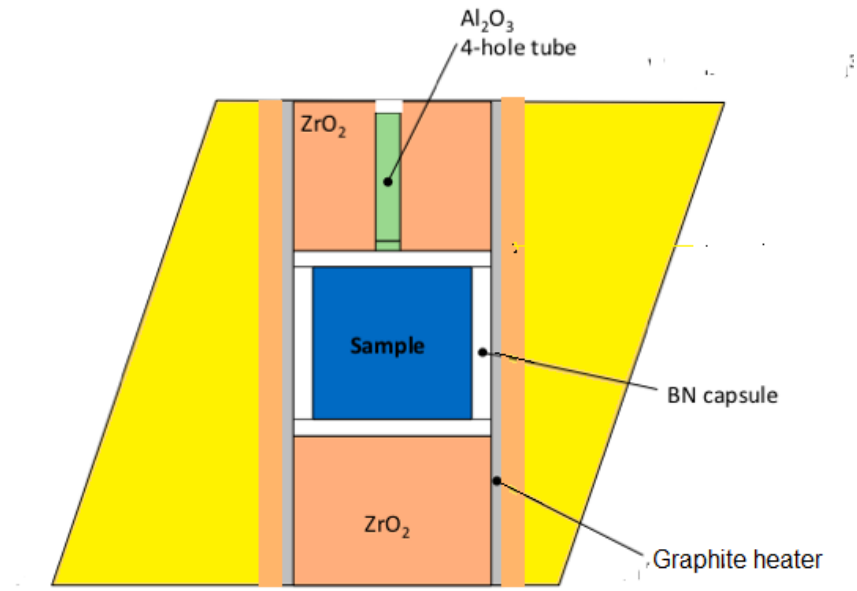

Figure 1.11: Schema of the set-up assembly used in the multi-anvil press. It shows the MgO octahedron, and the position of the ZrO_2 plugs, the graphite heater, the hexagonal boron nitride capsule with the sample inside.

Characterisation of pressure and themperature

The multi anvil press has been used for the pressure range of 10 - 15 GPa for the experiments in this thesis. Again, similar to the Paris-Edinburgh press, pressure in *in situ* experiments can be measured by the equation of state of known materials, while calibration curves are used for *ex situ* experiments. However, unlike the Paris-Edinburgh press, thermocouples (W 5% Re/ W 26% Re) are better suited to the geometry of the

multi-anvil press and thus they can be used, both *in situ* and *ex situ*, to measure the temperature of the syntheses.

3. The diamond anvil cell (DAC)

The diamond anvil cell is currently the device that is capable of reaching the highest static pressures. Pressures of around 400 GPa can be applied with the DAC and even higher values are attainable with some modifications [74]. The DAC transmits high pressures by trapping a tiny sample between the two cutlet faces of two opposed diamond anvils. Thus, a modest force applied on the wider table face of the diamond can generate an immense pressure on the smaller cutlet face, as shown in figure 1.12. Also, another great advantage of the DAC is its transparency to wavelengths above 2200 Å permitting *in-situ* Raman and other optical characterisations of the sample. Being a low Z element, it is also suitable for *in-situ* X-ray diffraction.

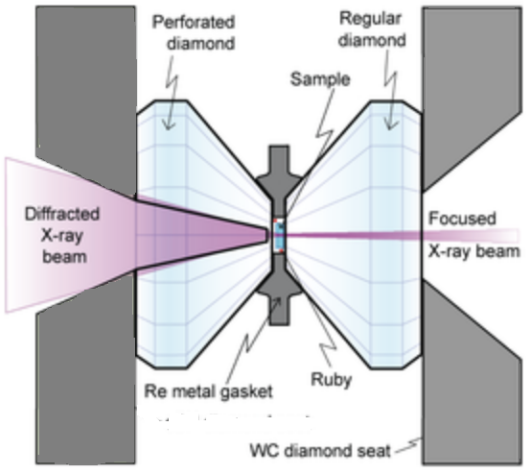

Figure 1.12: A schema of the generalised diamond anvil cell. The picture has been extracted from Ref. [75].

The gasket is generally a thin metal disc (usually rhenium) with a small hole that has the diameter of about half of the cutlet face. It is made by indenting the diamond into the metal disc and then drilling a tiny hole using a high energy micro-focused laser, or even, electro-erosion. The pressure transmitting medium (PTM) used is generally a soft solid or a fluid such as NaCl, KCl, nitrogen, ethanol, methanol, or argon. Gases such as argon, helium are popular because of their chemical inertness. However, some care is needed while selecting a PTM for high pressure experiments, since many candidates tend to crystallise with increasing pressure, which creates a quasi-hydrostatic environment and introduces errors in the experiments. In our experiments, KCl was chosen as the pressure transmitting medium, due to its transparency that helps with laser heating (discussed below) and its insulating properties that prevents heat dissipation as well as protects the diamonds from damage.

In our studies, we used membrane diamond anvil cell (MDAC) where a metallic toroidal membrane pushes on the piston when it is inflated by helium. The membrane initially generates an uniaxial force, which is then homogeneously spread all over the piston, thus allowing precise control of the pressure without touching or displacing the cell. The membrane is connected to the helium source through a pressure pneumatic drive system (PDS). Moreover, micro-valves present in the device also allow us to keep a high pressure value in the cell even when it is disconnected from the PDS.

Calibration of pressure

The DAC has been used to generate pressure in the range of 15-60 GPa. The pressure has been calibrated using both ruby and the diamond itself as an internal pressure standard at ambient temperature. Ruby is chemically inert, and has a strong fluorescence when it comes in contact with green laser light. The position of these fluorescence lines change with pressure and is well-known [76, 77]. This makes monitoring the ruby fluorescence a very popular strategy for pressure calibration. However, at elevated temperatures, ruby fluorescence peaks widen and decrease in intensity - they can no longer be used for pressure measurement above 700 K. The diamond from the anvils were used as the secondary pressure calibrant.

For determining the pressure under high temperature conditions, we can measure the change in unit cell size of a material whose equation of state is known, such as Au, Pt or MgO. However, *in-situ* XRD is required for this, and this strategy cannot be utilised in *ex-situ* conditions.

Heating system

Unlike large volume presses, resistive heating is not the only way of producing a high temperature value in a diamond anvil cell. While resistive heating can indeed be used for temperatures up to 1200 K, laser heating is crucial to obtain extremely high temperatures of up to 5000 K [78, 79]. The drawback of laser heating, however, is that the high temperature is only produced at the spot where the laser strikes the sample, leading to

very localised heating. In our experiments, we have used double sided laser heating to melt boron carbide under pressure. Double sided laser heating alleviates the problem of having a huge temperature gradient between the side of the sample where the laser heats and the other side.

4. The rotational tomographic Paris-Edinburgh cell (RoToPEC)

The rotational tomographic Paris-Edinburgh cell (RoToPEC) is a modification of the conventional Paris-Edinburgh Press which allows controlled torsional shear stresses between the opposed anvils [80], as shown in figure 1.13. The press is heavier than the conventional PE press at 197 kilograms because of its additional rotational components. Nonetheless, it can be easily disassembled and transported for performing *in-situ* experiments.

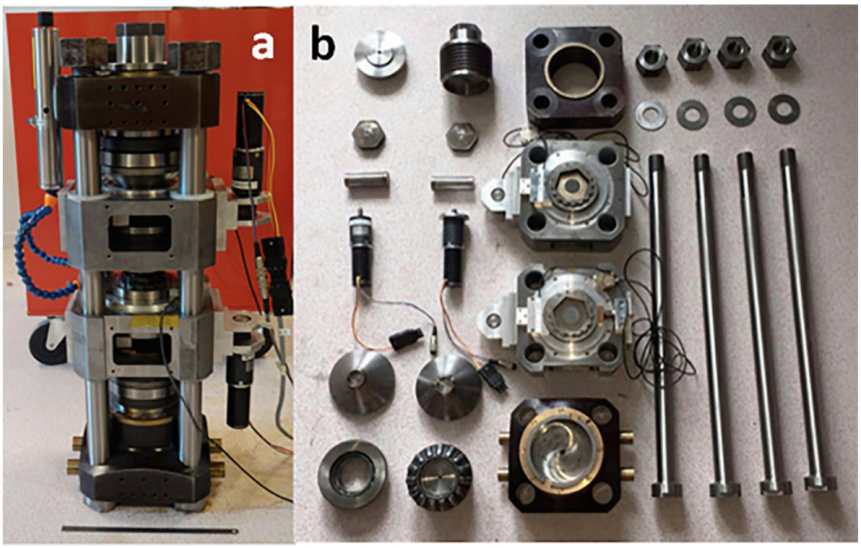

Figure 1.13: (a) Assembled RoToPEC, (b) Disassembled RoToPEC. The photos have been extracted from Ref. [80].

The most important aim of the ROTOPEC is to impart torsion to the sample inside the device, in order to put it in plastic regime. This allows vacancies and point defects to form in the sample. To this end, both anvils can rotate independently under pressure with no limitation in angle, thus permitting access to a huge range of stress regimes.

Working principle

The main difference between a RoToPEC and a standard PE cell is the presence of additional components that allow the independent rotational motion of the opposed anvils. The working principle of the RoToPEC is explained in the current section with the help of some magnified schematic cross-sections of the device. As the device is symmetric, only the bottom section is selected for the explanation. As shown in figure 1.14, the hydraulic ram pushes a part (#1 in figure) which transfers the force from the piston to the spherical thrust roller bearings (#2 in figure). Next, the conical part (#3 in figure) transmits the force on part (#4 in figure) mounted freely through the gearbox (#5 in figure). The part #4, in turn, applies it on the WC cross-section (#6 in figure) of the hexagonal anvil seats (#7 in figure).

As shown in Figure 1.15, the anvils (A) are inserted in the housing (C), which is fixed to the output of the reduction gearing (D). This gearbox (D) can produce a maximum local torque of 892 Nm, which is the main limiting factor of the RoToPEc. The gearbox has a reduction ratio of 160:1 and a yield of 0.6 at low speed - consequently, 9.3 Nm must be applied to the input of the gearbox to generate the necessary torque for rotation of the anvils. To facilitate this, a gear with tailored dimensions (E) is fixed to the input of

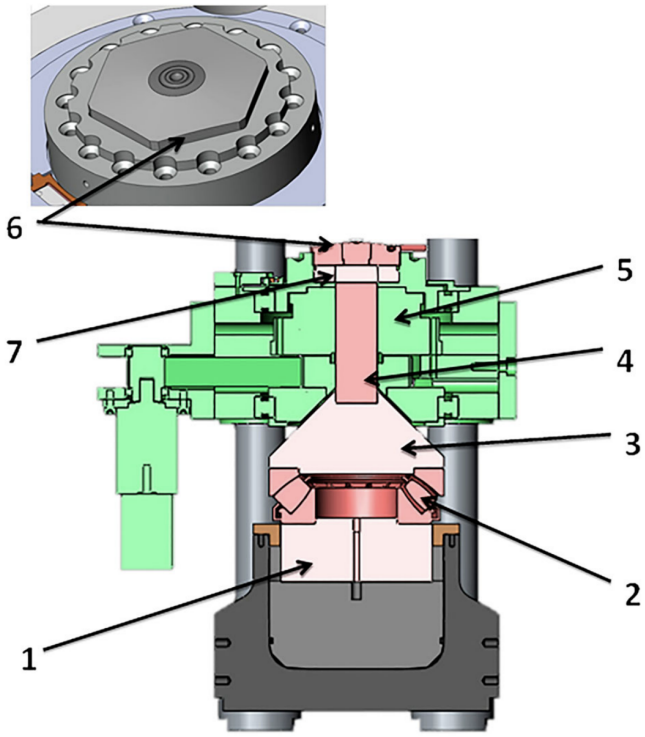

Figure 1.14: Magnified schema of the bottom part of the RoToPEC, detailing pressure transmission in the device. The number labels are explained in the text. The schema has been extracted from Ref. [80]

the gearbox and associated to a timing belt (F) and a second gear (G). This belt-pulley system has a further reduction ratio of 3:1 and a yield of 0.8. Therefore, the pulley attached to the motor shaft must finally provide 3875 Nm. However, the gear motor consisting of a motor (I) allowing 197.8 mNm of torque and a reducer (H) of ratio 100 with a yield of 0.65 can provide an oversized torque of 12,857 Nm, thereby comfortably exceeding the requirements. The rotation of the pulley is driven by ball bearings using an original motor support which is fixed to a sliding support. The latter, through tubular

nylon parts, slides with precision in compression along the columns of the press. On this sliding support, the ball bearings offer a very high precision guide for the rotation of the anvils. The motors which performs the anvil rotation are controlled with two encoders placed directly on the anvils, which provides much more accurate control.

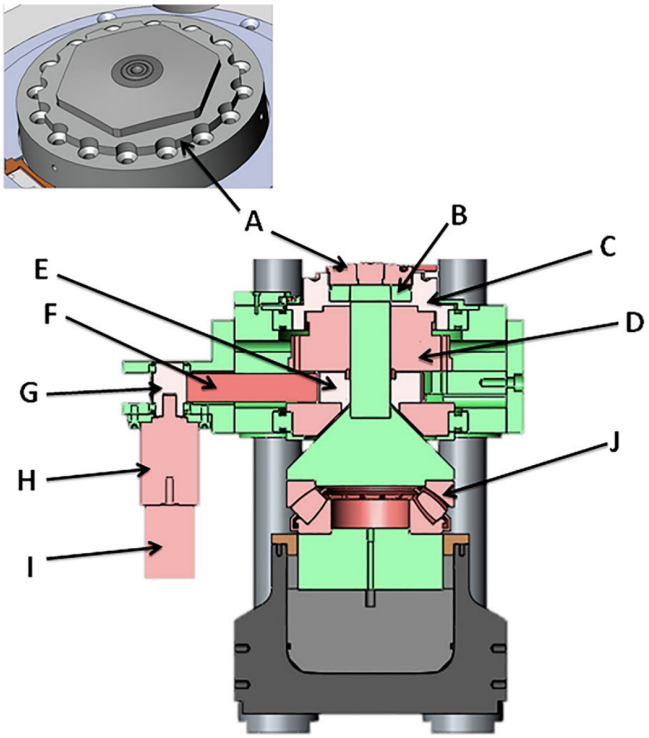

Figure 1.15: Magnified schema of the bottom part of the RoToPEC, detailing anvil rotation in the device. The alphabet labels are explained in the text. . The schema has been extracted from Ref. [80]

Heating system

The heating system of the RoToPEC is different from the conventional PE press. The electrical current is provided by an external copper piece which is compressed against

the anvil housing (C in Figure 1.15) using a spring. The copper piece has a shape adapted for allowing the anvils to rotate without interference. A coldstream air gun is used to provide cooling to the system to prevent the anvils and other parts from heat damage.

The RoToPEC has been used at a pressure of 5 GPa for our experiments, with varying degrees of rotation of the anvils to provide a comparative study of the induced deformations.

1.3.2 Experimental techniques: characterisation

The samples synthesised through the high pressure and high temperature devices described above were characterised using several techniques such as Raman Spectroscopy, X-Ray diffraction (XRD), Electron Dispersive Spectroscopy(EDS). These techniques are well-suited to both ambient and extreme conditions. Moreover, they are suitable for tiny amounts of samples, as obtained in HPHT syntheses, and are non-destructive. NMR (Nuclear Magnetic Resonance) could be an useful technique to identify the C-C chains (see Sec 1.1.1) but the produced sample volume has proved to be insufficient for this technique so far. Scanning Electron Microscopy (SEM) is used selectively to image some samples whenever needed.

X-ray diffraction (XRD)

X-Ray diffraction is a very popular tool for discovering information about the crystal structure of materials. The XRD 'signature' is also used to either identify crystals

or determine the structure of new crystals through refinement. While the study of crystal structure started as early as the 17th century and Wilhelm Röntgen discovered x-rays in 1895, the field of X-ray diffraction for studying crystal structure finally took off with the pioneering work of Von Laue in 1912 [81]. The field developed rapidly thereafter, the most notable being the efforts of William Henry Bragg and his son William Lawrence Bragg. The younger Bragg developed the Bragg's Law (see equation 1.2) and the father and son duo shared the 1915 Nobel Prize in Physics for their work in crystallography [82].

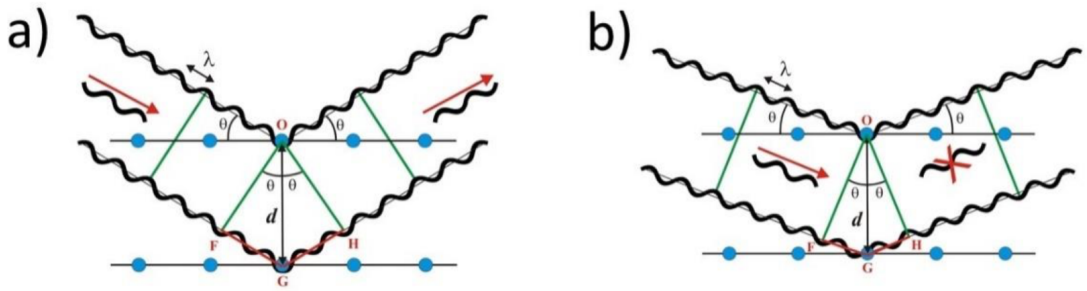

Figure 1.16: Diffraction of monochromatic X-ray on a regular array of atoms or 'scatterers': a) reflected waves are in phase, creating constructive interference b) reflected waves are in opposite phase, creating destructive interference.

The principle of XRD is demonstrated in figure 1.16. In a given crystal, the regular array of atoms form the scatterers on which electromagnetic waves, in this case, X-rays, impinge. The waves are scattered elastically by the atoms. The scattered waves face either destructive or constructive interference. The condition for constructive interference is given by Bragg's Law in equation 1.2.

$$2d_{hkl}sin\theta = n\lambda \tag{1.2}$$

where λ is the wavelength of the x-ray used, d_{hkl} or simply put, d is the atomic spacing between two planes, θ is the angle of incidence (and also, reflection) and n is an integer. Through Bragg's law, the structure of the crystal unit cell could be determined using the d value. However, in order to find out the symmetrical relationship between the atoms in the unit cell i.e their space group, we have to look at the relative intensities of the peaks. This is given by the diffracted wave amplitude, given by equation 1.3,

$$F_{hkl}(\overline{h}) = \sum_i f_{at,i}(\overline{h}) e^{-2i\pi(\overline{h}).\vec{r}_i} \tag{1.3}$$

where

$$f_{at,i}(Q) = \int_V^0 dV \rho_e(\vec{r}) e^{-2i\pi Q.\vec{r}_i} \tag{1.4}$$

Here, F_{hkl} is the structure factor, $f_{at,i}$ is the atomic form factor, $\overline{h}$ is the reciprocal lattice vector, ρ_e is the local electron density, $Q = k - k'$ is the momentum (k and k$'$ are the incident and scatterted wave vector respectively). The structure factor is crucial for atomic position refinement. Two important XRD techniques are Angle Dispersive XRD (ADXRD) and Energy Dispersive XRD (EDXRD).

In ADXRD, a monochromatic incident x-ray beam is used. The sample is rotated, which leads to change in the value of θ (equation 1.2). As λ is kept constant by the choice of the x-ray source, we obtain d_{hkl} as a function of θ. The ADXRD technique, in conjunction with a flat panel detector, can be considered as 2D ADXRD. It gives access to the 2D projection of the whole cone of the diffracted X-rays. Thus, 2D ADXRD is a very important tool to study crystal structure as it gives high quality data related to

d-spacing, atomic coordinates, space group, and preferential orientation in polycrystals. However, there are some drawbacks such as the relatively long acquisition time, and the need of greater spatial accessibility etc.

EDXRD is a technique that is more suited to synchrotron facilities. It uses polychromatic XRD beam at a constant angle ($2\theta_o$). To better understand the principle of EDXRD, it is necessary to apply Plank's equation($\lambda\epsilon = 12.398$ where λ is in $\mathring{A}$ and ϵ is in keV) to Bragg's Law (equation 1.2). This gives

$$\epsilon = \frac{6.199}{dsin\theta} \tag{1.5}$$

As seen from equation 1.5, at constant θ, EDXRD gives d values as a function of energy values ϵ. However, EDXRD has several drawbacks compared to ADXRD. The most important of these drawbacks is the lack of access to the entire cone of the diffracted X-rays, as only a part of it can be observed through the fixed ($2\theta_o$) angle. As seen in figure 1.17, the blue strip represents the EDXRD pattern compared to the entire 2D pattern given by ADXRD. Since the height h of the blue strip is insignificant compared to the entire cone of diffracted x-rays, EDXRD patterns are considered as 1D, which makes them of lower quality than ADXRD and unsuitable for detailed structure refinements. Moreover, other factors like the presence of fluorescence peaks, the limitation of the input count rate, the presence of a much greater background also work against the quality of the EDXRD data. However, EDXRD has undoubtedly some advantages with respect to ADXRD: the measurement of energies of all of the scattered electrons occurs simultaneously in this technique, and the summing of the different channels into the spectrum only takes

a few microseconds or picoseconds , thus greatly speeding up the acquisition time. This allows for a rapid structural analysis which is crucial for metastable phases as well as to study structural changes over time in synchrotrons.

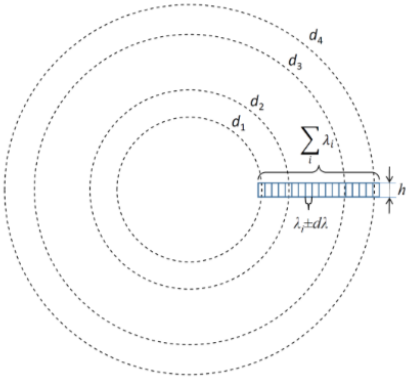

Figure 1.17: Schematic representation of ADXRD and EDXRD. ADXRD gives the entire 2D pattern in the picture, while EDXRD only gives access to the blue strip. The picture is taken from Ref. [83]

In conclusion, we can consider ADXRD and EDXRD to be complimentary techniques to be chosen depending on the aim and scope of the experiments.

The ADXRD powder diffraction patterns have been recorded in this work at IMPMC using a X'Pert ProPanalytical diffractometer equipped with a Cu Kα radiation source ($\lambda_{K\alpha 1}$ = 1.5406 Å, detector: XCelerator) in the Bragg Brentano geometry (0.04 ° Soller slits, 0.5 ° programmable divergence slit, 1° incident antiscatter slit, and 0.5 ° diffracted antiscatter slit, 0.04° Soller slits, and Iron filter.

The EDXRD patterns have been obtained at the Synchrotron Soleil, which has been explained more in detail in Sec 1.3.3.

Raman spectroscopy

Raman spectroscopy is a non-destructive technique to probe the chemical composition of materials, through detecting the vibrational, rotational and other states of its molecular system. Inelastic scattering of light, which is the premise on which the Raman effect lies, was predicted as far back as 1923 by Adolf Smekal [84]. However, it was observed in practice for the first time in 1928 in organic liquids by Indian scientists C.V. Raman and K.S. Krishnan. Raman won the Nobel Prize in Physics for this discovery in 1930 [85]. Later on, the theory of Raman effect was developed by Czechoslovak physicist George Placzek between 1930 and 1934.

When a monochromatic beam of light passes through a material, it affects the electric polarizability of the molecules. This creates an induced dipole moment, which further leads to bond oscillations in the material. This results in an outgoing radiation with some peculiarities. The outgoing radiation mainly shows a peak whose frequency ω is the same as that of the incoming light. At the same time, some satellites are present symmetrically around this peak with slightly different frequencies ($\omega \pm \delta\omega$) and much lower intensities. The main peak with frequency ω corresponds to the elastic scattering of light, and is called the Rayleigh peak. The satellite peaks are known as Raman peaks - the one with frequency ω - $\delta\omega$ is known as the Stokes peak, and that with frequency ω + $\delta\omega$ is known as the anti-Stokes peaks. The appearance of these satellites goes under the name of Raman effect, after the Indian physicist C.V. Raman. The frequency shifts between the Rayleigh and the Raman peaks correspond exactly to the frequency of the

oscillation of the nuclei in the material. This makes Raman effect a very powerful tool for probing the vibrational properties of materials, and through this, draw conclusions about their chemical natures.

At IMPMC, the Raman spectroscopy is taken in back-scattering geometry, using a Horiba Jobin Yvon HR800 Raman spectrometer with $\times$ 10 and $\times$ 20 objectives. The 514.5 nm line of an Ar^+ laser, with 5 μm beamspot, is used to measure the atomic vibration frequencies in the samples.

Scanning Electron Microscopy

Scanning electron microscopy (SEM) is a technique for high resolution imaging of the surface of materials. This technique provides much higher magnification of the samples (greater than 10^6 times) and better depth of field (up to 100 times) than that of traditional light microscopy. Moreover, using an energy dispersive spectrometer along with SEM can provide qualitative and quantitative information about the chemical composition of the material as well. SEM can be traced back to Manfred von Ardenne in 1937 [86] who first demonstrated a microscope with high resolution by scanning a very small area with a finely focused electron beam. Further work was done by several other groups in laboratories across the world, specially in Cambridge in 1950s and 1960S, which finally led to the first commercial instrument by Cambridge Scientific Instrument Company in 1965.

During SEM, an incident electron beam (in an energy range from 100 eV to 30 keV, depending on the sample) is used on the sample surface in a raster pattern. This causes

elastic and inelastic scattering at (and near) the surface of the sample. The high energy electrons that are emitted by an elastic scattering event are known as backscattered electrons, and their energy is comparable to the incident electron beam itself. However, the non-elastic scattering events such as collisions with a nucleus of the sample atom causes a substantial loss of energy - these lower energy emitted electrons are known as secondary electrons and their energy values are typically smaller than 50 eV.

A detector is then used to collect these emitted electrons from each position in the scanned area. The brightness displayed on a display monitor is a function of the intensity of the emitted electron signal, thus providing the morphology of the scanned area on the sample surface. To get high resolution images, a high vacuum is used to allow the electrons to travel without interruption from the sample surface to the detector. A biasing positive voltage is also used on the detector to improve the signal to noise ratio.

At IMPMC, a SEM-FEG Zeiss Ultra55 scanning electron microscope was used to image the samples.

Electron Dispersive X-Ray Spectroscopy

Electron dispersive X-Ray spectroscopy, commonly known as EDS or EDX, is a chemical microanalysis tool which is often used in conjunction with SEM.

When the sample is bombarded with an electron beam during SEM, the atoms of the sample surface give up their electrons. This electron vacancy is filled by other elec-

trons coming in from a higher state, along with the emission of X-rays, whose energy is characteristic to the element it was emitted from. The EDS detector measures the relative abundance of the emitted x-rays as a function of their energy, thus providing some information about the chemical composition of the sample.

The emitted X-ray energy values from the sample are compared to known characteristic X-ray energy values to establish the presence of a given element in the sample. Though it is more precise for heavier elements, atomic numbers ranging from Be (Z = 4) to U (Z = 92) can in principle be detected. An elemental mapping can be performed through EDS since the X-ray intensity is measured relative to its lateral position on the sample. Such maps are recorded using different colours as a function of the local relative concentration of the elements present.

1.3.3 Experimental techniques: Synchrotron facilities

A synchrotron is, by definition, an accelerator of elementary particles, commonly electrons. For the current work, we are only concerned with the light source type synchrotron. It can be divided into three main parts: linear particle accelerator where electrons are produced and initially accelerated; next, they are injected into the booster where they are pre-accelerated to GeV energies in synchrotron mode; and finally the storage ring where their energy achieves the working value of 2-8 GeV. The electrons are then manipulated to follow an undulating or wavy trajectory in the storage ring by insertion devices with periodic magnetic structures such as wigglers and undulators. This results in the emission of the magnetic Bremsstrahlung radiation at each bend,

which is known as the synchrotron radiation.

Synchrotron radiation differs dramatically from conventional X-rays that are used to characterise samples in the laboratory through XRD. The most important properties of this radiation are spectral continuity ranging from infrared to X-rays, the weak divergence of emission in the vertical plane, billions of times greater flux and luminance than in classic X-ray sources, polarisation in the horizontal plane, temporal structure in pulses, and certain spatial and temporal coherence. This makes the synchrotron radiation a very powerful tool for studying materials under extreme conditions, since it allows us to perform *in-situ* characterisation of the systems.

In the current work, the *in-situ* XRD results under high pressure and temperature (HPHT) conditions have been obtained using the facilities at the PSICHE beamline in the synchrotron SOLEIL, which is a 3^{rd} generation facility. PSICHE (Pressure, Structure and Imaging by Contrast at High Energy) beamline deals with tomography and *in-situ* characterisation under regular and high pressures using hard X-ray diffraction at ambient or high temperatures. The beamline delivers three different beam modes: the white beam mode (15-80 keV), the pink beam mode (filtered white, 25-70 keV) and the monochromatic beam mode (20 - 50 keV). Our experiments with large volume presses were performed in the white beam mode, which can result in a beam flux of up to 3×10^{15} phonons/s for 12×3.5 mm^2 spot size.

Apart from energy dispersive XRD (EDXRD) techniques EDXRD, the beamline is also equipped with combined angle and energy dispersive structural analysis and refinement

(CAESAR) system. The CAESAR system was originally proposed by Wang *et al.* [87]. Whereas EDXRD is advantageous in large volume press experiments in synchrotron environments because of its rapid acquisition time, background and waste signal removing efficiency, and high efficiency in working with limited sample volume and aperture, it has numerous disadvantages as well, as discussed in Sec. 1.3.2. The principal among these disadvantages are the complex corrections for intensity required for Rietveld refinement and the presence of detector artifacts. 1D *in-situ* ADXRD techniques can be used to overcome these shortcomings, but they require much longer acquisition times and a special soller slits system to remove the signal from the sample environment [88]. Thus, the combination of the complementary ADXRD and EDXRD in one system, as done in CAESAR, overcomes their respective drawbacks. During such measurements, the Ge detector spans the 2θ range (0 - 30°) and collects a series of 1D EDXRD data as a function of 2θ, over several thousand channels, covering the photon energy range, as shown in Figure 1.18. Thus, the data set forms a two dimensional array: Intensity (ϵ, 2θ). They can then be regrouped according to photon energies, giving rise to a great number of ADXRD (Intensity *vs* 2θ) data. As a result, using CAESAR, we can take advantage of the considerably faster EDX acquisition mode to get a vast set of ADX patterns in the whole energy range.

1.3.4 Theoretical techniques: density functional theory

The theoretical 'first principles' or '*ab initio*' approach is a bottom up modelling on the quantum level for materials [89]. It uses quantum mechanics to understand and predict

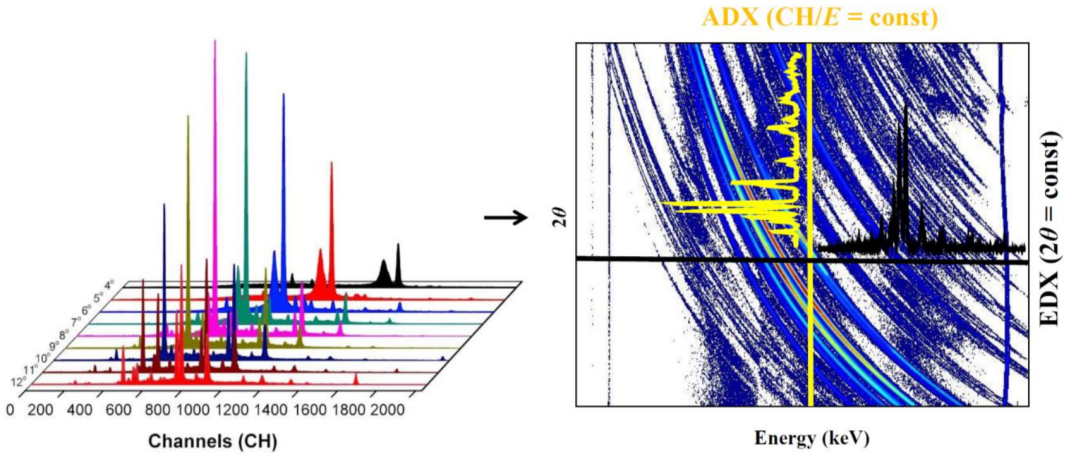

Figure 1.18: Representation of the set of EDXRD data in the 2D array in CAESAR.

material properties without relying on empirical parameters. This is a very powerful tool, especially in the domain of the design of new materials since not much experimental data would be available in the first place.

The basic equation that drives material modelling is the time independant many body Schrödinger equation,

$$\left[-\sum_i \frac{\hbar^2}{2m_e}\nabla_i^2 - \sum_I \frac{\hbar^2}{2M_e}\nabla_I^2 + \frac{1}{2}\sum_{i\neq j}\frac{e^2}{4\pi\epsilon_o}\frac{1}{\mid r_i - r_j \mid} + \frac{1}{2}\sum_{I\neq J}\frac{e^2}{4\pi\epsilon_o}\frac{Z_I Z_J}{\mid R_I - R_J \mid} - \sum_{i,I}\frac{e^2}{4\pi\epsilon_o}\frac{Z_I}{\mid r_i - R_I \mid}\right]\Psi = E_{tot}\Psi \tag{1.6}$$

Here, the first two terms refer to the kinetic energy of the electrons and nuclei with masses m_e and M_e respectively in the many body system. The third term is the sum over the Coulomb repulsion between an electron pair. The fourth term is the sum of the Coulomb repulsion between a pair of nuclei, and the fifth term is the sum of the Coulomb repulsion between an electron and a nucleus. Finally, E_{tot} is the total energy

of the system.

The clamped nucleus approximation assumes that the nuclei are held immobile i.e clamped in already known positions, since their mass is much heavier compared to electrons. Thus the second term in equation 1.6 is neglected and the fifth term amounts to a constant. In a second step, one relies on Hohenberg and Kohn theorem, which states that there is a one-to-one correspondence between the external potential felt by the electrons, and the ground state properties. Thus, each ground state observable can be expressed as a functional of the density. Moreover, the ground state density can be obtained by the minimisation of the total energy functions. Thirdly, in order to express total energy as a function of the density, one relies on a mean field approximation, which is at the basis of the Kohn-Sham equations. The kinetic energy is expressed by the kinetic energy of a non-interacting system: $T^{ks} = -\frac{\hbar^2}{2m}\nabla^2$. This, however, cannot be explicitly expressed as a functional of the density, but only as a functional of the Kohn-Sham orbitals. Then, the Coulomb repulsion is replaced by the Hartree potential V_H, given by equation 1.7, which is the 'average' potential experienced by each electron due to the density of the other electrons.

$$\nabla^2 V_H(r) = -4\pi n(r) \tag{1.7}$$

However, the mean field approximation treats electrons as classical particles. To remedy this, it is assumed that the electrons interact weakly and an additional potential V_X is added to the equation. V_X is derived from the Fock exchange operator and arises

from Pauli's exclusion principle, thus moving us back to quantum physics from classical territory. In the DFT, V_X also contains all of the many-body kinetic terms that have not been accounted for in T^{ks}. Finally, another potential term, V_C, is also added to account for the correlation between electrons. All these above mentioned approximations, combined with using atomic units some algebra to simplify the equation, map equation 1.6 into equation 1.8, also known as the Kohn-Sham equation.

$$\left[-\frac{\nabla^2}{2} + V_n(r) + V_H(r) + V_x(r) + V_c(r) \right] \phi_i(r) = \epsilon_i \phi_i(r) \tag{1.8}$$

Here, V_n is the Coulomb potential of the nuclei experienced by the 'Kohn-Sham' particle. The exchange potential V_X is approximated.

In the simplest local density approximation, the exchange potential at r is replaced by the exchange potential of an interacting electron gas having the same density.

$$V_X(r) = V_X(n) \tag{1.9}$$

where $n = n(r)$. However, unlike the exchange potential, we do not have a simple analytic expression for correlation energy $V_c(r)$ even for the interacting electron gas system. Thus, it is approximated by removing the known kinetic, Hartree and exchange contributions from the calculated total energy by Ceperley textitet al [90] and was subsequently parametrized by Perdew textitet al. [91]. Thus the correlation energy also becomes dependent on density, as in equation 1.9. Even though we now deal with several potentials

such as V_x and V_c whose exact forms are unknown, we have gained by mapping the initial many body wavefunction Ψ onto single particle wavefunctions ϕ_i.

Finally the total energy of the system is given by

$$E = F[n] + T[n] \tag{1.10}$$

This leads to equation 1.11

$$E = F[n] + T[n] = E_{ext}[n] + T[n] + E_H[n] + E_{xc}[n] \tag{1.11}$$

where $E_{ext}[n]$ is the external energy potential,$T[n]$ is the kinetic energy, $E_H[n]$ is the Hartree energy, and $E_{xc}[n]$ is a combination of the exchange and correlation energies.

The ground state density n_o can be determined through the Hohenberg-Kohn variational principle which states that n_o is precisely the function that minimises the total energy E. This minimisation yields equation 1.8. As already stated, the formalism would be exact in principle if we had exact values of the exchange and correlation potential V_{xc}. This is, however, not exact and we use approximations such as the LDA (Local Density Approximation) or the GGA (Generalized Gradient approximation) to practically solve equation 1.8.

The practical procedure for solving the Kohn-Sham equation (equation 1.8) is through self-consistent calculations. We begin by guessing a possible electron density $n(r)$ in

order to get a preliminary approximation to the Hartree and exchange and correlation potentials, through equations 1.7 and 1.9 and then the total potential through equation 1.11. Then, equation 1.8 is solved numerically, leading to new wavefunctions ϕ_i. These wavefunctions are then used to give a better estimate of the density n, using equation 1.12.

$$n(r) = \sum_i |\phi_i(r)|^2 \tag{1.12}$$

This loop of generating a new density n each time, and thereby refining the other energy values, is continued until the difference between the old and the new density falls within some desired tolerance value, thus leading to the achievement of self-consistency.

We used QUANTUM ESPRESSO [92], [93] suit of software to take advantage of DFT to calculate pertinent properties of some materials. The most important of these properties that we studied was the equilibrium structure of the materials while designing the ternary phase of boron, silicon and carbon.

Chapter 2

Boron carbide synthesis at moderate pressure (up to 5 GPa) *in situ* and *ex situ*

2.1 Introduction

Numerous studies have been performed on the synthesis of boron carbide with various reactants at ambient pressure, and also at low pressures (<50 MPa) with the hot pressing technique [18, 22]. Hot pressing results in the formation of dense boron carbide powders by mixing fine and pure powders of beta rhombohedral boron and graphite under a pressure lesser than 50 MPa and high temperatures. There have been several studies on the properties of boron carbide crystals at high pressures [42, 94–97]. However, only

one study has reported the synthesis of crystalline boron carbide without disorder at 8 GPa but the synthesis reactants are not detailed [98]. Boron carbide single crystal nanoparticles have also been synthesised in vacuum [99] and single crystalline boron carbide nanobelts have been synthesised using chemical vapour deposition (CVD) at atmospheric pressure [100].

So far, no study has recorded the synthesis parameters of boron carbide from its elemental components at high pressure. One of the main purposes of the current chapter is to fill this gap in the scientific literature. Consequently, I have done a systematic study of the formation of boron carbide at high pressure in order to fix the optimum parameters for synthesis, thereby establishing the domain of formation of boron carbide, and eventually discovering (a) new crystalline phase(s). It is also useful to focus on the synthesis from the elements in the first step of the study, as this not only leads to the purest products but also simplifies the characterisation process [101].

In the present chapter, I have mainly documented the optimum (P, T, reactants) parameters of the synthesis of boron carbide from elements (boron and carbon) under two values of high pressure - 2 GPa and 5 GPa. These results have also been partially presented in the International Symposium on Boron, Borides and Related Materials (ISBB) 2019 and published later [102].

At the same time, I have tried to find evidence of metastable C-C chains in boron carbide during the *in situ* syntheses using the PE press at the Soleil synchrotron. The existence of these chains has been predicted by Betranhandy *et al* [45] in the pressure range of 5

-7 GPa. The authors have calculated that upon exerting pressure, the vacancies, noted as "□", in the chain centre of the unit cell (($B_{11}C^p$) C□C) disappear and are replaced by C-C chains. Thus, the dangling bonds disappear and, instead, a carbon-carbon bond is formed. However, this ($B_1 1C^p$)C-C structure is metastable and thereby can only be identified in real time during synthesis through *in situ* X-ray diffraction. These C-C chains, if found, would be the first confirmed experimental record of the C-C chains in boron carbide and thus, it is of interest to us as we look to reinforce the dynamical strength of boron carbide. The role that C-C chains play in reinforcing boron carbide has been explained in detail in Sec 1.1.1 of Chapterβ boron1.

2.2 Experimental materials and methods

In the first set of *ex situ* experiments, crystalline β boron (Prolabo, purity 99.9 % , particle size 1-10 microns) and glassy amorphous carbon (Sigma-Aldrich, purity 99.95 % trace metals basis, particle size 2 – 20 microns) have been mixed in a mortar and pestle for 5 minutes in the stoichiometric ratio of 4:1. The same set of *ex situ* experiments has then been repeated after changing the reactant mixture into crystalline β boron and graphite (Goodfellow, purity 99.997 %, maximum particle size 75 microns). A third set of *ex situ* experiments was also done using amorphous boron (Pavezyum, purity >98.5 %, particle size <250nm) and glassy amorphous carbon as reactants.

All the *ex situ* syntheses have then been performed using the large-volume four-column Paris-Edinburgh press VX5 [103, 104] at two different pressures, 2 ± 0.2 GPa and 5 ±

0.2 GPa, under temperatures ranging from 1673 ± 20 K to 2573 ± 20 K, with a dwell time of 2 hours.

During each synthesis, the sample has been compressed slowly, in approximatively 4 hours, and once at the target pressure, the temperature has been increased at the rate of 2 K/s. The duration of the dwell time of the desired temperature was 2 hours, i.e. the maximum duration found in the literature for experiments at low pressure [105]. This should allow enough time for the elemental boron and carbon to diffuse and undergo the solid state reaction to form boron carbide. In order to verify that two hours was indeed enough to reach equilibrium, some of the experiments have been repeated for four hours each. The products formed in these experiments (duration: 4 hours) were identical to those formed during the 2 hour syntheses.

After the heating, the sample has been quenched rapidly and then slowly decompressed during 6 hours. The gasket has then been broken carefully and the synthesized product has been recovered. The process of the sample recovery from the gasket has sometimes led to the unwanted presence of a very small amount of boron nitride in the product, since boron nitride capsule formed the innermost part of the gasket assembly that hold the reactants.

The benefit of using a large volume press is that enough sample volume is produced to facilitate *ex situ* characterisation techniques. Therefore, the synthesized product has been characterised *ex situ* through X-ray diffraction and Raman spectroscopy. Scanning Electron Microscopy has been used to determine the grain size of the synthesized boron

carbide.

In situ experiments have also been performed at the PSICHE beamline in the Soleil synchrotron in order to identify the formation of the metastable C-C chains which have been predicted to form between 5-7 GPa [45].

2.3 Results of *ex situ* experiments

From the scientific literature, it has been observed that dense boron carbide ceramics form from commercial β boron and graphite at temperatures around 1573 K under pressure values less than 50 MPa by the spark plasma sintering method [105], as well as by the hot pressing method [106]. However, so far, there had been no study using different allotropes of elemental boron or carbon. It turns out that the allotropes have an effect on the initiation temperature, as our study will show.

The X-ray diffraction (XRD) of the synthesis from crystalline β boron and amorphous carbon at 2 GPa, as reported in figure 2.1, shows only the presence of β boron at synthesis temperatures of 1673 K and 1873 K. No boron carbide was formed at these temperatures. At 2073 K, significant change occurs in the powder XRD pattern, as boron carbide forms. The relative intensity of the boron carbide peaks becomes stronger with the increase of the synthesis temperature, while the relative intensity of the β boron peaks diminishes.

At 5 GPa, the temperature of the product formation varies significantly from what has been reported above for 2 GPa. Unlike what has been seen in the above-mentioned

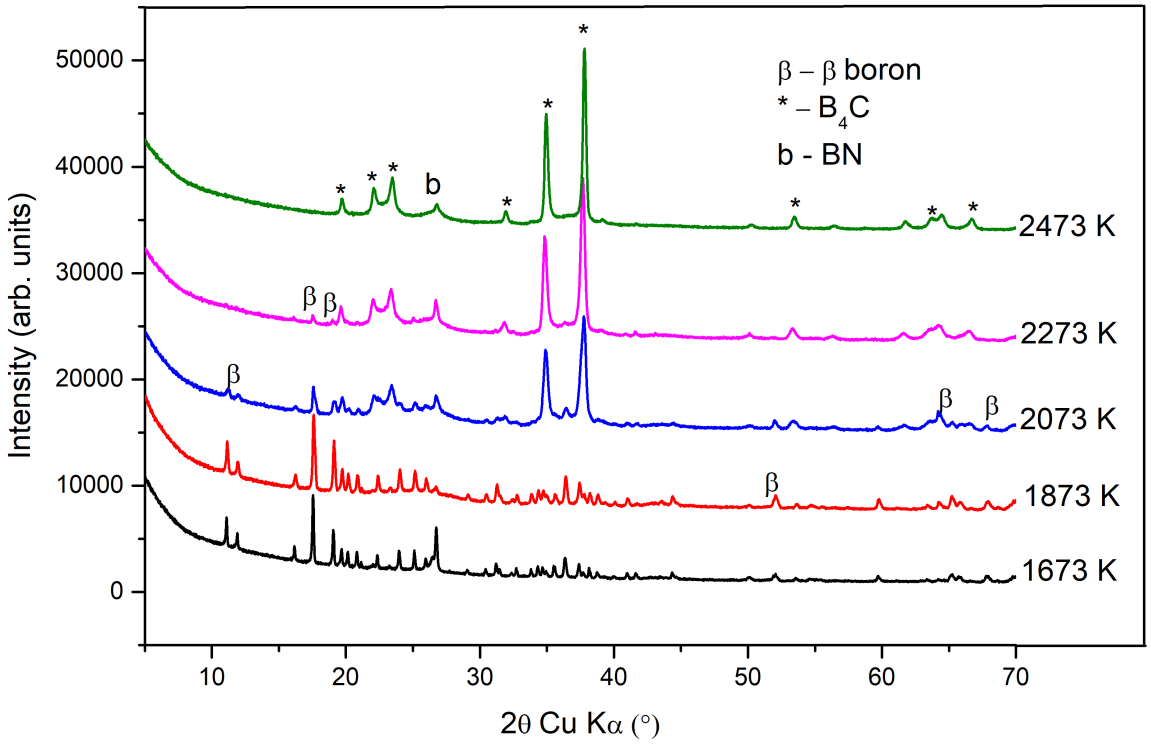

Figure 2.1: ex situ X-ray diffraction pattern of quenched sample from a mixture of crystalline β boron (COD ID : 9011170 33 [107]) and amorphous carbon under 2 GPa for 2 hours at various synthesis temperatures. Since β boron has numerous peaks, only the most prominent peaks have been marked – all the unmarked peaks in the figure are those of β boron.

2 GPa synthesis, boron carbide is not formed at 2073 K. Instead, the temperature of formation of boron carbide shifts to higher temperature, 2273 K for the 5 GPa synthesis. We also find the intermediate phase of α boron becomes the prominent phase between 1473 K to 2073 K. Finally, at 2473 K, boron carbide becomes the most prominent phase. Also, it is noted that the β boron peaks change a lot, especially between 2073 K and 2273

K. This can be attributed to the recrystallisation of β boron with a preferred orientation under HPHT conditions [108]. In figure 2.2, we show the XRD pattern at different temperatures for the 5 GPa series.

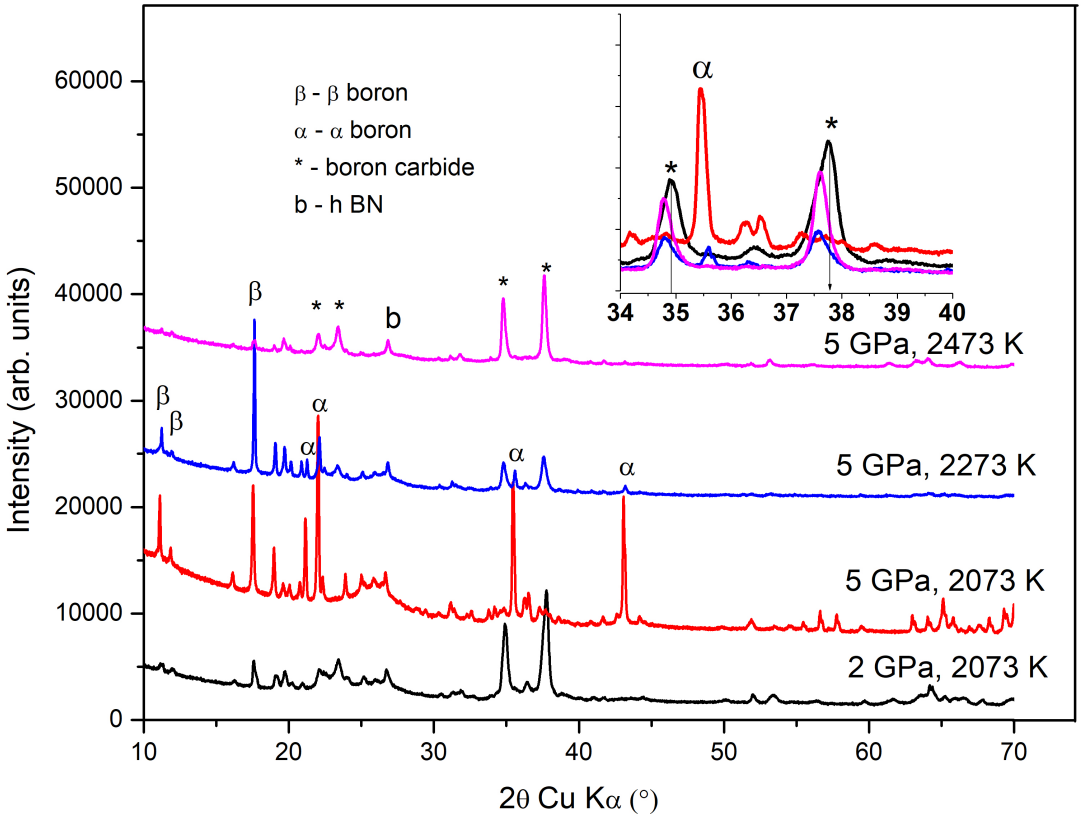

Figure 2.2: ex situ X-ray diffraction pattern of quenched sample from a mixture of crystalline β boron and amorphous carbon under 5 GPa for 2 hours. Since β boron (COD ID : 901110 33 [107]) has numerous peaks, only the most prominent ones have been marked – all the unmarked peaks are those of β boron. The inset is the zoom between 34 ° and 40 °, of the superposition of the curves of the main figure, to facilitate the comparison of the synthesis of boron carbide at 2073 K for 2 GPa, and the 5 GPa synthesis at 2073 K. The latter shows that no boron carbide (COD ID : 4124697 34 [109]) is present.

We have used room temperature micro Raman spectroscopy to investigate these results further. The combination of XRD analysis and the analysis of the Raman spectroscopy data establishes the intermediate phase to be alpha rhombohedral boron. It is found to form as an intermediate phase at 5 GPa, but not at 2 GPa. Raman peaks corresponding to the frequencies for α boron are not observed at 2 GPa, as shown in figure 2.3. The peaks corresponding to β boron for the samples subjected to 1673 K and 1873 K are due to the recrystallisation of β boron under HPHT conditions [108]. Raman peaks corresponding to α boron are present in the samples put under a pressure of 5 GPa and heated to 1473 K, 1873 K and 2073 K, as shown in figure 2.4. Then at 2273 K, the Raman peaks corresponding to boron carbide start appearing. The peaks are very feeble as at 2273 K. However, it is possible to identify boron carbide through the icosahedral peaks at 484 cm^{-1}, 530 cm^{-1}, 934 cm^{-1} and 1067 cm−1. At 2473 K, only the peaks corresponding to boron carbide in the Raman spectrum are observed. Both Raman spectroscopy and XRD results show that boron carbide formation starts at a temperature of 2273 K under a pressure of 5 GPa and at 2073 K under a pressure of 2GPa. This leads to the conclusion that the XRD and Raman spectroscopy results are consistent. The results of the Raman spectroscopy comparing the α boron and boron carbide peaks have been presented in table 2.1.

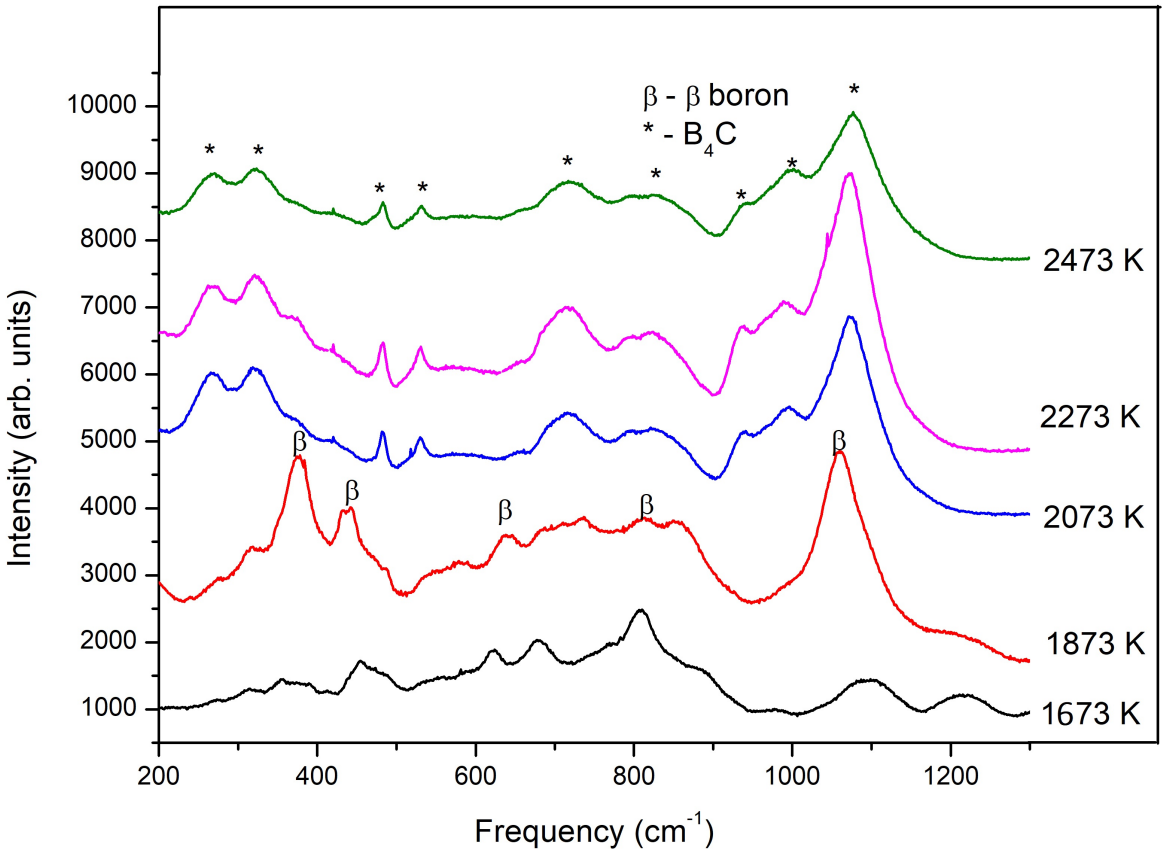

Figure 2.3: ex situ Raman spectroscopy pattern of quenched sample from a mixture of crystalline β boron and amorphous carbon under 2 GPa at various synthesis temperatures for 2 hours. The pattern shows the prominence of an intermediate α boron phase until the synthesis temperature of 2073 K and then boron carbide forms at the synthesis temperature of 2273 K. No trace of any intermediate α boron phase is found. This result is in accordance with the XRD results.

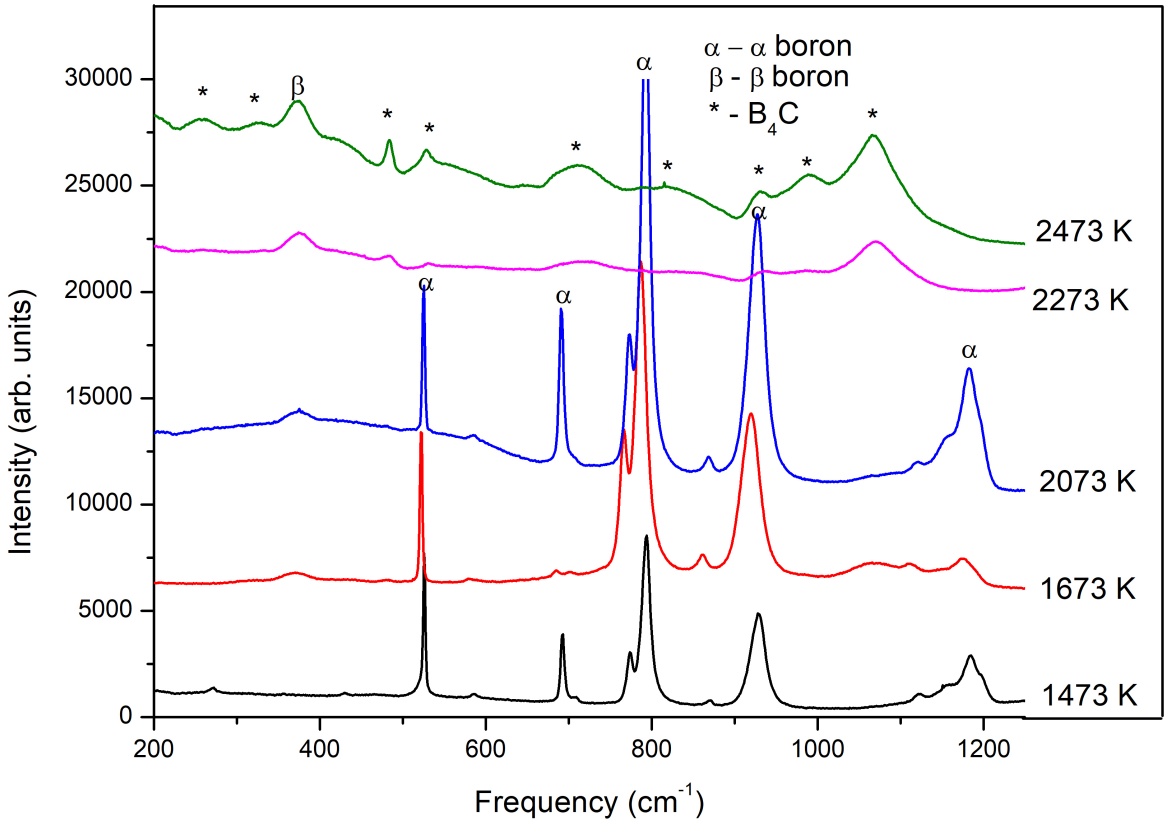

Figure 2.4: ex situ Raman spectroscopy pattern of quenched sample from a mixture of crystalline β boron and amorphous carbon under 5 GPa at various synthesis temperatures for 2 hours. The pattern shows the formation of boron carbide at the synthesis temperature of 2073 K, as expected from the XRD results. α boron is the prominent phase till the synthesis temperature of 2073 K, beyond which boron carbide forms.

Material	Raman peaks (cm^{-1})	2 GPa	5 GPa				
		2473 K	1473 K	1673 K	2073 K	2273 K	2473 K
α boron	508	-	✓	✓	✓	-	-
	708	-	✓	-	✓	-	-
	793	-	✓	✓	✓	-	-
	870	-	✓	✓	✓	-	-
	925	-	✓	✓	✓	-	-
	1122	-	✓	✓	✓	-	-
	1186	-	✓	✓	✓	-	-
Boron carbide	260	✓	-	-	-	-	✓
	320	✓	-	-	-	-	✓
	480	✓	-	-	-	✓	✓
	532	✓	-	-	-	✓	✓
	720	✓	-	-	-	✓	✓
	824	✓	-	-	-	-	✓
	967	✓	-	-	-	✓	✓
	998	✓	-	-	-	✓	✓
	1088	✓	-	-	-	✓	✓

Table 2.1: Summary of the Raman peaks corresponding to α boron and boron carbide peaks in the samples with reactants of β boron and amorphous carbon under 2 GPa and 5 GPa at various temperatures of synthesis. The reference Raman peaks have been taken from Ref. [110], Ref. [111], Ref. [112].

In the next step, the syntheses have been repeated with graphite (instead of amorphous carbon) and the same crystalline β boron. In this case, at 2 GPa, the synthesis temperature of boron carbide rises to 2273 K instead of 2073 K. In figure 2.5, I report the XRD pattern comparing the synthesis of boron carbide from amorphous carbon (at 2073 K) and from graphite (at 2273 K) at 2 GPa.

For the syntheses at 5 GPa, the temperature of formation of boron carbide with graphite increases as well from 2273 K to 2473 K. In figure 2.6, we report the comparison between the synthesis from crystalline boron and amorphous carbon and the synthesis from crystalline boron and graphite. No formation of α boron is detected. It is also noted that boron carbide never becomes the most prominent phase with these reactants, even at very high temperatures, unlike the syntheses with amorphous carbon.

In the third step, the syntheses have been repeated with amorphous boron (instead of β boron) and the amorphous carbon from the first set of experiments. In this case, at 2 GPa, the synthesis temperature of boron carbide decreases to 1873 K. In figure 2.7, we report the XRD pattern showing the synthesis of boron carbide from amorphous boron and amorphous carbon at 2 GPa.

At 5 GPa as well, the temperature of formation of boron carbide decreases from 2273 K (when β boron is used as a reactant) to 1873 K. In figure 2.8, the XRD patterns at different temperatures for the 5 GPa series are shown. It is observed that only very small XRD peaks of boron carbide appear at temperatures of synthesis of 1873 K and 2073 K - α boron remained the most prominent phase. Boron carbide becomes the most

prominent phase at 2273 K, similar to what was observed during the syntheses with β boron and amorphous carbon.Moreover, similar to the case of synthesis with β boron, no formation of α boron was recorded for the syntheses with amorphous boron at 2 GPa, which is in line with what was observed for the syntheses with β boron and amorphous carbon.

In Table 2.2, I have summarised the synthesis temperatures of boron carbide from various elemental reactants at different pressures.

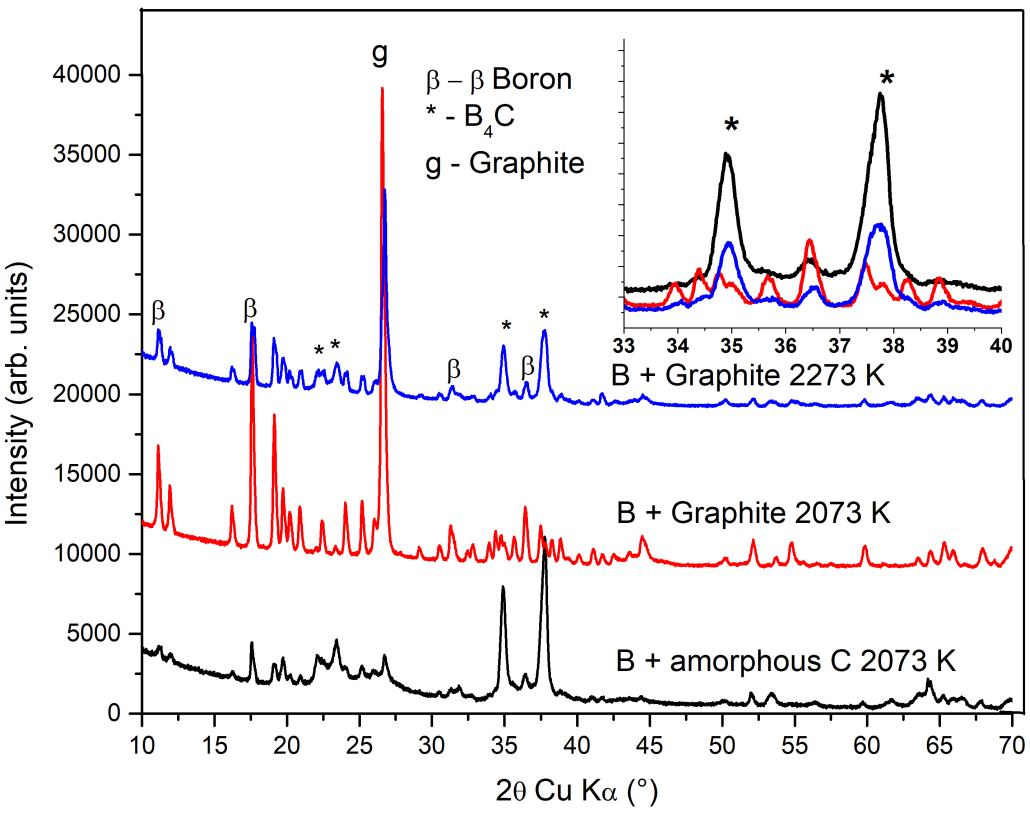

Figure 2.5: ex situ X-ray diffraction pattern of quenched samples from a mixture of crystalline β boron (COD ID :901110 33 [107]) and graphite (COD ID : 9000046 35 [113]) under 2 GPa for 2 hours. The diffractograms are compared to that of boron carbide formed from β boron and amorphous carbon at 2073 K under 2 GPa. All the unmarked peaks in the figure are those of β boron. The inset is the zoom between 33 ° and 40 ° of the superposition of the curves of the main figure (same colours). It shows the formation of boron carbide (COD ID : 4124697 34 [109]) at 2073 K for the amorphous carbon reactant, but boron carbide is absent with graphite at 2073 K.

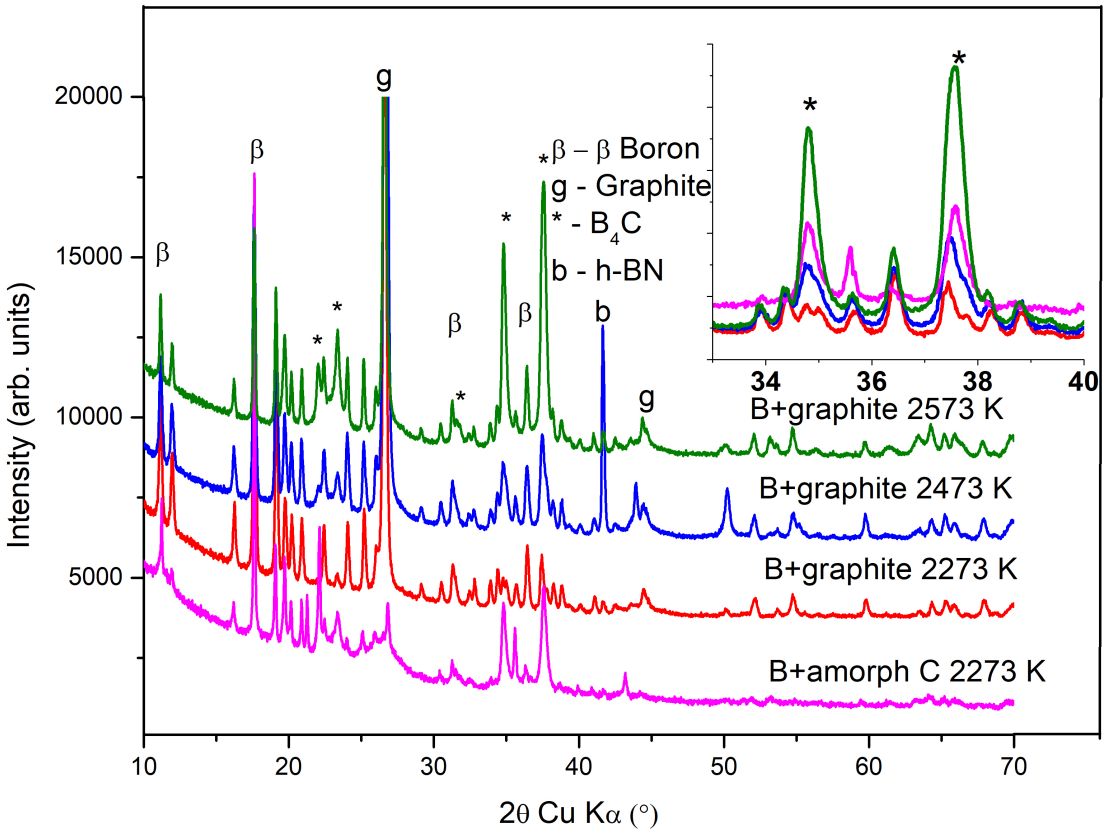

Figure 2.6: ex situ X-ray diffraction pattern of quenched sample from the mixture of crystalline β boron (COD ID : 901110 33 [107]) and graphite (COD ID : 9000046 35 [113]) under 5 GPa for 2 hours. The diffractograms are compared to that of boron carbide formed from β boron and amorphous carbon at 2273 K under 5 GPa. All the unmarked peaks in the figure are those of β boron. The inset is the zoom between 33 ° and 40 ° of the superposition of the curves of the main figure (same colours). It is shown that boron carbide (COD ID : 4124697 34 [109]) is formed at 2273 K with the amorphous carbon reactant, and only at 2473 K with the graphite reactant. No α boron is formed.

*

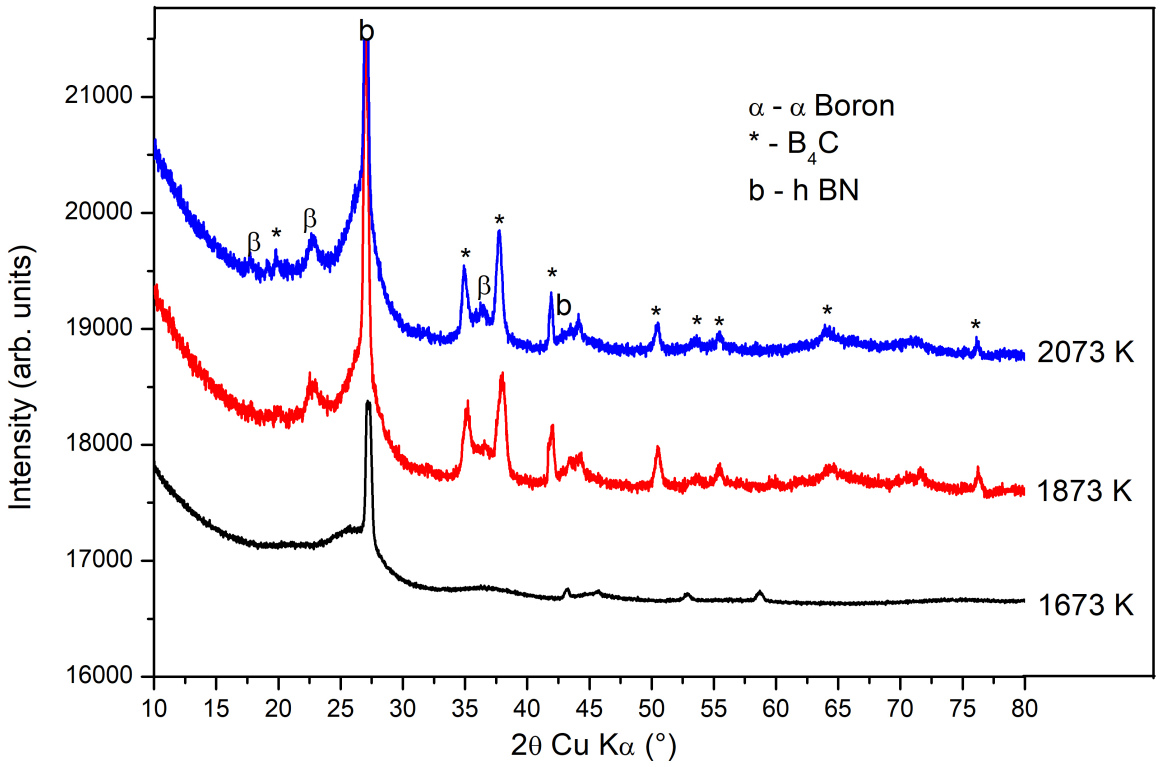

Figure 2.7: ex situ X-ray diffraction pattern of quenched sample from the mixture of amorphous boron and amorphous carbon under 2 GPa for 2 hours. It is shown that boron carbide (COD ID : 4124697 34 [109]) is formed at 1873 K with the amorphous boron reactant. No α boron is formed.

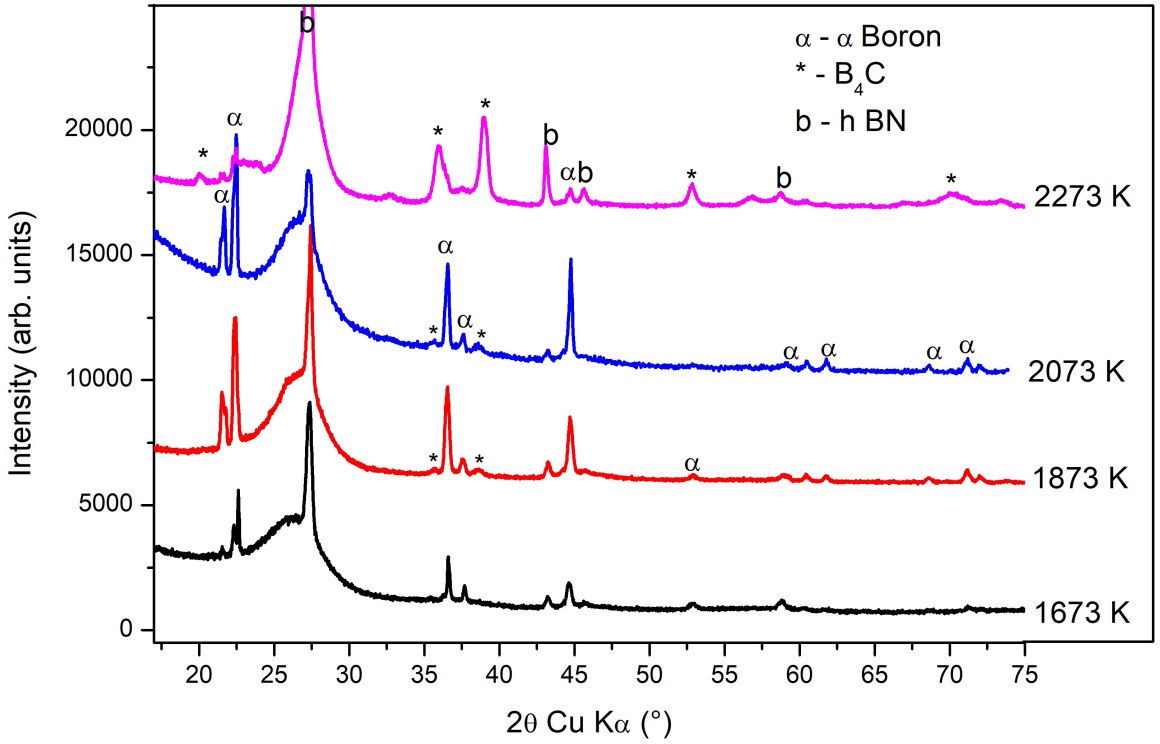

Figure 2.8: ex situ X-ray diffraction pattern of quenched sample from the mixture of amorphous boron and amorphous carbon under 5 GPa for 2 hours. It is shown that boron carbide (COD ID : 4124697 34 [109]) starts forming at 1873 K with the amorphous boron reactant, with α boron remaining the prominent phase. Boron carbide becomes the prominent phase at 2273 K.

Reference	Pressure	Reactants	Temperature of synthesis
Wang *et al*, 2009 [105]	20 MPa	boron + graphite	1573 K
Roszeitis *et al*, 2014 [106]	50 MPa	boron + graphite	1606 K
This work	2 ± 0.2 GPa	amorph. boron + amorph. carbon	1873 ± 20 K
This work	5 ± 0.2 GPa	amorph. boron + amorph. carbon	1873 ± 20 K
This work	2 ± 0.2 GPa	β boron + amorph. carbon	2073 ± 20 K
This work	2 ± 0.2 GPa	β boron + graphite	2273 ± 20 K
This work	5 ± 0.2 GPa	β boron + amorph. carbon	2273 ± 20 K
This work	5 ± 0.2 GPa	β boron + graphite	2473 ± 20 K

Table 2.2: Summary of the synthesis temperatures of boron carbide from elemental boron and carbon, depending on the pressure and on the solid-state form of carbon and boron, in ascending order of synthesis temperature and pressure.

2.4 Discussions on the *ex situ* experiments

The synthesis at 2 GPa follows a well-understood and direct path, similar to what has been reported in the literature [105], [106] for the low pressure syntheses. However, the synthesis temperature rises considerably. A temperature increase by more than 250 K with respect to that of ambient pressure is required to form boron carbide at 2 GPa. Only by 1873 K (in the case of amorphous boron and amorphous carbon), 2073 K (in the case of β boron and amorphous carbon) and 2273 K (in the case of β boron and graphite) do we find that boron carbide has formed.

Amorphous carbon turns out to be a better reactant than graphite for synthesising boron carbide at elevated pressures, since the use of graphite requires a further increase of the synthesis temperature. This is attributed to the higher reactivity of amorphous carbon because of its high concentration of dangling bonds [114–116] . Also, it has better carbon mobility than graphite [117]. Higher mobility of the carbon increases the diffusion of carbon throughout the reacting mixture - this allows the reactants to come in contact with each other thus leading to synthesis of boron carbide at lower temperatures. Amorphous boron is also found to be a better reactant than β boron - this can also be attributed to the better reactivity of amorphous boron compared to crystalline boron due to the former's absence of an ordered crystalline structure [118], [119]. However, at 5 GPa, both amorphous boron and β boron produces α boron as the prominent product up to 2073 K. This indicates that α boron is an intermediate step towards the formation of boron carbide from amorphous or β boron and amorphous carbon under a pressure of 5 GPa.

The synthesis temperature also increases with the increase of pressure in all of the cases except for that of amorphous boron as reactant. Yang *et al.* [119] have suggested that high pressure can decrease the reaction efficiency of boron greatly because in their experiments, the evaporation rate of the surface boron oxide would decrease as the pressure increased. However this does not explain the reason behind the increase of synthesis temperature when amorphous carbon is replaced by graphite, as the same crystalline β boron was used in both cases. Another possible explanation is that high pressure may inhibit the diffusion of carbon atoms through the interstitial spaces in

crystalline boron and thus, it would slow down the reaction. The application of higher temperature values would then favour the diffusion process that leads to the formation of boron carbide. Studies have also noted an inverse relationship between pressure and the reaction constant at the high pressure limit for chemically activated reactions [120]. Therefore, as the pressure applied during the synthesis increases, the reaction rate falls. This effect can be compensated by an increase in temperature, which results in the increased synthesis temperature of boron carbide.

However, this possible explanation raises an interesting question for the synthesis at eventually higher values of the pressure than those explored in the present study. If the temperature required for the formation of boron carbide continues to increase, it will eventually intersect the melting curve of boron carbide at high pressure. This intersection seems very probable as the melting line of boron carbide has been reported to decrease with pressure [95]. In such a case, the temperature that would be needed to offset the hindrance to the diffusion of boron and carbon atoms at high pressure may lie above the melting point of boron carbide for that pressure, and this may lead to new mechanisms of boron carbide formation under these pressure-temperature conditions.

For the syntheses at 5 GPa with amorphous carbon, the formation of α boron as an intermediate phase is observed before the formation of boron carbide. This is discussed in more details in Chapter 7.

The average crystallite size of the formed boron carbide had been determined using the Scherrer formula [121]. The average crystallite size (about 25 nm) was found to

decrease with pressure, and to increase with the synthesis temperature. The size was also found to slightly decrease when graphite is used as a reactant instead of amorphous carbon. Concerning the granulometry of the powder, Scanning Electron Microscopy showed a particle size of 3 - 6 microns irrespective of reactant mixture or synthesis temperature.

It is also worthwhile to try to find out the carbon concentration of the boron carbide synthesised using different reactants and different pressures. It is difficult to do so using XRD analysis techniques, because of the close atomic numbers of boron and carbon [7]. Chemical analysis has been used extensively in literature to find out the carbon concentration in boron carbides [8,13]. However, chemical analysis can overestimate the carbon present in the samples due to the presence of free carbon in boron carbides. In this work, I have deduced the approximate carbon content of the boron carbides synthesized through their lattice parameters [13,22]. In the literature, the carbon concentration was deduced as a function of three parameters - the hexagonal cell parameters a and c , in Å, and the rhombohedral cell volume in $Å^3$. The lattice parameters for my syntheses were calculated by the Le Bail refinement using the software Powdercell [122]. The unit cell volume values were then compared with the reference values in the literature [13,22] to get an approximate idea of the carbon content, as shown in table 2.3. These analyses were done for the boron carbides synthesised from amorphous carbon at the temperatures where boron carbide first appears. The results have shown that carbon content in boron carbides decreases with increase of the pressure of synthesis. This can be attributed to lower diffusion of carbon in boron as the pressure increases, leading to less carbon

incorporation in the unit cells: this argument also holds true for the rise of synthesis temperature with increase in pressure.

Pressure	Temperature	Reactants	a (Å)	c (Å)	V (Å^3)	at. % C
5 GPa	2473 K	β boron + graphite	5.617	12.160	332.251	12.8 - 16
5 GPa	2273 K	β boron + amorph. carbon	5.634	12.125	333.41	12.8 - 16
5 GPa	1873 K	amorphous boron + amorph. carbon	5.628	12.091	331.69	12.8 - 16
2 GPa	2273 K	β boron + graphite	5.613	12.091	329.941	16 - 17.4
2 GPa	2073 K	β boron + amorph. carbon	5.600	12.114	329.095	17.4 - 18.7
2 GPa	1873 K	amorph. boron + amorph. carbon	5.596	12.079	327.628	>18.7

Table 2.3: Atomic carbon concentration of the synthesised boron carbides as a function of hexagonal cell parameters (a and c) and the rhombohedral cell value (V) in ascending order of carbon concentration. The reference values for determining the carbon concentration from the cell volume were taken from Ref. [13] and Ref. [22].

2.5 Motivations guiding the *in situ* experiments

The *ex situ* experiments were primarily done with the objective of finding the metastable C-C chains at pressures between 5-7 GPa, as reported by Betranhandy *et al.* [45].

The *ex situ* syntheses showed the formation of intermediate phase of alpha rhombohedral boron in presence of amorphous carbon at 5 GPa before the formation of boron carbide occurs at higher temperatures. This led to questions whether other intermediate phases also appear during the synthesis of boron carbide from its elements under high pressure.

If these possible intermediate phases are metastable, they would not be present in the *ex situ* recovered samples. Thus, *in situ* studies of the synthesis steps of boron carbide from its elements is the best way to verify if any other intermediate phases apart from α boron forms.

At the same time, *ex situ* syntheses and characterisations are a good way to corroborate the findings of the *ex situ* experiments.

2.6 Results of *in situ* experiments

In situ syntheses and characterisation were done on a few samples of crystalline β boron and amorphous carbon. The samples were subjected to a pressure of 2 GPa, and the temperature was slowly increased. At each step of the temperature increase, a diffractrogram was produced using the synchrotron beam in order to understand the evolution of the reactants into the final product in real time. Figure 2.9 shows the evolution of one of the samples (run BC3) with temperature, when the beam was focused on the center of the sample mixture. In the figure, the data obtained with the synchrotron radiation has been converted to Cu K-α in order to facilitate the treatment and analysis of the data.

The *in situ* results corroborate the *ex situ* findings in that boron carbide appears to form at 2073 K from a mixture of β boron and amorphous carbon under a pressure of 2 GPa. However, it also shows that some peaks of β boron appear, disappear and reappear during the course of the heating. This can be the result of the formation of

re-crystallised β boron that is produced when commercial β boron is subjected to high pressure and temperature conditions [108].

Unfortunately, the attempts to repeat the syntheses at 5 GPa in *in situ* conditions which is essential for the identification of the metastable C-C chains failed during the present run. The experiment was planned to be repeated in the alloted beamtime at the SOLEIL Sychrotron in April 2020. However, the beamtime has been shifted to December 2020 because of the pandemic of Covid-19.

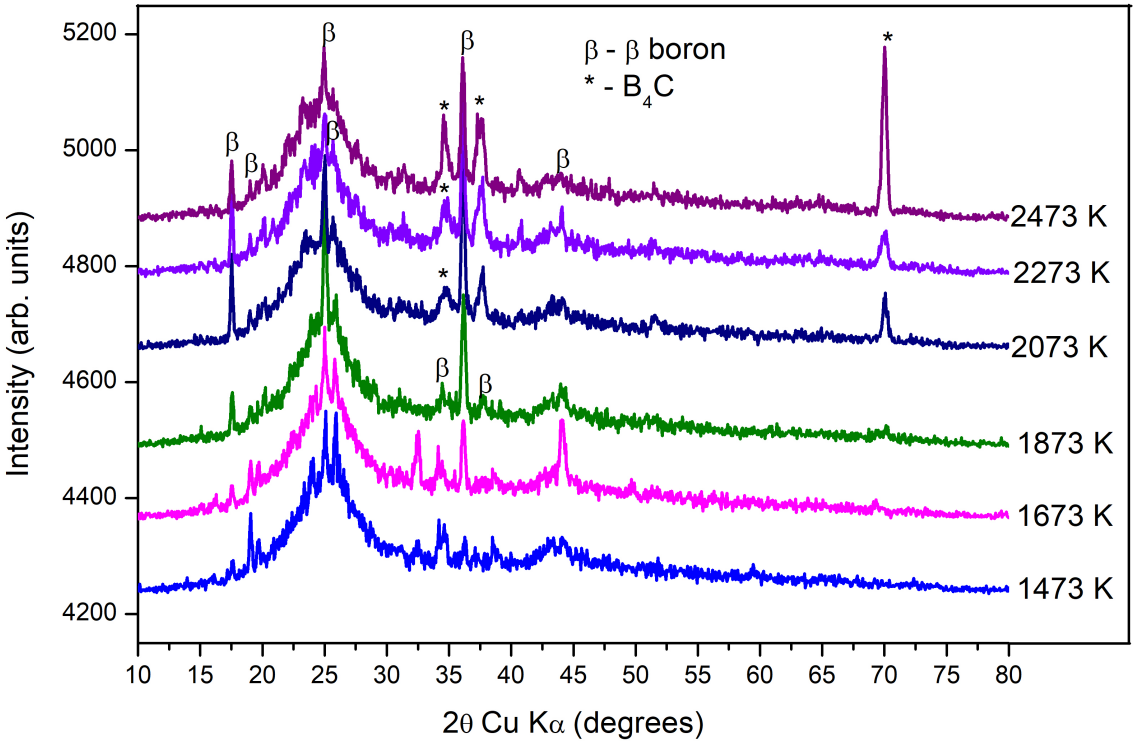

Figure 2.9: in situ diffraction pattern taken at the center of the sample of a mixture of crystalline β boron and amorphous carbon at 2 GPa. The data obtained from the synchrotron radiation was converted to that of Cu K-α radiation.

2.7 Discussions on the *in situ* experiments

The *in situ* results corroborate the findings of the *ex situ* experiments with respect to the formation of boron carbide from amorphous carbon and β boron under a pressure of 2 GPa.

However, one of the purposes of doing the *in situ* experiments was the identification of

the metastable C-C chains that are predicted to form by Betranhandy *et al.* between 5 - 7 GPa [45]. As the chains are predicted to be metastable, they would have a high probability of not being present in the quenched products obtained from the *ex situ* experiments. Hence, a real time *in situ* synthesis and characterisation is probably the only way to identify them. Some setbacks were encountered when we attempted to synthesize these metastable C-C chains, most notable of them being that the *in situ* experiments undertaken at 5 GPa could not take place.

The *in situ* data obtained at 2 GPa do not show any peak which can be identified as C-C chains. The most obvious explanation behind that is that the pressure of 2 GPa is too low for the formation of the metastable phase. However, there is also an additional issue. β boron is a highly disordered element having an unit cell with approximately 105 atoms - this results in a large number of diffraction peaks. Moreover, under high pressure and temperature (HPHT) conditions, β boron undergoes recrystallisation [108], as seen also in the Raman spectroscopy results in figure 2.9, which can make it even harder to follow the evolution of the different β boron peaks, and identify if and when a new peak corresponding to the C-C chains appear. Even though much of the β boron converts to α boron under high temperatures at a pressure of 5 GPa, the remaining β boron peaks are numerous enough to cause problems in the identification of C-C chains, as seen in figure 2.2. However, these issues are not dead-ends and it is possible to design experiments that overcome these issues.

A possible solution is to use a mixture of amorphous boron and amorphous carbon

at 5 GPa in order to identify the C-C chains. As shown in our *ex situ* experiments, amorphous boron crystallises to alpha rhombohedral boron before its conversion to boron carbide at 2273 K under a pressure of 5 GPa. α boron has a much more ordered structure, leading to much less reflections in the diffraction pattern. There is also no known recrystallisation of α boron under HPHT conditions. This would make it much easier to follow the evolution of the diffraction peaks and identify if the predicted C-C chains form. Evidently, α boron itself could also have been used directly as a starting material. However, α boron is not commercially available and thus the intermediate conversion of α boron using amorphous boron as a starting material is necessary.

2.8 Conclusions

As will be elaborated further in Chapter 7, the work done in this chapter resulted in a new method to produce α boron in quantities larger than existing methods.

The optimum synthesis parameters of boron carbide at high pressures (up to 5 GPa) from elemental boron and carbon have been studied for the first time, using the large volume Paris-Edinburgh press.

The present study has shown that the mechanism of elemental formation of boron carbide is heavily dependent on pressure, which affects the temperature of formation of boron carbide. In the next chapter, we will study the other end of the industrially available high-pressure region, 10 GPa – 15 GPa, using multi-anvil cell, in order to observe the effect of high pressure on the formation temperature of boron carbide.

Amorphous carbon has proven to be a better reactant than graphite for the synthesis of boron carbide, since it lowers the temperature of formation, both at 2 GPa and at 5 GPa. Amorphous boron has also followed this trend, since it results in lower temperature of formation of boron carbide both at 2 GPa and 5 GPa, when compared with β boron.

In situ experiments have corroborated some of the findings of the *ex situ* syntheses. However, in order to investigate the presence of the metastable C-C chains, further *in situ* syntheses and characterisations are required at 5 GPa with a reactant mixture of amorphous boron and amorphous carbon.

In conclusion, in this chapter, I have made significant progress towards fulfilling parts of the second objective of the thesis - Synthesis under high pressure and high temperature (HPHT) conditions to find C-C chains.

Chapter 3

Boron carbide synthesis at high pressure (13 GPa) *in situ* and *ex situ*

3.1 Introduction

In the previous chapter, the optimum synthesis parameters of boron carbide in HPHT conditions up to a pressure value of 5 GPa were established using the Paris-Edinburgh cell. The results showed that the synthesis parameters of boron carbide from elements are highly dependent on pressure: the temperature required for the formation of boron carbide increases with the increase of pressure. If the synthesis temperature continues to increase, it will eventually intersect the melting curve of boron carbide at high pressure

since the melting line of boron carbide has been reported to decrease with pressure [95]. In such a scenario, the synthesis temperature of boron carbide may lie above the melting point of boron carbide for a specific high pressure value, and this may lead to new mechanisms of boron carbide formation under these pressure-temperature conditions. Therefore, it is worthwhile to study the synthesis of boron carbide from elements at higher pressure values to discover the synthesis mechanisms of boron carbide.

The *in situ* study of synthesis of boron carbide at high pressure would also allow us to look for the metastable C-C chains, as reported by as Betranhandy *et al.* [45] (see Sec 2.1). These chains are predicted to form between 5-7 GPa, and higher pressure should be more favourable for their formation.

However, the Paris-Edinburgh cell can only be used for high pressure experiments up to 7 GPa with a large volume of sample. The large volume press (LVP) that is most suitable for high pressure experiments up to 15 GPa is the multi-anvil press (MAP). We have used this device at a pressure of 13 GPa to establish the synthesis temperature of boron carbide from elements.

In the course of these experiments, the important effects on thermal cycling on the synthesis temperature of boron carbide were also discovered.

3.2 Experimental materials and methods

A mixture of crystalline β boron (Prolabo, purity 99.9 % , particle size 1-10 microns) and glassy amorphous carbon (Sigma-Aldrich, purity 99.95 % trace metals basis, particle size

2 – 20 microns) have been mixed in a mortar and pestle for 5 minutes in the stoichiometric ratio of 4:1.

Both the *in situ* and *ex situ* experiments were performed using the DIA module of the multi-anvil press (See Sec 1.3.1). A pressure of 13±0.5 GPa was attained on both cases over a span of 8 hours. The *in situ* experiment was performed in the PSICHE beamline of the SOLEIL synchrotron.

For the *in situ* experiment, the reactant mixture was put in the set-up shown in figure 3.1. The commonly used graphite heater, as shown in figure 1.11, was replaced with a TiB_2 heater. This is because graphite can transit into diamond at a pressure of 12 GPa and ∼2500 K [123], leading to loss of electrical conductivity. Thus, a graphite heater would be unsuitable for the pressure (13 GPa) and temperature ranges (300 - 2473 K) used in the current experiments. An amorphous boron octahedron was used instead of MgO, since amorphous boron is more transparent to X-rays, which is important for *in situ* characterisation. Pressure was estimated using MgO as a pressure calibrant [124, 125].

The temperature for the *in situ* experiment was not increased uniformly because of a problem in the power supply: instead, a thermal cycling took place. The temperature was increased to a specific value for around 3 minutes, the EDXRD pattern was recorded in the center of the sample, and then the temperature dropped to 300 K. Next, the temperature was raised to the next higher value and the same process was repeated. The upper limit of the temperature that was attained in each successive cycle has been

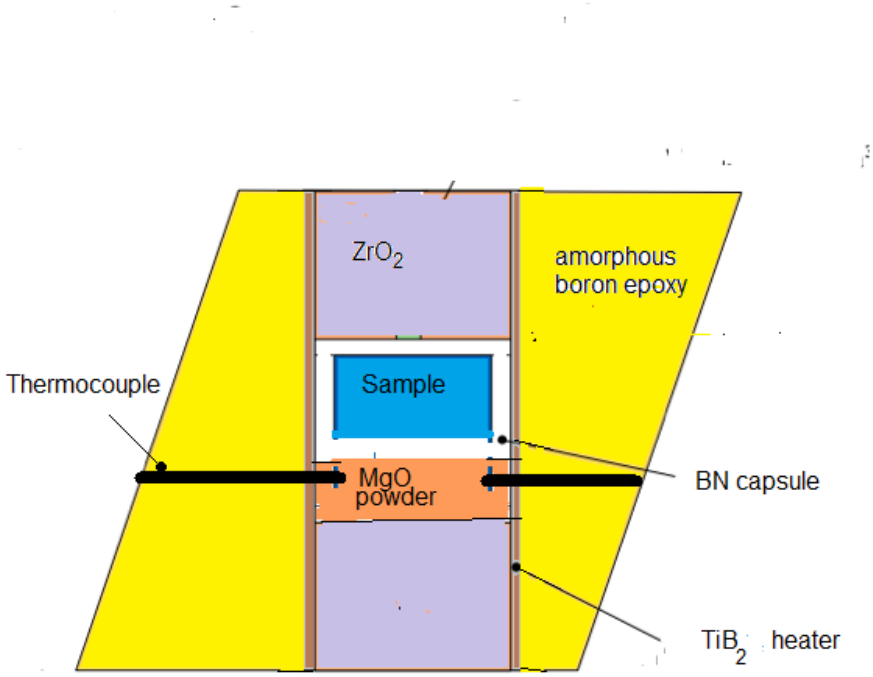

Figure 3.1: The sample assembly used for the in situ multi-anvil experiment. TiB_2 heater was used inside an amorphous boron epoxy octahedron.

recorded in table 3.1. After the final quenching to 300 K, the sample was then decompressed slowly over 4 hours. Finally, a diffractogram was taken using the CAESAR system (see Sec 1.3.3).

For the *ex situ* experiment, a different type of set up was used, as shown in figure 3.2. The main difference is the use of rhenium foil as the heater and $LaCrO_3$ sleeve as a thermal insulator. The metal heater allows us to have a greater sample volume, which is important for *ex situ* characterisation. The temperature was raised slowly and constantly at a rate of 2 K/s. Then, the sample was subjected to a dwell time of 30 minutes to the *ex situ* sample: no thermal cycling was performed on this sample. Pressure was fixed at

Cycle number	Lower temperature	Higher temperature
1	300 K	875 K
2	300 K	1170 K
3	300 K	1360 K
4	300 K	1670 K
5	300 K	1912 K
6	300 K	2430 K

Table 3.1: The upper and lower values of temperature attained during each cycle in the in situ run.

13 GPa by using a calibration curve determined beforehand, with an error of evaluation of ± 0.2 GPa.

After the dwell time of 30 minutes, the sample was quenched rapidly by removing the electrical power. The decompression was done slowly over the span of 4 hours. The sample was then recovered carefully and subjected to characterisation by *ex situ* X-ray diffraction.

Both the *ex situ* and *in situ* recovered samples were also subjected to Raman spectroscopy.

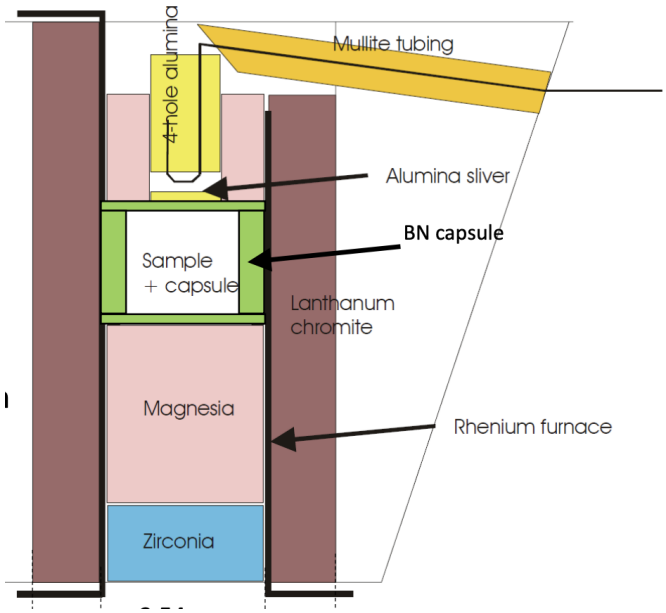

Figure 3.2: The sample assembly used for the ex situ multi-anvil experiment. Rhenium foil was used as a heater instead of the $LaCrO_3$ used in the in situ run.

3.3 Results

3.3.1 X-ray diffraction

During the *in situ* run, a series of EDXRD patterns were taken immediately after the temperature was raised in each cycle and before the system was quenched. Figure 3.3 shows the EDXRD patterns as a function of rising temperature at 13 GPa. In the figure, the data obtained with the synchrotron radiation has been converted to Cu K-α in order to facilitate the treatment and analysis of the data.

As the upper limit of temperature is increased in each cycle, only various β boron peaks are observed up to 1912 K, as is expected from previous experiments (see Sec 2.6). This

can be attributed to the recrystallisation of β boron under high pressure and temperature conditions [108], as has also been observed in Sec 2.7.

However, in the last cycle, as temperature is increased to 2430 K, the formation of boron carbide is observed.

After the last cycle of temperature increase, the system is quenched and EDXRD is performed again to observe whether boron carbide remains in the system. As the last pattern in figure 3.3 shows, the boron carbide peaks have remained unchanged after quenching.

After this, the sample was decompressed and another XRD pattern was taken using the CAESAR system. Figure 3.4 shows the CAESAR pattern: it is observed that boron carbide has remained in the sample after the process.

In order to verify whether temperature cycling had any effect on the formation of boron carbide, a second experiment was performed. In this *ex situ* experiment, the temperature was raised to 2473 K slowly without any cycling. The XRD performed on the recovered sample after the experiment is shown in figure 3.5: no boron carbide peaks have been observed in the sample. In order to establish this, the XRD diffractogram has been compared to that of the boron carbide formed at 2473 K under 2 GPa in the inset of figure 3.5. The 2θ angles between 33° - 40° shows the most prominent peaks of boron carbide (012) and (104) under Cu Kα radiation. As is evident from the comparison, the sample quenched after a HPHT treatment at 13 GPa and 2473 K has not formed any boron carbide. Some trace amounts of γ orthorhombic boron [126] was found in the

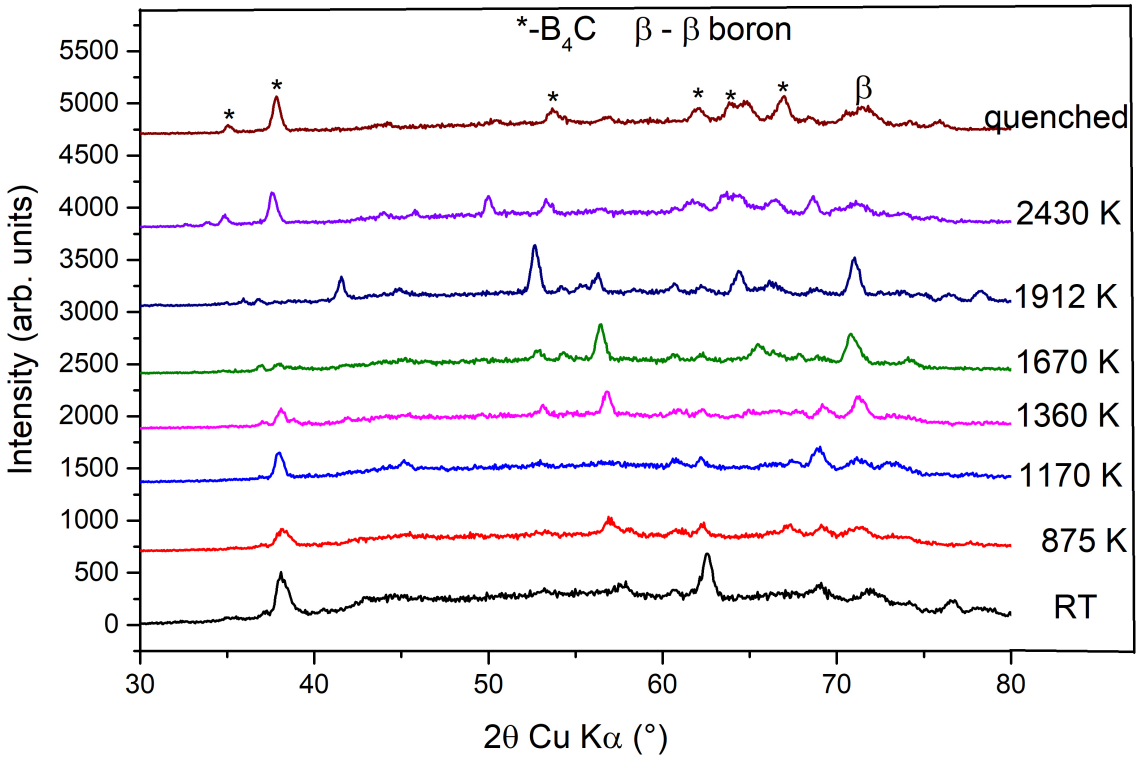

Figure 3.3: in situ diffraction pattern taken at the center of the sample of a mixture of crystalline β boron and amorphous carbon at 13 GPa for various temperatures during the in situ run. The data obtained from the synchrotron radiation was converted to that of Cu K-α radiation. All the unmarked peaks are those of crystalline β boron.

sample, but no α boron was formed, contrary to the case at 5 GPa (see Chapter 7). the quenched sample is overwhelmingly composed of β rhombohedral boron.

3.3.2 Raman spectroscopy

Figure 3.6 shows the results of the Raman spectroscopy done on the recovered samples from the *in situ* and *ex situ* synthesis. Crystalline β boron peaks were found in both of

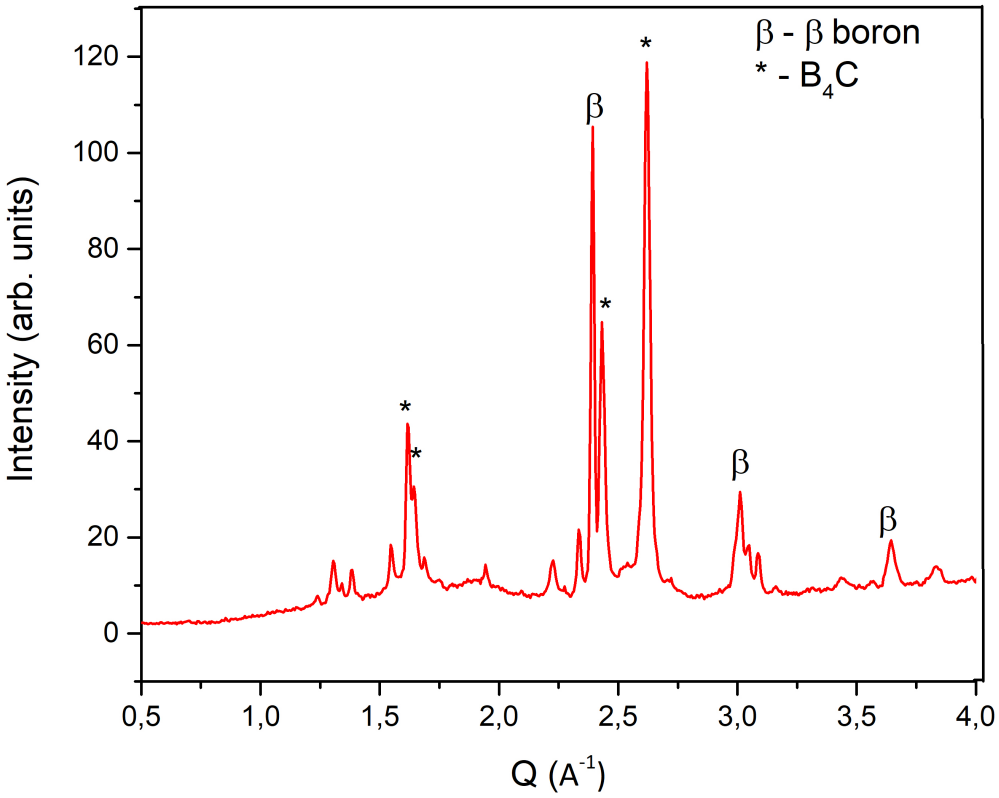

Figure 3.4: in situ diffraction pattern taken at the center of the sample of a mixture of crystalline β boron and amorphous carbon at ambient conditions after applying a pressure of 13 GPa and temperature cycling during the in situ run. The data was obtained from the synchrotron radiation using the CAESAR system. All the unmarked peaks are those of crystalline β boron.

the samples, while the *in situ* synthesis had additional boron carbide peaks. No peaks corresponding to γ boron or α boron were found in either of the samples.

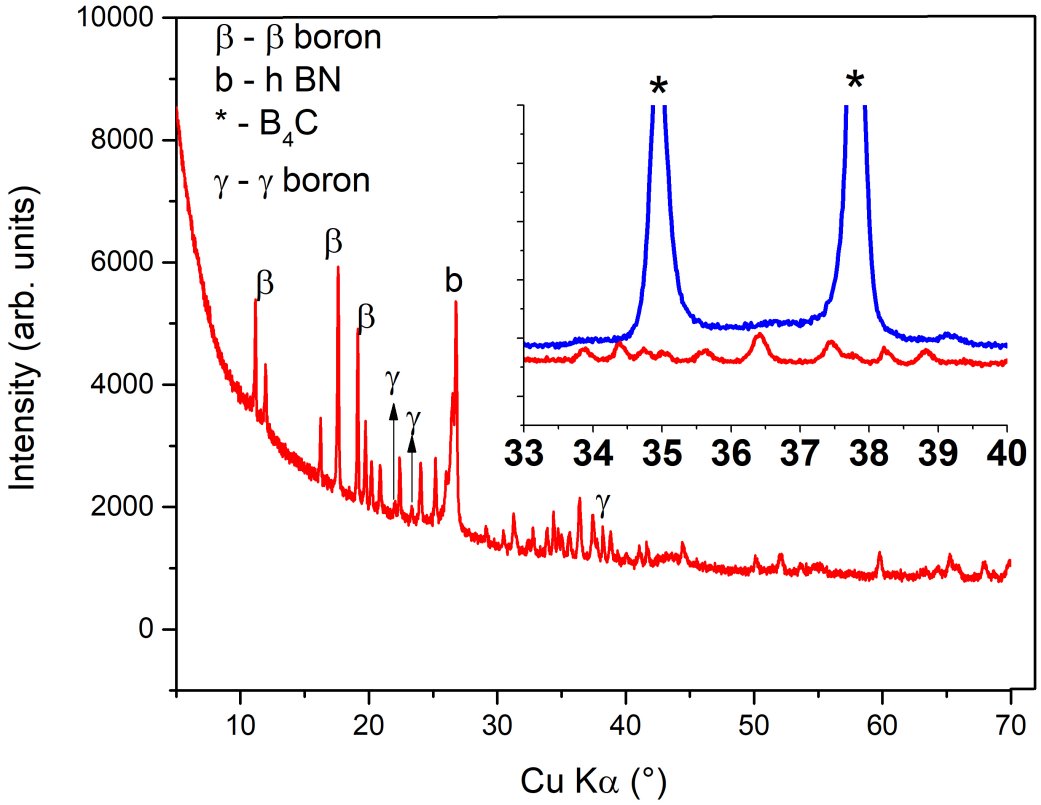

Figure 3.5: X-ray diffraction pattern of quenched sample from the mixture of crystalline β boron (COD ID : 901110 33 [107]) and amorphous carbon under 13 GPa at 2473 K for 1 hour. The inset is the zoom between 33 ° and 40 ° of the superposition of the curve of the product (same colour as main plot) and the diffractogram of B_4C taken from figure 2.1. It is shown that no new peaks corresponding to boron carbide (COD ID : 4124697 34 [109]) form in the sample.

*

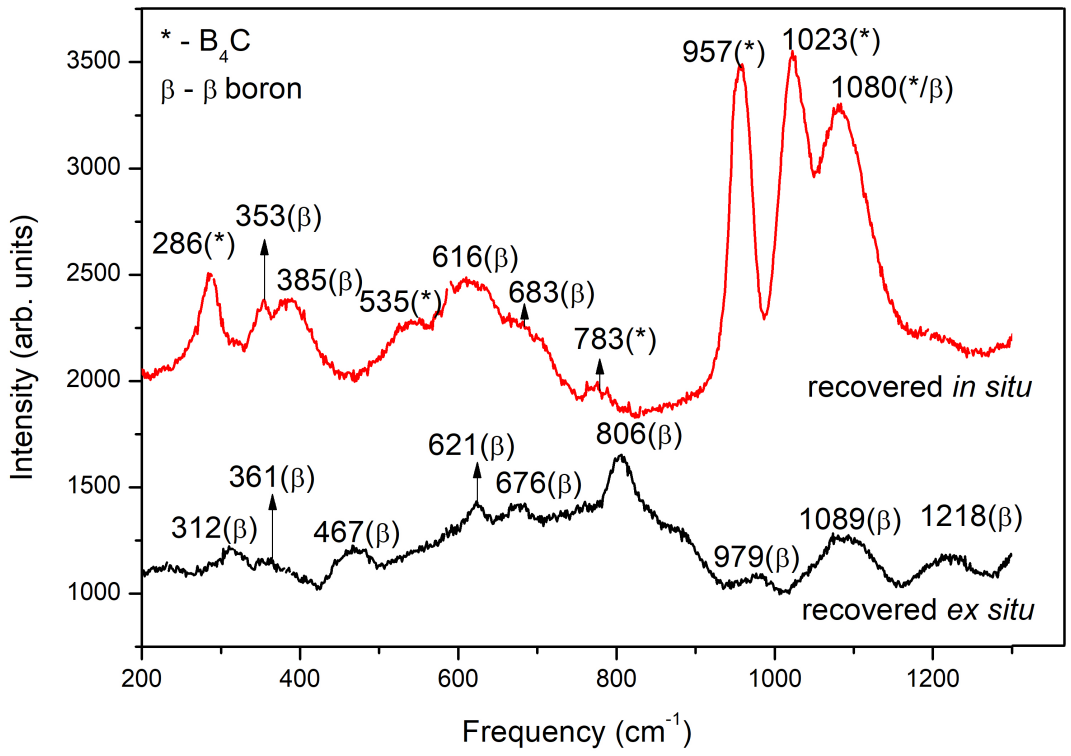

Figure 3.6: Raman spectroscopy of recovered samples from the in situ and ex situ synthesis. The ex situ sample shows only β boron peaks after HPHT treatment, while the in situ sample shows both β boron and boron carbide peaks.

3.4 Discussions

3.4.1 Formation of boron carbide

From the conclusions of Chapter 2, it was seen that the synthesis temperature of boron carbide appeared to increase with pressure up to 5 GPa. If a linear increase of temperature of synthesis is assumed with respect to pressure, as shown in figure 3.7, boron

carbide would be expected to form at $\sim$ 3000 K at 13 GPa from a reactant mixture of β boron and amorphous carbon. However, when the melting curve of boron carbide given by Mukhanov *et al.* [95] is linearly extrapolated (see figure 3.7), it can be observed that this temperature of 3000 K lies much above the temperature of fusion of boron carbide (2500 K) at 13 GPa. Therefore, this might result in new mechanisms in the synthesis of boron carbide from its elements, as discussed in Chapter 2. However, it is also worthwhile to note here that the melting curve of Mukhanov *et al.* was given by experiments done only till 7.5 GPa, and the experimentally determined melting points at different pressures did not seem to monotonically decrease with increase in pressure: the melting curve could therefore change its behaviour at higher pressures. Also, the melting point of boron carbide is known to depend on its widely varying stoichiometry [127].

However, during the *in situ* experiment at 13 GPa, it was found that boron carbide formed in the last cycle when the temperature was raised to 2433 K: this is much lower than the expected temperature of synthesis of 3000 K. No melting of boron carbide was observed.

When the same experiment was repeated without the thermal cycling in *ex situ* conditions at 2473 K, no boron carbide was formed. This established that the synthesis temperature of boron carbide from elements at 13 GPa is above 2473 K, when steady heating is used.

Hence, it is evident that the thermal cycling had played a role in the synthesis of boron carbide from its elements at a lower temperature.

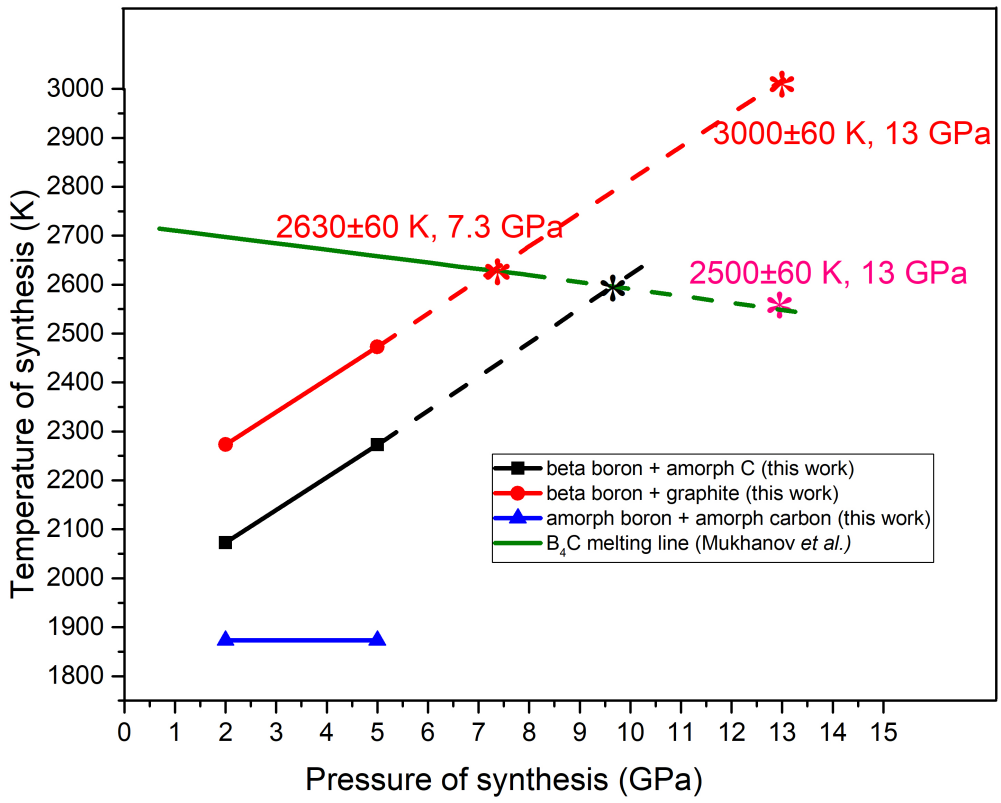

Figure 3.7: Melting curve of boron carbide (B_4C) in comparison with the synthesis temperatures of boron carbide at different pressure values starting from different elemental reactant mixtures in 4:1 ratio. The red discs, black squares and blue triangles denote the experimental parameters at which boron carbide is synthesised. The solid lines show the linear fitting of the experimental points, while the dashed lines show the linear interpolation at higher pressure. The stars of different colours highlight the important points in the (P,T) space. The error bar on the melting curve is ± 60 K.

Some work has been done on the effects of thermal cycling in chemical reactions.

Barratt *et al.* [128] have shown through computational models that some hypothetical processes generate higher yields under forced thermal cycling than under single, fixed

temperature conditions. Thermal cycling can also hasten phase transitions in some cases, as shown by Lee *et al.* [129]. They have shown the kinetic transition of γ Fe-17 wt % Mn alloy into ϵ phase due to thermal cycling: this can be attributed to the increase in transformation kinetics at the numerous nucleation sites introduced through thermal cycling.

Luk'yanenko *et al.* [130] have performed both theoretical and experimental investigations into the effect of thermal cycling on the high temperature interaction of titanium with gases like oxygen and nitrogen. They report that thermal cycling had intensified the diffusion displacements of impurity atoms. The diffusion coefficients of these oxygen and nitrogen impurity atoms increase both in the matrix and in the newly-formed phase. This had strongly affected the conditions of formation and growth of the new phase because the number of possible nucleation centers on the phase boundary had permanently increased with time and the energy barrier of the phase transformation has decreased as well.

Thus, it can be hypothesised that the damage created in the β boron structure due to the thermal cycling has permitted easier diffusion of the carbon atoms in the structure, leading to nucleation sites of boron carbide. This has resulted in the formation of boron carbide at a lower temperature than that would be needed by a steady fixed temperature condition. The changes that this process would create in the EDXRD pattern of the reacting materials is difficult to observe in this specific case, because of the recrystallisation of β boron peaks under HPHT conditions.

In the Raman spectroscopy results shown in figure 3.6, the difference between the two spectra is evident. The *ex situ* sample only consists of β boron peaks, while the *in situ* sample has additional boron carbide peaks as well. However, the Raman peaks of boron carbide in this case seem to be significantly different than those observed for boron carbide in Sec 2.3. The 480 cm^{-1} peak of the (480/532)cm^{-1} pair seems to have shifted to 385cm^{-1} or disappeared. The three peaks towards the 1200cm^{-1} end of the spectrum (957, 1023 and 1080 cm^{-1}) are much larger than the rest of the peaks. The boron carbide peak at 998 cm^{-1} seems to have shifted to 1023 cm^{-1}. These changes may be attributed to structural changes of boron carbide due to the thermal cycling. However, further investigation is required with TEM (transmission electron microscopy).

3.4.2 Formation of γ orthorhombic boron

From the HPHT phase diagram of boron [108, 126], it appears that a phase transition from β rhombohedral boron to γ orthorhombic boron should occur under the temperature and pressure conditions of the experiments done in the current chapter.

No γ boron is obtained as a result of the *in situ* experiment. This can be attributed at least partly to the effects of thermal cycling which might have affected the mechanism of transition of β boron to γ boron.

However, only trace amounts of γ boron formation is observed in the quenched product of the *ex situ* experiment.

No γ boron was found in the Raman spectroscopy results. Even though γ boron is a

HPHT phase, it has been successfully quenched to ambient conditions in the literature [126, 131]. However, all the phase transitions in the literature were observed in pure boron, while the reacting mixture in the current experiments has β boron and carbon in a 4:1 ratio.

Therefore, the reason behind the relative absence of γ boron in the quenched *ex situ* sample might be the presence of amorphous carbon in the reacting mixture. In Chapter 2, it was observed that the phase of α rhombohedral boron was stabilised by amorphous carbon till 2273 K under a pressure of 5 GPa, much beyond the temperature of 1500 K predicted by Parakhonskiy *et al.* [108]. This is investigated in more details in Chapter 7. It is possible that carbon donates electron to the deficient β boron structure and thus stabilises the β boron structure at 2400 K under 13 GPa. γ boron is not electron-deficient, the B_{12} icosahedra and the B_2 dumbbells at the orthorhombic site create a partly ionic boron boride ($B_2^{\delta+}B_{12}^{\delta-}$) [126].

3.4.3 Formation of C-C chains

The C-C chains which would form in this pressure range are metastable and thus, could only be potentially observed during the *in situ* synthesis of boron carbide. In the *in situ* synthesis done in the current chapter, boron carbide was observed only at the last temperature of 2430. All the peaks observed correspond to either boron carbide or β boron, as shown in figure 3.3.

C-C chains in $(B_{11}C)$C-C are expected to give rise to an intense peak E_g predicted at 1184 cm^{-1}. In $(B_{10}C_2)$C-C, intense modes are expected between 1200 and 1300 cm^{-1},

depending on the location of the carbon atoms on the icosahedra [5]. Such modes cannot be detected in the spectra of figure 3.6. However, the Raman spectroscopy was done in *ex situ* conditions, which is not ideal when looking for metastable phases.

In the *in situ* X-ray diffraction , it is also difficult to differentiate the numerous reflections of β boron peaks from potential peaks of the metastable phase, specially due to recrystallisation of β boron at HPHT conditions [108], as has also been discussed in Section 2.7. Moreover, the mechanism of formation of boron carbide is also different in the current experiment, because of the temperature cycling. This might have interfered with the formation of the metastable C-C chain.

3.5 Conclusions and perspectives

The synthesis experiments at the higher pressure value of 13 GPa have shown that the synthesis temperature of boron carbide from β boron and amorphous carbon is at least above 2473 K, with steady heating. The temperature of synthesis of boron carbide has been shown to decrease with thermal cycling that allows easier diffusion of carbon into the boron structure.

The boron carbide that formed during thermal cycling was identified by X-ray diffraction. However, there are some changes in the Raman spectroscopy of the sample.

The metastable C-C chains predicted in this pressure range could not be observed in the *in situ* experiment. This can be attributed to the change in mechanism of formation of boron carbide because of temperature cycling.

Few more experiments were planned at higher values of temperature to identify the synthesis temperature of boron carbide at 13 GPa. Besides, experiments were planned with different reactant mixtures such as amorphous boron and amorphous carbon to see if that has an effect on the temperature of synthesis, similar to the case of the syntheses at 2 GPa and 5 GPa (see Chapter 2). However, these experiments could not take place because of the lockdown imposed by the epidemic of Covid 19 and will be pursued later.

Amorphous carbon in the reacting mixture has also appeared to stabilise β boron in a domain of the boron phase diagram where γ orthorhombic boron would be expected. This is similar to what was discovered in this work earlier, where amorphous carbon stabilised α boron over β boron in a domain where the latter was considered to be the stable phase. Further experiments would need to be performed at 13 GPa and 2473 K with only β boron as a reactant to definitively conclude the role of carbon in this stabilisation of β boron.

Chapter 4

Synthesis of new phases of boron carbide at very high pressure with laser heating in the diamond anvil cell (DAC)

4.1 Introduction

In this chapter, I have subjected boron carbide to very high temperature and pressure conditions to find evidence of the theoretically predicted C-C chains.

Jay *et al.* [6] have predicted that the thermodynamically stable phase of boron carbide

above 50 GPa at 1000 K is $(B_{10}C_2)$C-C. This new phase, with 28.6 % carbon concentration, has C-C chains that improve its mechanical strength. This is because the C-C chain already present in this phase would be less susceptible to forming chain centre vacancies. This protects the new phase from the resulting discontinuous decrease in volume when the chain ends come together to form a C-C bond and the ensuing mechanical failure, as has been described in Section 1.1.1.

Boron carbide has been raised to the high pressure value of 50 GPa by Yan *et al.* [42]. The pressurisation was done non-hydrostatically without using a pressure transmitting medium (PTM). The sample was not heated, and they observed amorphisation of boron carbide when the samples were depressurised after the non-hydrostatic compression. Apart from this depressurisation amorphisation, no other phase change was observed. They also observed no changes when the compression and decompression was done more hydrostatically with powdery NaCl as pressure transmitting medium.

Hushur *et al.* [97] have put boron carbide single crystals to high pressure values up to 70 GPa at ambient temperature. They observed a phase transition near 40 GPa which led to optical transparency. The optical transparency seemed to increase rapidly around 55 GPa. They attributed this to changes in the C-B-C chain of $B_{4.3}C$. However, they have not looked for C-C chains or the presence of the $(B_{10}C_2)$C-C phase in the sample.

In this chapter, I have thus detailed the first experimental attempts to subject boron carbide to very high pressure as well as high temperature in order to find evidence of C-C chains.

4.2 Materials and Methods

Two different samples of commercial B_4C powder (Alfa Aesar, 99+ % purity) was raised to the pressure values of 25 GPa and 50 GPa respectively in diamond anvil cells (DAC) and subjected to double sided laser heating developed in-house at IMPMC. The working principle of a diamond anvil cell as well as a schema of a generalised diamond anvil cell have been provided in Section 1.3.1.

Since boron carbide single crystal was commercially unavailable, the experiments were performed with powder sample. However, boron carbide is highly incompressible and it was found impossible to compress the powder into flakes suitable for laser heating. As a result, the sample hole in the rhenium gasket was filled completely with boron carbide powder. No pressure transmitting medium was used. The pressurisation and depressurisation was, hence, non-hydrostatic. The Raman signal from the diamond of the DAC was used as a pressure calibrant [132].

In the first experiment, hereby referred to as DAC 1, the pressure was accidentally raised to 25 GPa, and then immediately decompressed non-hydrostatically to 18 GPa. The sample was then heated by double-sided Nd:YAG laser, and finally decompressed to ambient conditions.

In the second experiment, hereby referred to as DAC 2, the pressure was raised to 50 GPa, the sample was then heated locally using double sided Nd:YAG laser heating to 1250 K. Finally, the sample was decompressed to ambient conditions very slowly over a

period of 24 hours.

Both samples were characterised by *ex situ* Raman spectroscopy in 4 stages: a) before pressurisation, b) after pressurisation, c) after heating and d) after decompression. For each spectra, 3 acquisitions were taken of 200 seconds each.

The sample that was raised to 50 GPa was also characterised by *ex situ* XRD in 2 stages: a) after heating, and b) after decompression. Since the sample hole had shrunk because of the high pressure, a smaller collimator had to be used, which came at the cost of the peak resolution of the XRD data.

4.3 Results

4.3.1 Experiment at peak pressure of 25 GPa

Figure 4.1 shows the comparison between the Raman spectroscopy done on the boron carbide powder in the diamond anvil cell and that on the decompressed sample at 18 GPa after attaining a peak pressure of 25 GPa.

The non-hydrostatically decompressed sample shows complete amorphisation. None of the principle boron carbide peaks that were visible before pressurisation are present in the latter sample. A broad peak has appeared at 1137 cm^{-1}, which is superceded by the signal from the diamond beginning at 1300 cm^{-1} : this peak could correspond to the amorphous boron carbide Raman peak.

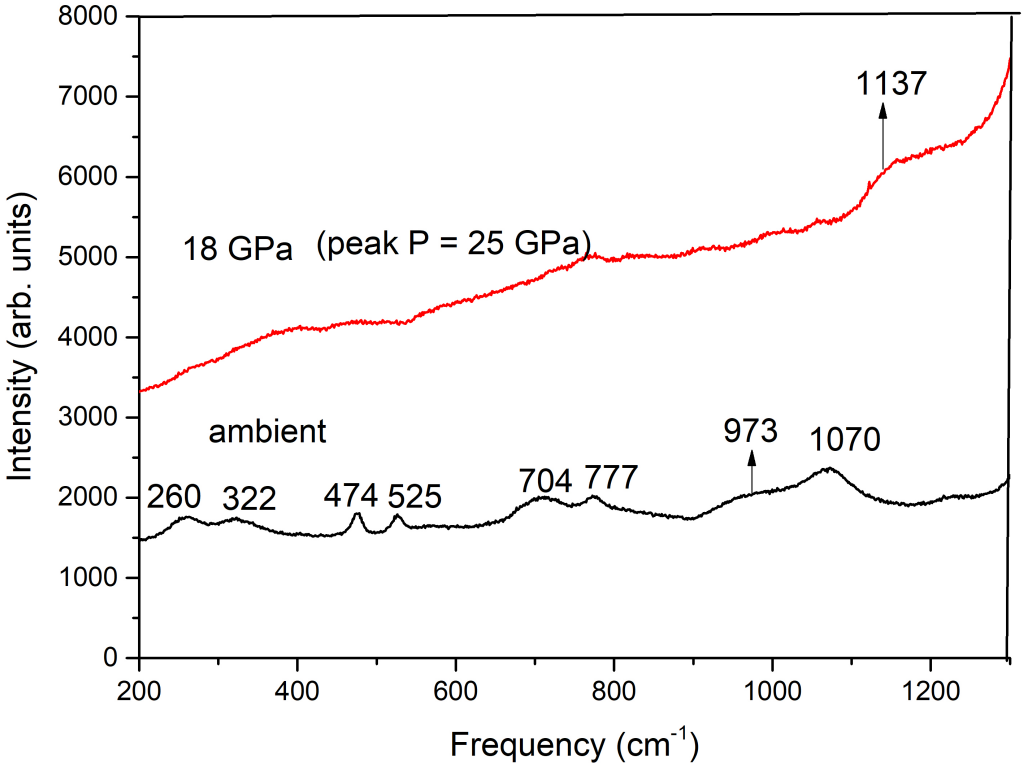

Figure 4.1: ex situ Raman spectra of boron carbide powder inside the DAC before pressurisation, and after non-hydrostatic depressurisation to 18 GPa after a peak pressure of 25 GPa.

In a second step, the sample was heated. Due to the relatively large sample volume, the two beams from the double sided laser heating could not couple. The heat generated was hence quickly dissipated by the diamond. As a result, the temperature reached could not be calibrated. However, some changes in the Raman pattern have been observed at the centre of the sample where the laser struck the sample surface, as shown in figure 4.2. These changes have disappeared once the sample was completely decompressed to ambient pressure, and the sample have become, once again, completely amorphous.

Figure 4.3 shows the Raman spectroscopy at the edge of the sample, far from the laser heating spot. No crystallisation is observed at this position after the centre of the sample was heated.

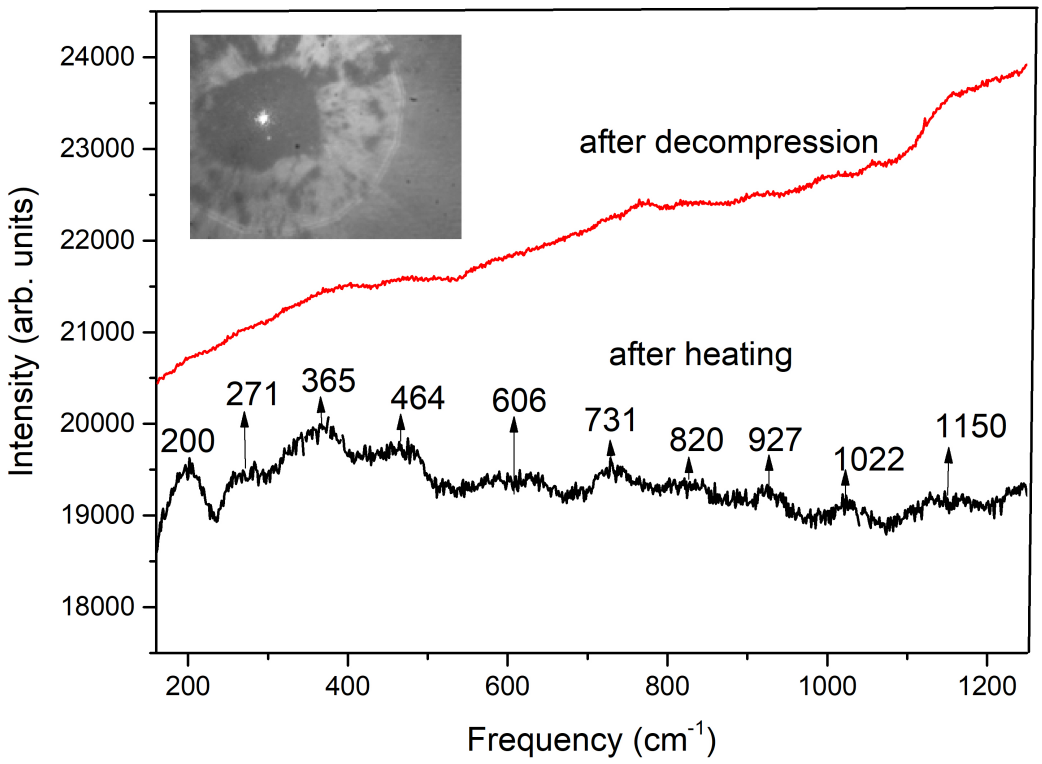

Figure 4.2: ex situ Raman spectra of boron carbide powder inside the DAC after heating at 18 GPa, and after non-hydrostatic depressurisation to ambient pressure. The Raman spectra has been taken in the centre of the sample, where the laser hit the sample. The position where the Raman spectroscopy was done is shown in the inset image.

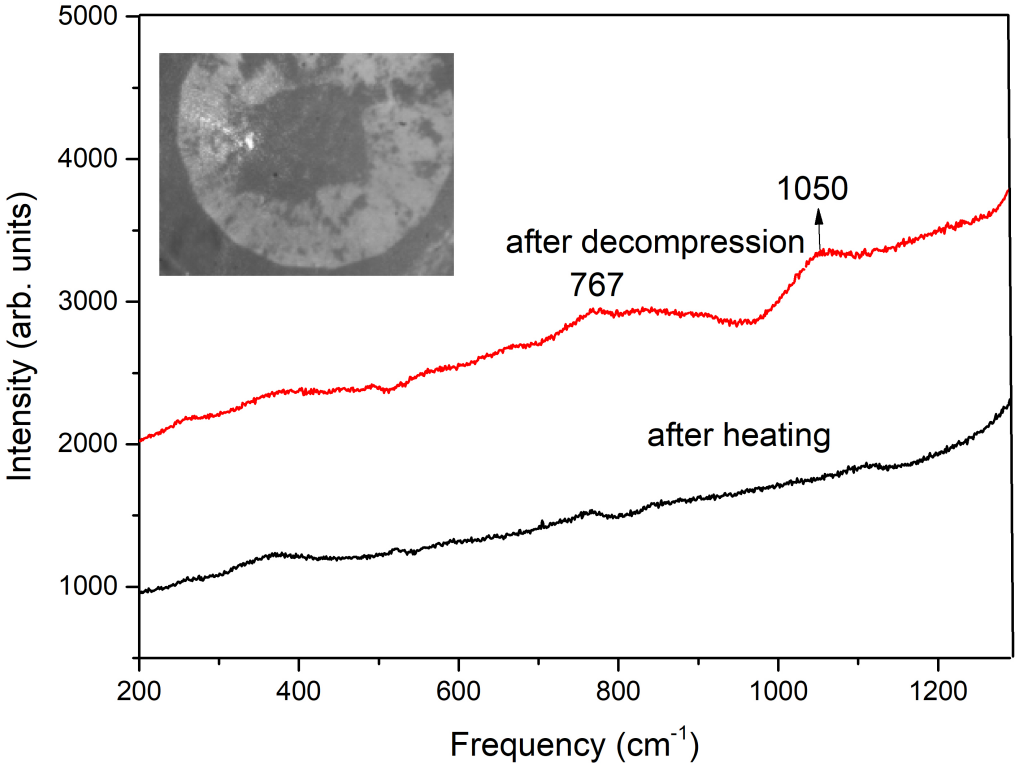

Figure 4.3: ex situ Raman spectra of boron carbide powder inside the DAC after heating at 18 GPa, and after non-hydrostatic depressurisation to ambient pressure. The Raman spectra has been taken at the edge of the sample, far from where the laser hit the sample. The position where the Raman spectroscopy was done is shown in the inset image.

4.3.2 Experiment at peak pressure of 50 GPa

Figure 4.4 shows the comparison between the Raman spectroscopy done on the boron carbide powder in the diamond anvil cell and that on the pressurised sample at 50 GPa.

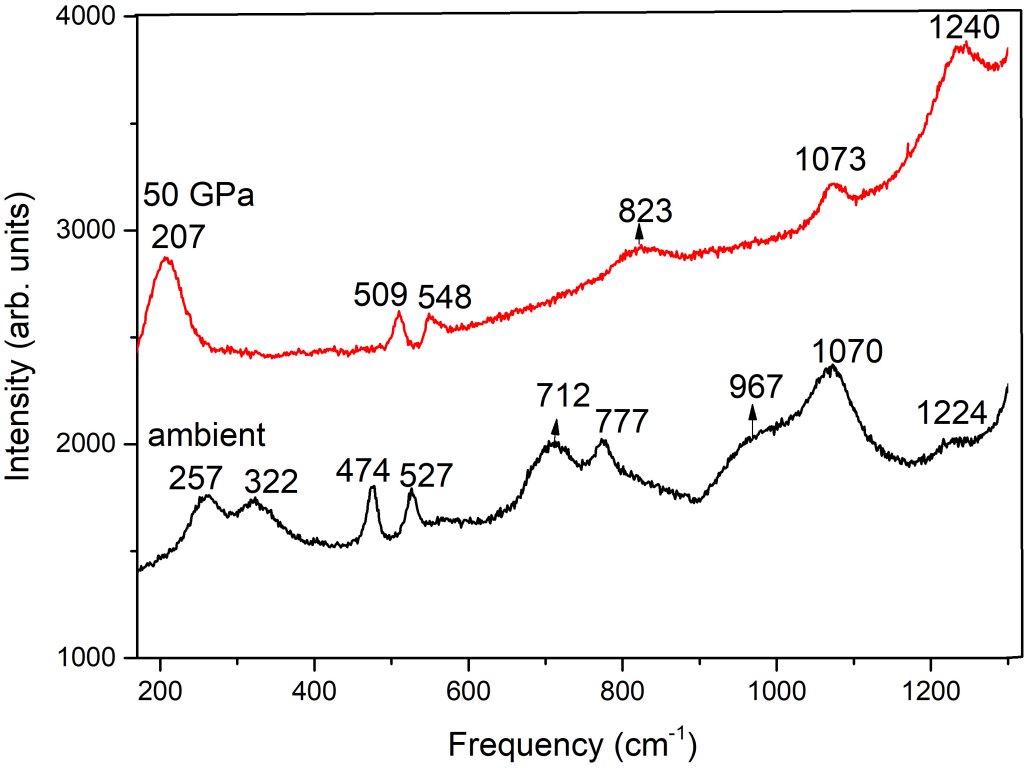

Figure 4.4: ex situ Raman spectra of boron carbide powder inside the DAC before pressurisation, and after pressurisation to 50 GPa.

It is important to note here that the gasket hole had shrunk to a diameter of 70µm as the pressure was increased. The temperature was raised to ∼1250 K, determined by pyrometry and Raman spectroscopy was done at various places on the sample immediately after. Then the cell was decompressed and the process was repeated. Figure 4.5 shows the comparison between the spectra after heating and that after depressurisation at the centre of the sample. Figure 4.6 does the same for a position at the edge of the sample.

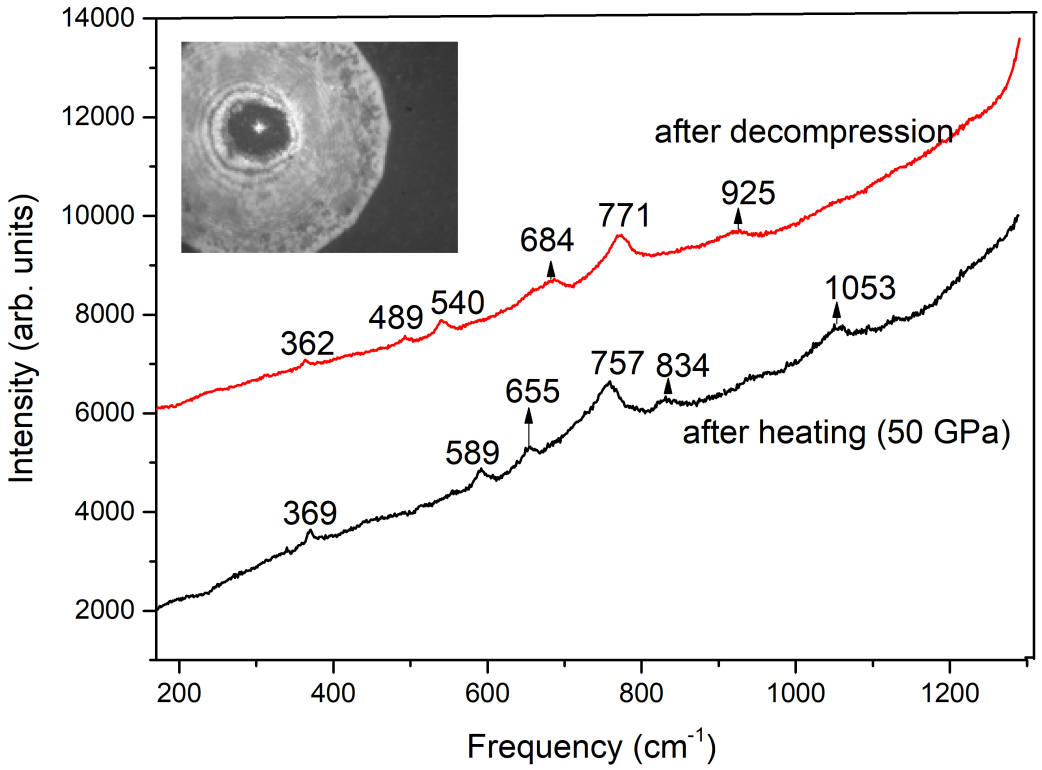

Figure 4.5: ex situ Raman spectra of boron carbide powder inside the DAC after heating to 1250 K at 50 GPa, and after non-hydrostatic depressurisation to ambient pressure. The Raman spectra have been taken at the centre of the sample. The position where the Raman spectroscopy was done is shown in the inset image.

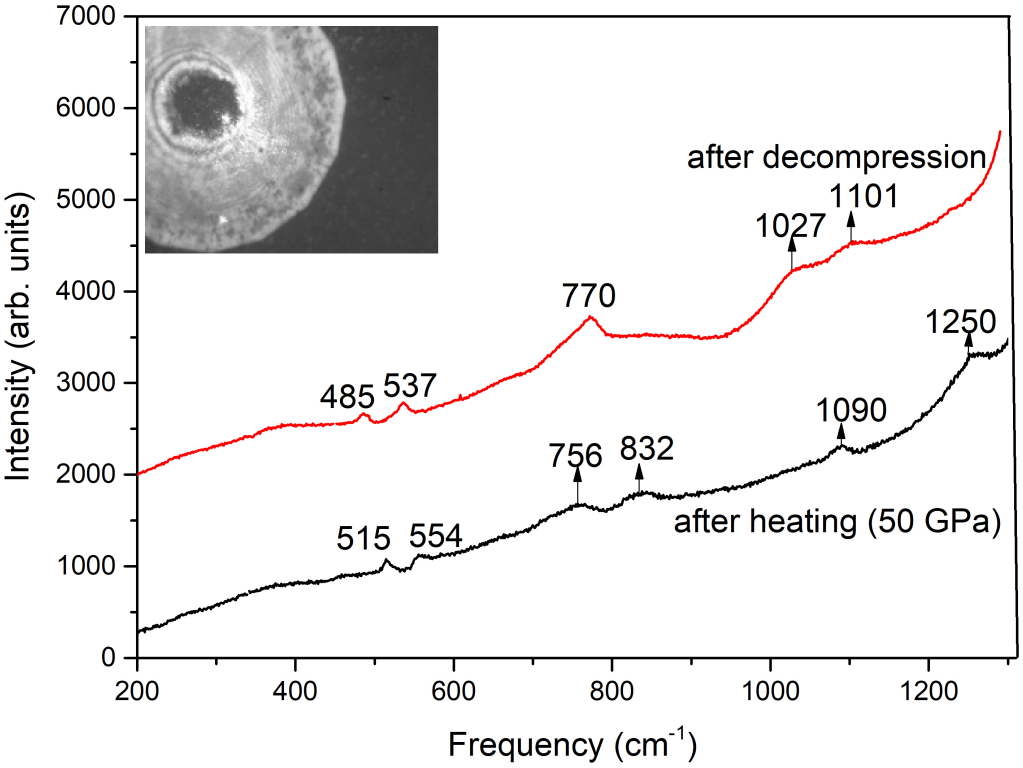

Figure 4.6: ex situ Raman spectra of boron carbide powder inside the DAC after heating to 1250 K at 50 GPa, and after non-hydrostatic depressurisation to ambient pressure. The Raman spectra have been taken at the edge of the sample. The position where the Raman spectroscopy was done is shown in the inset image.

After heating, the sample was kept under the pressure of 50 GPa and a X-ray diffraction pattern was taken. However, the diffraction pattern was not taken immediately after heating, unlike the Raman spectroscopy pattern: this might have caused some relaxing of the sample. After decompression to ambient conditions, another X-ray diffraction was done. Figure 4.7 shows the comparison between the two XRD patterns, taken at 50 GPa

after heating, and ambient conditions, after decompression.

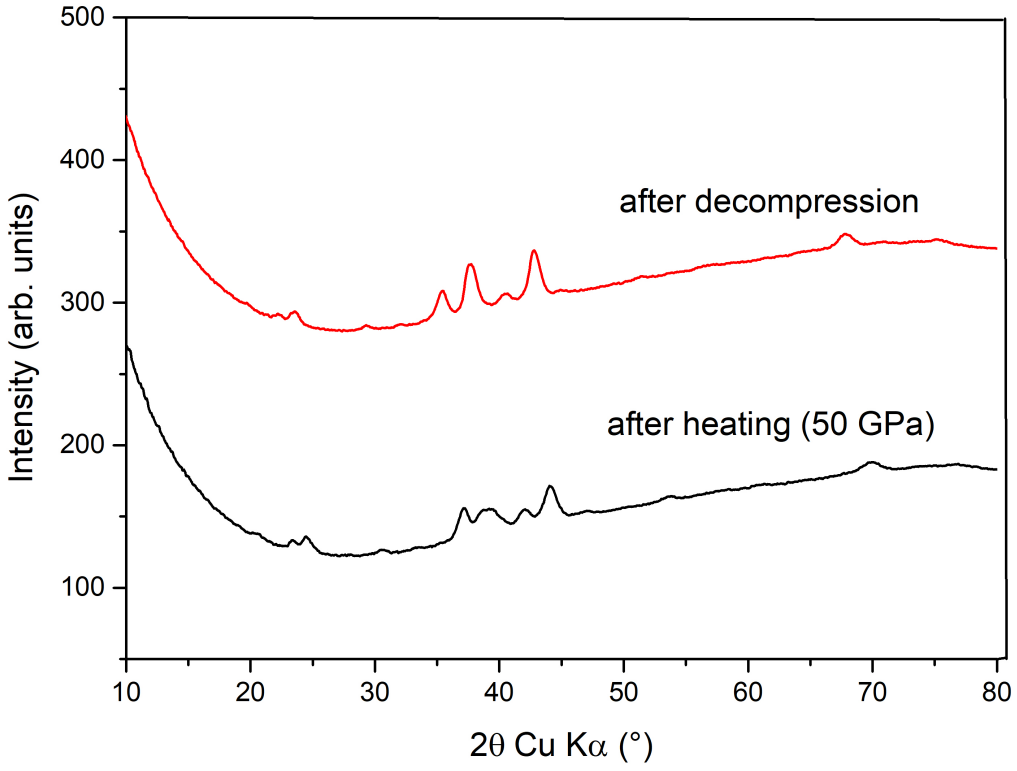

Figure 4.7: ex situ X-ray diffraction of boron carbide powder inside the DAC after heating at 50 GPa, and after non-hydrostatic depressurisation to ambient pressure.

4.4 Discussions

4.4.1 Experiment at peak pressure of 25 GPa

The subsequent depressurisation to 18 GPa after increasing the pressure to 25 GPa in non-hydrostatic conditions show complete amorphisation of the boron carbide powder. Since the focused laser beam used for the Raman spectroscopy has a size of 10 µm, and

no crystalline boron carbide peak has appeared in the 18 GPa sample, it can be said that the amorphous areas of boron carbide has a size greater than 10 µm. This amorphisation of boron carbide is in accordance with the results reported by Yan *et al.* [42].

When the centre of the sample is heated by interaction with the Nd:YAG laser, as shown in figure 4.2, some recrystallisation of boron carbide peaks occurs. Reddy *et al.* [112] have observed that the icosahedral structure displaced from the crystalline matrix is retained in the shear-induced amorphous bands in boron carbide through atomic-scale observations using aberration-corrected transmission electron microscopy. The application of heating might have thus caused the feeble Raman peaks observed in figure 4.2 to appear: these correspond to the icosahedra. The mode at 464 cm^{-1} may be attributed to the mode *Ico 7*, which is a pseudo-rotation of the C-B-C chain. However, the mode at 539 cm^{-1}, typical of the libration of the icosahedron, could not be detected. However, the stress resulting from further decompression to ambient conditions would cause the recrystallisation to disappear, resulting in the boron carbide sample becoming completely amorphous again.

However, when Raman spectroscopy was done on the edge of the sample after heating, as shown in figure 4.3, no recrystallisation was observed. This can be attributed to the local nature of the heating at the centre and the quick dissipation of the heat through the diamond before it could reach the edge of the sample. Therefore, the edge of the sample was not heated at all.

4.4.2 Experiment at pressure of 50 GPa

Raman spectroscopy

When the Raman spectra before and after pressurisation to 50 GPa are compared in figure 4.4, a few differences become apparent immediately. The pair of peaks at 257 and 322 cm^{-1} has disappeared and a single intense peak at 207 cm^{-1} has appeared in its place. The pair of peaks at 474 and 527 cm^{-1} has moved to higher frequencies of 509 and 548 cm^{-1}, as is expected. The pair at 712 and 777 cm^{-1} has been replaced by a single peak at 823 cm^{-1}. However, the peak at 1070 cm^{-1} has remained quasi-constant. The peak at 1224 cm^{-1} has moved to 1240 cm^{-1} and has become much more intense.

As the sample was heated, its Raman spectrum at the centre changes completely, as shown in figure 4.5: this points towards a possible phase change. This new phase(s) seems to have been retained when the sample was slowly brought back to ambient pressure, with an expected movement of the Raman peaks towards lower frequencies. These frequencies have been compared in table 4.1 to those predicted in Ref. [5] for different high pressure phases of boron carbide.

Peaks after heating (50 GPa) (expt.)	Peaks after decompression (expt.)	B_4C (theory)	$(B_{11}C^p)C\square C$ (theory)	$(B_{11}C^p)$C-C (theory)	(B_{12})C-C (theory)	$(B_{10}C_2^p)_{diff}$C-C (theory)	Name	Symmetry (theory)
369	362	1095	**398**	570	573	581	Ch5, cs	A_{1g}
		536 549	481 488	410 491	**389**	527 538	Ico5, lib	E_g
589	489	536 549	481 **488**	410 **491**	389	527 538	Ico5, lib	E_g
655	540	**536 549**	481 488	410 491	389	**527 538**	Ico5, lib	E_g
		479 488	**529 533**	592 621	583	562 NA	Ico7, pcr	E_g
757	684	**699**	713	**692**	**673**	**702**	Ico17	A_{1g}
		840 841	819 831	**692 708**	646	NA NA	Ico13	E_g
834	771	737 **768**	730 **754**	726 **770**	709	NA NA	Ico11	E_g
1053	925	808 815	801 827	876 **918**	862	NA NA	Ico20	E_g
		1052 1056	1096 1108	885 1184	957	1225 1233	Ico23	E_g
		994	1057	984	998	1053	Ico21	A_{1g}
		719	795	805	729	842	Ico9	A_{1g}
		1098 1139	1218 1223	1048 1059	1056	1118 1138	Ch3, cr	E_g

Table 4.1: Experimental Raman peaks (cm^{-1}) at the centre of the sample at 50 GPa after heating and corresponding theoretical peaks (cm^{-1}) of B_4C, $(B_{11}C^p)C\square C$, $(B_{11}C^p)$C-C, (B_{12})C-C and $(B_{10}C_2^p)_{diff}$C-C at ambient pressure. □ stands for the boron vacancy in the C-B-C chain. Theoretical frequencies in bold font correspond to the new peak. Theoretical mode frequency, name and symmetry from table 4.2 of Ref. [5] have been extracted in tables 1.2 and 1.3 of Chapter 1. pcr, lib, asis, sis, cs and cr stand respectively for the pseudo-chain rotation, libration of the icosahedra, anti-symmetric and symmetric intericosahedral stretching, symmetric chain stretching and chain rotation modes. 'NA' stands for non attributed peaks.

In this case, significant changes are also seen at the edge of the sample because of the heating, as seen in figure 4.6. Since both the sample area and volume in this case is more than twice as much smaller than that of the 18 GPa sample, it is possible that the edge was also heated by thermal dissipation. These frequencies have been compared in table 4.2 to those predicted in Ref. [5] for different high pressure phases of boron carbide.

In both the centre and the edge of the sample, all of the new peaks that have appeared could potentially be explained by polymorphs having C-C chains and a combination of B_{12}, $B_{11}C$ and $B_{10}C_2$ icosahedra.

However, at the edge of the sample, all of the peaks could also be explained by theoretical peaks of B_4C, as shown in table 4.2.

At the centre, the peak 925 cm^{-1} (after decompression to ambient pressure) can only be explained by the phase $(B_{11}C^p)$C-C and the peak 362 cm^{-1} can be explained by either (B_{12})C-C or $(B_{11}C^p)C\square C$. However, in calculations, the presence of vacancies in the chain is exclude, as C-C bonds form instead.

This could be the due to the formation of polytypes with C-C chains at the centre of the sample. The laser strikes the centre of the sample directly before the heat generated is dissipated by the diamond and hence, the most effective heating takes place at that position.

Peaks after heating (50 GPa) (expt.)	Peaks after decompression (expt.)	B_4C (theory)	$(B_{11}C^p)C\square C$ (theory)	$(B_{11}C^p)$C-C (theory)	(B_{12})C-C (theory)	$(B_{10}C_2^p)_{diff}$C-C (theory)	Name	Symmetry (theory)
515	485	536 549	**481 488**	410 **491**	389	527 538	Ico5, lib	E_g
		479 488	529 533	592 621	583	562 NA	Ico7, pcr	E_g
554	537	**536 549**	481 488	410 491	389	**527 538**	Ico5, lib	E_g
		479 488	**529 533**	592 621	583	562 NA	Ico7, pcr	E_g
756	685	**699**	713	**692**	**673**	**702**	Ico17	A_{1g}
		840 841	819 831	**692 708**	646	NA NA	Ico13	E_g
832	770	737 **768**	730 **754**	726 **770**	709	NA NA	Ico11	E_g
1090	1027	**1052 1056**	1096 1108	885 1184	957	1225 1233	Ico23	E_g
		1098 1139	1218 1223	1048 1059	1056	1118 1138	Ch3, cr	E_g
		994	**1057**	984	998	**1053**	Ico21	A_{1g}
1250	1101	**1052 1056**	1096 **1108**	885 1184	957	1225 1233	Ico23	E_g
		1098 1139	1218 1223	1048 1059	1056	**1118 1138**	Ch3, cr	E_g
		1095	398	570	573	581	Ch5, cs	A_{1g}
		719	795	805	729	842	Ico9	A_{1g}
		808 815	801 827	876 918	862	NA NA	Ico20	E_g

Table 4.2: Experimental Raman peaks (cm^{-1}) at the edge of the sample at 50 GPa after heating, after decompression to ambient pressure and corresponding theoretical peaks (cm^{-1}) of $(B_{11}C^p)C\square C$, $(B_{11}C^p)$C-C, (B_{12})C-C and $(B_{10}C_2^p)_{diff}$C-C at ambient pressure. $\square$ stands for the boron vacancy in the C-B-C chain. Theoretical frequencies in bold font correspond to the new peak. All notations are same as table 4.1.

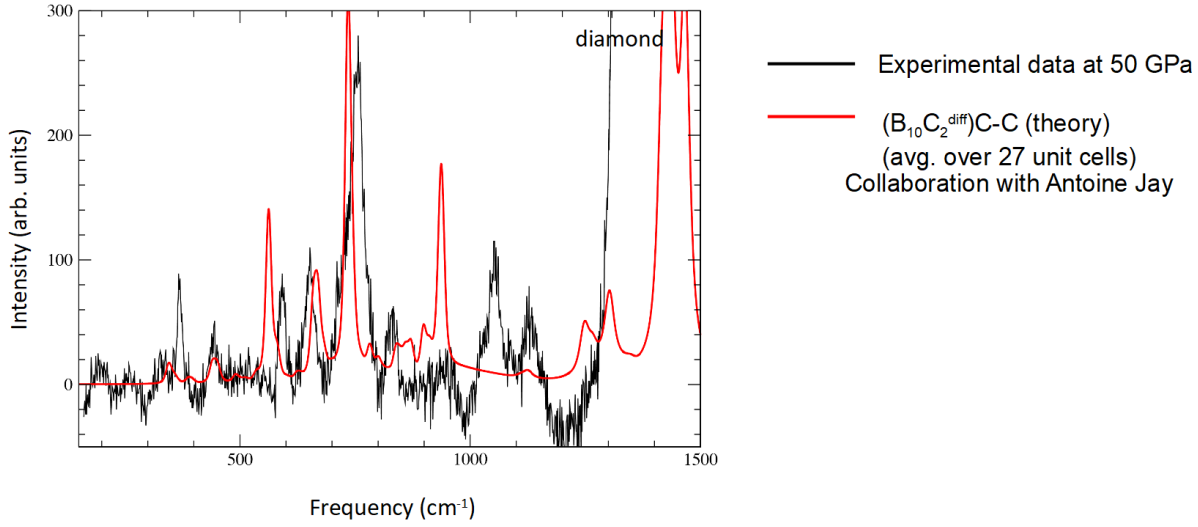

Figure 4.8: ex situ Comparison between the experimental Raman spectra of the boron carbide powder inside the DAC obtained at the centre of the sample at 50 GPa after laser heating (black line) and the theoretical Raman spectra of $(B_{10}C_2^p)_{diff}$ C-C averaged over 27 unit cells.

In the figure 4.8 , the experimental Raman spectra at 50 GPa after laser heating has been superposed on the theoretical spectra predicted at 50 GPa for the expected thermodynamically stable phase at this pressure, $(B_{10}C_2^p)_{diff}$C-C. The theoretical Raman spectra was calculated using 376 atoms with 27 unit cells in order to produce rhombohedral averaging. The fit is surprisingly good considering the complex structure of boron carbide.

However, much work remains to be done : the background generated by the Raman spectra of diamond needs to be subtracted more rigorously and theoretical Raman spectra calculations averaging over other configurations of the $(B_{10}C_2)$C-C unit cell, with carbon atoms at different positions, need to be performed.

X-ray diffraction

Since a smaller collimator was used during the X-ray diffraction in order to avoid the signal from the rhenium gasket, the peak resolution was reduced.To compensate for this, I have considered the complete peak width of the diffraction peaks and then searched for a match amongst the predicted phases in Ref. [5]. These comparisons have been tabulated in table 4.3. The XRD pattern seems to have been retained after the decompression from 50 GPa to ambient pressure, though the shape of some of the peaks have slightly changed.

From table 4.3, it can be seen that all peaks could be explained by B_4C without any phase change. This can be attributed to the diffraction pattern being an average of the entire sample volume, and not just the centrally heated area. As seen from the results of the Raman spectroscopy, the sample shows potential phase change near the centre and not necessarily towards the edges. However, it is also possible that signals from other phases are present in the diffraction results, but they could not be identified because of the poor peak resolution of the data.

In situ X-ray diffraction using synchrotron facilities would be a good manner of investigating the local area of the sample that is heated, thus effectively identifying the phase formed.

Peaks after heating (50 GPa) 2θ	Peaks after decompression 2θ	B_4C (theory) 2θ	$(B_{11}C^p)C\square C$ (theory) 2θ	$(B_{11}C^p)$C-C (theory) 2θ	(B_{12})C-C (theory) 2θ	$(B_{10}C_2^p)_{diff}$C-C (theory) 2θ
23.03 - 23.91	21.53 - 22.82	21.98	22.38			
23.91- 25.49	22.82 - 24.30	23.49	23.82	23.89	24.27	23.84
36.29 - 37.87	34.11 - 36.49	34.89	35.47	37.20	37.32	37.25
37.87 - 40.95	36.58 - 38.86	37.84	38.30	37.20	37.62	37.25
41.14 - 42.63	39.55 - 41.03	40.05	40.56	40.46	40.28	40.73
43.02 - 45.40	41.73 - 44.31	41.62	42.34	44.69	44.93	44.70
68.66 - 71.14	66.59 - 68.97	66.83	67.69	66.17		66.61

Table 4.3: Experimental x-ray diffraction peaks of the sample at 50 GPa after heating, after decompression to ambient pressure and corresponding theoretical peaks of $(B_{11}C^p)C\square C$, $(B_{11}C^p)$C-C, (B_{12})C-C and $(B_{10}C_2^p)_{diff}$C-C at ambient pressure. $\square$ stands for the boron vacancy in the C-B-C chain. 2θ values are given in Cu K-α. Calculations from table B.13 of Ref. [5].

4.5 Conclusions and perspectives

Probable formation of C-C chains was observed in boron carbide at 50 GPa pressure after heating at 1250 K. The phase change was observed by Raman spectroscopy, but could not be identified by X-ray diffraction in the absence of *in situ* facilities.

Amorphisation of boron carbide was also observed when the pressure was non-hydrostatically decreased from a peak pressure of 25 GPa.

However, no amorphisation was observed during non-hydrostatic decompression after the new phase was formed at 50 GPa.

Experiments would be performed later in this pressure range using boron carbide single crystals. This would allow both hydrostatic and non-hydrostatic pressurisation and decompression. Also, using single crystals would facilitate the use of KCl as insulators between the diamond and the sample: this would prevent heat dissipation through the diamonds, resulting in more stable heating.

The ideal would be to perform this experiment in a synchrotron: in some experimental lines, (like ID27 at ESRF, Grenoble), it is possible to carry out locally both Raman spectroscopy and X-ray diffraction at the same time in the precise spot where the laser heats the sample. Hence both the Raman spectroscopy and XRD results would be accessible in *in situ* conditions at very high temperatures and pressures. This could not be done during the period of this thesis work because first the ESRF and then the line ID27 were under reconstruction.

Chapter 5

Deformation of boron carbide powder using the Rotational Tomographic Paris-Edinburgh Cell (RoToPEC)

5.1 Introduction

I have used the RoToPEC (Rotating Tomography Paris Edinburgh Cell, see Sec 1.3.1) to create torsion in boron carbide under a pressure of 5 GPa. By applying a dynamical stress, my objective was to bring boron carbide in the plastic regime, to observe the defects that are formed, and to check whether vacancies (noted as □) are observable.

Thereby, my aim is to verify the eventual presence of C□C arrangements between the icosahedra after the plastic regime has been reached.

A more exhaustive study at various temperature values (up to 1000 K) and pressure values (up to 7 GPa) was planned initially. This is because different combinations of temperature and pressure will have variable effects on the creation and displacement of defects. However, the time constraint imposed by the pandemic of Covid 19 made it important to narrow down the number of experiments to one set of temperature and pressure value with three different degrees of rotation of the RoToPEC. We have chosen to avoid the experiments at high temperature as this might anneal some of the defects created.

Therefore, I have chosen a pressure value of 5 GPa at room temperature for my torsion experiments using RoToPEC. The reasons for having chosen such a value of pressure is the following one: the Hugoniot elastic limit (HEL) of boron carbide is known to be 17 GPa [18, 133, 134]. DFT-GGA calculations have shown that when boron carbide is heated to a temperature of 2000 K (resp. 1000 K), the thermal expansion is equivalent to an internal pressure of -12.2 GPa (resp. -6.9 GPa). Thus, it can be seen that when, in a shock wave experiment, a dynamical stress of 17 GPa (the HEL of boron carbide) is applied, leading to an elevation of temperature close to 2000 K, this amounts to a state of stress at ambient temperature of (17-12.2) GPa = 4.8 GPa [6]. Therefore, I choose a value of 5 GPa during the generation of the torsion at ambient temperature, and I expect this to be a good approximation of the non-hydrostatic conditions as those

near the HEL for boron carbide. A possible annealing of defects due to the elevated temperature has not been considered in the above estimation of the pressure.

5.2 Experimental materials and methods

Commercial boron carbide (Alfa Aesar, 99+ % purity) has been put inside a pyrophyllite gasket, as shown in figure 5.1. The powder was confined inside the gasket by using a MgO plug on each side. The gasket was then placed inside the RoToPEC and subjected to a pressure of 5 GPa.

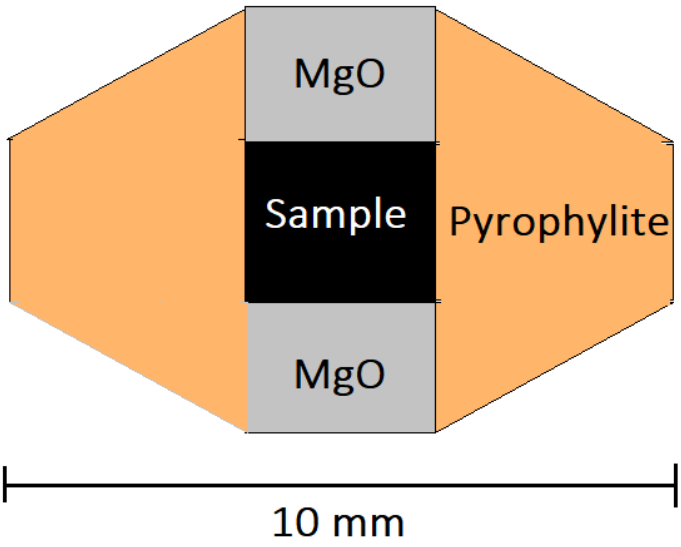

Figure 5.1: Gasket assembly for RoToPEC experiments. The sample is put directly inside the pyrophillite gasket, and is confined by a MgO plug on each end.

Three such experiments were performed, with different degrees of rotation of the anvils : 90°, 180° and 270°. In all of the experiments, only the lower anvil has rotated, the upper one being fixed. The speed of rotation of the anvil was maintained to 0.01°/second. The experimental parameters have been tabulated in table 5.1. After each experiment, the pressure was released slowly over thirty minutes.

Experiment name	Degree of rotation (°)	Speed of anvil (°/sec)	Anvil that rotates
RP 1	270	0.01	the lower one
RP 2	180	0.01	the lower
RP 3	90	0.01	the lower one

Table 5.1: Experimental parameters used for the deformation experiments done using the RoToPEC.

Since the deformations in the samples were created using torsion ($\tau = r \times F$, where τ is torque, r is the radial distance and F is the force applied), it was expected that the deformations would be a function of the radial distance of the location of the boron carbide particles with respect to the centre of the assembly. This is to say that in principle there would be no deformation at the centre of the assembly, and maximum deformation would occur on the edge. Keeping this in mind, it was decided to not recover the sample from the gasket, as was done in Chapter 2 for the Paris-Edinburgh press experiments. If the pyrophillite gasket was broken and the sample was recovered in the case of these RoToPEC experiments, the undeformed boron carbide powder at the center would be mixed with the deformed powder at the edge,s making characterisation

complicated to analyse. It would also deprive us of the opportunity to characterise the defects as a function of the radial distance.

In order to avoid this pitfall, two different routes were followed in order to characterise the samples. First, the deformed samples were characterised in the SOLEIL synchrotron, using energy dispersive x-ray diffraction (EDXRD). This allowed us to characterise different points in the sample volume locally, using the powerful synchrotron radiation without the requirement of any sample recovery from the gasket. Figure 5.2 shows the locations of all of the points on a cross-sectional view of the sample volume where EDXRD was done in order to characterise the samples. The size of the slits both in front of and behind the sample in the synchrotron was around 30 microns. This means that the size of the sample that was scanned at each position was also around 30 microns, which is very small compared to the diameter of the total boron carbide sample, which is around 3.5 mm. The positions were chosen assuming that the deformations in the sample would be radially symmetric.

Next, the gaskets were prepared for characterisation by Raman spectroscopy. Each of the gasket was embedded in a cold resin. The resin mixture was made by mixing 2 parts by weight of acrylic KM-U and 1 part by weight of methyl methacrylate. The gasket was then placed in the middle of a mould and the resin mixture was poured over it. The set-up was allowed to rest for 2 hours till the resin solidified. The gasket embedded in the resin was then polished using the macropolishing device by Mecapol, until the sample surface was exposed on both sides, as shown in figure 5.3. The polishing was done as

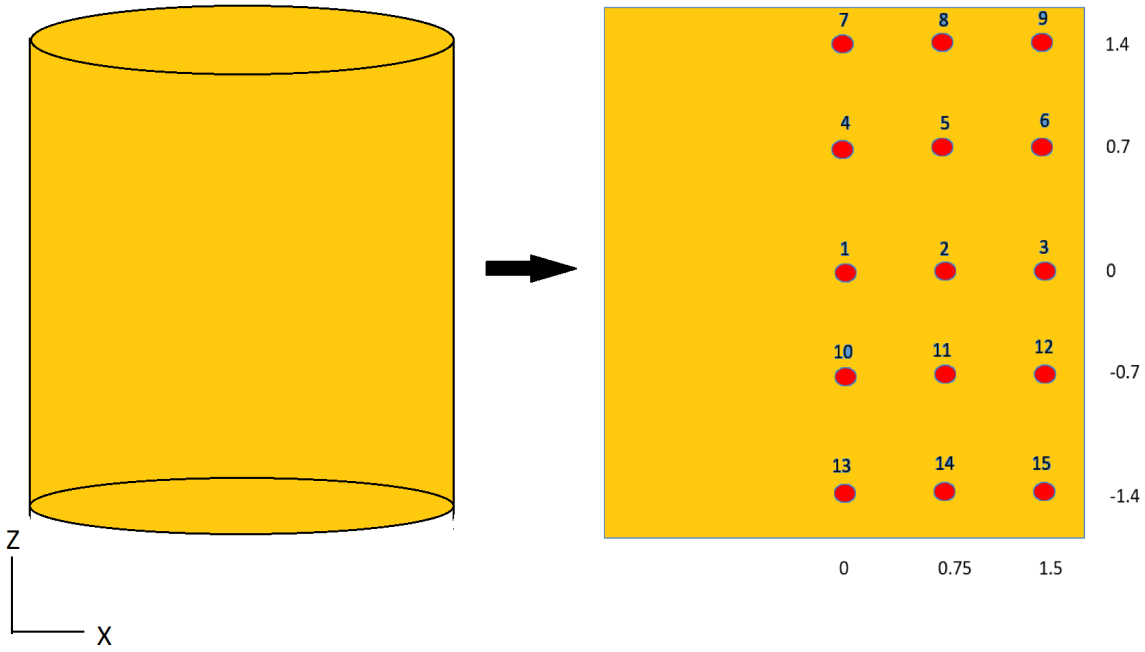

Figure 5.2: Positions in the gasket where EDXRD was done in each of the samples (red colour). The (0,0) coordinates refer to the centre of the sample, marked with the label "1". The deformation is supposed to be minimum at the centre, while the maximum deformations are expected at the points (1.5,1.4) and (1.5, -1.4), given by the labels "9'" and "15" respectively. The point coordinates are given in mm, with the sample centre as the origin. The rectangular shape of the sample results from the projection of the cylindrical sample on the X-Z plane.

gently as possibly with a 120 grit sandpaper at a speed of 100 revolutions per minute. Raman spectroscopy was then done on both the upper and lower exposed surfaces of the samples.

It is important to note that the EDXRD and the Raman spectroscopy were therefore not done on the same areas of the sample. Since the sample shapes are cylindrical, the

Figure 5.3: The gasket embedded in the resin and then polished, in order to facilitate Raman spectroscopy. The sample was polished on both the top and bottom circular surfaces and one of these sides is shown in the image. The black circle seen in the centre of the gasket is the sample. Raman spectroscopy was done in various points on the sample surface.

EDXRD was performed within the sample volume on the rectangular cross-section of the samples (figure 5.2). Raman spectroscopy, however, was performed on the top and bottom circular areas of the sample surfaces (figure 5.3), as these were the only areas that could be accessed without destruction of the samples. I note here that while the polishing was done very gently, its effect on the sample (local heating etc) is not known and has not been considered here in this first analysis.

5.3 Results

5.3.1 Energy dispersive x-ray diffraction

Energy dispersive x-ray diffraction (EDXRD) was performed post-mortem in the SOLEIL synchrotron on 15 different points in each of the three samples, leading to 45 different EDXRD patterns. Due to the constraint of space, I have only shown a few of these

EDXRD patterns in the present chapter. The EDXRD data has been converted to the corresponding peaks for Cu K-α radiation, in order to compare them with the XRD pattern of the reference boron carbide powder at ambient pressure.

Figure 5.4 shows the diffraction peaks for the experiment RP1 (see table 5.1) at the centre of the assembly on the positions 1, 2 and 3 (see figure 5.2). There were several new peaks that appeared in the diffraction pattern at the edge of the sample (position 3), which could be interpreted as the appearance of a new phase because of the applied torsion. This is also coherent with the expectation that maximum deformations will occur at the edge of the sample.

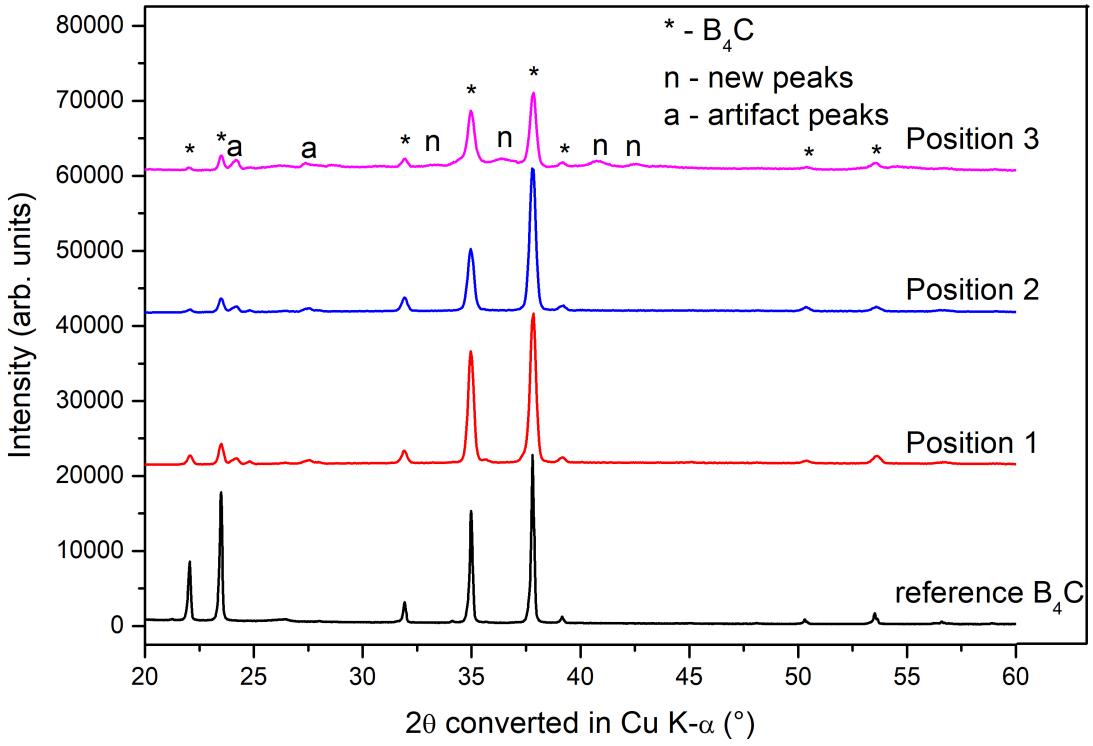

Figure 5.4: X-ray diffraction pattern of the rectangular cross-section of the gasket rotated by 270° in the RoToPEC (experiment RP1). The black line shows the reference boron carbide powder at ambient pressure. Position 1 refers to the center of the sample, position 2 refers to a location in the middle along the radial distance while position 3 refers to the edge of the sample.

In order to demonstrate the effect of the degree of rotation on the samples, I have shown the EDXRD patterns on the same positions in RP2 and RP3 (see table 5.1) in figure 5.5 and figure 5.6 respectively. These patterns showed no difference with respect to the distance from the centre. There were three unknown peaks that appeared in all of the

spectra, and one should avoid to consider them as an evidence for the formation of a new phase, as will be explained in Sec 5.4.

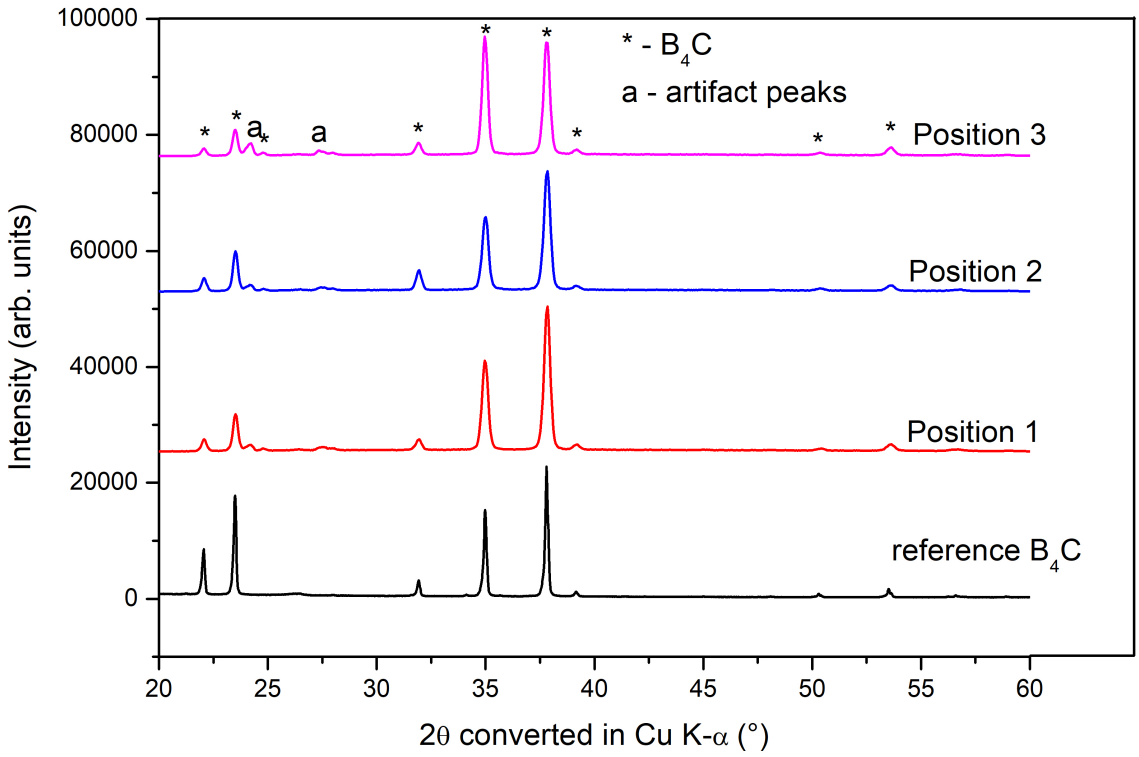

Figure 5.5: X-ray diffraction pattern of the rectangular cross-section of the gasket rotated by 180° in the RoToPEC (experiment RP2). The black line shows the reference boron carbide powder at ambient pressure. Position 1 refers to the centre of the sample, position 2 refers to a location in the middle along the radial distance while position 3 refers to the edge of the sample.

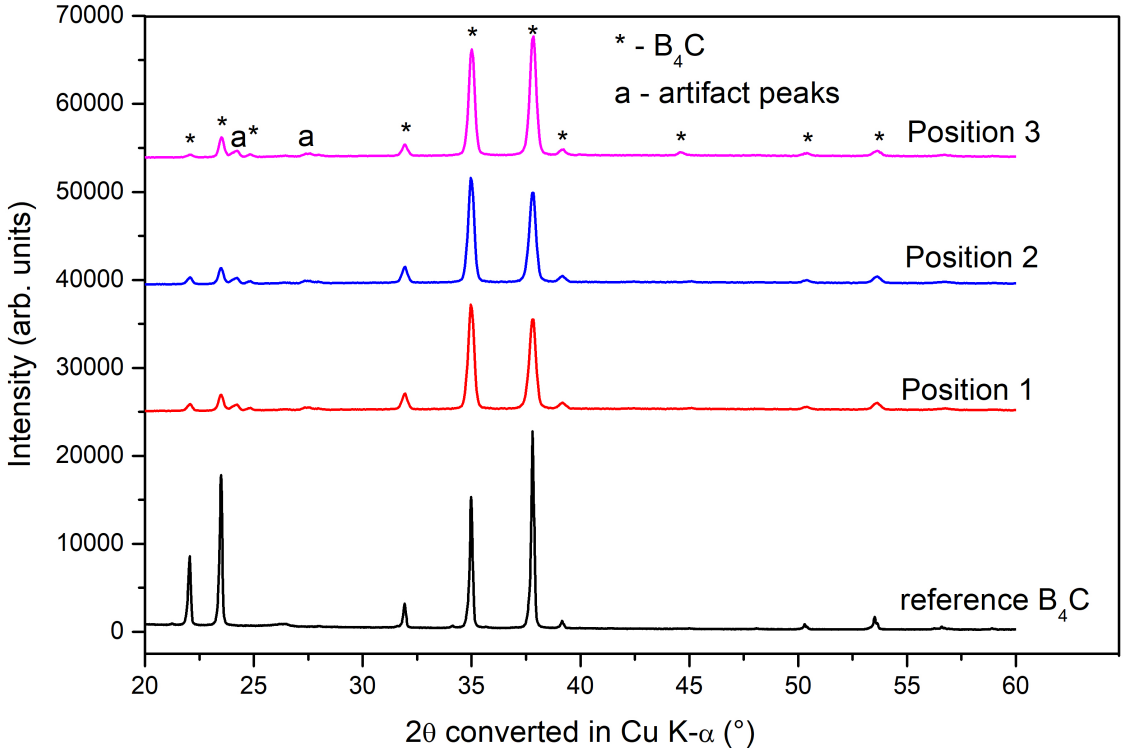

Figure 5.6: X-ray diffraction pattern of the rectangular cross-section of the gasket rotated by 90° in the RoToPEC (experiment RP3). The black line shows the reference boron carbide powder at ambient pressure. Position 1 refers to the center of the sample, position 2 refers to a location in the middle along the radial distance while position 3 refers to the edge of the sample.

5.3.2 Raman spectroscopy

After having characterised the samples by EDXRD, a study of the Raman spectroscopy on the sample embedded in the resin (figure 5.3) was done. Again, only a few of the more pertinent spectra could be reported because of the constraint of space. Figures 5.7, 5.8 and 5.9 show spectra along three different directions on the circular surfaces of the

sample RP1 (see table 5.1). Again, changes in the spectra have begun to appear as the laser beam moves away from the centre towards the edge. However, as seen in figure 5.9, the appearance on these spectral changes does not strictly depend on the radial distance from the centre.

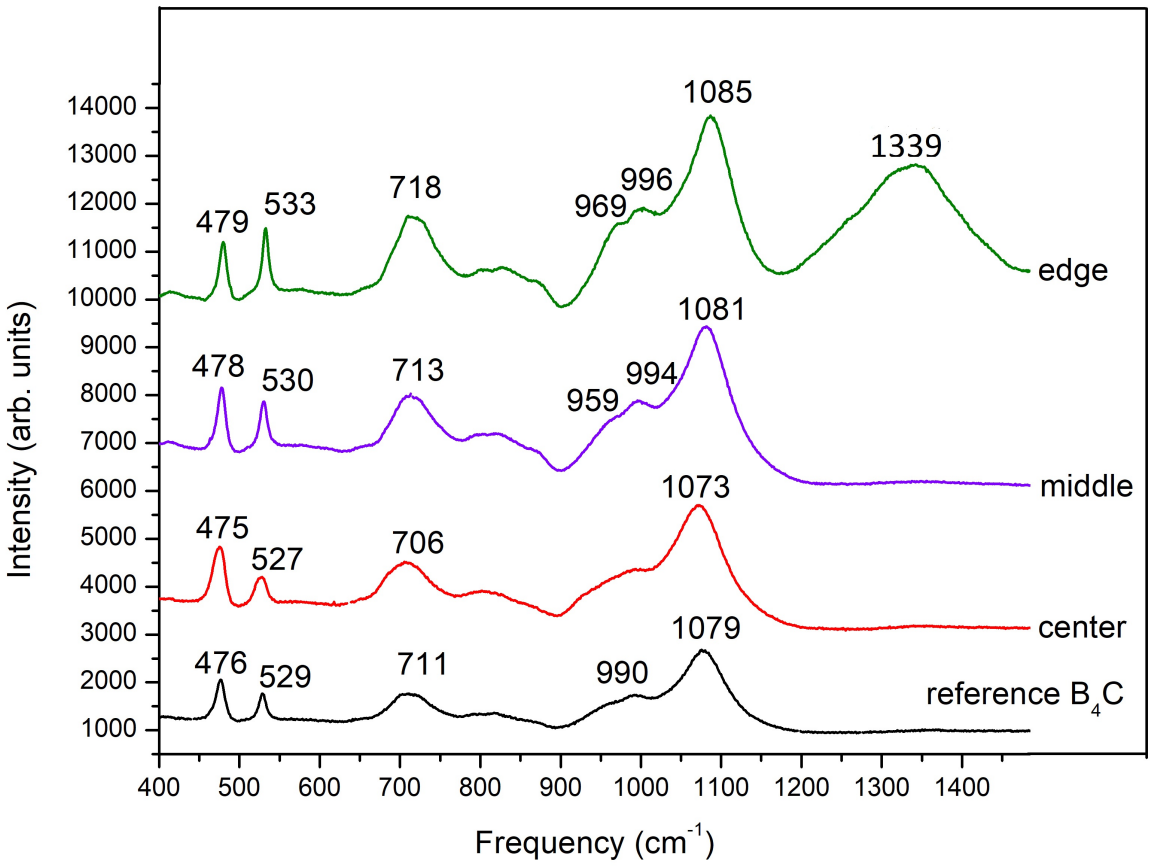

Figure 5.7: Raman spectroscopy of the circular surface of the gasket rotated by 270° in the RoToPEC (experiment RP1) along one direction. The position where the spectrum was taken has been varied from the disc-centre to the disc-edge along the radius. The black line shows the reference boron carbide powder at ambient pressure.

Figures 5.10 and 5.11 show some of the Raman spectra obtained for the samples RP2 and

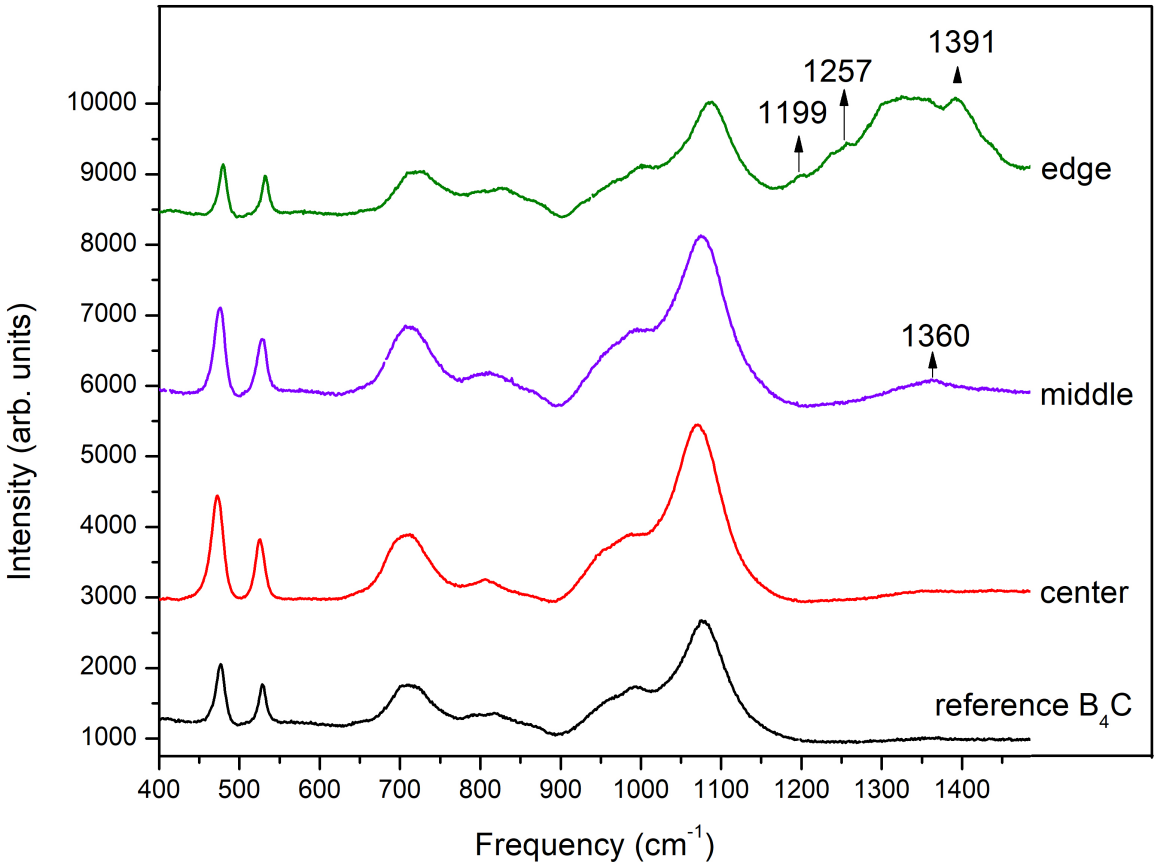

Figure 5.8: Raman spectroscopy of the circular surface of the gasket rotated by 270° in the RoToPEC (experiment RP1) along a direction other than those of figure 5.7. The three positions where the spectra were taken have been varied from the centre of the disc to the edge along the radius. The black line shows the reference boron carbide powder at ambient pressure.

RP3 respectively. There have been some changes in the spectra for RP2 while no change has been observed for RP3. This observation thus underscores once again the effect of the angle of rotation in creating deformation and thus defects in the sample.

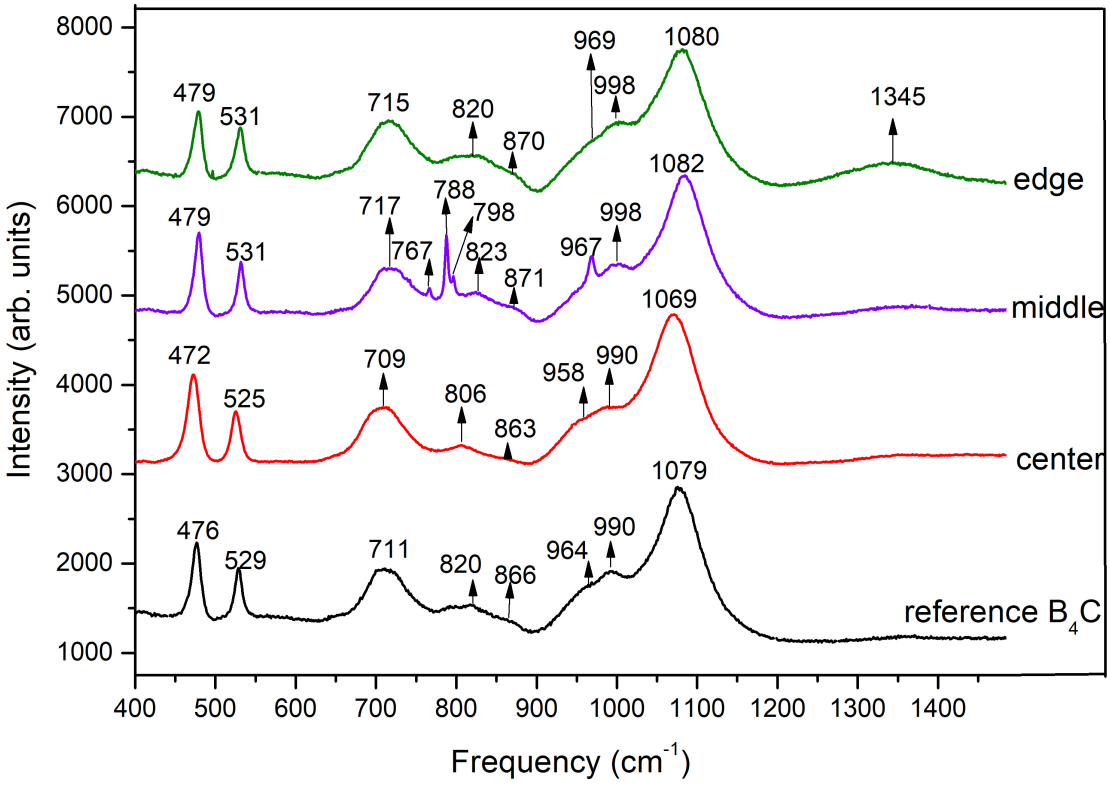

Figure 5.9: Raman spectroscopy of the circular surface of the gasket rotated by 270° in the RoToPEC (experiment RP1) along a direction other than that of figures 5.7 and 5.8. The three positions where the spectrum was taken have been varied from the centre of the disc to the edge along the radius. The black line shows the reference boron carbide powder at ambient pressure.

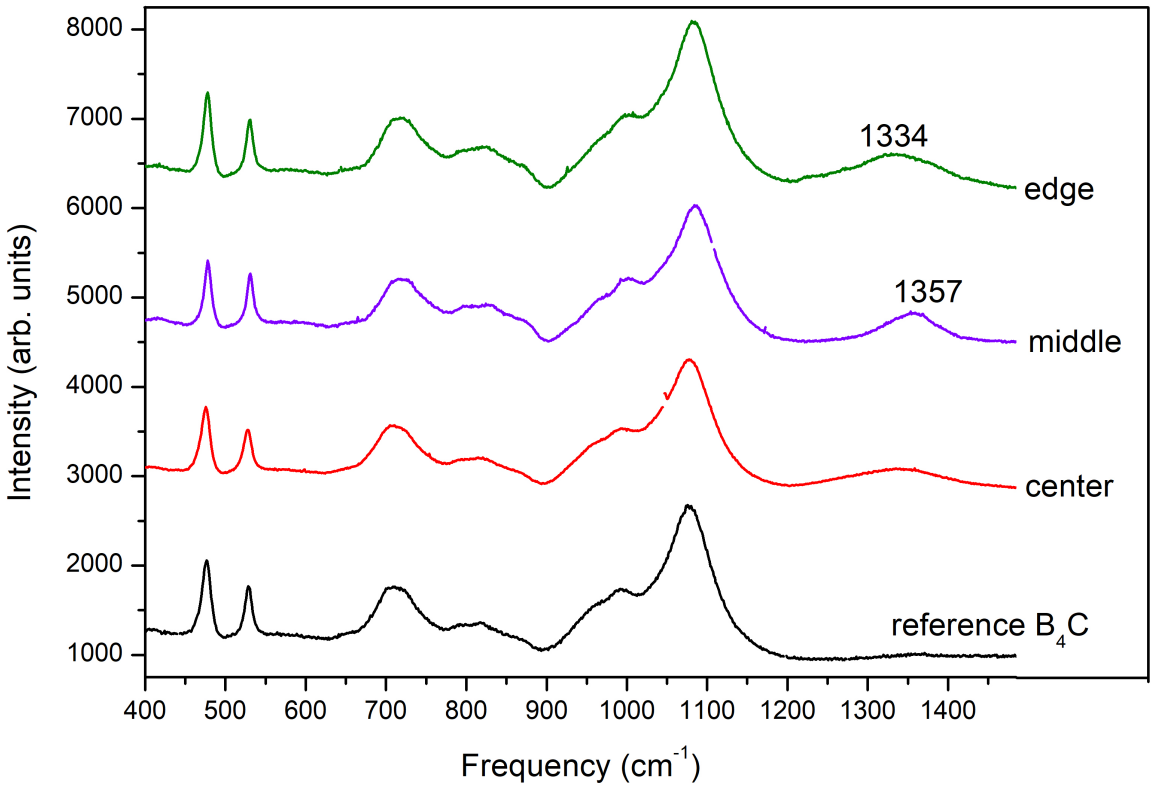

Figure 5.10: Raman spectroscopy of the circular surface of the gasket rotated by 180° in the RoToPEC (experiment RP2) along one direction. The three positions where the spectrum was taken have been varied from the centre of the disc to the edge along the radius. The black line shows the reference boron carbide powder at ambient pressure.

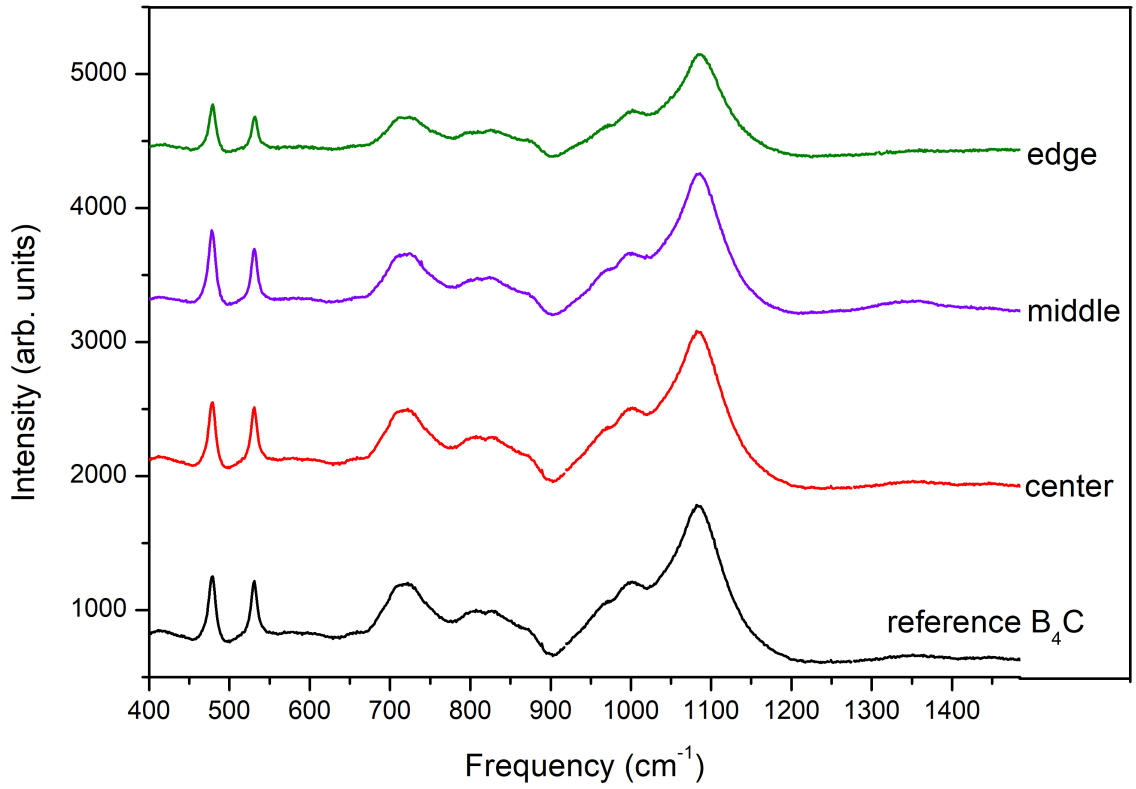

Figure 5.11: Raman spectroscopy of the circular surface of the gasket rotated by 90° in the RoToPEC (experiment RP3) along one direction. The three positions where the spectrum was taken has been varied from the centre of the disc to the edge along the radius. The black line shows the reference boron carbide powder at ambient pressure.

5.4 Discussions

Both the XRD patterns and Raman spectroscopy of the RP3 sample show the formation of new peaks. These peaks can be explained by the formation of vacancies in the crystal structure of boron carbide due to the torsion generated by the RoToPEC. In order to verify this hypothesis, the changes in the spectra have been compared with the spectra of various defective boron carbides calculated with density functional theory (DFT) in the generalized gradient approximation (GGA) during the Ph.D. work of Antoine Jay (see appendix B of Ref. [5]).

5.4.1 Comparison of EDXRD spectra

The comparison for the EDXRD spectrum in figure 5.4 has been summarized in table 5.2. As can be seen, 5 peaks out of the 7 new peaks can be explained by the theory, as coming from the formation of boron vacancies in the C-B-C chains of boron carbide, due to the torsion generated in the RoToPEC.

Moreover, the calculations performed in Ref. [5] have predicted that the most intense peak for ($B_{11}C^p$) C□C would be at 35.47°and 38.30°. The first of these two peaks nicely corresponds to the most intense of the new peaks, that has appeared at 36.29°. The second of these two peaks is more difficult to evidence as, in the calculations, it is close to a peak of B_4C at 37.84°.

However, with regards to the first three peaks at 24.2°, 27.4°and 28.6°, it is worth noting that these peaks appear in all of the spectra taken through EDXRD in the synchrotron,

whatever the torsion angle, even near the centre of the samples where the torsion, and hence, the deformation would be negligible. So they might be attributed to an artifact from the system of EDXRD, and not to a peak arising because of defects formed in the sample itself. If one excludes these peaks, four peaks are new and all of them coincide with those expected by the theory on ($B_{11}C^p$) C□C.

The mean squared error of all the peaks seen in position 3 of RP1 corresponding to ($B_{11}C^p$) C□C in table 5.2 has been calculated as $\frac{1}{8}\sqrt{\sum_i (2\theta^{expt} - 2\theta^{theory})^2}$. It amounts to 0.20°, with respect to the aforementioned calculation of undeformed distorted ($B_{11}C^p$) C□C at ambient pressure. Similarly, the mean squared error of the peaks is 0.14 °for undeformed ($B_{11}C^p$) CBC (theoretical B_4C) at ambient pressure. Thus, both the mean squared errors are on the same order of magnitude, which is remarkable and is a strong argument in favor of the presence of ($B_{11}C^p$) C□C in addition to B_4C, as the presence of B_4C alone is not able to explain all of the new peaks.

The two most intense peaks among the new peaks are the (104) ad (021) plans in the hexagonal representation (see also section 5.4.3), i.e. the (211) and ($1\bar{1}0$) plans in the trigonal representation. Remarkably, the (211) peak is indeed one of the two most intense peak predicted by the theory, the second one being the peak ($1\bar{1}1$) plan at 2θ=38.30°.

Attribution of new peaks *hkl*	New EDXRD peaks 2θ (°)	Peaks common to undeformed B_4C 2θ (°)	($B_{11}C^p$) C□C (theoretical) 2θ (°)	B_4C (theoretical) 2θ (°)	$R\bar{3}m$ trigonal *hkl*	$R\bar{3}m$ hexa *hkl*	Cm *hkl*
			19.96	19.72	1 0 0	1 0 1	0 0 1/1 1 0
		22.04	22.38	21.98	1 1 1	0 0 3	$\bar{2}$ 0 1
		23.47	23.82	23.49	1 1 0	0 1 2	$\bar{1}$ 1 1/2 0 0
artifact ?	24.2		-	-			
artifact ?	27.4		-	-			
artifact ?	28.6		-	-			
		31.91	-	31.97	1 $\bar{1}$ 0	1 1 0	0 2 0/1 1 1
1 $\bar{1}$ 0	33.35		32.34	-	1 $\bar{1}$ 0	1 1 0	0 2 0/1 1 1
		34.94	-	34.89	2 1 1	1 0 4	$\bar{2}$ 0 2/$\bar{3}$ 1 1
2 1 1	36.29		35.47	-	2 1 1	1 0 4	$\bar{2}$ 0 2/$\bar{3}$ 1 1
		37.73	38.30	37.84	1 $\bar{1}$ 1	0 2 1	0 2 1/2 0 1
		39.15	39.68	39.14	2 1 0	1 1 3	$\bar{1}$ 1 2/$\bar{2}$ 2 1/3 1 0
2 0 0	40.75		40.56	40.05	2 0 0	2 0 2	2 2 0/0 0 2
2 2 1	42.51		42.34	41.62	2 2 1	0 1 5	$\bar{4}$ 0 1/$\bar{3}$ 1 2

Table 5.2: Characterization of the new EDXRD peaks that have appeared in RP1 at position 3 (rotation by 270°, largest expected deformation). The first nine theoretical peaks having the lowest 2θ values are reported for ($B_{11}C^p$) C□C and B_4C. 2θ values are given in Cu K-α. Theoretical peaks are given in the average $R\bar{3}m$ (# 166)] structure experimentally observed for (undeformed) B_4C. Corresponding hkl Miller indices are reported in the last column. □ stands for the boron vacancy in the C-B-C chain. Calculations from table B.13 of Ref. [5].

The EDXRD spectrum for RP2 and RP3, however, does not show much change, except for the peaks at 24.2°, 27.4°and 28.6° which might not be because of defects formed in boron carbide, as explained above. This observation once again underscores the effect of the degree of rotation on the defects formed in the sample.

5.4.2 Comparison of Raman spectra

This observation also holds true for the spectra obtained by Raman spectroscopy. The larger the torsion angle, the larger the number of changes in the spectra. The circular surfaces of RP1 has demonstrated a lot of changes, followed by some minor changes in the spectra of RP2 and no changes at all in the spectra of RP3.

The Raman spectra of distorted B_4C are similar to the undeformed one, and in agreement with the theoretical spectra for this compound (table 5.3). The torsion shifts the peak positions by a few cm^{-1}. There are however a number of new peaks which cannot be explained by the presence of B_4C only.

In figure 5.7, which has been performed on RP1, a very prominent peak has appeared at 1339 cm^{-1}. This peak corresponds to amorphous boron carbide (1330 cm^{-1}). As reported by several authors [41,42,112], boron carbide forms amorphous shear bands under dynamic stress, as has been discussed in Sec 1.1.1. However, the peak corresponding to the amorphous boron carbide has a similar intensity as the crystalline boron carbide peaks. In fact, in none of the Raman spectra obtained so far has the amorphous boron carbide peak been more intense than the crystalline boron carbide peaks. Since the laser beam spot of the micro-Raman spectrometer used in these analyses is around 10

micrometers, it would be safe to say that the amorphous zones are very localised with areas much smaller than 10 micrometers. This is in accordance with what has been reported by Chen *et al.* [41] in that the amorphous boron carbide bands, when present, are extremely localised.

Figure 5.8 has been obtained in another direction along the radius of one of the circular faces of RP1. A small peak is observed around 1360 cm^{-1} for the spectra taken at the middle of the sample along the radius. This can be attributed to amorphous carbon or graphite (1350 cm^{-1}) [135]. This is not unusual as commercial boron carbide is known to contain a certain amount of free carbon in the samples. Therefore, this does not signify the formation of defects nor vacancies in the sample. At the edge, several new peaks have appeared. The big hump corresponds again to amorphous boron carbide, but one could observe three other peaks near the hump : 1199, 1257 and 1391 cm^{-1}. The first two peaks might correspond to the 1184 cm^{-1} and 1223 cm^{-1} peaks of ($B_{11}C^p$) C-C and ($B_{11}C^p$) C□C, as calculated in Ref [5] (table 5.4). However, there has not been any corresponding peaks identified for the last peak at 1391 cm^{-1}.

Figure 5.9 has been obtained in yet another direction on RP1. Here, we observe only a small amorphous boron carbide at the edge. However, in the middle, quite a few new peaks have appeared at 767, 788, 798, and 967 cm^{-1}. Some of them could be matched to different predicted peaks of ($B_{11}C^p$) C□C as well as other polymorphs, as shown in table 5.4. In fact, it is observed from tables 5.3 and 5.4 that the entire spectra observed at this middle position could be either explained by peaks of the reference B_4C or by

the peaks of ($B_{11}C^p$) C□C, which points to the formation of small zones (less than 10 micrometers) of ($B_{11}C^p$) C□C.

However, the peaks corresponding to ($B_{11}C^p$) C□C that have been noted in figure 5.8 have not appeared in this spectra. Moreover, the peak at 967 cm^{-1} is much sharper than the hump observed in the reference B_4C around the same frequency. Since this peak does not correspond to any of the ($B_{11}C^p$) C□C peaks as well, it might be the case that some other polymorph, namely ($B_{11}C^p$) C-C or (B_{12}) C-C, might also be present. Table 5.4 shows this possibility of the formation of C-C chains in the sample. This is possible if the C□C intericosahedral arrangements that had been previously formed under torsion collapsed under the applied pressure of 5 GPa to form the C-C chains. This would be in accordance with what has been predicted by Raucoules *et al.* [46], and explained in detail in Sec 1.1.1 of the current work.

New peaks(expt.)	Distorted B_4C(expt.)	Reference B_4C(expt.)	B_4C(theory)	Name	Symmetry(theory)
	479	476	**488**	Ico7, pcr	E_g
	531	529	**536**	Ico5, lib	E_g
			699	Ico17	A_{1g}
	717	711	**719**	Ico9	A_{1g}
767		-	**768**	Ico11	E_g
788		-			
798		-			
			808	Ico20	E_g
	823	820	840	Ico13	E_g
	871	866	-		
967*	967	964	-		
	998	990	994	Ico21	A_{1g}
			1052	Ico23, asis	E_g
			1069	Ico24, sis	A_{1g}
	1082	1079	**1095**	Ch5, cs	A_{1g}
			1139	Ch3, cr	E_g

Table 5.3: Experimentally determined new peaks after B_4C torsion, distorted B_4C and reference B_4C, and theoretical peaks of undeformed B4C (in cm^{-1}). New peaks have appeared in RP1 in figure 5.9 (rotated by 270°). All of the peaks of reference B_4C are present in the deformed sample. The '' signifies a much sharper peak at the frequency than the one observed for reference B_4C. Theoretical mode frequency, name and symmetry from table 4.2 of Ref. [5] have been extracted in tables 1.2 and 1.3 of Chapter 1. pcr, lib, asis, sis, cs and cr stand respectively for the pseudo-chain rotation, libration of the icosahedra, anti-symmetric and symmetric intericosahedral stretching, symmetric chain stretching and chain rotation modes. Theoretical frequencies in bold font are expected to be the most intense ones (see table 2.11 and fig. 2.15 of Ref. [5]).*

New peaks(expt.)	Distorted B_4C(expt.)	$(B_{11}C^p)$C□C(theory)	$(B_{11}C^p)$C-C(theory)	(B_{12})C-C(theory)	Name	Symmetry
		398	**570**	573	Ch5, cs	A_{1g}
	479	481	**491**	389	Ico5, lib	E_g
	531	529	**621**	583	Ico7, pcr	E_g
	717	713	**692**	673	Ico17	A_{1g}
			692	646	Ico13	E_g
				709	Ico11	E_g
				729	Ico9	A_{1g}
767		754	**770**		Ico11	E_g
788		795	**805**		Ico9	A_{1g}
798		801			Ico20	E_g
	823	819			Ico13	E_g
	871		876	862	Ico20	E_g
			885		Ico23	E_g
				957	Ico23	E_g
967*	967		**984**		Ico21	A_{1g}
	998			998	Ico21	A_{1g}
			1059	1056	Ch3, cr	E_g
		1057			Ico21	A_{1g}
	1082	1096			Ico23, asis	E_g
				1078	Ico24, sis	A_{1g}
		1133	**1120**		Ico24, sis	A_{1g}
			1184		Ico23, asis	E_g
		1223			Ch3, cr	E_g

Table 5.4: Same experimental data as in table 5.3, and theoretical peaks (in cm^{-1}) of undeformed $(B_{11}C^p)$ C□C, $(B_{11}C^p)$ C-C and (B_{12}) C-C corresponding to the new peaks. □ stands for the boron vacancy in the C-B-C chain. Theoretical frequencies from table 4.2 of Ref. [5] have been extracted in tables 1.2 and 1.3 of Chapter 1 of the current work. Theoretical frequencies in bold font are expected to be the most intense ones for $(B_{11}C^p)$ C-C (see fig. 4.1 of Ref. [5]).

In the spectra shown for RP2 in figure 5.10, one can notice the presence of only a feeble peak corresponding to amorphous boron carbide at the edge of the sample. There has been no new peaks corresponding to another polymorph of boron carbide. The spectra obtained for RP3 in figure 5.11 have shown no changes with respect to undeformed boron carbide.

5.4.3 Tentative determination of the stress gradient

However, in figure 5.9, the new peaks have appeared on the middle of the radial distance and not, as was expected, at the edge. This leads to the hypothesis that the defects formed were not a direct function of radial distance, contrarily to what was expected. In order to verify this, the two most prominent peaks of the boron carbide EDXRD spectra, peaks corresponding to (021) and (104) plans in the hexagonal representation of the trigonal structure, have been followed exhaustively to note the change in peak position and the FWHM (Full width at half maximum) with respect to the reference B_4C powder at ambient pressure. As the relative peak position and FWHM is proportional to the deformation produced, it would allow one to determine if the defects are produced as a direct function of radial distance. Figures are shown here as examples to prove that this is not the case - the relative peak positions and FWHM have no simple direct relationship with the radius. It is possible that the defects have been generated as a function of radial distance and then, there were relaxation of the defects over time, which led to the complicated strain gradient that we see now. It would be useful to follow the evolution of the defects generated over time through *in situ* RoToPEC experiments

in the SOLEIL synchrotron, to see if that is indeed the case. It is however difficult to verify that in post mortem characterisations like has been done here.

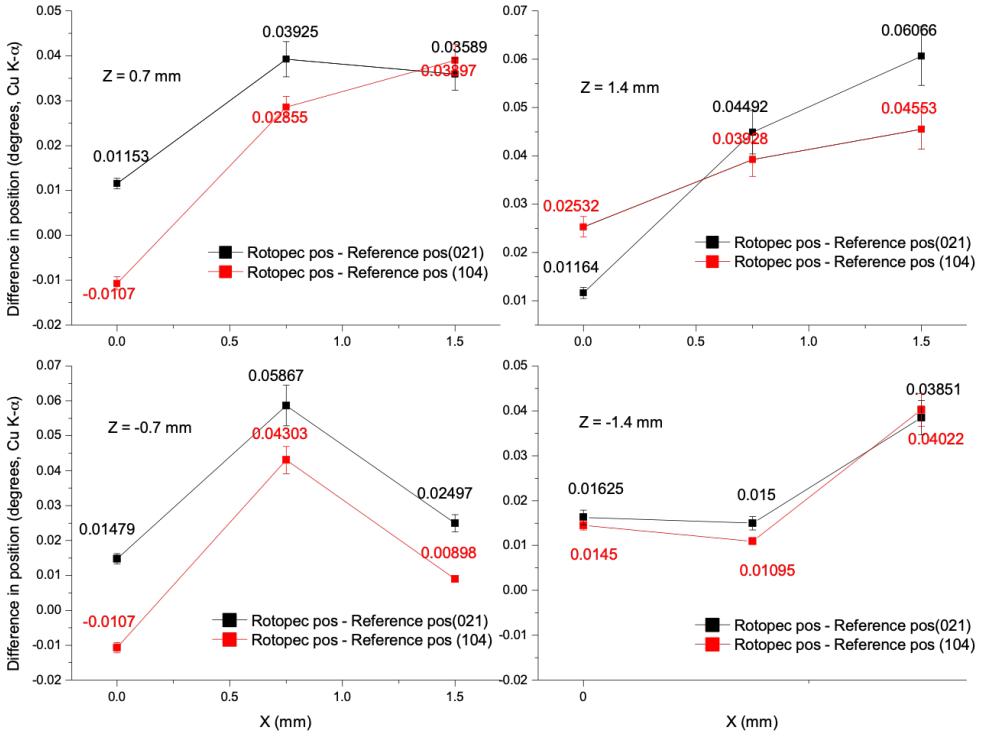

Figure 5.12: Analysis of the shift in XRD peak positions of the (021) and (104) plans in the hexagonal representation of the trigonal structure of the deformed boron carbide sample RP1 (rotated by 270°) with respect to the reference boron carbide powder at ambient pressure. z represents the height of the particle position from the centre of the rectangular cross-section, as shown in figure 5.2.

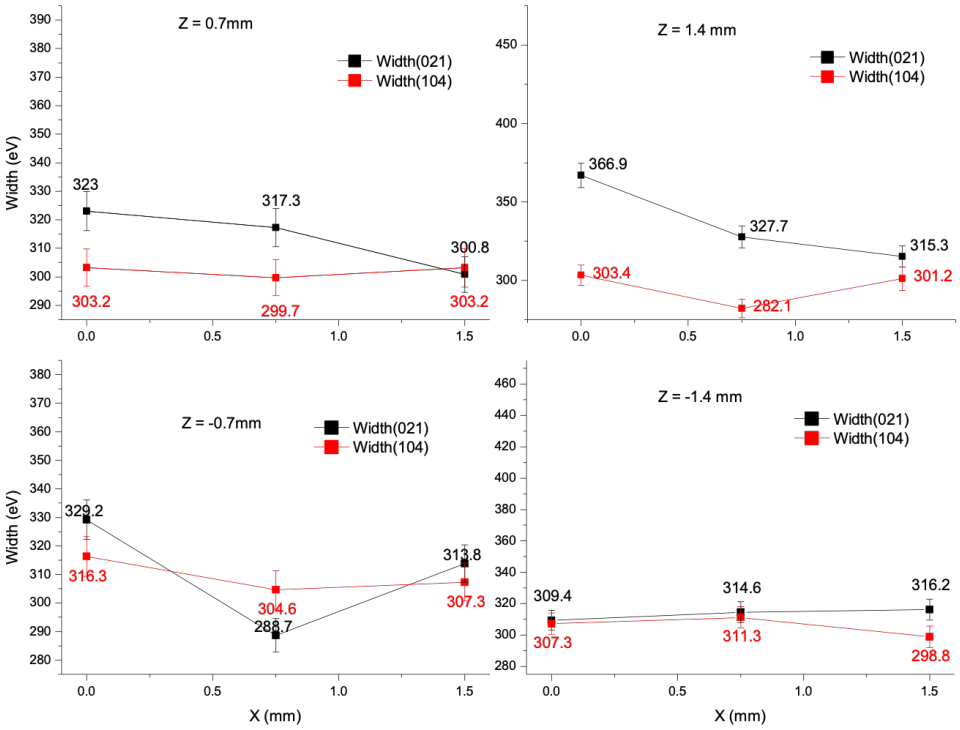

Figure 5.13: Analysis of the shift in the FWHM of the XRD peaks of the (021) and (104) plans in the hexagonal representation of the trigonal structure of the deformed boron carbide sample RP1 (rotated by 270°) with respect to the reference boron carbide powder at ambient pressure. z represents the height of the particle position from the centre of the rectangular cross-section, as shown in figure 5.2.

5.5 Conclusions

It is possible to come to several important conclusions from this chapter. Both EDXRD and Raman spectroscopy have provided evidence that chain vacancies and C-C chains are produced in boron carbide under the non-hydrostatic torsional stress generated in a RoToPEC, as predicted by Raucoules *et al.* [46].

However, both the deformation generated and the defect concentrations need to be quantified. Indeed, it is evident from the results that the defects formed depends greatly on the degree of rotation of the gasket, and a quantification of the deformation would be valuable. This can be done by repeating the same experiments with a wire inserted at different locations of the sample and noting the deformation of the wire using radiography. A quantification of the defects would be an interesting outcome. Obtaining an absolute value of the quantity of defects is a difficult task, and a realistic aim could be to study the defect concentration change as a function of the deformation, with respect to a carefully chosen reference state.

The question of the determination of the complicated stress gradient with respect to the radial distance is a possible topic for further investigations in a synchrotron.

My experiment have been performed at room temperature. That would not result in achieving the HEL in boron carbides, and therefore would not cause any mechanical failure in my samples. However, this will bring boron carbide into the plastic regime, and produce defects and vacancies similar to those produced in boron carbides as it

approaches the HEL, thus giving an opportunity to study these defects in a controlled and systematic manner. Higher temperatures can be used in later experiments to approach the HEL more closely and, eventually, investigate the probable effect of defect annealing.

Other characterisations of the samples such as Nuclear Magnetic Resonance (NMR) can also prove useful in order to identify the defects formed specially in the boron carbide chains of the sample. However, NMR requires a larger sample volume, and thus, multiple RoToPEC experiments with the same experimental parameters need to be done to generate enough sample volume for NMR.

In conclusion, this chapter marks the fruition of the first objective of the current work, as explained in Sec 1.2, which was to study the formation of vacancies under non-hydrostatic conditions. It also raises the question of the possible formation of C-C chains, which requires complementary experiments.

Chapter 6

Introduction of silicon atoms into boron carbide under pressure

6.1 Introduction

The new idea that was explored in the current chapter is to strengthen the triatomic C-B-C chains between the icosahedra of boron carbide (B_4C) by using pressure to insert silicon atoms into the chains.

Until now, silicon has only been introduced at ambient pressure as a doping element. Silicon appeared as a byproduct of the main chemical reaction of B4C growth from molten copper [56], or, more recently, was injected [57, 136]. The limit of solubility of silicon in boron carbide depends on the temperature. It is 2.5 at.% at 2323 K [58, 59]. It has been shown in literature that silicon modifies the deformation behavior

of the material [136], with ambivalent results: the introduction of silicon lessens the amorphisation of the material, but promotes direct fracture. As a result, many micro-fractures appear instead of the shear bands containing amorphous boron carbide (or carbon).

The approach followed in this chapter is very different. In the previous chapter (Chapter 5), it was established that the proportion of amorphised zone formed by deformation using torsion is very small. The results in Chapter 5 showed the appearance of defects which was attributed to gaps in the boron carbide chain. The use of high pressure in this chapter is intended to facilitate the introduction of silicon atoms, and to form a B-C-Si ternary phase, unlike what has been previously reported in literature.

My objective is based on the fact that an isomorphic icosahedral phase with Si-Si chains has been calculated in the boron-silicon binary system [137] and, remarkably, the phase is quasi iso-structural compared to $B_{2.5}C$ theoretically. predicted by calculations [6]. As a result, it seemed interesting to me to study the possibility of the appearance of a ternary phase having the same structure as $B_{2.5}C$ and $B_{2.5}Si$.

The main objective of this chapter is therefore to study the result of syntheses using high pressure [102], with the experiments being guided by calculations based on the density functional theory.

6.2 Calculations: DFT-LDA and DFT-GGA

DFT-LDA and DFT-GGA calculations were performed using the QUANTUM ESPRESSO suite [92,93] to find out the relative thermodynamic stability of the different polymorphs produced when one (or two) atom(s) of silicon substitutes one atom of the unit cell of B_4C. Here, the 15-atom unit cell of B_4C, with 20 at.% C concentration, at the theoretical equilibrium volume and geometry, has been used. The silicon atom(s) were in substitution in one (or two) of the 15 positions in place of one (or two) boron atom(s) or of one (or two) carbon atom(s) in the atomic positions of the B_4C unit cell given in table 6.1. The pairs of positions (1,2), (4,5), (6,7) and (9,11) have been found to be equivalent positions for silicon insertion throughout all the calculations, and hence they have been issued the same labels.

The total energy E_{total} and the formation energy E_{form} have been computed with the expression

$$E_{form} = E_f = E_{total} - \frac{n_B}{12} E_{total}^{\alpha - B_{12}} - \frac{n_C}{2} E_{total}^{diamond} - \frac{n_{Si}}{2} E_{total}^{silicon} , \qquad (6.1)$$

where the formation energy has been computed from, for instance, α boron and diamond and face-centered cubic (f.c.c.) silicon. Diamond is more safely represented in DFT-GGA than graphite, as the latter requires the inclusion of van der Waals interactions, which is beyond the scope of the present study.

The equations used for the calculation of formation enthalpy of the different stoichiometry of the B-C-Si compounds from different starting reactants, as well as detailed com-

mentaries on the results obtained have been documented in Appendix B.

The different stoichiometry of the B-C-Si ternary phase whose formation enthalpy was calculated has been marked in a ternary phase diagram in figure 6.1, in conjunction with other existing or proposed materials such as B_4C, SiC, SiB_6, $B_{2.5}Si$ and $B_{2.5}C$.

The total energy (E) has been obtained using the DFT in the pseudopotential and plane wave method for the 15-atom B_4C, 2-atom C, 12-atom B, 2-atom Si and 2-atom SiC (cubic and wurtzite). The size of the plane wave basis has been limited with a cut-off energy of 80 Ry. A Monkhorst-Pack grid of 12^3 k-points has been used to sample the Brillouin zone (BZ) [138]. The numerical precision on the total energy is around 0.003 eV/at. Both the local density approximation (LDA) and the generalized gradient approximation (GGA) in the PW91 form [139] have been used. Pseudopotentials for boron, carbon and silicon atoms were those of Ref. [61, 140] for the DFT-LDA calculations. Pseudopotential files named respectively B.gga.pw91.UPF, C.gga.pw91.UPF, as in Ref. [6], and the file Si.rel-pbe-rrkj.UPF of the QUANTUM ESPRESSO web site, were used in the GGA-calculations. The PW91 exchange in correlation GGA functional has been used in the calculations of the compounds.

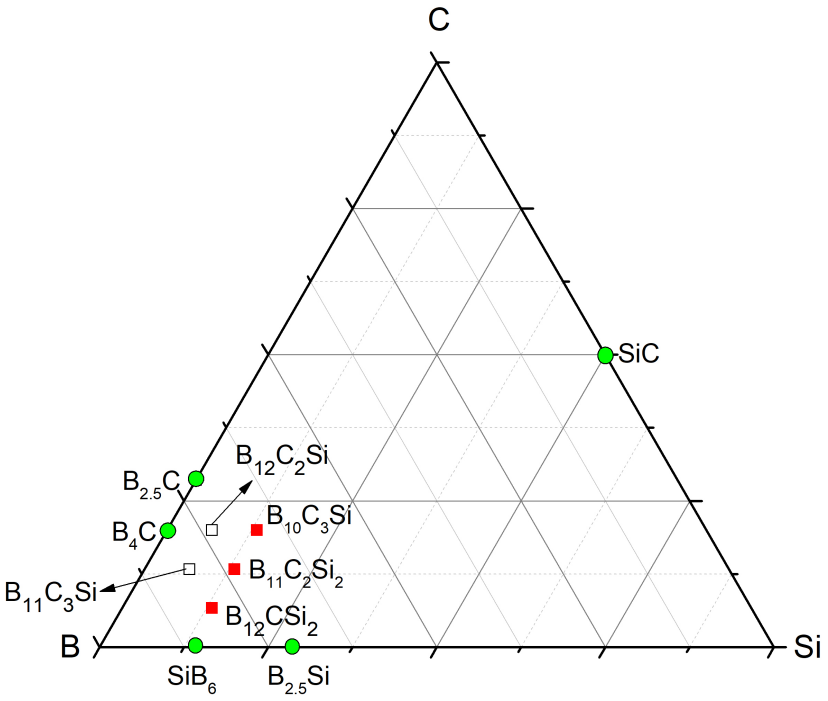

Figure 6.1: Triangle plots showing the stoichiometries of the proposed B-C-Si compounds (in red and white squares) whose formation enthalpy was calculated in the current work. Green circles represent the compounds that already exist in the B-C-Si phase diagram (B_4C, SiC, SiB_6 or those that have been proposed in the literature ($B_{2.5}C$ and $B_{2.5}Si$. White square signifies the stoichiometries with 1 Si atom replacement in the ($B_{11}C^p$)C-B-C unit cell, while red squares signify the stoichiometries with 2 Si atom replacement.

Position number	atom type	Label	a_1	a_2	a_3
1	BP	P2	-0.005916273	-0.008117238	-0.330336445
2	BP	P2	-0.330336445	-0.008117238	-0.005916273
3	BP	P3	-0.007877438	-0.340330667	-0.007877438
4	BP	P4	0.002744436	0.012257776	0.324855897
5	BP	P4	0.324855897	0.012257776	0.002744436
6	BE		0.196126434	0.197607745	-0.317031650
7	BE		-0.317031650	0.197607745	0.196126434
8	BE		0.189985738	-0.314278034	0.189985738
9	BE	E	-0.196219576	-0.197414293	0.311657770
10	BE		-0.192991176	0.315931766	-0.192991176
11	BE	E	0.311657770	-0.197414293	-0.196219576
12	CC	Si-B-C	0.379284345	0.392705819	0.379284345
13	CC	C-B-Si	-0.375146570	-0.384124014	-0.375146570
14	BC	C-Si-C	0.500523718	0.508546692	0.500523718
15	CP	P1	0.003827740	0.322058270	0.003827740

Table 6.1: The (arbitrary) atomic position number, the type of atom, the labels used in the current chapter to indicate the atomic positions and the crystal coordinates of the atomic positions in the base-centered monoclinic B_4C unit cell at equilibrium, as function of the ($\mathbf{a_1}$, $\mathbf{a_2}$, $\mathbf{a_3}$) vectors of the Bravais lattice. BP (BE) stands for boron in the polar (equatorial) position in the icosahedron respectively, BC (CC) stands for the boron (carbon) atom in the chain respectively, and CP stands for the carbon atom in the polar position of the icosahedron.

6.2.1 Insertion of 1 silicon atom in the boron carbide 15-atom unit cell

The calculations have been done for all of the 15 different models of the atomic structure. Initially LDA calculations were used for brute force substitution, and then the cell parameters ("vc-relax" type of calculations) were relaxed. The LDA calculations were at 0 K and at pressure values of 0 GPa, 25 GPa, 50 GPa and 100 GPa. To compute the formation energy of the models, various starting reactant combinations have been accounted for, such as *i)* α boron, diamond and silicon, *ii)* boron carbide, silicon, α boron or boron carbide, silicon, carbon (depending on the stoichiometry of the final product) *iii)* α boron, diamond, cubic silicon carbide and *iv)* α boron, diamond, hexagonal silicon carbide. Later, DFT-GGA calculations were used to recompute the formation enthalpies for the reactant mixtures of *i)* α boron, diamond and silicon and *ii)* α boron, diamond, cubic silicon carbide at 0 K and pressure values of 0 GPa, 25 GPa, 50 GPa and 100 GPa.

The proposed ternary polymorph could only be thermodynamically stable (feasible) at 0 K if its formation enthalpy is negative. After having replaced one silicon atom in all the 15 positions shown in table 6.1, it has been found that the formation enthalpy is negative at some pressure value up to 100 GPa when one silicon atom is substituted in the positions P1, C-Si-C and Si-B-C.

Figures 6.2, 6.3 and 6.4 show the evolution of the formation enthalpies for silicon substitution in P1, C-Si-C and Si-B-C respectively.

To compare the formation enthalpy, it is mandatory to account for the fact that stoichiometries in boron, carbon and silicon differ among the various compounds, and chemical potentials have to be introduced in the formalism to account for this. The scheme of Ref. [46] has been extended to account for ternary compounds.

The enthalpy of formation of a ternary compound depends on the conditions of pressure and stoichiometry: [141]

$$\Delta\Omega_f = E_{form} + \sum_{i=B,C,Si} n_i \mu_i, \tag{6.2}$$

where E_{form} is the formation enthalpy of the compound with respect to α boron, diamond and f.c.c. silicon of equation 6.1. The last term of the right-hand side of equation 6.2 with $i = B$ (resp. $i = C, Si$) represents the exchange of atoms with one reservoir of boron (resp. carbon, silicon) atoms. Our reservoirs are two reservoirs of B_4C and SiC, which are the two compounds having the lowest formation energy.

The number of exchanged atoms n_i is positive when the atom is transferred from the supercell to the reservoir, and μ_i is the excess chemical potential at which the exchange is performed.[1]

E_{form} has in fact been computed in equation 6.1 as :

$$E_{form} = E_{total} + \sum_{i=B,C,Si} n_i \mu_i^0 \tag{6.3}$$

where eventually the total energy is replaced by the enthalpy, $H{=}E{+}PV$, and involves calculating total energy E and volume V at a fixed pressure P. The chemical potentials of

[1]The excess μ_i and absolute μ_i^* chemical potentials are related by $\mu_i = \mu_i^* - \mu_i^0$. In each reservoir $\mu_i^* = \mu_i^0$.

the three reference states μ_B^0, μ_C^0 and μ_{Si}^0 have been taken to be the enthalpy H *per* atom of solid boron (α-boron), solid carbon (diamond) and solid silicon (f.c.c. silicon).[2]

Pristine B_4C^p and SiC are formed from solid boron + carbon and solid carbon + silicon with the formation enthalpy ΔH_f. This fixes the relationship between the μ_B and μ_C, and between μ_C and μ_{Si}. In our simplified scheme, only one chemical potential is left as an independent variable,

$$3\mu_C + 12\mu_B = \Delta H_f(B_4C^p), \mu_C + \mu_S i = \Delta H_f(SiC) \tag{6.4}$$

where $\Delta H_f(B_4C^p) = H(B_4C^p) - 3\mu_C^0 - 12\mu_B^0$ and $\Delta H_f(SiC) = H(SiC) - \mu_C^0 - \mu_{Si}^0$. The values of μ_B, μ_C, and μ_{Si} must be negative, pressure-dependent, and lie between the silicon rich (($\mu_S i = 0$) and carbon-rich limit ($\mu_C = 0$) given by the formation energy of SiC. The formation energy of B_4C then constrains the domain of the chemical potential of boron, as reported in the upper axis of figure 6.5.

As one can see, the atomic configuration with the lowest formation energy is the substitution at the polar site of the carbon atom. The formation energy is negative for any value of the chemical potential of silicon fixed by the silicon-rich side (μ_{Si}=0) and the silicon chemical potential fixed by the formation of silicon carbide (μ_{Si}=-0.57 eV). It is of the same order of magnitude as the formation energy of B4C (-1.8 eV/unit cell [61]) although higher in energy. In the same interval, μ_C goes from 0 to -0.57 eV, and the boron chemical potential runs from -0.15 eV to -8.505 $\times$ 10^{-3} eV (upper scale of the

[2]The excess μ_i and absolute μ_i^* chemical potentials are related by $\mu_i = \mu_i^* - \mu_i^0$. In each reservoir $\mu_i^* = \mu_i^0$.

figure).

Second in energy, the configurations with the silicon atom at the chain centre, or substituted at other polar site (i.e., in presence of a C^{P1} atom in the icosahedron) turn out to have very close values of the formation energy. For clarity, only one value has been reported with an error back which accounts for the scattering induced by the other configurations. The formation energy is however positive.

Configurations with equatorial or chain-end substitution are higher in energy.

In conclusion, the account of the variation of stoichiometry enables me to formally compare the formations energy of the various compound with 1 substitutional silicon atom and various B and C stoichiometries. The comparison is reported for the ambient pressure and for the value of 26.7 GPa in respectively figures 6.5 and 6.6. The overall picture with respect to the previous figure is unchanged: the polar carbon atom replacement by one Si substitution is thermodynamically stable at ambient pressure and at 26.7 GPa.

6.2.2 Insertion of 2 silicon atoms in the boron carbide 15-atom unit cell

In the next step, two atoms of silicon were also inserted into the B_4C unit cell. Since that would lead to a large number of possible combinations, one silicon atom was fixed in the P1 position, while the second silicon atom was substituted in the other 14 positions of the unit cell. One set of calculation was also performed at 100 GPa where the first

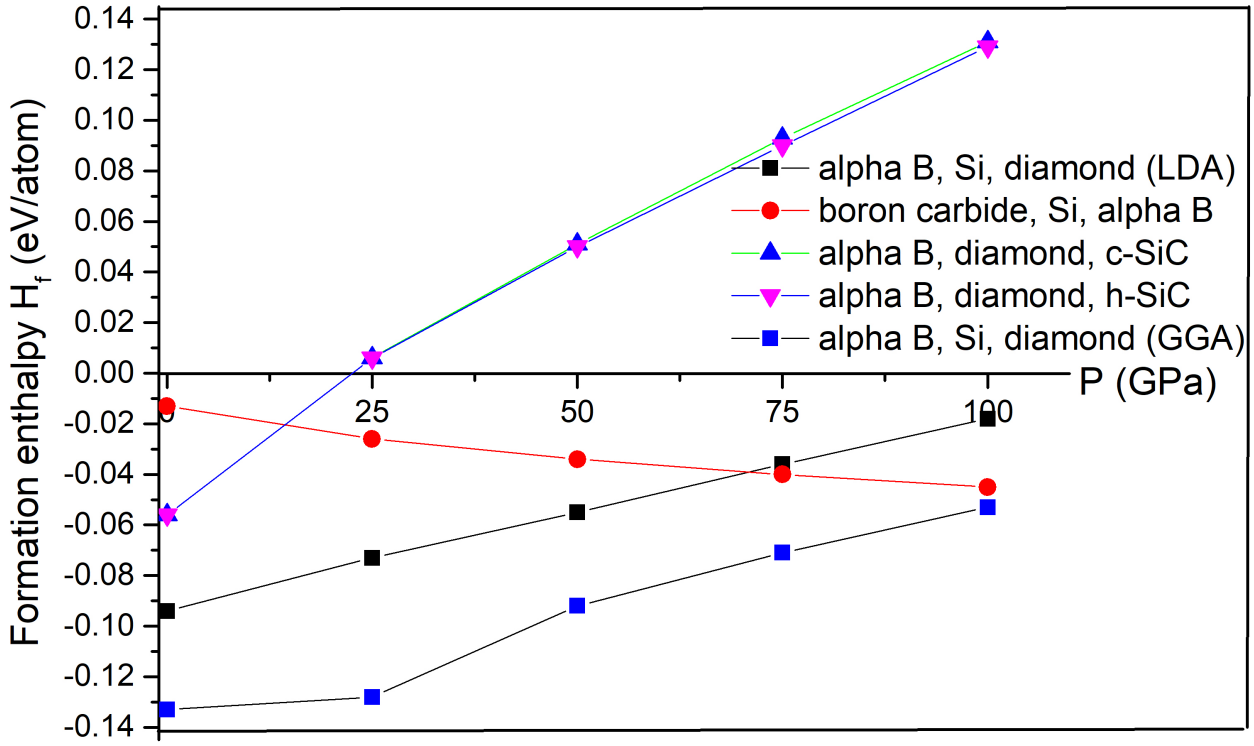

Figure 6.2: Calculations in DFT-LDA and DFT-GGA. Formation enthalpy in eV/atom of $(B_{11}Si^{P1})$C-B-C as a function of pressure in GPa. The calculations have been done in DFT-LDA for various reactant mixtures. For the reactant mixture of α boron, diamond and silicon, the calculations have been repeated using DFT-GGA.

silicon atom was fixed at the position C-Si-C, and the second silicon atom was placed at the remaining 14 positions.

In the case of two silicon atoms in the unit cell, we find that pressure aids significantly

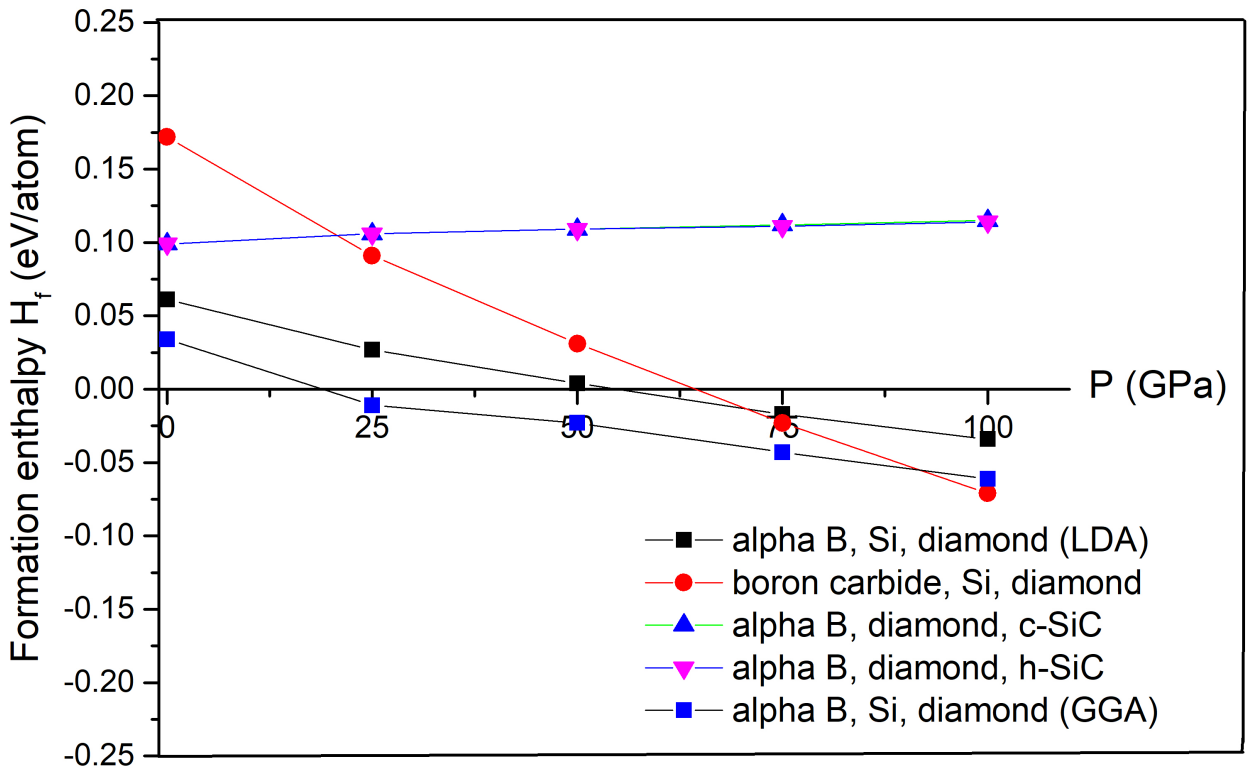

Figure 6.3: Calculations in DFT-LDA and DFT-GGA. Formation enthalpy in eV/atom of $(B_{11}C^{P1})$C-Si-C as a function of pressure in GPa. The calculations have been done in DFT-LDA for various reactant mixtures in DFT-LDA. For the reactant mixture of α boron, diamond and silicon, the calculations have been repeated using DFT-GGA.

in lowering the formation enthalpy: at 0 GPa, none of the polymorphs were thermodynamically feasible but at 100 GPa, 9 of the 14 possible silicon positions became feasible (See Appendix B for values of the formation enthalpy).

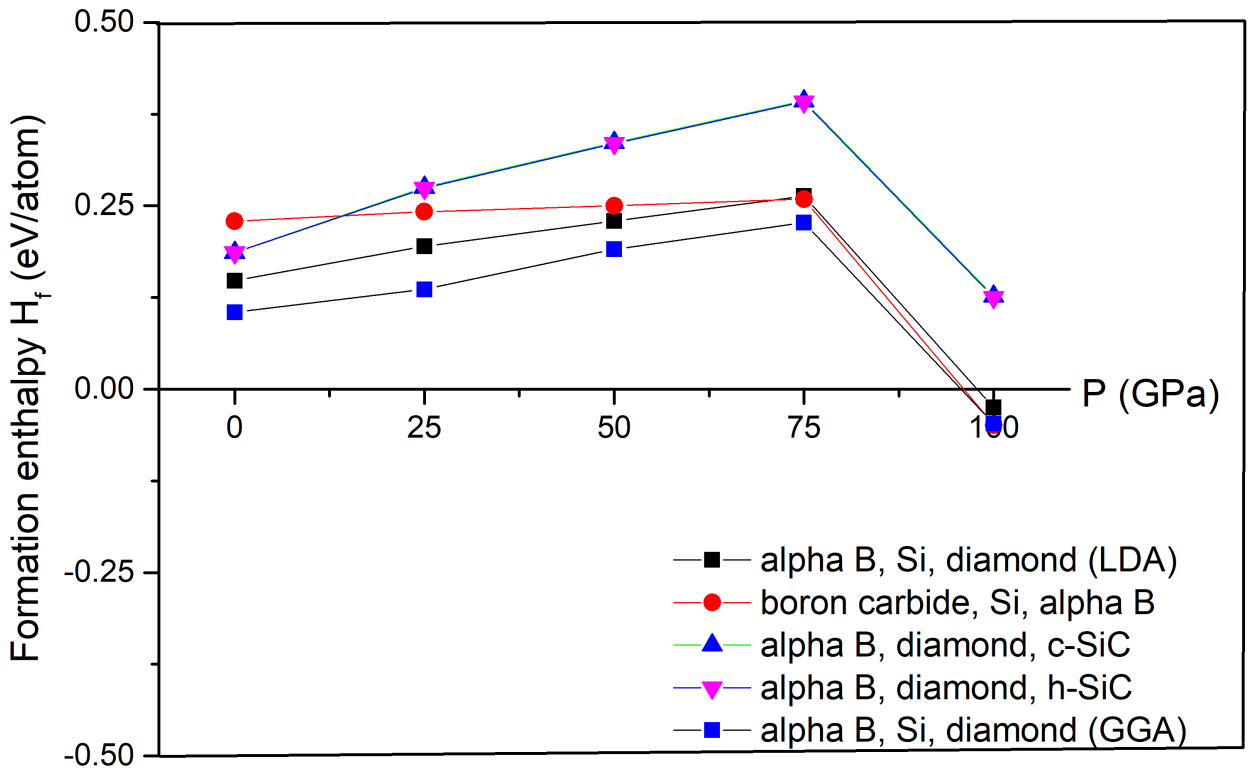

Figure 6.4: Calculations in DFT-LDA and DFT-GGA. Formation enthalpy in eV/atom of $(B_{11}C^{P1})$*Si-B-C as a function of pressure in GPa. The calculations have been done in DFT-LDA for various reactant mixtures. For the reactant mixture of* α *boron, diamond and silicon, the calculations have been repeated using DFT-GGA.*

In the current section, all of the positions that have attained negative formation enthalpy at some pressure value have been plotted as a function of pressure. Figures 6.7, 6.8, 6.9, 6.10, 6.11 and 6.12 show the formation enthalpy as a function of pressure for the

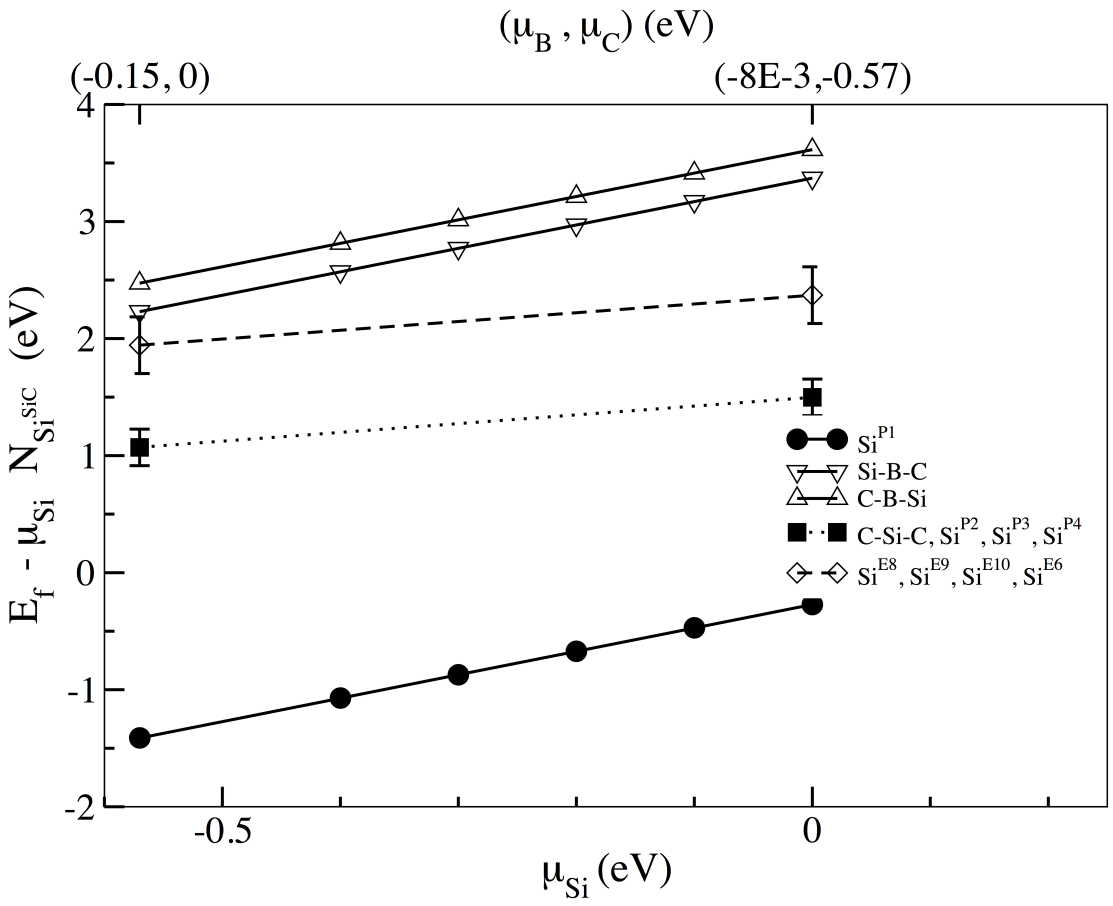

Figure 6.5: Formation enthalpy in eV/unit cell at ambient pressure. Comparison of the compounds with 1 silicon substitution, as a function of the chemical potential of silicon. The error bars are given by the various configuration of a substitution. Calculations in DFT-LDA. One configuration is consistently found to have negative formation energy, i.e., to be thermodynamically stable.

polymorphs ($B_{11}Si^{P1}$)C-Si-C, ($B_{11}Si^{P1}$)C-B-Si, ($B_{10}Si^{P2}Si^{P1}$)C-B-C, ($B_{10}Si^{P3}Si^{P1}$)C-B-C, ($B_{10}Si^{P4}Si^{P1}$)C-B-C and ($B_{10}Si^{P9}Si^{P1}$)C-B-C respectively.

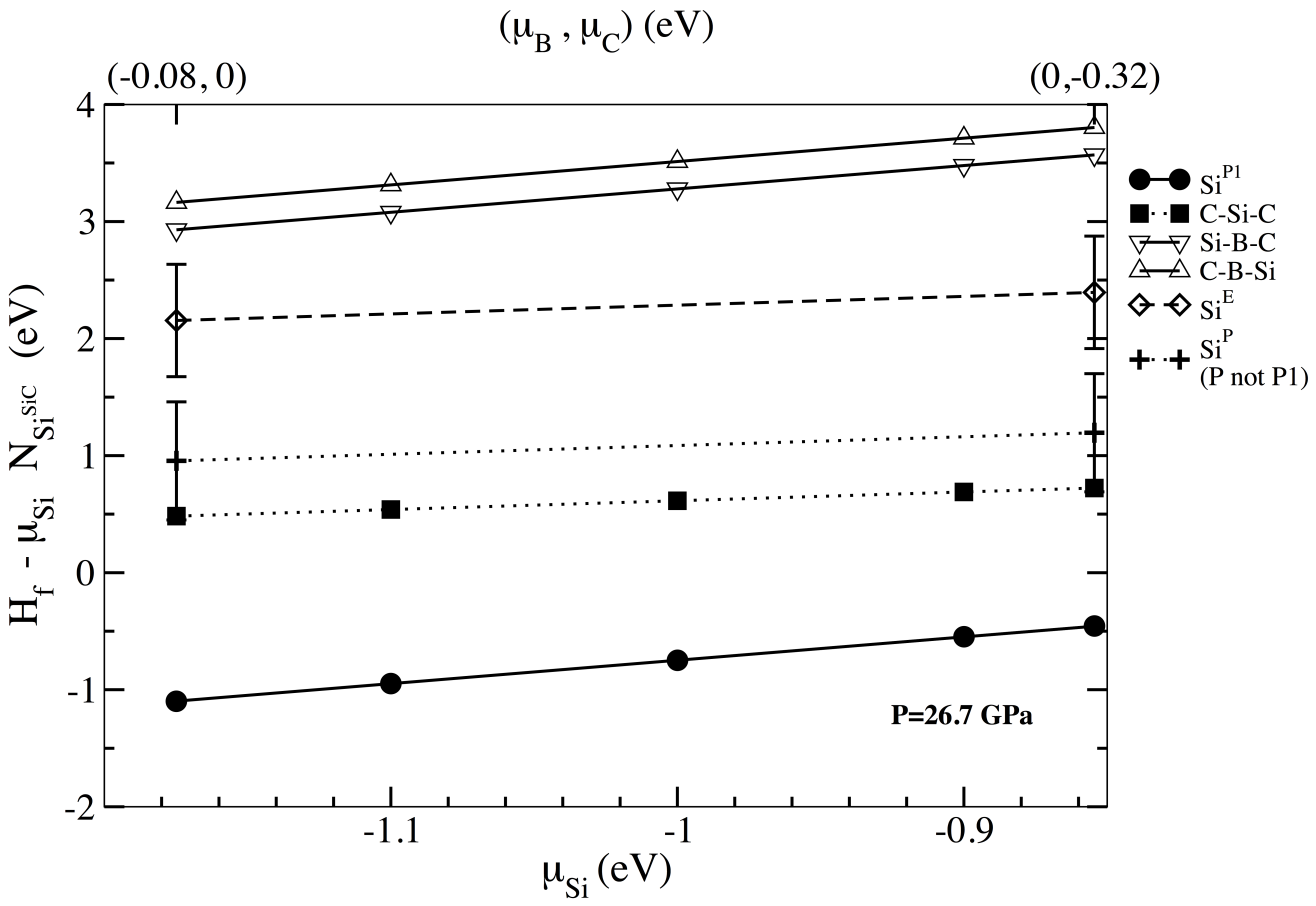

Figure 6.6: Formation enthalpy in eV/unit cell at P=26.7 GPa. Same as in 6.5, excepted that the C-S-C and Si^P, $P \neq P1$, have been made distinct. Calculations in DFT-LDA.

All of the compounds with 1 Si and 2 Si atoms substitutions have been compared at ambient pressure in figure 6.13, as a function of the silicon chemical potential. As one can see, the 1-atom Si^{P1} substitution has the lowest energy. Within the accuracy of our calculations, the $Si^{P1}Si^{P4}$ is also close to becoming thermodynamically stable for small values of the Si-chemical potential.

Upon application of a pressure of 26.7 GPa, many of the 2-Si atom substitutions become thermodynamically stable (figure 6.14). In particular, the 1-atom Si^{P1} substitution is in competition with 2-atom substitutions where the second atom lies at the chain center, or in a polar site of the same pole as $P1$ ($P4$ position).

When this is compared to the addition of carbon in B_4C, it is found that the substitution of two atoms in the structure depends heavily on the type of the atoms, *i.e.*, carbon or silicon atoms.

The formation of the C-C-C chain is not favourable in boron carbide (see table 3.1 of Ref. [5]), and it becomes dynamically unstable under pressure, with negative eigenvalues of the dynamical matrix. However, the placement of two carbon atoms inside the icosahedron in the so-called "diff" position, *i.e.* on two different poles and not in antipodal positions [6], is favourable and is compatible with the formation of C-C chains, leading to $B_{2.5}C$. It forms at significantly high pressure [6].

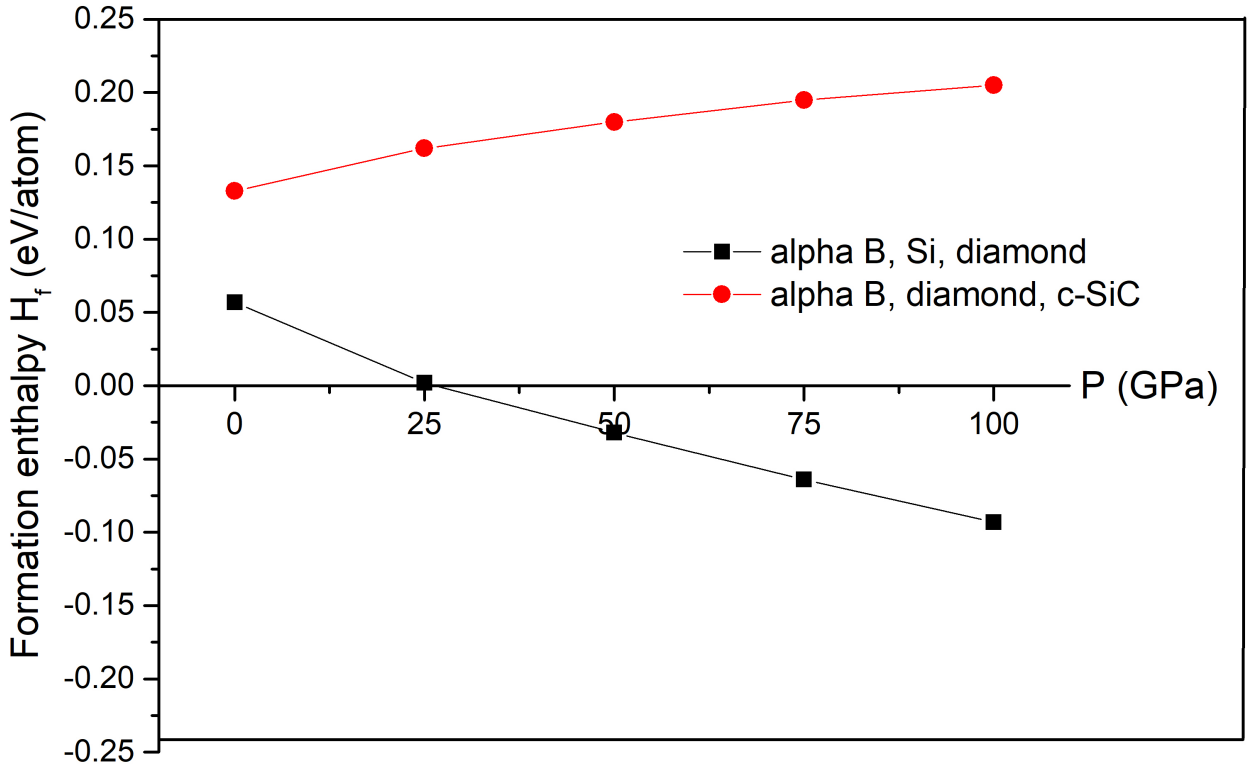

Figure 6.7: Calculations in DFT-LDA. Formation enthalpy in eV/atom of $(B_{11}Si^{P1})$*C-Si-C as a function of pressure in GPa. The calculations have been done in DFT-LDA for various reactant mixtures in DFT-LDA.*

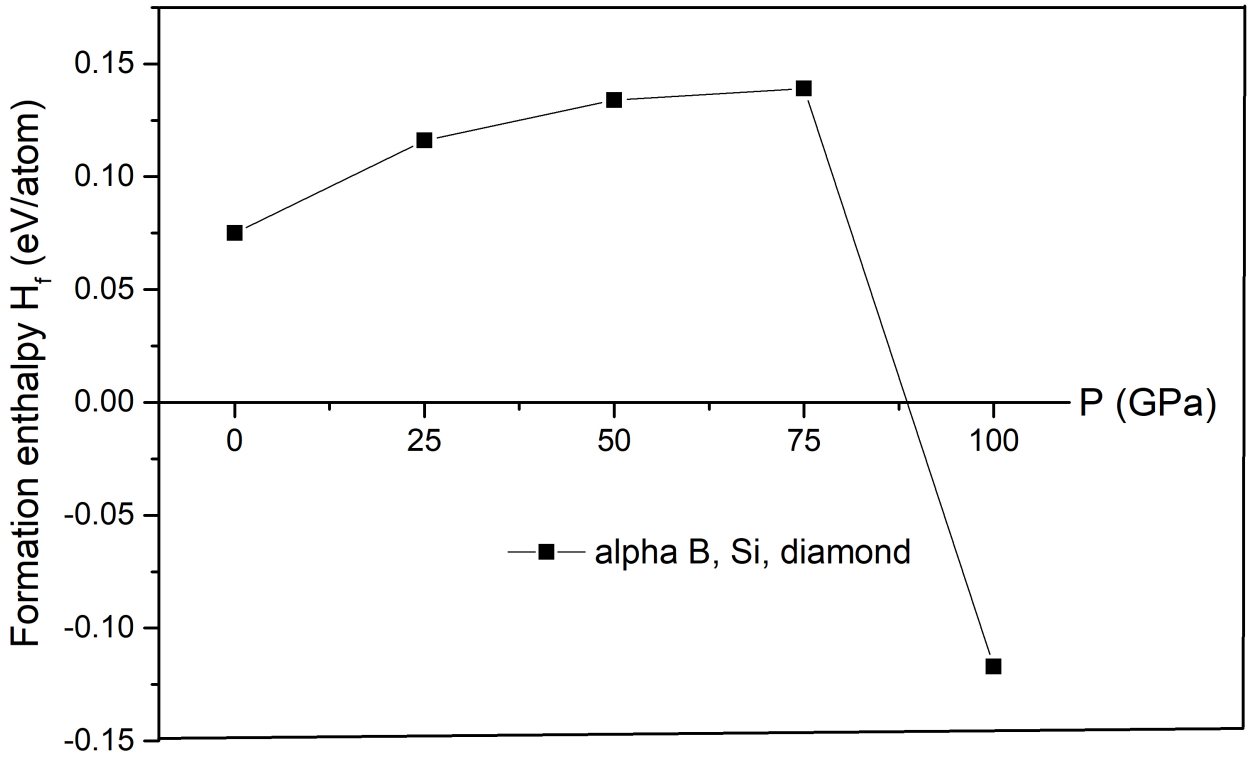

Figure 6.8: Calculations in DFT-LDA. Formation enthalpy in eV/atom of $(B_{11}Si^{P1})$*C-B-Si as a function of pressure in GPa.*

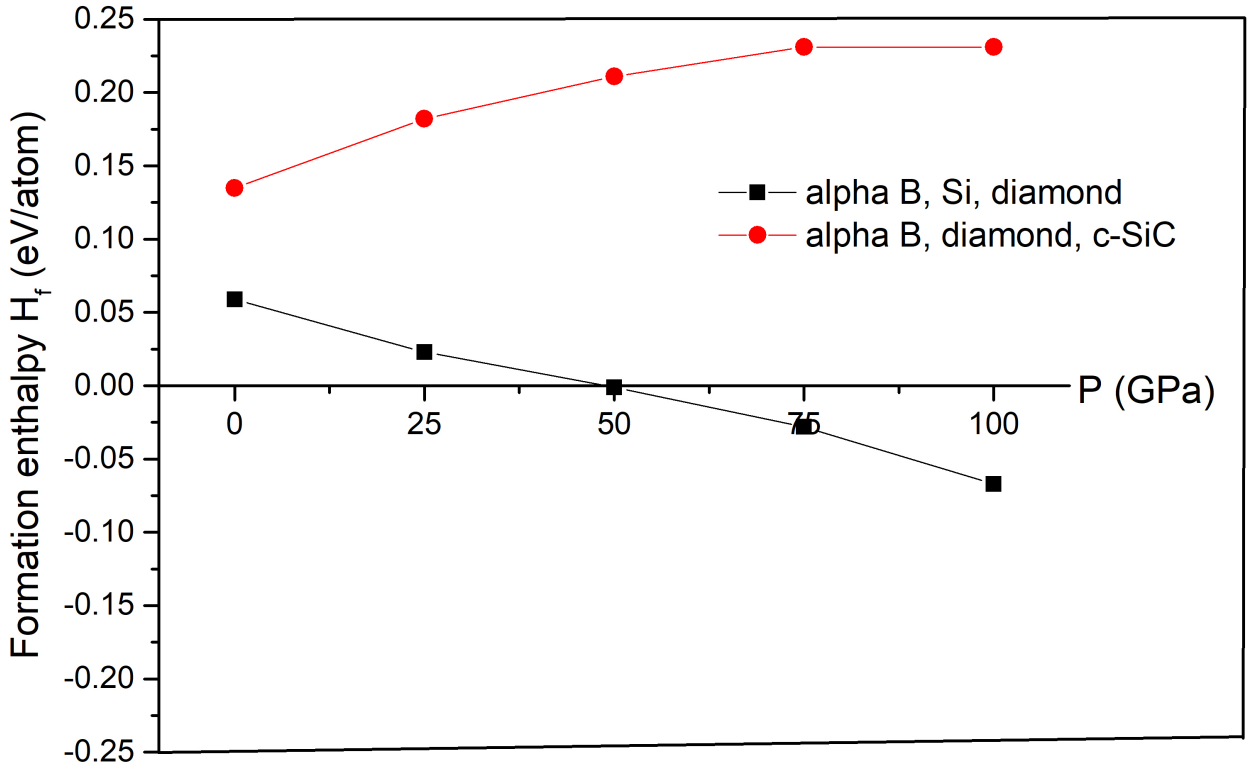

Figure 6.9: Calculations in DFT-LDA. Formation enthalpy in eV/atom of $(B_{10}Si^{P2}Si^{P1})$*C-B-C as a function of pressure in GPa. The calculations have been done in DFT-LDA for various reactant mixtures.*

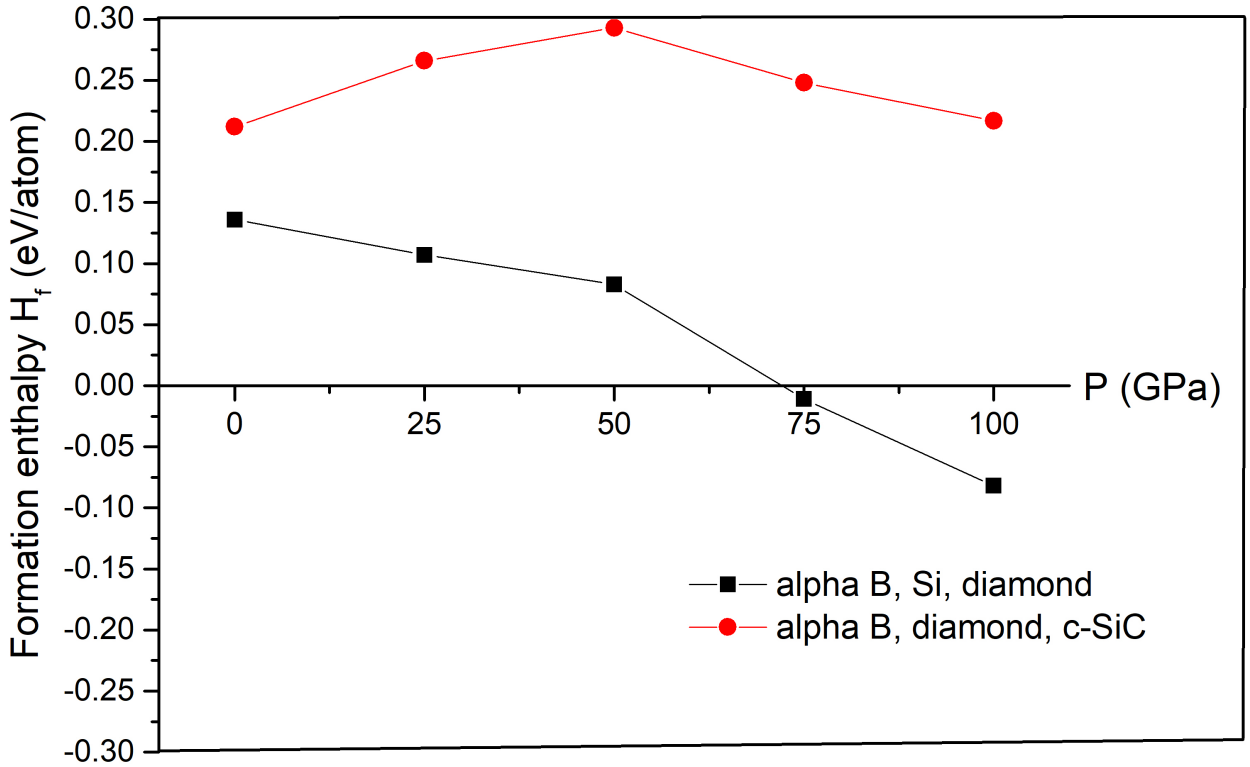

Figure 6.10: Calculations in DFT-LDA. Formation enthalpy in eV/atom of $(B_{10}Si^{P3}Si^{P1})$*C-B-C as a function of pressure in GPa. The calculations have been done in DFT-LDA for various reactant mixtures.*

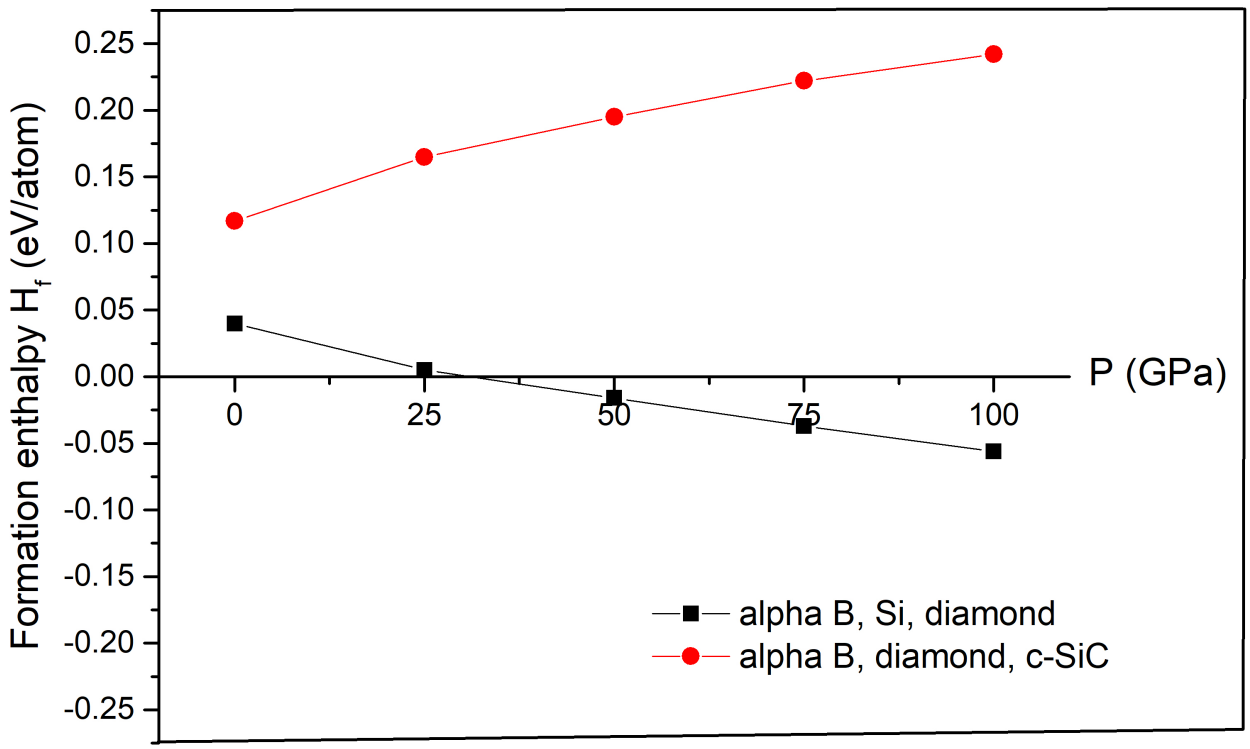

Figure 6.11: Calculations in DFT-LDA. Formation enthalpy in eV/atom of $(B_{10}Si^{P4}Si^{P1})$*C-B-C as a function of pressure in GPa. The calculations have been done in DFT-LDA for various reactant mixtures.*

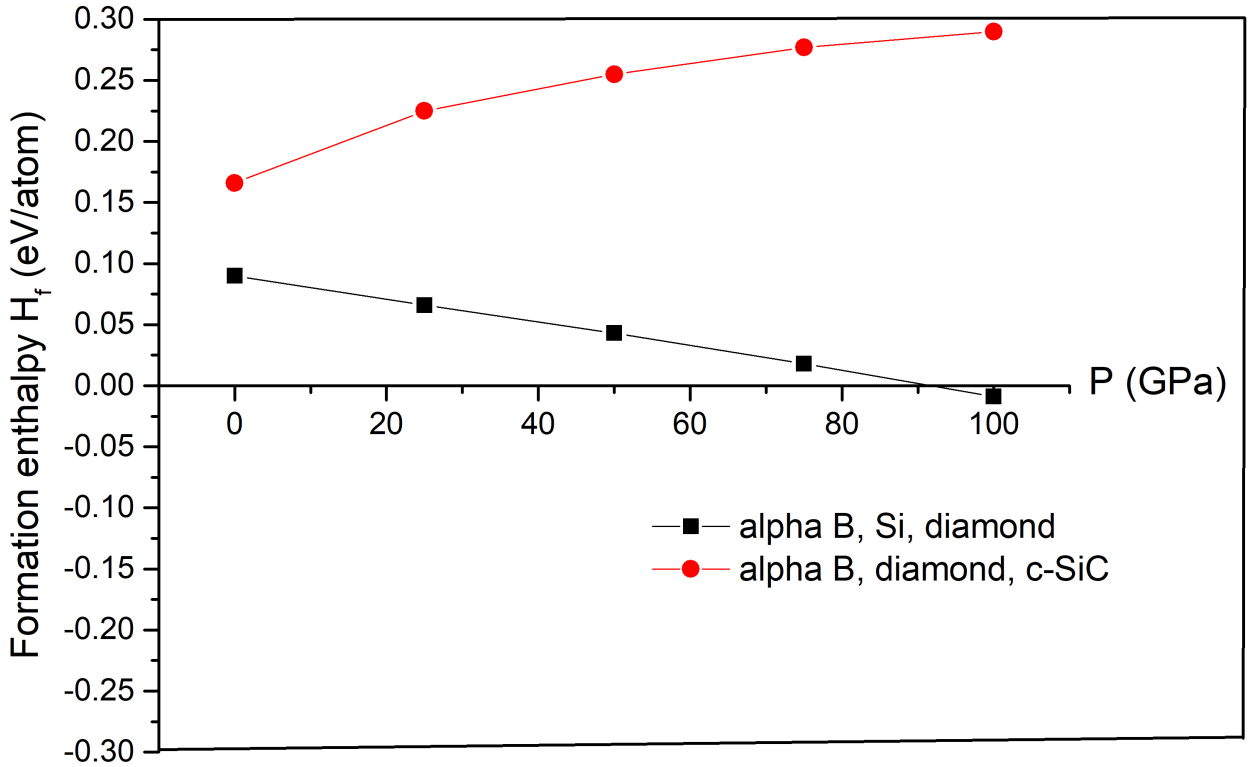

Figure 6.12: Calculations in DFT-LDA. Formation enthalpy in eV/atom of $(B_{10}Si^{P9}Si^{P1})$*C-B-C as a function of pressure in GPa. The calculations have been done in DFT-LDA for various reactant mixtures.*

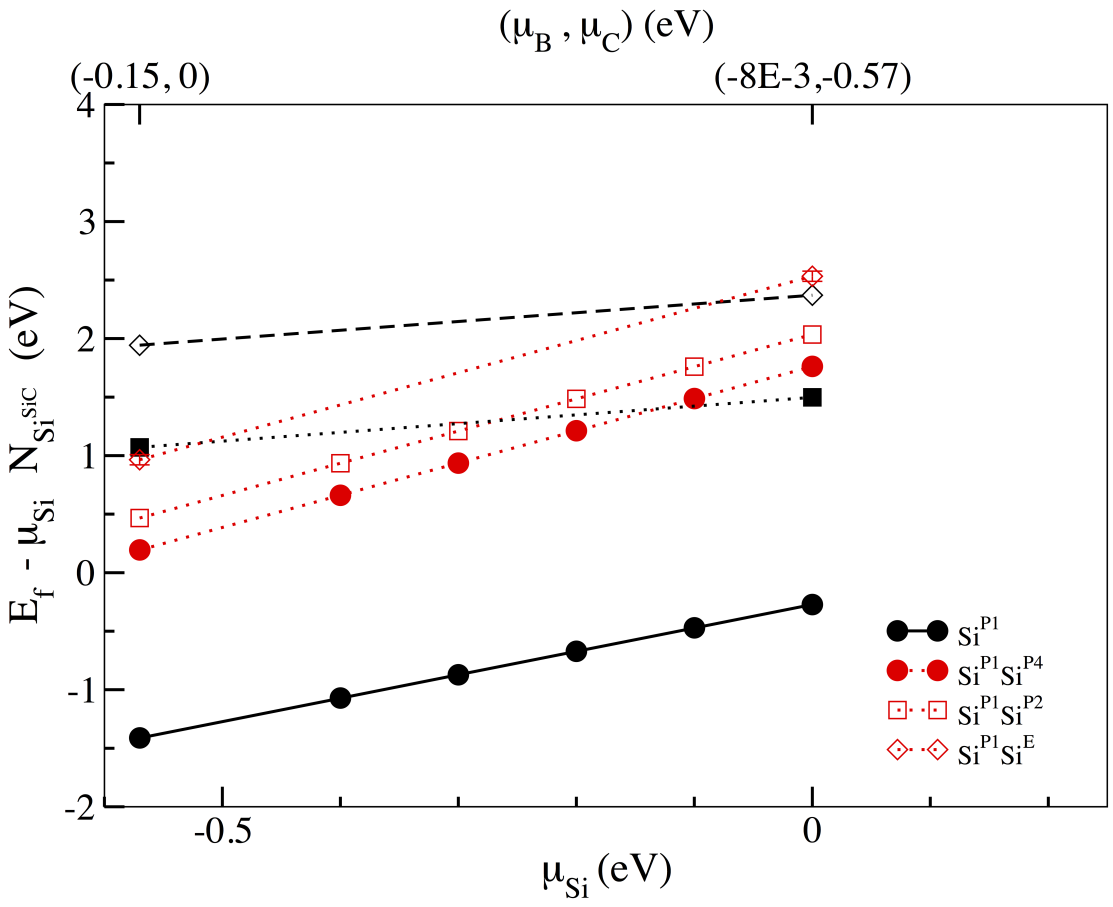

Figure 6.13: Formation enthalpy at ambient pressure in eV/unit cell. Comparison of the compounds with 2-silicon substitutions (of which one Si in the P1 position) and the compounds with 1-silicon substitution, as a function of the chemical potential of silicon. The error bars are given by the various configurations of a 2-atom substitution. Calculations in DFT-LDA. The error bars and the legend for the 1 Si substitution have been omitted for clarity, and are the same as in figure 6.5. Only the 1-Si configuration that have the lowest energy have been reported.

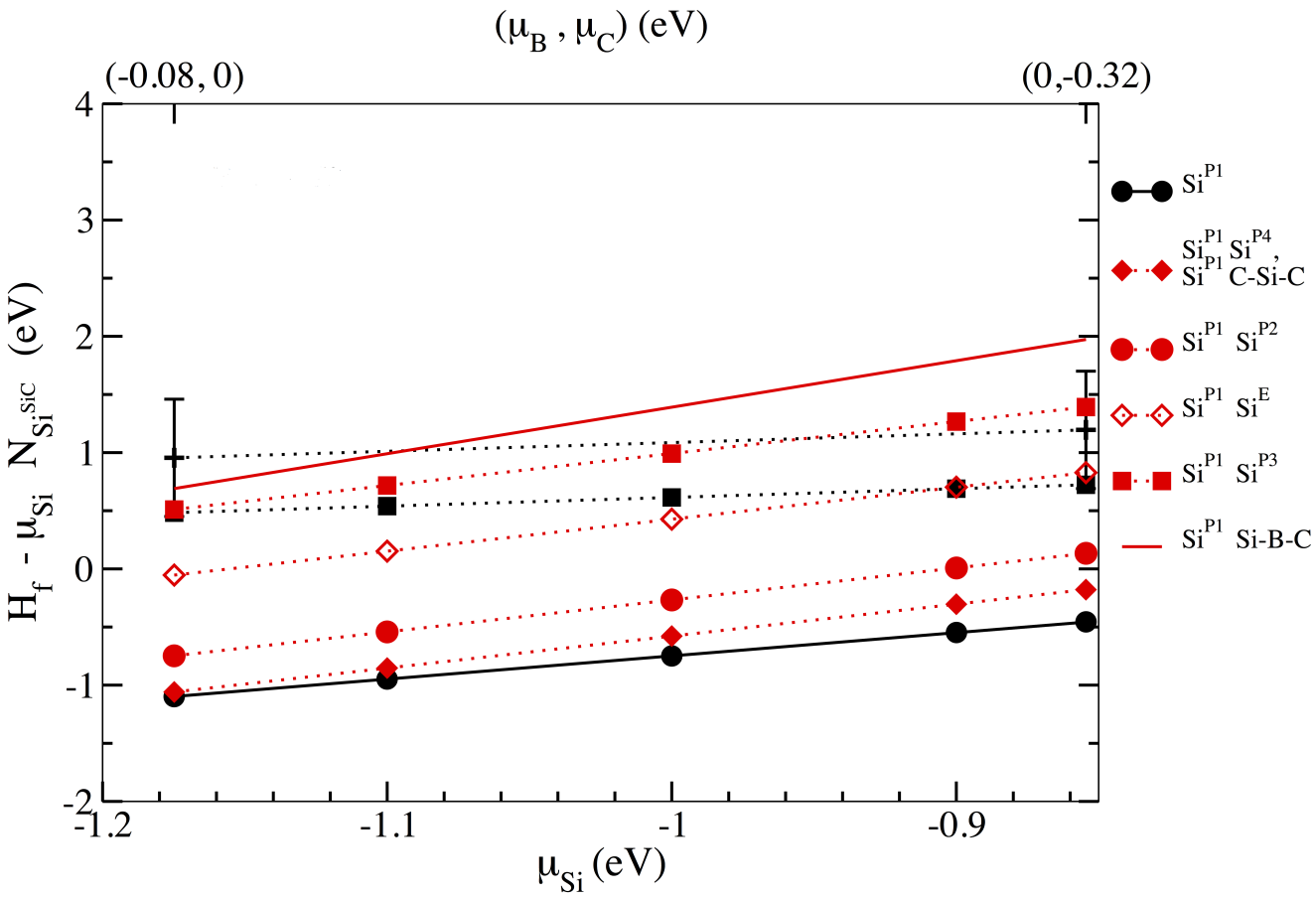

Figure 6.14: Formation enthalpy at P=26.7 GPa in eV/unit cell. Same as in figure 6.13. Many of the 2-Si configurations (in red colour) have become thermodynamically stable under pressure. The configurations in which the second Si atom is at chain center or in the polar position P4, on the same pole as P1, have quasi similar formation enthalpy as the 1-Si substitution (black colour) within the accuracy of our calculations, in the Si-poor domain. Only some of the 1 Si substitutions have been reported in this figure. Calculations in DFT-LDA.

6.3 Discussions on calculations

All the positions where insertion of one silicon atom into the B_4C unit cell result in negative formation enthalpy and hence, thermodynamically stable polymorphs at 0 K, have been recorded in table 6.2 as a function of pressure and reactant mixtures. The same has been done in table 6.3 for insertion of two silicon atoms in the B_4C unit cell. From the tables, it can be seen that a combination of elemental boron, carbon and silicon should be preferred as starting materials, and that silicon carbide should be avoided.

For the enthalpy calculations with relaxed cell parameters, pressure has very different effects on the insertion of silicon in the unit cell. It is found that both one and two silicon atom(s) substitutions in a larger number of positions in the unit cell become feasible with the increase in pressure.

However, an exception is $(B_{11}Si^{P1})$C-B-C, whose formation enthalpy increases with an increase in pressure, when the reactant mixture of elemental boron, carbon and silicon (figure 6.2) is considered. In this configuration, the Si atom has the same location as carbon in B_4C; in B_4C as well, it has been shown that pressure lowers the stability [6]. Thus, both $(B_{11}Si^{P1})$C-B-C and $(B_{11}C^{P1})$C-B-C show the same behavior as a function of pressure. Pressure has therefore the paradoxical effect of lowering the stability of the P1 substitution, and to favour the insertion of Si in other positions of the icosahedron.

The formation enthalpy also increases with pressure in all of the configurations when

	Reactants						Silicon positions (negative formation enthalpy)				
	Si	C	α-B_{12}	B_4C	c-SiC	h-SiC	0 GPa	25 GPa	50 GPa	75 GPa	100 GPa
LDA	✓	✓	✓				P1	P1	P1	P1, C-Si-C	P1, C-Si-C, Si-B-C*
	✓		✓	✓			P1	P1	P1	P1	P1, Si-B-C*
	✓	✓		✓			-	-	-	C-Si-C	C-Si-C
		✓	✓		✓		P1	-	-	-	-
		✓	✓			✓	P1	-	-	-	-
GGA	✓	✓	✓				P1	P1, C-Si-C	P1, C-Si-C	P1, C-Si-C	P1* , C-Si-C, Si-B-C

Table 6.2: Summary of the polymorphs with 1 Si substitution having negative formation enthalpy starting from various reacting mixtures. The positions of the respective silicon substitutions are shown in the table. The asterisks are put to note the polymorph with the lowest formation enthalpy in the cases where multiple polymorphs with the same stoichiometry have negative formation enthalpy.

silicon carbide is used as a reactant. This comes from the fact that pressure lowers the stability of silicon more than that of silicon carbide, consistent with the bulk moduli of these materials. Indeed, the bulk moduli and pressure derivatives are 225 GPa [142–145]

Reactants				Silicon	positions	(negative	formation	enthalpy)
Si	C	α-B_{12}	c-SiC	0 GPa	25 GPa	50 GPa	75 GPa	100 GPa
✓	✓	✓		-	-	C-Si-C*, P2, P4	C-Si-C*, P2, P3, P4	C-Si-C* , P2, P3, P4, P9, C-B-Si
	✓	✓	✓	-	-	-	-	-

Table 6.3: Summary of the polymorphs with 2 Si substitutions having negative formation enthalpy starting from various reacting mixtures. The positions of the second silicon substitutions are shown in the table, while the first Si atom was always substituted at the P1 position. The asterisks are put to note the polymorph with the lowest formation enthalpy in the cases where multiple polymorphs with the same stoichiometry have negative formation enthalpy.

and 4.1 [145] for SiC and 99.785 GPa and 4.23 for silicon [146–148].

The behaviour of the formation enthalpies under pressure is driven by the variation of volume and by the relative change of the internal energy.

The role of the volume change turns out to be important for ($B_{11}C^{P1}$)Si-B-C beyond 100 GPa. Indeed, the formation enthalpy of ($B_{11}C^{P1}$)Si-B-C shows a dramatic decrease beyond 100 GPa. The sudden decrease in the formation enthalpy appears due to a drastic decrease in the volume of the polymorph, from $\approx$ 93.2 Å^3 at 75 GPa to $\approx$ 82.7 Å^3 at

100 GPa. In comparison, in ($B_{11}Si^{P1}$)C-B-C, the volume decrease is more than twice smaller, from $\approx$ 92.0 Å^3 at 75 GPa to 87.2 Å^3.

As mentioned above, the behaviour of the formation energy under pressure is also affected by the relative changes in the internal energy, i.e., the total energy of a polymorph, with respect to the reference elements or compounds. These changes are representative of the compressibility of the materials since the bulk modulus of a material is the second order derivative of the total energy with respect to pressure. The internal energy (total energy) of B and Si becomes higher as pressure increases, whereas the internal energy of diamond remains (quasi) constant. This is in agreement with the fact that diamond is the less compressible material, with a bulk modulus of 445 GPa [149], compared to the bulk modulus of 213-224 GPa for α boron [150]. By comparison, the internal energy of the B-Si-C polymorphs, for both 1 Si atom and 2 Si atom substitutions, increases less than that of elemental B+Si, which makes the B-C-Si structure more stable than elemental boron, silicon and carbon.

This is expected to be even more apparent in the experiments: the bulk modulus of β boron is slightly smaller than that of α boron, and that of graphite (to say nothing of amorphous carbon) is smaller than that of diamond. This makes the B+Si+C composition of initial reactants interesting from the viewpoint of the effect of pressure. On the contrary, with respect to SiC, the internal energy of SiC increases 3 times slower than in elemental B or Si. Therefore, pressure does not help with insertion of silicon into the structure. Therefore, we concluded that we have to bypass the formation of SiC during

syntheses with silicon.

The comparison between the GGA and the LDA calculations have shown that the formation enthalpy is lower for the same polymorphs in case of GGA calculations. This results in some polymorphs attaining negative formation enthalpy at lower pressures than that in LDA calculations, as shown in figure 6.3. This may be due to the underestimation of the internal energy and the unit cell volume by DFT-LDA [151]. However, the DFT-LDA and DFT-GGA calculations already done agree on the general trend of the effect of pressure and different reactant mixtures on the formation enthalpy of the different polymorphs, even though the pressure at which, for instance, the formation energy changes its sign may be different in the two calculations(figure 6.3).

A limitation of the present calculations is that they have been done at 0 K. The parameters of temperature and entropy would be needed to be introduced in order to calculate the Gibbs formation energy (G). For boron carbide , however, it has been found that the inclusion of the vibrational entropy only marginally changes the stability of the formation energy with respect to elemental boron and carbon [6]. Calculation of entropy would be needed if one would like to investigate the effect of atomic disorder in the structure at elevated temperature: This is beyond the scope of the present chapter.

Another limitation is that the stability of the B-C-Si phases with respect to mechanical deformation was not explored. This could be done by inspecting the tensor of the elastic constants, or by inspecting the dynamical matrices with respect to ionic displacements. In absence of these results, no conclusion could be drawn with respect to the mechanical

and dynamical stability of the phases.

6.4 Experimental materials and methods

From my calculations, it appeared that the Si substitution is thermodynamically stable in the polar carbon position in the icosahedron, at pressures up to 25 GPa and 0 K. This leads to a stoichiometry of (B_{11}Si)C-B-C. To verify if this phase can be produced experimentally, a trial experiment was done at IMPMC using the Paris-Edinburgh press VX5. The working of the Paris-Edinburgh press and the methods of the temperature and pressure calibration has been explained in Sec 1.3.1 of β boronChapter 1.

For the *ex situ* synthesis at IMPMC, β boron, amorphous carbon and silicon (Alfa Aesar, 99.99 % purity) were mixed in the atomic ratio of 12 : 2 : 1 and mixed for 5 minutes. The sample was then put inside the gasket assembly. Next, the pressure was increased over 3 hours to a value of 2.6 GPa. The temperature was then increased to 2473 K at a rate of 2 K/s to overcome the kinetic barriers. The dwell time was kept at 1 hour. After the heating, the sample was quenched rapidly and decompressed slowly over 6 hours. The gasket was then broken carefully and the synthesised product was characterised.

For the *in situ* synthesis at Synchrotron SOLEIL, the same sample mixture was put under 4 GPa of pressure in a Paris-Edinburgh press and the temperature was slowly raised to 2473 K as EDXRD patterns were taken at regular intervals (run BC4). Six CAESAR patterns (see Sec 1.3.3) were also taken to understand the evolution of the sample with the increase in temperature. Since a Caesar pattern takes 45 minutes to be

acquired, the sample stayed in this intermediate temperature steps for long periods of time. Therefore, the sample also remained at the highest temperature of 2473 K for 45 minutes, before being rapidly quenched.

After the *in situ* run, the amorphous boron gasket had, however, melted into the anvil because of the high temperatures. Therefore, the polishing mechanism employed in Sec 5.2 was used again to expose the upper surface of the sample. Further characterisations like Raman spectroscopy, scanning electron microscopy (SEM) and electron dispersive X-ray spectroscopy (EDX) was done on the exposed surface.

6.5 Results of *ex situ* experiments

Figure 6.15 shows the XRD diffractogram of the recovered sample from the *ex situ* synthesis. Some boron carbide seemed to have formed in the sample, but the peaks are slightly shifted to the left by around 0.5°. This is shown in the inset of figure 6.15, where the spectra is compared to that of the B_4C spectra obtained from the synthesis done from elements at 2 GPa and 2473 K in Chapter 2. Many of the β boron peaks are also shifted towards the left. In table 6.4, the new peaks, denoted by 'new phase/s' in the product in the figure 6.15 are enumerated and their possible assignment is mentioned.

The formation of hexagonal silicon carbide has also been observed. Some peaks corresponding to SiB_n where n=4, 6, 14 were found as well. These peaks have been enumerated in table 6.5.

Peak positions (2θ Cu Kα)	Assignment
37.21	shifted boron carbide peak (021)
40.83	shifted β boron peak (404)
45.77	unidentified
51.73	shifted β boron peak (238)
55.11	unidentified
59.05	shifted β boron peak (431)
60.13	unidentified
61.60	unidentified
62.89	unidentified
67.48	shifted β boron peak (348)
68.98	shifted β boron peak (532)

Table 6.4: Assignment of the peaks denoted by new phase/s in figure 6.15.

Peak positions (2θ Cu Kα)	Assignment
33.59	hexagonal silicon carbide
35.7	hexagonal silicon carbide
42.39	SiB_n
43.94	SiB_n

Table 6.5: Assignment of the peaks denoted by silicon carbide and SiB_n in figure 6.15.

However, silicon has not been completely used during the synthesis, resulting in the (111), (220) and (311) silicon peaks in the product.

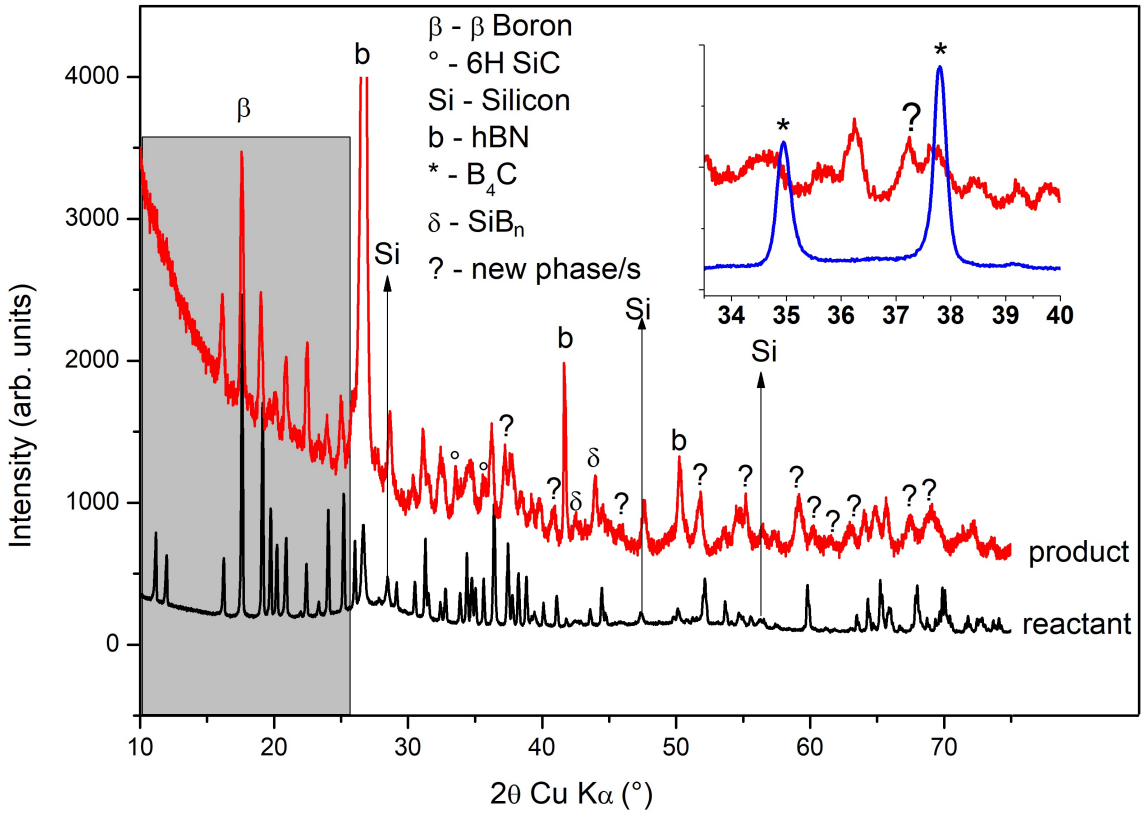

Figure 6.15: X-ray diffraction pattern of quenched sample from the mixture of crystalline β boron (COD ID : 901110 33 [107]), amorphous carbon (COD ID : 9000046 35 [113]) and silicon (COD ID : 90085 65 [152]) under 2.6 GPa at 2473 K for 1 hour. The inset is the zoom between 33 ° and 40 ° of the superposition of the curve of the product (same colour as main plot) and the diffractogram of B_4C taken from figure 2.1. It is shown that some new peaks are slightly shifted towards the left compared to boron carbide (COD ID : 4124697 34 [109]) peaks.

6.6 Results of *in situ* experiments

An exploratory run with elemental boron, carbon and silicon was attempted in the beamtime allotted in the PSICHE beamline of SOLEIL synchrotron. The run (BC4)

consisted of *in situ* EDXRD and several CAESAR scans (See 1.3.3). The methodology is explained in details in Sec 6.4.

6.6.1 Energy dispersive X-ray diffraction

The EDXRD results, given in figure 6.16 shows the evolution of the reactant β boron, amorphous carbon and silicon powder at 4 GPa with increase in temperature.

Similar to what was seen in Sec 2.6, recrystallisation of β boron peaks are observed as the temperature increases.

Silicon peaks also become sharper with the increase of temperature till the silicon melts. An intense silicon carbide peak appears at 1273 K before the melting of silicon. It is difficult to identify whether the silicon carbide peak belongs to hexagonal or cubic structure from the EDXRD pattern. However, comparisons with the Caesar patterns (see Sec 6.6.2) and *ex situ* Raman spectroscopy (see Sec 6.6.3) confirms the final product to be hexagonal silicon carbide.

Boron carbide peaks start appearing around 2273 K, as was expected from the results of Chapter 2. However, there is no shifting of the boron carbide peaks, as was observed in Sec 6.5.

An intense peak corresponding to new phase/s and a peak corresponding to SiB_n have also appeared, which would be discussed in Sec 6.6.2.

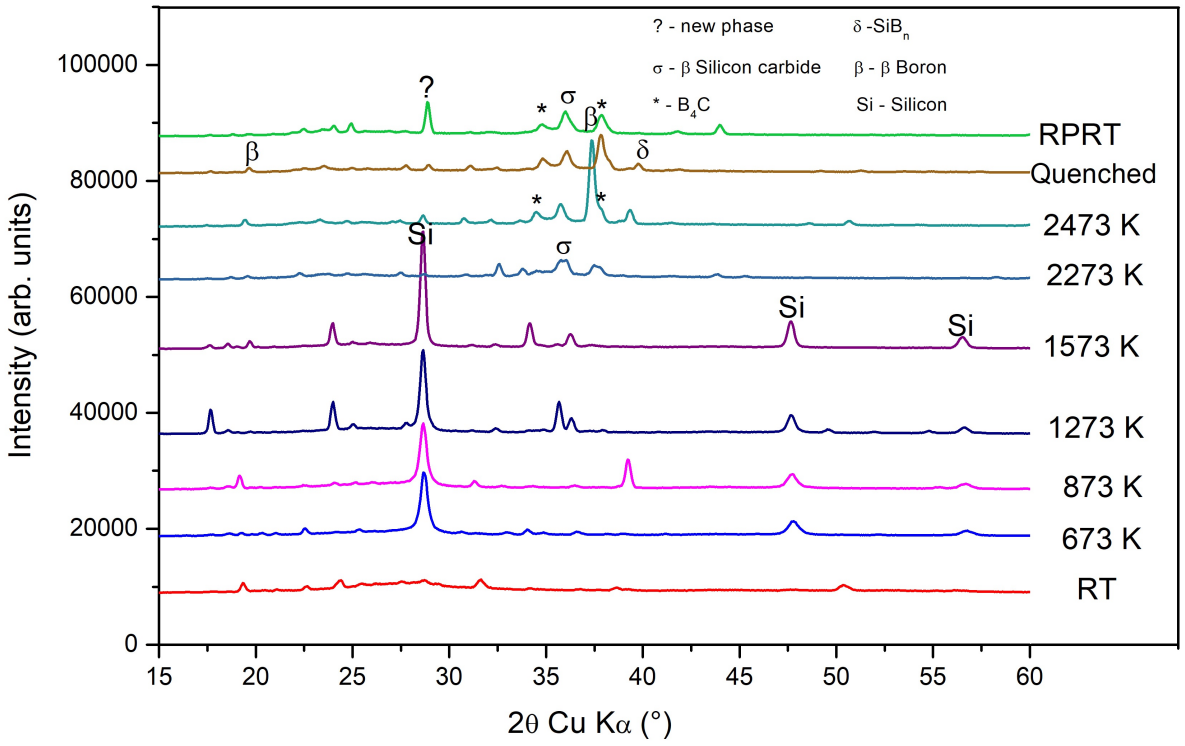

Figure 6.16: in situ diffraction pattern taken at the centre of the sample of a mixture of crystalline β boron, amorphous carbon and silicon at 4 GPa for various temperatures during the run BC4. The data obtained from the synchrotron radiation was converted to that of Cu K-α radiation. All the unmarked peaks are those of crystalline β boron.

6.6.2 CAESAR results

The CAESAR system was used at the centre of the sample assembly at a few temperature values during the run BC4 to get a fuller picture.

Several silicon carbide peaks were found during the CAESAR, which established the phase to be hexagonal silicon carbide.

A few boron carbide peaks were also found, which were unshifted in accordance with the EDXRD results.

However, the first three peaks marked as new phase/s in the final RTRP spectra of figure 6.17 could correspond to shifted β boron peaks, as shown in table 6.6.

Peaks (Q in $Å^{-1}$)	Assignment
1.13	Shifted β boron peak (110)
1.74	Shifted β boron peak (211)
3.52	Shifted β boron peak (054)
6.56	unidentified

Table 6.6: Assignment of the peaks denoted by new phase/s in figure 6.17.

Some SiB_n peaks were also found where n corresponds to 4, 6 or 14.

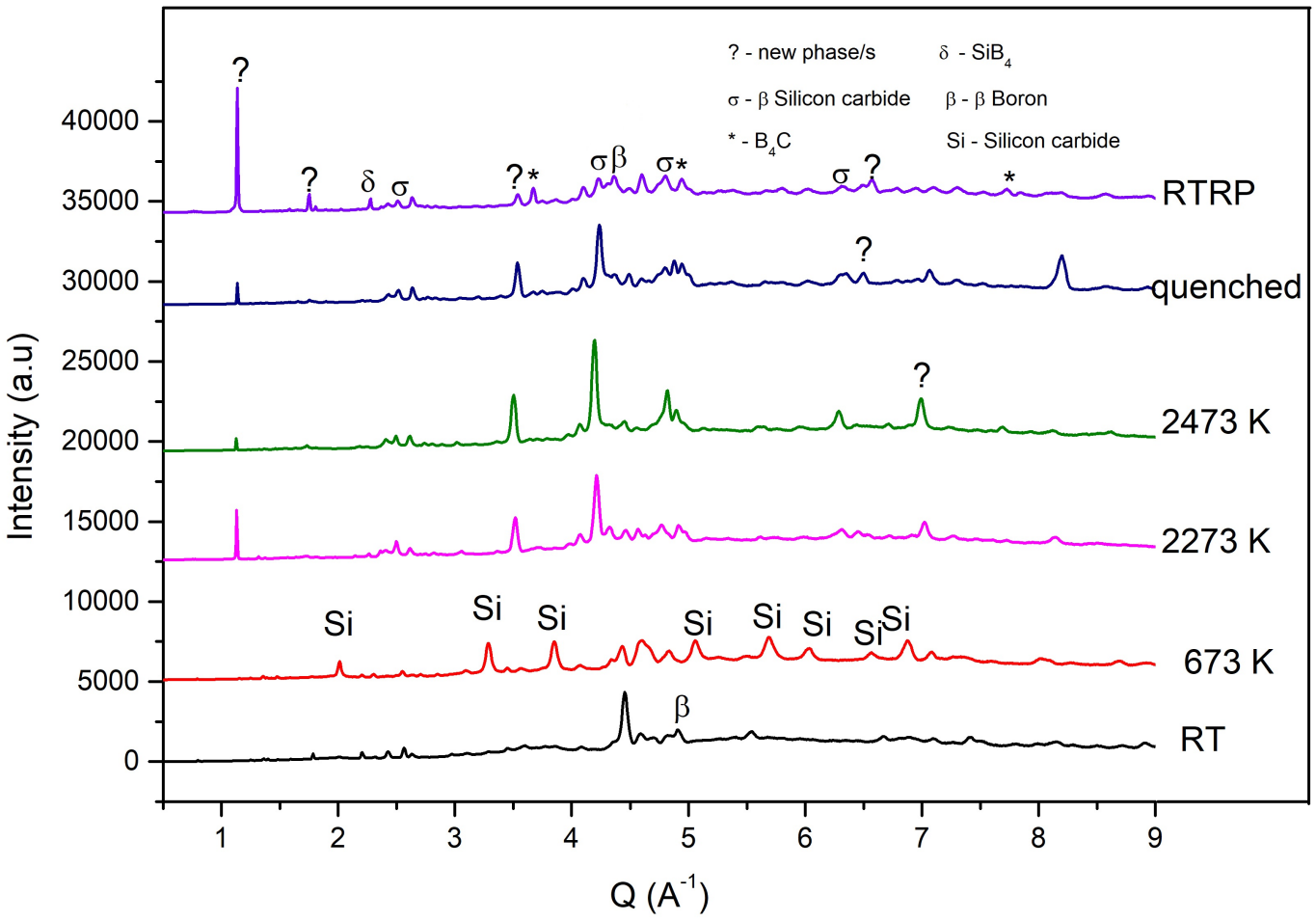

Figure 6.17: in situ diffraction pattern taken at the centre of the sample of a mixture of crystalline β boron, amorphous carbon and silicon at 4 GPa for various temperatures. The data was obtained from the synchrotron radiation using the CAESAR system. All the unmarked peaks are those of crystalline β boron.

6.6.3 *Ex situ* characterisation

After the run BC4, the amorphous boron epoxy gasket had melted into the anvils because of the high temperatures attained during the run. Therefore, the sample could not be recovered in the usual method by breaking the gasket, as outlined in Chapter 2. The polishing method employed in Chapter 5 was used to expose the upper surface of the sample. Raman spectroscopy, SEM and EDX was done on this exposed sample surface which was still attached to the anvil.

Raman spectroscopy

Raman spectroscopy was performed at various points on the surface of the sample.

Figure 6.18 shows the unambiguous presence of hexagonal silicon carbide (6H SiC) Raman peaks. This, coupled with the CAESAR results, has confirmed the presence of hexagonal silicon carbide in the sample.

Figure 6.19 shows peaks for recrystallised β boron [108]. The sharp Raman peaks of recrystallised β boron after HPHT treatment has also been confirmed in the current work in Chapter 7.

Some peaks corresponding to new phase/s have appeared. However, it is difficult to confirm whether they are shifted β boron peaks or those of SiB_n compounds, since the Raman peaks of all these compounds are not clearly defined in the literature.

Raman peaks corresponding to boron carbide was also observed. However, the silicon

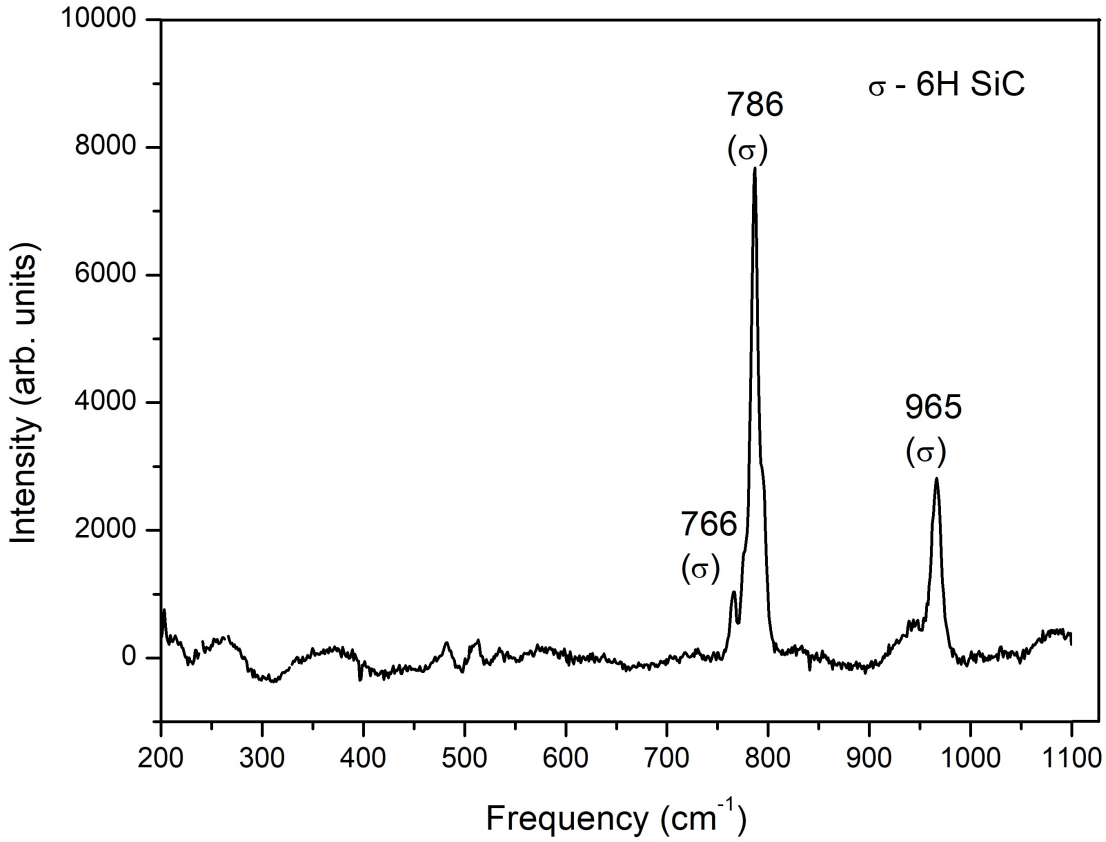

Figure 6.18: ex situ Raman spectroscopy pattern at a random point at ambient conditions on the surface of the recovered sample from the in situ synthesis done in SOLEIL synchrotron with a reactant mixture of crystalline β boron, amorphous carbon and silicon under 4 GPa.

carbide peaks were much more well-defined compared to the boron carbide peaks, which is evident when figures 6.18 and 6.19 are compared.

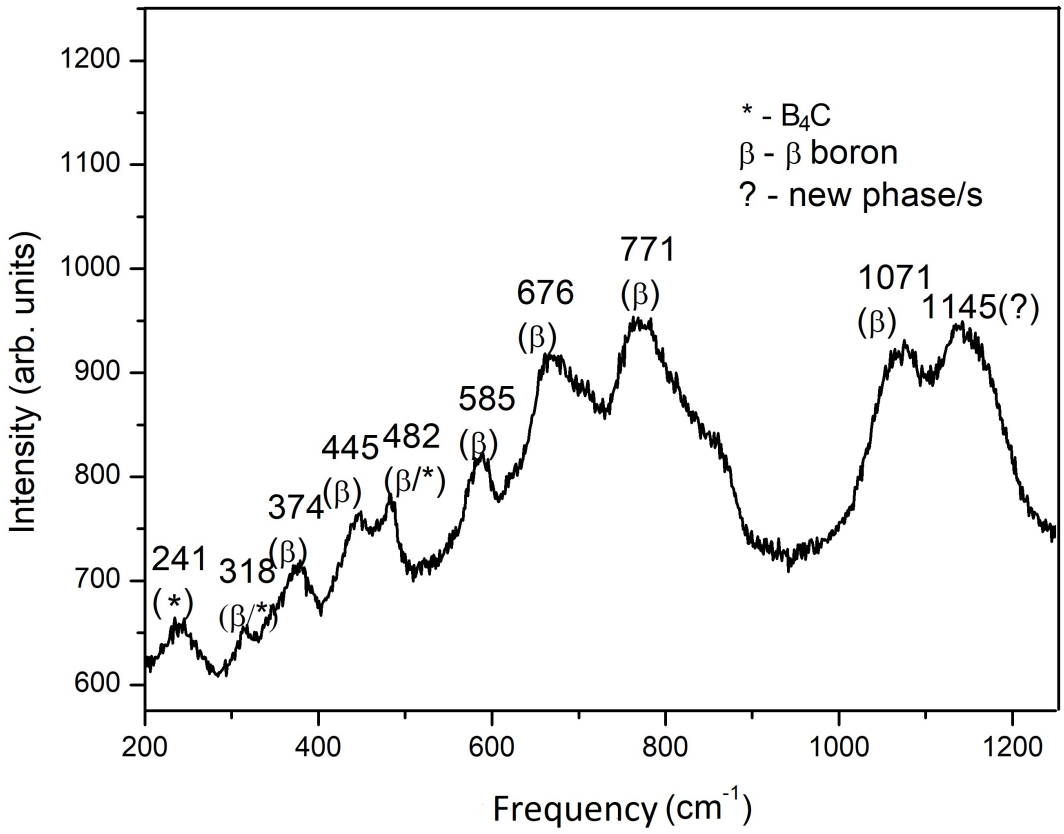

Figure 6.19: ex situ Raman spectroscopy pattern at a random point on the surface of the recovered sample from the in situ synthesis done in SOLEIL synchrotron with a reactant mixture of crystalline β boron, amorphous carbon and silicon under 4 GPa.

Scanning electron microscopy and electron dispersive X-ray spectroscopy

Scanning Electron Microscopy (SEM) was performed on the surface of the sample to understand the morphology of the synthesized products. It was complemented with EDX to map the positions of the silicon, carbon and boron atoms in the sample.

The SEM images, as shown in figure 6.20, have established the very heterogenous nature of the sample. The images are in ascending order of magnitude, with the image (a) corresponding to the entire sample surface. The lighter areas in image (b) corresponded to boron, and the darker areas corresponded to a mixture of elements. The EDX of image (c) has been shown in figure 6.21.

The first image in the EDX is a composite mapping of boron and silicon. It shows the presence of zones where the only element present is β boron: no silicon is present in these zones. This is understandable, as a large atomic percentage of β boron (74%) was added to the reacting mixture: it establishes that all the β boron added has not reacted.

It also shows zones which correspond to the presence of both boron and silicon: this may correspond to the insertion of silicon in boron and boron carbide.

The highest concentration of carbon in the carbon map corresponds to the zones where boron is absent, but silicon is present: this establishes the formation of silicon carbide, as also seen in the XRD and Raman spectroscopy characterisations. These silicon carbide zones vary in size from 10-20 micrometers.

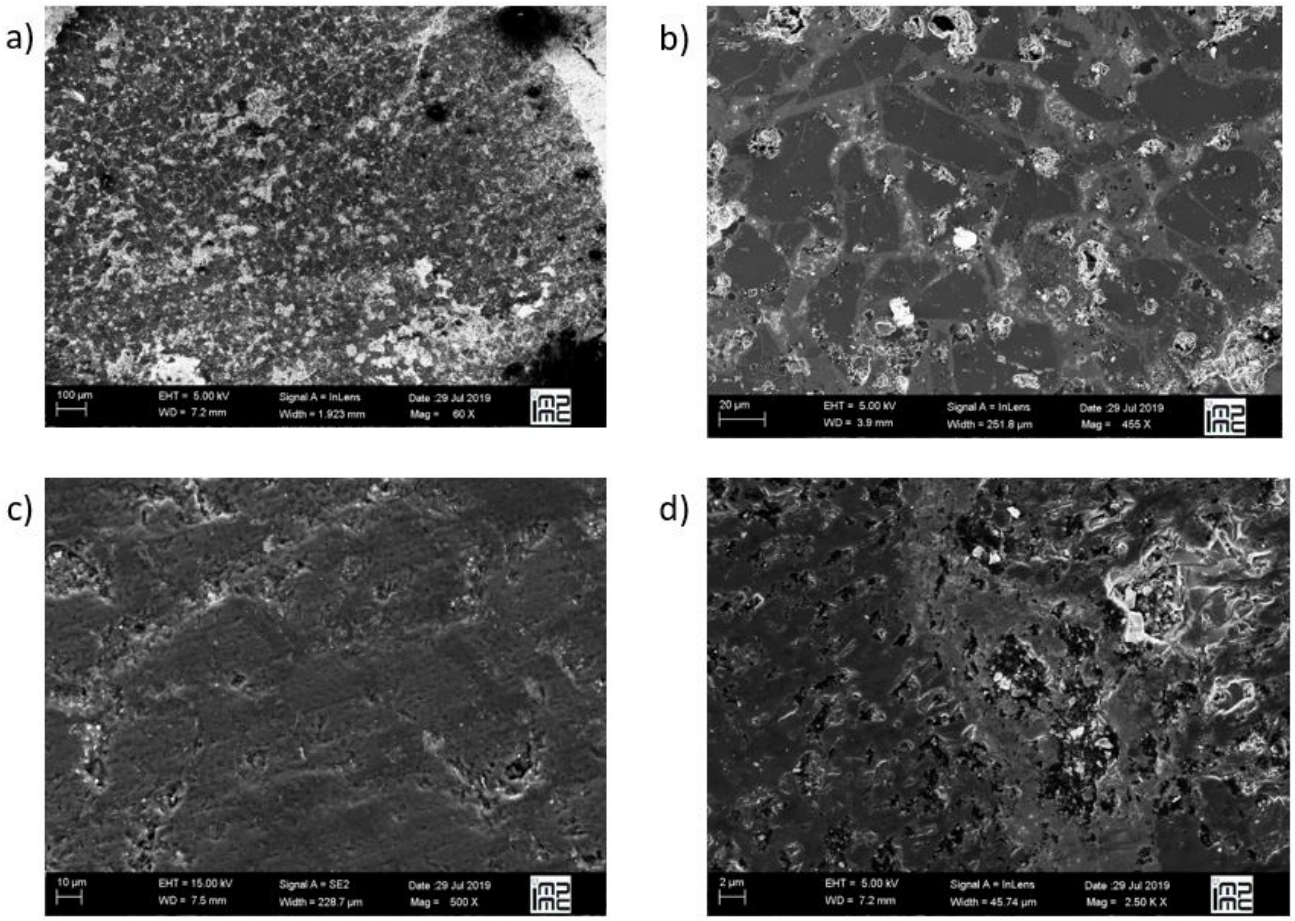

Figure 6.20: Images obtained from scanning electron microscopy on the surface of the recovered sample from the in situ synthesis done in the Soleil synchrotron with a reactant mixture of crystalline β boron, amorphous carbon and silicon under 3.5 GPa. The images are given in increasing order of magnification. The surface is shown to be very heterogeneous.

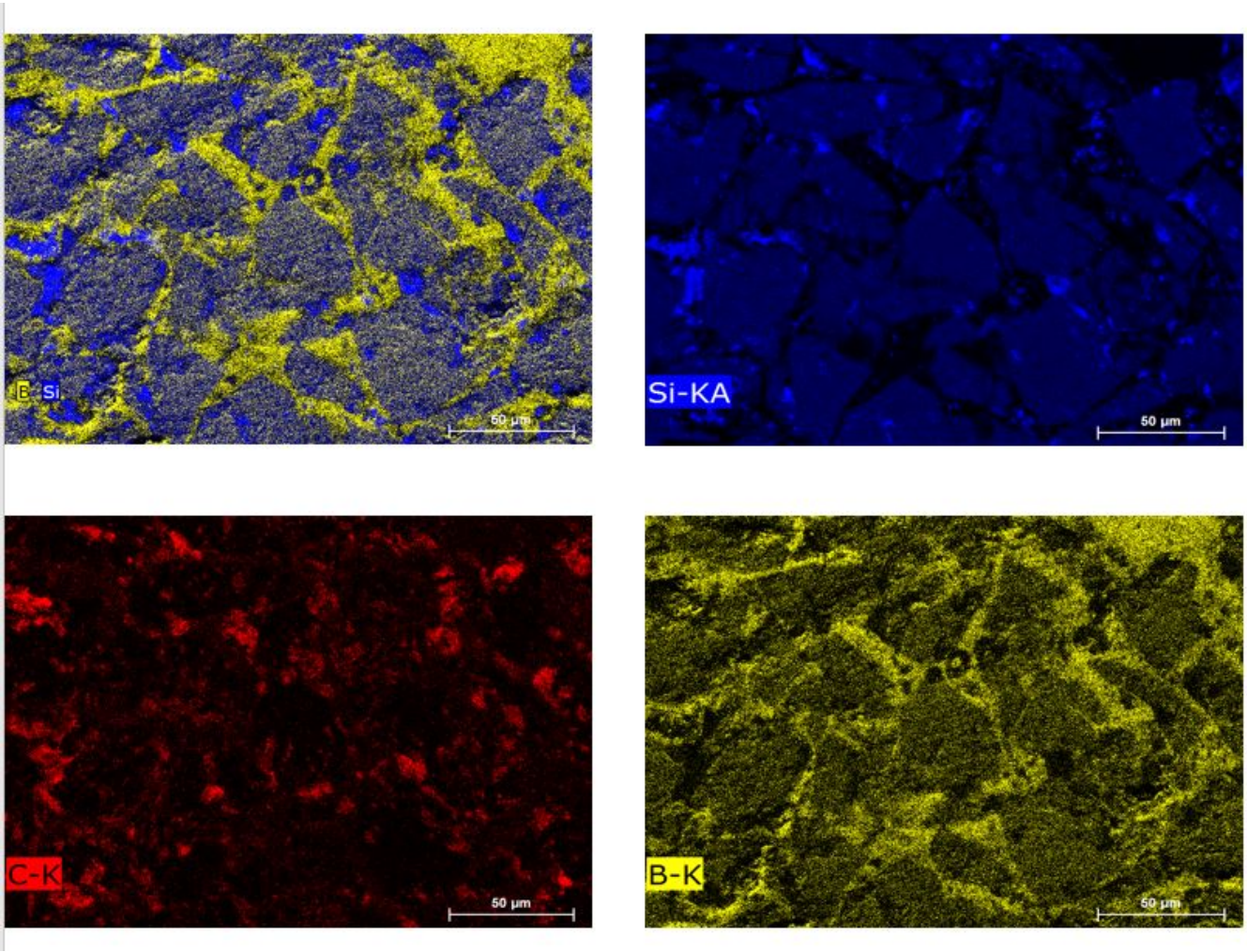

Figure 6.21: Electron dispersive X-ray spectroscopy done on the image c) from figure 6.20 of the recovered sample from the in situ synthesis done in SOLEIL synchrotron with a reactant mixture of crystalline β boron, amorphous carbon and silicon under 3.5 GPa. The images show the mapping of combined boron and silicon, silicon, boron and carbon in clock-wise direction starting from top left.

6.7 Discussions on the experiments

6.7.1 Comparison of *ex situ* and *in situ* experiments

The combination of the *ex situ* and *in situ* experiments has led to some interesting observations.

After the *ex situ* experiment, silicon peaks remained in the XRD pattern of the product, which might signify that the reaction had not reached an equilibrium state and a longer dwell time is needed. In spite of this, we do find the presence of some shifted boron carbide and boron peaks. The peaks are shifted towards lower 2θ values: this can indicates the insertion of silicon into boron and boron carbide. Specially, the insertion of silicon into boron carbide is promising for the synthesis of a ternary phase.

However, in the *in situ* experiment, no shift of the boron carbide peaks are observed, even though some shifted boron peaks are obtained in the XRD pattern: this could signify silicon insertion in boron, but not in boron carbide. Also, significant amounts of hexagonal silicon carbide is obtained, which is established by CAESAR, Raman spectroscopy and EDX results.

At first glance, this might seem perplexing since both the experiments attained the same maximum temperature of 2473 K. Moreover, the *in situ* experiment took place at a higher pressure value. In theory, this could deter silicon insertion into the boron carbide unit cell when elemental boron, carbon and silicon are used as reactants, as seen in figure 6.2. However, the pressure difference of 1.5 GPa is not significant for DFT

calculations.

One of the main differences between the two experiments is the heating rate used to reach the maximum temperature of 2473 K. While the *ex situ* experiment was done with a relatively quick heating rate of 2 K/s, the *in situ* experiment took over 90 minutes to reach the maximum temperature, because of the numerous CAESAR scans taken.

Therefore, during the 45 minutes steps at lower temperatures, silicon could have reacted with carbon to form silicon carbide, along with some SiB_n compounds and silicon insertion into boron structure. Limandri *et al.* have reported that silicon carbide synthesis starts as a solid state reaction even before the melting of silicon [117], which seems to be the case here as well. Thereby, not enough silicon is left for insertion into boron carbide when finally boron carbide starts forming around 2273 K. This is also backed by the fact that no silicon XRD peaks remain in the sample after quenching and decompression. Raman spectroscopy has also not revealed any silicon peak during the post-treatment.

Thus, a faster heating rate could prevent the intermediate step of silicon carbide formation at lower temperatures, and aid in the formation of a ternary B-C-Si compound. This is also agreed upon by the theoretical results in Sec 6.3, where the conclusion was that silicon carbide formation needs to be avoided.

6.7.2 Ways to avoid silicon carbide formation

Two plans of action were envisaged for avoiding the formation of silicon carbide.

The first option is using ultra-rapid heating using induction to attain the target boron carbide synthesis temperature (2273 - 2473 K) almost instantaneously, thus avoiding silicon carbide formation at lower temperatures. This can be made possible by an induction heater project currently under development at IMPMC. However, the project is at the testing stage and would need some time to be fully functional. A beam-time was obtained for April 2020 at PSICHE beamline in SOLEIL synchrotron for the testing of the induction heating equipment in conjunction with the B, C, Si ternary compound synthesis.

The second option is to use SiB_6 instead of elemental silicon as a starting material, as was done by Khan *et al.* [55] for synthesizing silicon doped boron carbide. The idea behind this is that SiB_6 would decompose and release silicon atoms at a high enough temperature under pressure to avoid silicon carbide formation and aid the formation of the ternary phase. There are some issues with the second option: SiB_6 is not commercially available and its HPHT phase diagram is also not known.

Both these options were scheduled to be tried at the beamtime allotted in April 2020 in SOLEIL Synchrotron. However, unfortunately, the pandemic of Covid 19 has necessitated the postponement of the beamtime to December 2020. Thus, these results could not be furnished at this moment.

6.7.3 Formation of hexagonal silicon carbide

Another point of interest in the current results is the formation of hexagonal silicon carbide instead of cubic silicon carbide. In an earlier study, Limadri *et al.* [117] has

shown that cubic silicon carbide (3C SiC) was formed in a pressure range from 0.8 to 11 GPa. However, in my experiments at 2.5 GPa and 4 GPa, hexagonal silicon carbide (6H SiC) was present in the quenched sample - this was established by both XRD and Raman spectroscopy. This may be attributed to the difference in temperature ranges. Limadri *et al.* performed their synthesis within a temperature range of 300 - 1880 K, while in my experiments, the temperature was as high as 2473 K. 6H SiC is known to be more stable at high pressures and high temperatures. Sugiyama *et al.* [153] have reported the phase transition from 3C-SiC to 6H-SiC under 2.5 GPa to be 2473 K. This might signify that 3C SiC was synthesized during my experiments at lower temperatures and there was a phase transition to 6H SiC at 2473 K. However, it is difficult to verify that from the EDXRD pattern since only one SiC peak corresponding to the highest peak for both 3C SiC and 6H SiC is present. The CAESAR results, however, show 6H SiC at both 2273 K and 2473 K at 4 GPa.

6.8 Conclusions and perspectives

A theoretical study of formation enthalpies at various pressures and 0K has been performed using DFT to estimate the feasibility of the formation of a ternary B-C-Si compound. Exploratory follow-ups were done experimentally to these calculations using both *ex situ* and *in situ* resources.

Both the DFT calculations and the synthesis attempts agree on the conclusion that silicon carbide formation is to be avoided in order to obtain a ternary phase consisting

of boron, carbon and silicon.

Two possible methods were discussed to avoid silicon carbide formation in the intermediate temperature range: this would keep silicon available for insertion into the boron carbide unit cell at the formation temperature of boron carbide (around 2273 K for 4 GPa) from elements. One method is the use of an ultra rapid induction heating system, and the other one is the use of Si_6 as a starting material. The pros and cons of this methods are discussed.

Both these options were scheduled to be tested at the SOLEIL synchrotron on April 2020. The beamtime has now been shifted to December 2020 because of the pandemic of Covid 19. Thus, the results of these options would be part of my postdoctoral work.

Chapter 7

Formation of α boron as intermediate phase during HPHT synthesis of boron carbide from elements

7.1 Introduction

α rhombohedral boron, with its combination of semiconducting properties, natural richness of the ^{10}B isotope that reacts with neutrons, resilience to irradiation, can be useful in a variety of fields, notably nuclear and space applications. For example, use of α boron can result in the production of optimized neutron detectors, and potentially facilitate

the production of individual dosimeters. However, access to large quantities of α boron is required for the realisation of all these applications.

It is very difficult to produce α rhombohedral boron, specially in industrial settings. The methods generally used to synthesise α boron are incompatible with the hygiene and safety standards recommended for manufacture on an industrial scale. A synthesis of α boron has been described in literature from the toxic and corrosive reagent BI_3, on a surface heated between 1073 K and 1273 K [154]. The use of BBr_3 or BCl_3 reagents would also suffer from the same drawbacks linked to the dangers of using boron halides. Other known routes for the synthesis of α boron are expensive since they use noble metals and /or heavy metals such as platinum (Pt) or palladium (Pd), with very low yields [155]. More recently, the high pressure synthesis of α boron from rhombohedral β boron has also been described in literature [108]. This α boron preparation must be done in the presence of finely divided platinum (Pt), and in a Pt chamber, or even in gold (Au). Since the implementation of a reactor consisting of these noble metals is not possible in an industrial production site, this synthesis route is incompatible with the manufacture of large parts comprising α boron and/ or with production rates requiring the handling of large volumes of α boron.

However, as reported in Chapter 2, the synthesis of boron carbide from its elements at moderate pressure has resulted in the formation of large quantities of an intermediate phase of α boron, without using expensive Pt or Pd catalysts. The α rhombohedral boron structure of this intermediate phase has been identified by its red colour, X-ray

diffraction and Raman spectroscopy. In the current chapter, I have established that the α boron formed is indeed one single phase and has no doping of carbon.

The phase diagram of boron has been investigated at length in the scientific literature. However, despite decades of studies, there is no consensus over this phase diagram, especially at high temperatures and pressures. In fact, boron is the last elemental crystal whose phase diagram is still not well-established [156]. The main problem at elevated temperatures and pressures is that there are a number of competing phases at each pressure and temperature point [156], and the stability of these phases might depend on both the kinetics and the thermodynamics of the process.

Concerning theoretical calculations to establish the stability of various boron polymorphs, the extremely complicated and still debated structure of β rhombohedral boron is a major roadblock. However, the general wisdom is that α boron is a metastable phase with respect to β boron at ambient conditions, in the same manner as diamond is a metastable phase with respect to graphite. In some calculations, α boron has been found to be marginally more stable than β boron at zero temperature and zero pressure; It was shown to undergo a phase transition and transform into β boron at high temperature [157]. In another theoretical work, β boron was modelled with a slightly different atomic structure [158] which made it the thermodynamical stable phase at any temperature when zero point energy was considered, and α boron remained as the metastable phase.

From an experimental viewpoint, the more stable phase at ambient conditions has been

established to be β rhombohedral boron with α boron being metastable at these conditions [126, 159]. This also seems reasonable considering β boron is widely available commercially, unlike α boron. On the other hand, Parakhonshiy *et al.* [108] have argued that α boron has higher thermodynamic stability at ambient conditions: this was based on the interpolation of their HPHT experiments to ambient conditions. In all of these cases, there is consensus that β boron is the most stable solid phase beyond 1500K for all pressures ranging from ambient to 5 GPa.

However, in the experiments done in this work, it is found that α boron forms even at temperatures as high as 2073 K at the cost of β boron under a pressure of 5 GPa. Moreover, no metal catalyst such as Pt, Pd or Au is required for this phase transition from β rhombohedral boron to α rhombohedral boron. It is also worthwhile to note here that the phase diagrams present in the literature only concern themselves with phase changes of pure elemental boron under HPHT conditions with the presence of only metal catalysts in some cases. They do not take into account the effect of carbon on the stable boron phase, which is the case in the current work.

This leads us to question of the role of carbon in the α boron synthesis in the experiments done in the current work. Carbon has the potential to play a variety of roles - it can stabilise the atomic structure of the α boron, or act as a catalyst. This question has also been discussed qualitatively in the current chapter.

The work discussed in this chapter has led to the submission of a patent : " Préparation du bore α rhomboédrique en présence d'une source de carbone". A more detailed picture

has been given in the patent document, which cannot be disclosed here since it remains under measures of confidentiality.

7.2 Structure and properties of α rhombohedral boron

α rhombohedral boron has the simplest structure of the known boron phases. The elemental crystallographic unit cell of this phase has the $R\,\bar{3}m$ space group and contains 12 atoms per unit cell. The icosahedral B_{12} units are located in the corners of a primitive rhombohedral unit cell, which is shown in figure 7.1. It is not very dissimilar to the crystal structure of boron carbide $(B_{11}C)$C-B-C, with the exception of the carbon atom in the icosahedron, and the C-B-C chains: the difference between the structures of boron carbide, α boron and β boron is shown in figure 7.2.

In calculations, α boron has been shown to undergo phase transitions under pressure at 0 K, such as the nonmetal-to-metal transition in α rhombohedral boron at 160 GPa [160] or a structural transition from the α rhombohedral to the body-centered-tetragonal phase at 270 GPa [161].

The Vickers hardness of α boron is as high as 42 GPa [163], while the density is estimated to be 2.460 g/cm^3.

Experimentally, α boron has a band gap of 2 eV [164], and consequently, appears to have a characteristic red colour. However, it can also appear yellowish [110] or black [164,165]. This can be the result of indirect interband transition at 300 K through indirect bandgaps of 0.73 eV, 1.49 eV, 1.63 eV and 2.055 eV.

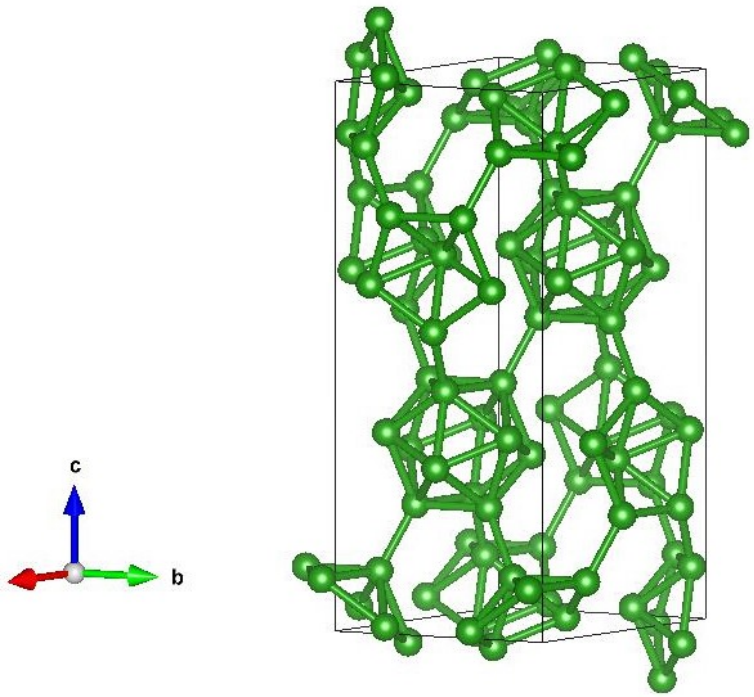

Figure 7.1: Unit cell of α rhombohedral boron, given in the rhombohedral setting, visualised through VESTA [162].

The direct bang gap of $\sim$ 2 eV also gives α boron semiconducting properties, unlike the disordered β boron structure [160]. This, coupled with boron's natural richness of the B^{10} isotope that reacts with neutrons, can result in applications such as solid state neutron counters in the nuclear industry. This has been illustrated in the US Patent US20150060680A1 [166].

Boron phases are also resilient to radiation damage. The damage under irradiation [167] of crystals containing B_{12} icosahedra, such as β boron or α boron, is much less severe than in other materials with a cubic crystal structure such as silicon - or with a hexagonal crystal structure - such as gallium nitride or boron nitride. The atoms of the icosahedra,

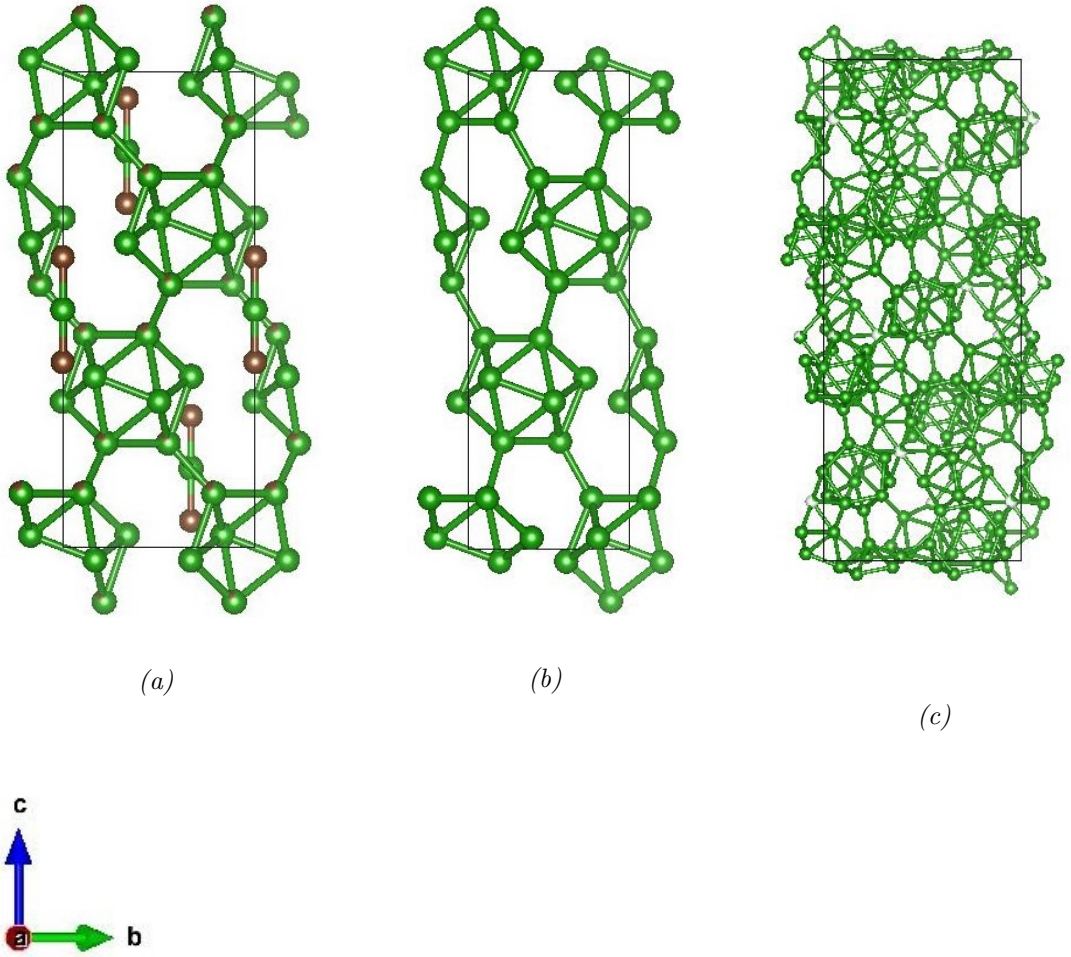

Figure 7.2: Unit cell of (a) boron carbide, (b) α rhombohedral boron, and (c) β rhombohedral boron, given in the rhombohedral setting, visualised through VESTA [162]. The green balls represent the boron atoms, while the red balls represent carbon atoms. The β boron unit cell is very densely packed with 105 atoms/unit cell, while the α boron and boron carbide unit cells are very similar, with the exception of the C-B-C chains, and the polar carbon atom. In case of boron carbide, $\frac{1}{6}$ of the polar atoms of the icosahedra are red, since one of the six polar atoms can be carbon in each icosahedron.

displaced by irradiation, return to their initial position by a self-healing mechanism [168–170]. α boron combines the described irradiation resistance with semi-conducting electronic properties, making it suitable for space applications.

7.3 Experimental Results

The method of synthesis of α rhombohedral boron under HPHT conditions without a metal catalyst has been described in Chapter 2. Sec 2.2 of Chapter 2 describes in detail the experimental parameters of the formation of α boron from mixtures of β rhombohedral boron and amorphous carbon, as well as amorphous boron and amorphous carbon at 5 GPa. Figure 7.3 shows the X-ray diffraction pattern of quenched sample from a mixture of crystalline β boron and amorphous carbon under 5 GPa for 2 hours. α rhombohedral boron is the most prominent phase from 1473 K to 2073 K. This is corroborated by the Raman spectroscopy pattern shown in figure 2.4 of Chapter 2. X-ray diffraction also establishes the formation of α boron from a starting mixture of amorphous boron and amorphous carbon in figure 2.8. The α boron formed when the mixture of β boron and amorphous carbon was subjected to a pressure of 5 GPa and a temperature of 1473 K and then quenched was characterised by optical microscopy which establishes its dark red colour, as shown in figure 7.4. The size of the polycrystalline particles formed during the synthesis was determined to be between 100 - 250 micrometers through optical microscopy.

However, it is important to note here that α boron formation was not observed at the

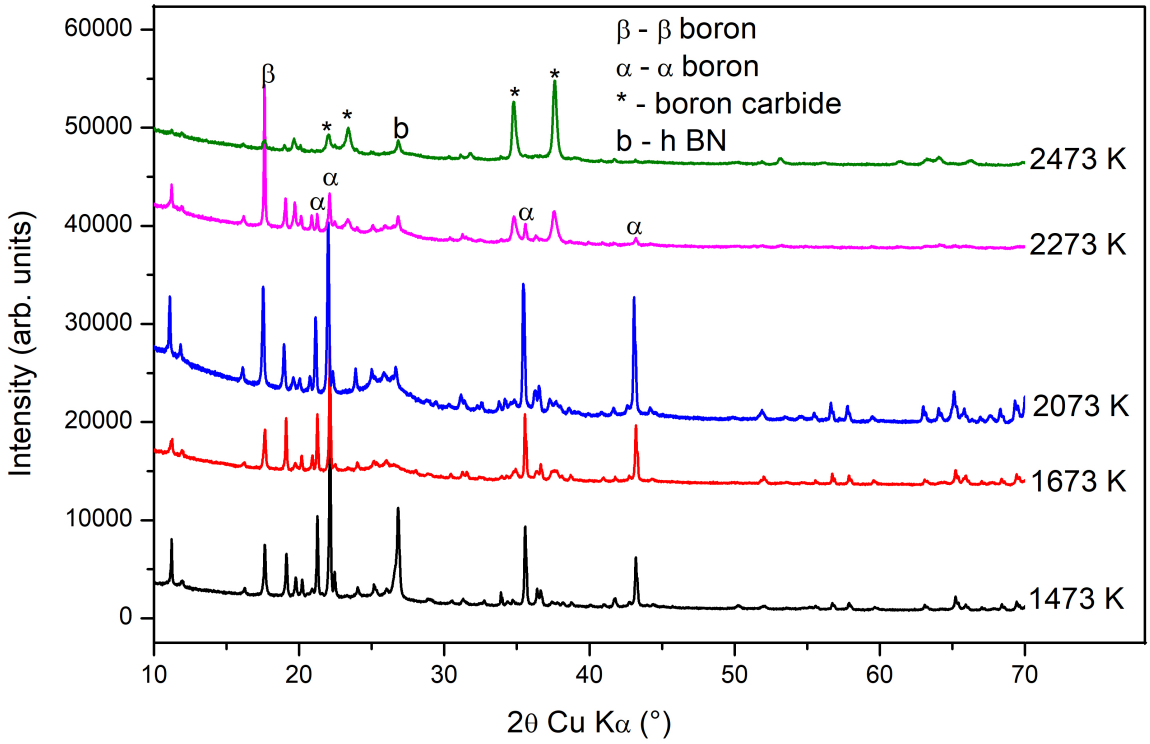

Figure 7.3: ex situ X-ray diffraction pattern of quenched sample from a mixture of crystalline β boron (COD ID : 901110 33 [107]) and amorphous carbon under 5 GPa for 2 hours. Since β boron (COD ID : 901110 33) has numerous peaks, only the most prominent ones have been marked – all the unmarked peaks are those of β boron. α boron (COD ID : 9008561) is the most prominent phase till 2073 K.

lower pressure of 2 GPa with any of the different reactant mixtures, as seen in figure 2.1 for β boron and amorphous carbon, figure 2.7 for amorphous boron and amorphous carbon and figure 2.5 for β boron and graphite.

Furthermore, when graphite is used in the reactant mixture, α boron does not form at

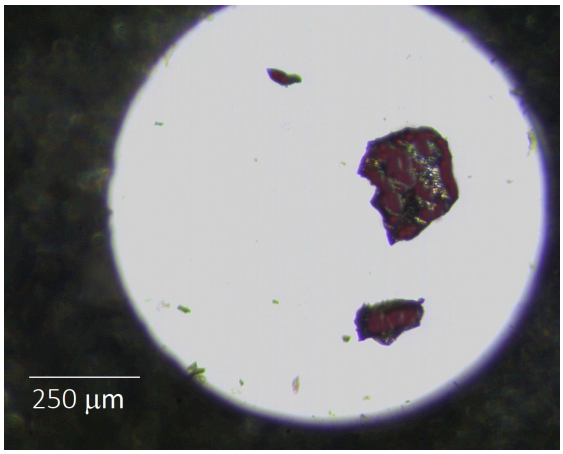

Figure 7.4: The polycrystalline particles of α rhombohedral boron, formed from the HPHT treatment (5 GPa, 1473 K) of a quenched mixture of crystalline β boron and amorphous carbon, as viewed under an optical microscope.

any pressure value, as seen in figures 2.5, 2.6.

A series of experiments were next performed on only crystalline β boron at various temperatures (1473 $\pm$ 20 K, 1673 $\pm$ 20 K, 2073 $\pm$ 20 K, 2273 $\pm$ 20 K, 2473 $\pm$ 20 K) under a pressure of 5 $\pm$ 0.2 GPa in the Paris-Edinburgh press, following the same methodology as in Sec 2.2. This was to ensure that the amorphous carbon present in the reactant mixture indeed had a role in the formation of α boron. The first experiment in the series consisted of subjecting β boron to a pressure of 5 GPa and a temperature of 1473 K for 2 hours. The quenched sample was then characterised through XRD and Raman spectroscopy. Figures 7.5 and 7.6 compare the XRD diffractogram and Raman spectroscopy of this quenched sample to β boron at ambient conditions that has not been subjected to HPHT treatment respectively.

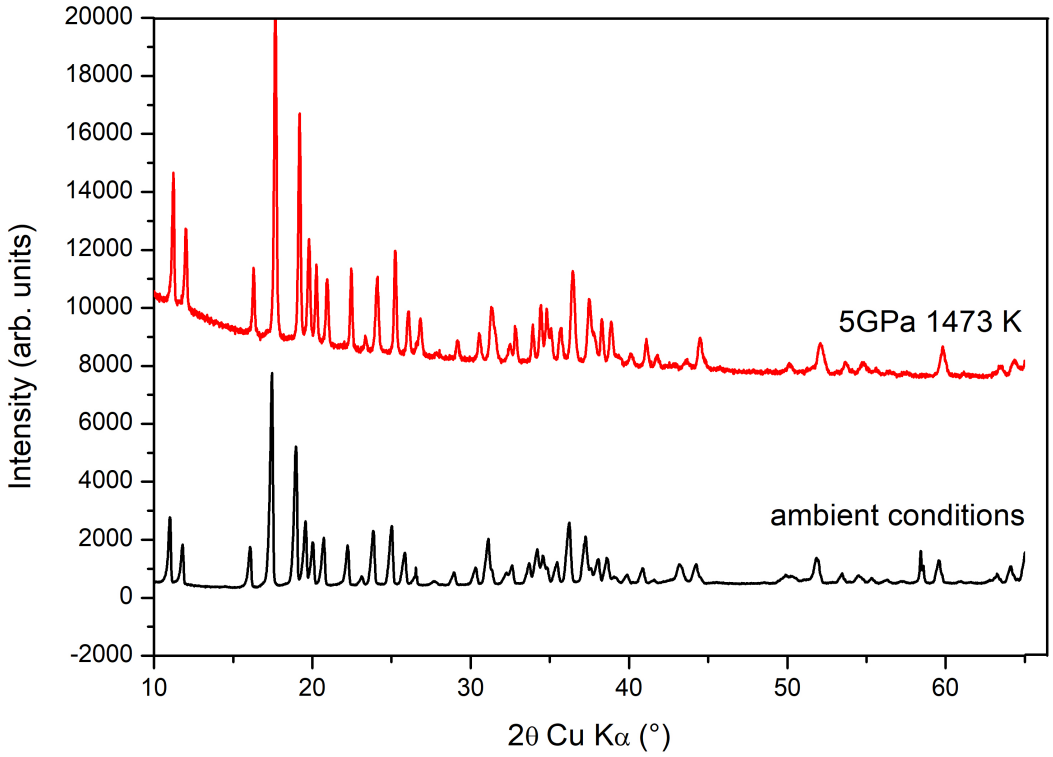

Figure 7.5: ex situ X-ray diffraction pattern of quenched sample of crystalline β boron (COD ID : 901110 33 [107]) subjected to 1473 K under 5 GPa for 2 hours in comparison with that of β boron not subjected to HPHT treatment. All the unmarked peaks are those of β boron (COD ID : 901110 33).

The XRD pattern of the HPHT treated sample has shown no changes. The Raman spectroscopy of the HPHT treated sample however shows sharper and more well-defined peaks. This is expected due to recrystallisation of β boron under HPHT conditions. The Raman spectrum of this recrystallised sample is characterised by much sharper Raman peaks. However, α boron does not form when β boron is heated to 1473 K under 5 GPa,

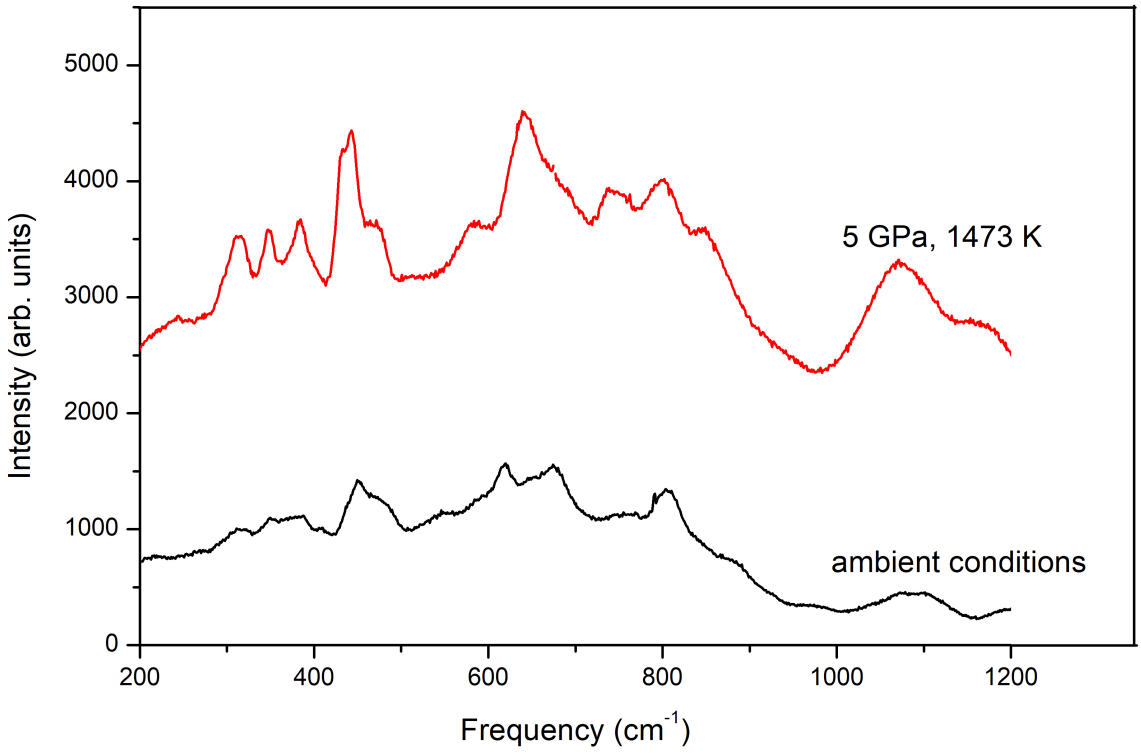

Figure 7.6: ex situ Raman spectroscopy of quenched sample of crystalline β boron subjected to 1473 K under 5 GPa for 2 hours in comparison with that of β boron not subjected to HPHT treatment. All the unmarked peaks are those of β boron.

unlike the result when amorphous carbon is added alongside β boron and subjected to the same HPHT treatment. This is demonstrated by comparisons between the XRD patterns and Raman spectroscopy of the two quenched samples in figures 7.7 and 7.8 respectively.

The reactant β boron subjected to HPHT conditions above 1673 K were very hard and well-sintered, and therefore, they could not be ground into a fine powder in or-

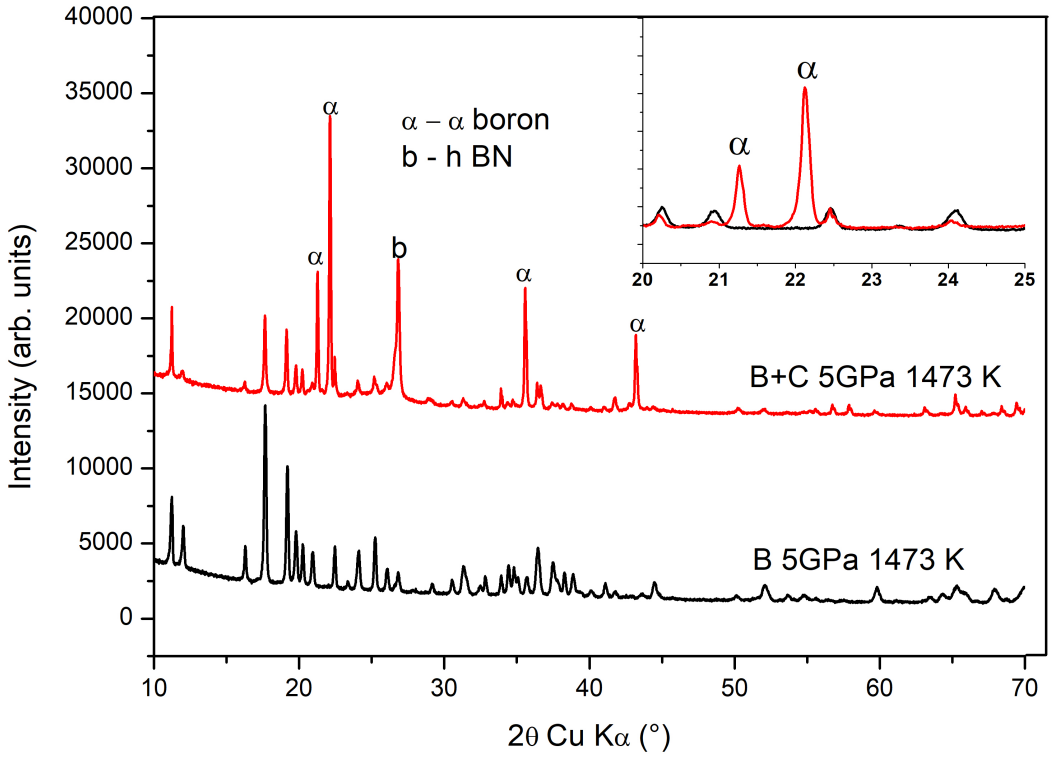

Figure 7.7: ex situ X-ray diffraction pattern of quenched sample of a mixture of crystalline β boron and amorphous carbon subjected to 1473 K under 5 GPa for 2 hours in comparison with that of a quenched sample of β boron subjected to the same HPHT treatment. All the unmarked peaks are those of β boron (COD ID : 901110 33 [107]). α boron (COD ID : 9008561 [171]) forms in the quenched sample of the mixture of β boron and amorphous carbon, unlike in the case of only β boron.

der to perform powder XRD using the set-up with the copper anode. They were instead put inside a capillary and subjected to XRD using a set-up which has Mo anode ($\lambda_{MoK\$\alpha}1 = 0.70931\mathring{A}$), $asseeninFigure$ 7.9.α boron has not formed in any of these quenched samples, in the absence of amorphous carbon. Raman spectroscopy could not

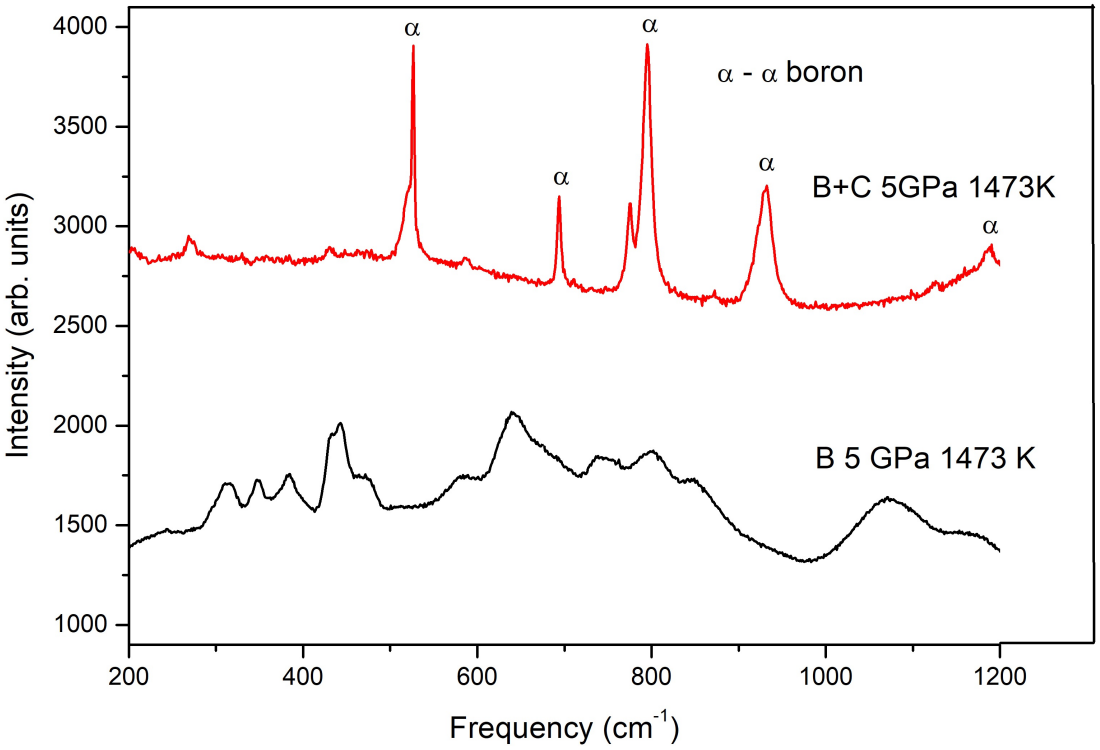

Figure 7.8: ex situ Raman spectroscopy of quenched sample of a mixture of crystalline β boron and amorphous carbon subjected to 1473 K under 5 GPa for 2 hours in comparison with that of a quenched sample of β boron subjected to the same HPHT treatment. All the unmarked peaks are those of β boron. α boron forms in the quenched sample of the mixture of β boron and amorphous carbon, unlike in the case of only β boron.

be performed on these hard sintered samples since the Raman spectroscopy arrangement in IMPMC requires the sample to be vertically placed on a glass slide, and these samples were too heavy to attach to a glass surface through adhesive force.

From the results shown in this chapter, it is clear that carbon plays a role in the formation

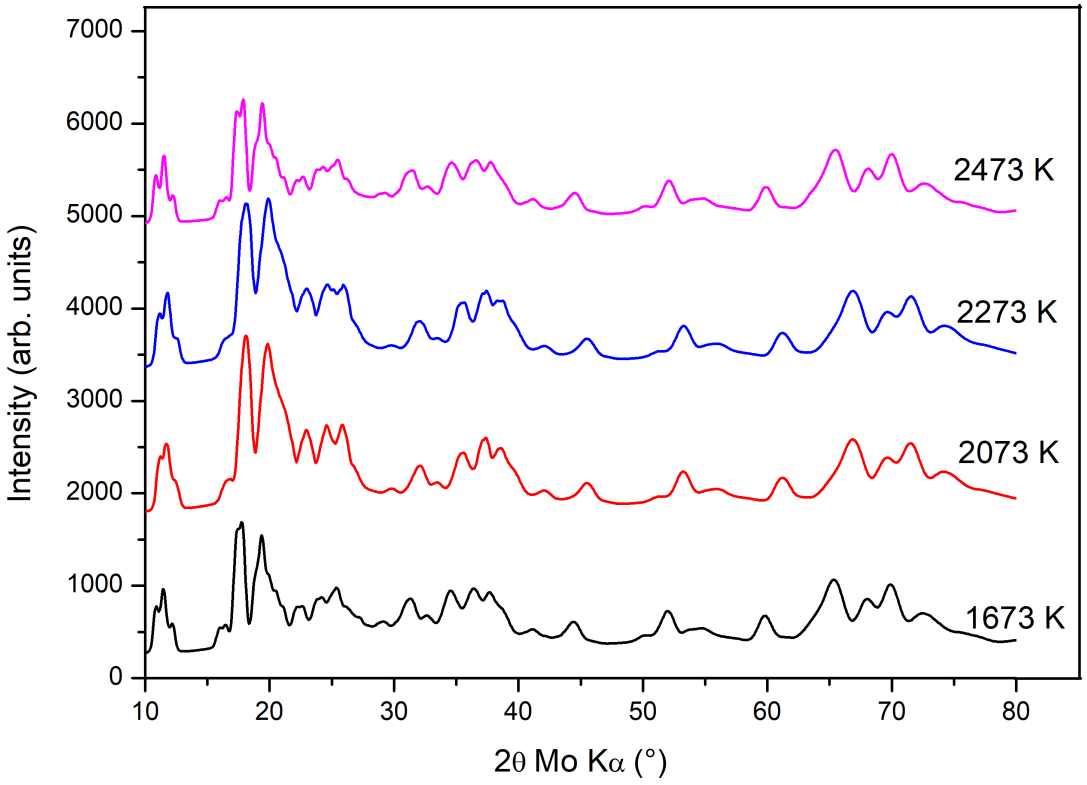

Figure 7.9: ex situ X-ray diffraction pattern of quenched samples of crystalline β boron (COD ID : 901110 33 [107]) subjected to various temperatures under 5 GPa for 2 hours. All the peaks are those of β boron (COD ID : 901110 33).

of α boron from the reactant β boron, since the syntheses under HPHT conditions with only β boron showed no phase change.

7.4 Theoretical results

Theoretical calculations were performed by Yeonsoo Cho and Nathalie Vast [172] in tandem with experimental work described in this chapter following an 'as close as Covid 19 would allow' relationship.

The study aimed at investigating the relationship between the atomic structure of α rhombohedral boron (α-B_{12}) and that of boron carbide by inserting carbon impurities into α-B_{12}, and looking at the modifications of the physical properties from two viewpoints: the formation energy, and the optical properties. Thereby, one aims to understand the role of carbon in the formation of α boron as well as the manner in which carbon is inserted into the structure to form boron carbide.

The study was done in three steps. In the first step, the band structure of pristine α boron was studied using density functional theory going beyond standard exchange and correlational functionals. For this purpose, the HSE06 hybrid functional was used to calculate the band structures - it is a hybrid functional designed by Heyd, Scuseria, and Ernzerhof [173] in order to modify the calculation in long-range part of the exchange integrals and exchange potential. It aims at reproducing the band gap of semiconductors and insulators faithfully.

In the second step, various impurities have been introduced in the structure of α boron, as substitutional atoms, eventually combined with a vacancy (V), or as interstitials, in the positions favouring the formation of boron carbide: in the chain-centre position and

in the chain end positions. These atomic positions have also been found to favour the insertion of lithium in α-B_{12} [174, 175]. The formation energy has been computed with and without relaxing the volume and shape of the unit cell. Thermodynamically stable impurities have been found, as well as those which barely induce a volume change.

In the third step, the band structure modification has been studied for impurities which barely induce a volume change. This has involved a carbon atom in substitution of a boron atom of the icosahedron, either in polar or equatorial positions. Modifications induced in the band structure have been studied, looking for an eventual change of colour, as occurs for coloured centres of other insulators. The knowledge of such a colour change could facilitate the detection of carbon impurities in α boron crystals.

We want to stress some limitations of these calculations: the impurity was studied within the elemental unit cell, thus producing "impurity bands" rather than isolated defects. The study of isolated defect requires the use of supercells calculations containing hundreds of atom, which was beyond the scope of an internship [172].

7.4.1 Band gap calculations

The band gap of α boron has first been calculated using DFT-LDA and DFT-GGA-PW91 [139] to be 1.44 eV and 1.52 eV respectively, in good agreement with previous calculations, in which band gap values where found to be 1.46 eV [160], 1.54 eV [158] or 1.72 eV [161] at ambient pressure. However, since standard exchange and correlational functionals underestimate the band gap values, HSE06 was used to calculate a reliable value of the band gap. Thereby, the indirect band gap of α rhombohedral boron was

found to be 1.98 ± 0.02 eV, between the Z point and the Γ point of the Brillouin zone. The direct band gap was found to be at the Γ point and to be 2.37 ± 0.02 eV.

Experimentally, Horn has suggested a band gap of approximately 2.0 eV from optical experiments [164,176,177]. Consistently, in Ref. [164], the crystal has the characteristic red colour. The band gap was found to be 2.4 eV from electron energy loss experiments [178].

In conclusion, our result of a band gap of 1.98 ± 0.02 eV explains the dark red colour of α boron which was found in the experiments of the current chapter.

7.4.2 Formation energy of the carbon based impurities in the structure

Various kinds of impurities have been introduced in α-B_{12}, in the form of n_C carbon atoms. Boron atoms have also been introduced in three impurity sites to study their effect in the formation of boron carbide, B_4C, in which one boron atom is in the O_h octahedral interstitial position of the α-B_{12} structure.

The total energy E^{imp}_{total} and the formation energy E^{imp}_{form} have been computed in DFT-GGA (table 7.1) with the expression

$$E^{imp}_{form} = E^{imp}_{total} - \frac{n_B}{12} E^{\$\alpha}_{total}$$

-B_{12} − $\frac{n_C}{2} E^{diamond}_{total}$, (7.1)where the formation energy has been computed from α boron and diamond. Diamond is better represented in DFT-GGA than graphite, as the latter requires the inclusion of van der Waals interactions, which is beyond the scope of the

present study.

In the present study, two kinds of calculations have been performed. Firstly, the full relaxation of the volume and shape of the unit cell, and of the atomic positions in the unit cell, has been achieved to minimise the total energy and then the formation enthalpy has been computed. In this case, all of the results are at the pressure of 0 GPa. Secondly, the impurity has been introduced at the volume fixed by the equilibrium lattice parameters of α-B_{12}. Then, the enthalpic contribution at pressures of 2 GPa and 5 GPa has been estimated from the volume variation obtained at P=0 GPa between the unit cell containing the impurity and the unit cell of α boron (table 7.2).

Thermodynamically stable impurities

In the current section, I have given the thermodynamical results, i.e., those obtained with full relaxation of the volume and shape of the unit cell, and of the atomic positions in the unit cell.

• Stable carbon impurities

The formation energy turns out to be negative in two cases (table 7.1, lines 2 and 3), beside the case of boron carbide formation (first line). This means that the formations of both these impurities are favoured with respect to the segregation of the B+C mixture into α-B_{12} and elemental carbon.

The first stable impurity is when two carbons are in interstitial positions with the T_d tetrahedral symmetry (second line). We note that the formation energy of only one

carbon atom at such a position is positive (line 4).

The second stable impurity is favoured when, in addition to having two carbons in tetrahedral sites, a boron atom is substituted by a carbon atom in the polar site of the icosahedron (line 3). We note that the introduction of only one carbon atom in the tetrahedral site, combined with the boron substitution by a carbon atom in the icosahedron, is positive (line 6).

In conclusion, it is found that thermodynamically, α-B_{12} is stabilised by carbon diffusion to chain-end atomic positions; that the occupation of both chain end positions is mandatory; and that, then and only then, the boron substitution by carbon into the icosahedron is still favourable, with the boron atom going to the chain center, as in B_4C (line 1).

Atom(s)	Location	Type	Name		0 GPa	Fixed volume
3C+B	Mix	S + triple I	p+2T$_d$+O$_h$	B_4C ($B_{11}C^p$) C-B-C	-2.23	8.15
3C	Interico	double I	2T$_d$	(B_{12}) C...□...C	-1.01	8.12
2C	Mix	S+double I	p+2T$_d$	($B_{11}C^p$) C...□...C	-0.77	18.47
C	Interico	I	T$_d$	(B_{12}) □...□...C	0.72	**3.26**
	Ico	S	p	($B_{11}C^p$)	1.41	**1.99**
2C	Ico	S+I	p+T$_d$	($B_{11}C^p$) □...□...C	1.73	9.61
C+V	Ico	S+V	p+□	($B_{10}C^p$□)	1.89	**3.18**
C+B	Mix	S+I	p+ O$_h$	($B_{11}C^p$) □...B...□	2.48	8.14
C	Ico	S	e	($B_{11}C^e$)	2.69	**3.11**
C+V	Ico	S+V	e+□	($B_{10}C^e$□)	2.73	4.56
C+2V	Ico	S+double V	p+2□	(B_9C^p□$_2$)	3.88	5.37
			e+2□	(B_9C^e□$_2$)	4.97	6.38
B	Interico	I	O$_h$	(B_{12}) □...B...□	7.48	7.76

Table 7.1: Theoretical formation energy (eV/impurity) of various kinds of impurities in α boron, at 0 GPa, and at the volume fixed by the thermodynamical equilibrium of α boron ($R\bar{3}m$ symmetry, a=5.054 Å, α=58.13 deg*, DFT-GGA-PW91) by order of decreasing stability at P=0 GPa. The lowest formation energy values at fixed volume are reported in bold font. Boron carbide (first line) is given for reference. With respect to α-B_{12}, it contains one carbon atom in substitution (S) in the polar site of the icosahedron (Ico),and three intersititial (I) atoms that form the C-B-C chain in the intericosahedral (Interico) space: 2 carbon atoms in the tetrahedral-symmetry T_d intericosahedral site and one boron atom in the octahedral symmetry O_h site. 'Mix' stands for an impurity containing both S and I. 'V' stands for a vacancy and is symbolically represented by the square. Calculations in DFT-GGA-PW91.*

• Carbon in the icosahedron

The total energy is considerably lower in the case when a carbon atom is substituted for a polar boron atom ($B_{11}C^p$) of the icosahedron (line 5), than that in the case for an equatorial boron atom ($B_{11}C^e$) (line 9). The latter case gives a bigger formation energy: 3.11 eV for $B_{11}C^e$ with no relaxation (not shown [172]), and 2.69 eV when full relaxation of the unit cell is accounted for, as shown in table 7.1. The formation energy is around 1.3 eV higher than the formation energy of the $B_{11}C^p$ impurity.

• Insertion of a carbon-vacancy center (CV and CV_2)

Replacing a polar boron atom with a carbon atom and placing a vacancy in the antipodal site shows the biggest formation energy (not shown [172]). This implies that the CV center is more likely to be in the form of a carbon atom in the polar position with a neighboring vacancy site (line 7).

On the other hand, when a carbon atom is situated in an equatorial site, the vacancy is rarely located in the neighbouring polar site, or in an antipodal equatorial site (not shown [172]). The vacancy would rather be in another equatorial site, especially one of the first neighboring ones (line 10).

In general, the formation energy is estimated to be much higher in $B_{10}C$ than in $B_{11}C$, which makes the CV_2 center less likely to be formed (lines 11-12).

• Role of the boron atom

The introduction of an additional boron atom into the α boron structure is unlikely both

in the presence of a $B_{11}C^p$ or B_{12} icosahedron (table 7.1, resp. line 8 and last line). It however stabilises the ($B_{11}C^p$) C...□... C structure (line 3) to form boron carbide (line 1). The introduction of a boron atom at the chain center is the last insertion step to achieve the thermodynamical stability of boron carbide.

Atom(s)	Location	Type	Name		ΔV (Å^3/imp.)	2 GPa (eV/imp)	5 GPa
3C+B	Mix	S + triple I	p+2T$_d$+O$_h$	B$_4$C ($B_{11}C^p$) C-B-C	22.5	0.28	0.70
3C	Interico	double I	2T$_d$	(B_{12}) C...□...C	22.3	0.28	0.69
2C	Mix	S+double I	p+2T$_d$	($B_{11}C^p$) C...□...C	18.1	0.23	0.57
C	Interico	I	T$_d$	(B_{12}) □...□...C	15.8	0.20	0.49
	Ico	S	p	($B_{11}C^p$)	$\approx$ 0	$\approx$ 0	$\approx$ 0
2C	Ico	S+I	p+T$_d$	($B_{11}C^p$) □...□...C	12.7	0.16	0.40
C+V	Ico	S+V	p+□	($B_{10}C^p$□)	-4.0	**-0.05**	**-0.12**
C+B	Mix	S+I	p+ O$_h$	($B_{11}C^p$) □...B...□	18.1	0.23	0.57
C	Ico	S	e	($B_{11}C^e$)	1.9	0.02	0.05
C+V	Ico	S+V	e+□	($B_{10}C^e$□)	-5.2	**-0.07**	**-0.16**
C+2V	Ico	S+double V	p+2□	(B_9C^p□$_2$)	-4.3	**-0.05**	**-0.13**
			e+2□	(B_9C^e□$_2$)	-3.8	**-0.05**	**-0.12**
B	Interico	I	O$_h$	(B_{12}) □...B...□	4.7	0.06	0.15

Table 7.2: Theoretical volume change ΔV (Å^3/impurity) of various kinds of impurities in α boron at 0 GPa. Impurities are given by order of decreasing stability at P=0 GPa, and symbols are as in table 7.1. The enthalpic contribution (eV/impurity) has been estimated from $P\Delta V$ with P=2 GPa and P=5 GPa. Negative enthalpic contributions are given in bold font. The volume variation is quasi zero for ($B_{11}C^p$) (line 5).

7.4.3 Formation of impurities at the fixed volume of α boron

The thermodynamically stable impurities studied in the previous paragraph induce large volume changes, because the insertion of carbon atoms in tetrahedrally symmetric sites implies large relaxations (table 7.2, lines 1-3). The lattice requires some time to accommodate such large volume changes. This may provide a disadvantage in the kinetic competition between the formation of α boron and the formation of boron carbide.

In contrast, the formation of some of the other impurities either do not induce any volume change, such as $(B_{11}C^p)$ (line 5), or provoke only moderate ones, of the order of a few $Å^3$/impurity (lines 7, 9-13). We note that a volume change magnitude of the order of $Å^3$ is nonetheless expected to be able to destabilize the crystal if the impurities are present in large number. Most of these impurities involve a boron substitution in the icosahedron, eventually combined with a vacancy or more than one vacancies, forming CV or CV_2 centers (line 7, 9-12). They have all positive formation energies and their formations require external energy (table 7.1).

Interestingly, $(B_{11}C^p)$, which implies a boron substitution by a carbon atom in the polar site of the icosahedron, has a formation energy typical of an impurity formation in other semiconductors (1.99 eV before relaxation, and 1.41 eV after relaxation, see line 5 of table 7.1). It induces/requires no volume change of the unit-cell of α boron. It has the lowest formation energy among impurities which induce small volume modifications. For this reason, it could be the first step in the formation of boron carbide in non thermodynamical conditions. The modifications of the band structure brought in by

substitutional carbon is studied in the next section.

The boron substitution by a carbon atom in the equatorial site (line 9) and the formation of a CV center (line 7) come second in low formation energies and they do not require a large volume change either. These two impurities have similar formation energy before relaxation (3.1±0.1 eV), the relaxation favouring the CV center.

Finally, the introduction of a boron atom at the O_h interstitial position (chain centre, last line) does not imply a large change of volume either. However the formation energy is much larger (7.76 eV before relaxation, and 7.48 eV after relaxation).

In conclusion, the carbon diffusion at chain-end atomic positions implies a large volume change which requires some relaxation time so that the lattice can adapt. If some energy is available, the boron substitution in the icosahedron occurs without volume change, and carbon impurities are introduced in the icosahedron at moderate energy cost.

7.4.4 Effect of pressure

A rough estimation of the effect of pressure is reported in table 7.2 for 2 GPa and 5 GPa. A complete calculation would require the estimation of the volume change induced by an impurity at those pressure. Here the volume change at 0 GPa has been considered to have the main effect.

It is seen that, as expected from the previous discussions, pressure tends to increase the formation energy of impurities in chain-like tetrahedral positions, while the boron substitution by carbon in the icosahedron is quasi-insensitive to pressure.

7.4.5 Band gap modifications by a carbon impurity

• Details of the calculations

The study of the band gap modification has been performed at fixed unit cell volume and shape. We have seen that for a carbon substitution in the polar site, the volume change with respect to α boron is quasi zero. The GGA equilibrium lattice parameters have been used for the GGA calculations (a=5.054 Å, α=58.13 deg). The HSE06 equilibrium lattice parameters have been obtained for a 1x1x1 **q** point mesh, i.e., the exact exchange contribution has been computed with a mesh as dense as the **k**-point mesh. This results in a slightly smaller unit cell volume than in GGA (a_{HSE06}=5.032 Å, α_{HSE06}=57.92 deg). The effect of the lattice parameters on the GGA or HSE06 band structures turn out to be small.

The band gap GGA calculations have been performed with a 8x8x8 **k**-point mesh centered at Γ. The HSE06 iband gaps have been computed with a 8x8x8 **k**-point mesh centered at Γ and a 8x8x8 **q** point mesh, ensuring full convergence of the calculations [172].

The band gap was calculated with, for instance, a C atom instead of one boron atom in the unit cell of α-B_{12}. This makes, for instance, the compound $B_{11}C$ and, in principle, lowers the crystal symmetry from rhombohedral to monoclinic. In the following, the results were interpreted keeping the average rhombohedral symmetry. Additionally, as a carbon atom replaces a boron atom, the extra valence electron contributes to the metallicity of $B_{11}C$. We thus need to treat the impurity-containing cells as metals, as

impurities have been considered in the neutral charge-state only.

A limitation of the present calculations is the study of the impurity within the elemental unit cell instead of a supercell. If dangling bonds were present (which is not the case for the impurities studied of this section), energy levels would be generated inside the band gap, and these energy level would show a dispersion, i.e. the energy level would vary at different **k** points in the Brillouin zone. For an isolated defect, the energy level should be non dispersive, as expected from a localized defect state. Thus, our calculations produce "impurity bands" rather than isolated defects. The study of an isolated defect requires the use of supercells calculations containing hundreds of atoms, which would be needed for most of the impurities of table 7.1. However, the impurity band picture suffices to qualitatively study the changes brought in the band structure by the introduction of carbon atoms because no dangling bonds are generated in this case.

• Carbon impurity substituting a boron atom of the icosahedron

Unlike in the band structures of α-B_{12}, the indirect gap values are defined by the conduction bottom (C.B.) at the F point (instead of the Γ point in α-B_{12}) and the valence top (V.T.) at the Z point for $B_{11}C$, both in GGA and HSE06. For $B_{11}C^p$, the $Z \rightarrow F$ band gap value, 1.30 eV, is quasi degenerate with the $Z \rightarrow \Gamma$ bandgap value, 1.35 eV, within the accuracy of our calculations. HSE06 however lifts the degeneracy, leading to values of 1.53 eV for the $Z \rightarrow F$ band gap and 1.72 eV for the $Z \rightarrow \Gamma$ energy difference.

In GGA, the value of the indirect band gap is decreased from 1.52 eV in α-B_{12} to 1.30 eV or 1.35 eV (resp. 1.39 eV) upon carbon substitution in the polar (resp. equatorial) site

of the icosahedron. In HSE06, the value of the indirect band gap is decreased from 1.98 eV in α-B_{12} to 1.53 eV (resp. 1.62 eV) upon carbon substitution in the polar (resp. equatorial) site of the icosahedron. Thus the location of the carbon substitution has a moderate effect (90 to 92 meV) on the value of the indirect band gap.

In wide contrast, the location of the carbon substitution modifies the position of the bottom of the conduction band at Γ and thus, is expected to have an effect as large as 278 meV on the value of the direct band gap: the latter is defined at the Γ point in GGA, and was 1.87 eV in α-B_{12}. This value is decreased to 1.76 eV in the case of the polar boron substitution by carbon ($B_{11}C^p$) and is increased to 2.03 eV in the case of the equatorial boron atom substitution ($B_{11}C^e$). In HSE06, the values of the direct band gap are and 2.18 eV and 2.66 eV in case of, respectively, polar or equatorial substitution, which is to be compared to the value of 2.37 eV for pristine α boron. Thus the location of the carbon substitution has an effect of 481 meV in HSE06 and 278 meV in GGA.

Experimentally, α boron appears as red. This means that it absorbs green to violet photons. Then the band gap should be between 720 nm and 630 nm i.e., between 1.722 eV and 1.968 eV. One sees that carbon insertion in α boron should decrease the band gap enough so that the red color is lost during the synthesis. Therefore, in all probability, no carbon is inserted into the synthesised α boron.

7.5 Discussions

Since it is established that carbon plays a role in the formation of α boron from β boron at 5 GPa and temperatures up to 2273 K, I first set out to verify whether there is carbon impurities in the structure of the reactant β boron or the α boron that is formed. This is difficult to achieve experimentally, since carbon and boron are both light materials with atomic numbers close to one another. Calculations, as discussed in Sec 7.4, is useful in predicting the thermodynamic stability of such carbon doped structures.

I have attempted to deduce whether carbon has been incorporated in the structure by looking at the changes in the lattice parameters of the quenched β boron and α boron at various temperatures of synthesis. This has been done through Rietveld refinement [179] of the X-ray diffractograms using FullProf program [180] and the results have been tabulated in table 7.3.

Material	Synthesis temperature	Lattice parameters		
		a	b	c
α boron	starting parameters	4.908	4.908	12.567
	1473 K.	4. 904	4.904	12.553
	1673 K	4.907	4.907	12.563
	2073 K	4.908	4.908	12.564
β boron	starting parameters	10.9251	10.9251	23.8143
	1473 K	10.9446	10.9446	23.8056
	1673 K	10.9621	10.9621	23.8190
	2073 K	10.9713	10.9713	23.7955

Table 7.3: Lattice parameters of α and β boron obtained through Rietveld analysis of the XRD diffractograms. The a and b lattice parameters of β boron shows an increasing trend with synthesis temperature, which can be due to the inclusion of carbon atoms impurity in interstitial positions.

Taking the significant value up to 2 places after the decimal, the lattice parameters a and b of the β boron rhombohedral structure appears to increase consistently with increase of synthesis temperature, suggesting that there might be some carbon inclusion in interstitial sites. However, α boron does not show this trend of increasing lattice parameters with the temperature of synthesis.

It is also important to note that at 2 GPa of synthesis pressure, there is no formation of α boron, and boron carbide forms at a lower temperature of synthesis consistently,

whereas, at 5 GPa of synthesis pressure, α boron is formed, and boron carbide forms at a higher temperature of synthesis at the expense of α boron. From this, it is inferred that there is a kinetic competition between the formation of α boron and that of boron carbide. Figure 7.10 is a qualitative representation of the kinetic competition at play under 5 GPa of synthesis pressure.

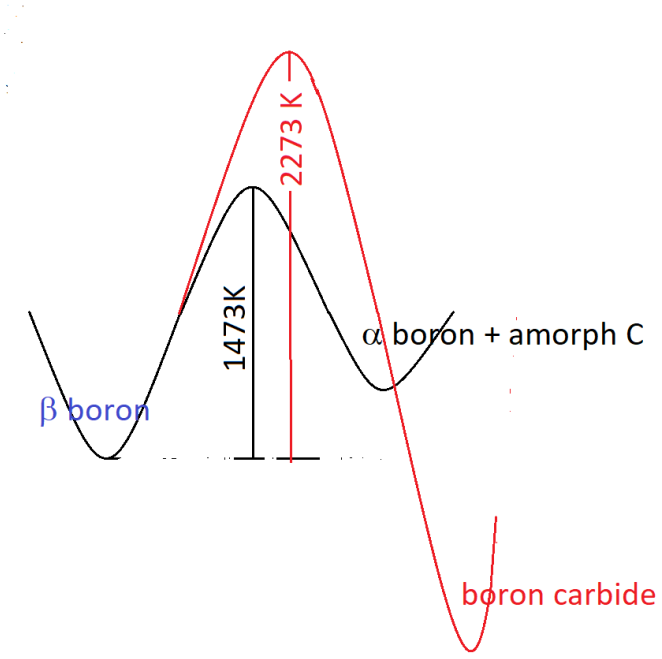

Figure 7.10: Qualitative representation of the kinetic barriers at play between the synthesis of α boron and boron carbide from a starting mixture of β boron and carbon under 5 GPa of synthesis pressure.

The formation of α boron from the mixture of β boron and amorphous carbon requires an activation energy of 1473 K under a pressure of 5 GPa. Wade's counting rule shows that the B_{12} icosahedron of α boron is electron deficient. However, carbon, in this case,

can act as an electron donor, thus stabilising the α boron structure. This is observed when noble metals such as Pt or Au are used as catalysts as well - they donate electrons to stabilise the metastable α boron structure.

The pressure plays a defining role in stabilising α boron as well. For an electron to pass from the donating orbital to the accepting orbital, the molecules must be brought close together by conventional forces in order to facilitate the overlap of the orbitals [181]. Applying a certain threshold of pressure (5 GPa in this case) can thus bring the molecules close enough for electron donation to take place, thus stabilising the otherwise metastable phase of α boron.

At 2273 K, the kinetic barrier for producing boron carbide is attained, which is also thermodynamically more stable than the initial reactant mixture of β boron and amorphous carbon. Here, carbon enters into the boron structure and starts forming boron carbide.

7.6 Conclusions

This chapter highlights the formation of an intermediate α boron phase from a reactant mixture of β boron and amorphous carbon (or amorphous boron and amorphous carbon) under a pressure of 5 GPa within a temperature range of 1473 K - 2273 K in the Paris-Edinburgh press.

Various parameters such as pressure, temperature and reactant mixture affecting the synthesis of the α boron phase has been discussed. It has also been established that

β boron does not form α boron on its own under the same temperature and pressure conditions without the addition of amorphous carbon - amorphous carbon thus plays a vital role in this α boron synthesis.

The role of amorphous carbon as an electron donor to stabilise the α boron structure has been discussed qualitatively. Therefore, α boron is considered to be an intermediate phase before amorphous carbon enters into the structure to form boron carbide above a certain temperature.

Some carbon might also enter the α boron structure as impurities but this has been shown to be energetically unfavourable, except in the case of some interstitial positions. However, this would lead to large volume change, which would not be favourable kinetically. Moreover, the insertion of carbon in the α boron structure could also not be determined as all of the fingerprints of α boron (XRD, Raman spectra and the characteristic red colour) are not modified enough to establish carbon insertion.

Finally, this novel method of α boron synthesis using inexpensive precursors and industrially attainable pressure and temperature values have resulted in the deposition of a patent - this can have a wide variety of uses ranging from nuclear to space applications.

Conclusions and Perspectives

Conclusions

In this work, several ways to reinforce boron carbide was explored. In the beginning of the thesis, three objectives were defined as the guiding principles for this work. I will now outline the conclusions of this work based on these objectives.

1. **Experiments using torsion to study the formation of vacancies under non-hydrostatic conditions, which can explain the reasons behind the observed mechanical failure of the material.**

   This has been pursued in Chapter 5 using torsion generated in a Rotational tomography Paris-Edinburgh cell (RoToPEC). Raman and XRD signature of boron vacancies in the C-B-C chain was found: this establishes the formation of vacancies under non-hydrostatic conditions.

2. **Synthesis under High Pressure High Temperature (HPHT) conditions to find C-C chains that have been predicted theoretically to stabilise the boron carbon structure.**

Some preliminary evidence of formation of C-C chains have been found when commercial boron carbide was subjected to HPHT conditions using a diamond anvil cell with double-sided laser heating. At the same time, optimum synthesis parameters of pure boron carbide from its elements was investigated for the first time in HPHT conditions in the pressure range of 2 - 13 GPa. The synthesis temperature is observed to be affected by different parameters such as pressure of synthesis, reactant phases and temperature cycling. An intermediate phase of α rhombohedral phase was found, which resulted in the deposition of a patent.

3. **Synthesis of boron carbide with silicon under pressure to reinforce the bonds, and thus prevent mechanical failure.**

   Density functional theory (DFT) calculations were performed to verify the thermodynamic stability of a ternary phase of boron, carbon and silicon. The calculations predicted that substitution of silicon in the polar carbon position in the icosahedron is the most feasible thermodynamically at high pressures. However, silicon carbide formation need to be avoided for the formation of this ternary phase. Experimental attempts to synthesise this ternary phase also showed the need to avoid the formation of silicon carbide. Some silicon doping of boron carbide was achieved.

Perspectives

A number of experiments are foreseen in the near future that have been postponed due to the pandemic of Covid 19. The principal ones amongst them will take place in December 2020 during the beamtime allotted at the SOLEIL Synchrotron. The investigations that

have been planned for this beamtime would be achieved using the Paris-Edinburgh press and they are listed below.

- Investigation into the formation of C-C chains at 5 GPa using amorphous boron as a reactant, which simplifies the characterisation when compared to using crystalline β boron as reactant.
- Investigation of the effect of using SiB_6 as a reactant in order to avoid the synthesis of silicon carbide during the formation of a ternary phase of silicon, boron and carbon.
- Investigation of the effect of using rapid induction heating in order to avoid formation of silicon carbide during the formation of a ternary phase of silicon, boron and carbon.

Another experiment that has been planned in the near future consists of using single crystal boron carbide in diamond anvil cell using double sided laser heating: this would enable me to repeat the experiment in more hydrostatic conditions using NaCl as a pressure transmitting medium and find further experimental proof of the presence of C-C chains in boron carbide at this HPHT region. However, this experiment would be best suited to an *in situ* environment like ID 27 at ESRF, Grenoble where Raman spectroscopy and X-ray diffraction can be performed simultaneously at the precise zone that is heated by the laser. A proposal will be submitted for this experiment next year when the ID 27 will be open.

Further investigations into the formation of boron carbide from its elements at high

pressure (10 - 15 GPa) would also be interesting. Specially, the mechanism of formation of boron carbide beyond its melting point at a particular pressure has not been investigated in the literature before. The effects of thermal cycling on the boron carbide crystal structure could also be investigated using characterisation tools like transmission electron microscopy (TEM).

Résumé

Le carbure de bore est une céramique largement utilisée avec des applications allant des abrasifs à des fins de défense comme les armures de sécurité et les gilets pare-balles. Ces applications dépendent de ses propriétés mécaniques telles qu'une dureté élevée - la dureté Vickers est de 38 GPa, une densité spécifique aussi faible que 2,52 g/cc et une stabilité chimique élevée. Cependant il perd progressivement sa résistance mécanique face à des sollicitations dynamiques au-delà de sa limite élastique Hugoniot (HEL).

L'objectif de ce travail est d'explorer différentes manières de renforcer le carbure de bore en utilisant la synthèse à haute pression comme outil. À cette fin, différentes voies de renforcement ont été suivies au cours des trois dernières années.

Une presse à enclume rotative spéciale, la cellule de tomographie rotative Paris Edinburgh (RotoPEC), a été utilisée pour appliquer une contrainte de torsion au carbure de bore sous une pression de 5 GPa à température ambiante pour étudier les lacunes développées dans le carbure de bore, ce qui est une raison possible pour sa résistance décroissante au-delà de sa Limite Élastique Hugoniot (HEL).. Les dommages et défauts ponctuels ultérieurs ont été analysés à pression ambiante par microdiffraction des rayons X à dispersion d'énergie au synchrotron et par spectroscopie Raman, combinées à des calculs basé sur la théorie de la fonctionnelle de la densité (DFT). Nous montrons qu'en dehors des signaux dus à B_4C, de nouveaux pics apparaissent dans les deux méthodes de caractérisation. Les calculs DFT des structures atomiques et des fréquences de phonons nous permettent d'attribuer la plupart des nouveaux pics à des lacunes de bore dans les

chaînes intericosaédriques du carbure de bore. La conséquence drastique de la présence de telles lacunes de chaîne dans le carbure de bore conduit au régime plastique est la formation de nouvelles liaisons carbone-carbone dans les chaînes, un mécanisme que nous proposons afin d'expliquer la défaillance mécanique du carbure de bore sous un chargement dynamique au-delà de 20 GPa.

Des appareils à haute pression comme la presse Paris-Edimbourg, la presse multi-enclumes et la cellule à enclume diamant ont été utilisés pour synthétiser de nouvelles phases de carbure de bore. Il avait déjà été prédit que ces phases auraient amélioré la résistance mécanique grâce aux calculs de la théorie fonctionnelle de la densité. Dans le cadre de ces expériences, les paramètres de synthèse du carbure de bore dans des conditions de haute pression et haute température ont été optimisés et de nouvelles techniques de synthèse pour d'autres matériaux industriellement pertinents comme l'alpha-bore ont également été établies. À cette fin, des mélanges stœchiométriques de bore cristallin bêta rhomboédrique et de carbone vitreux amorphe ont été soumis à des températures allant de 1473 K à 2473 K à des pressions de 2 GPa, 5 GPa et 13 GPa. Des synthèses similaires ont été répétées pour le bore et le graphite cristallins, et le bore amorphe et le carbone amorphe. Lorsque la pression de synthèse augmente, la température de formation du carbure de bore augmente également. De plus, la température de réaction est affectée par le choix des réactifs ainsi que par le cyclage de température sous pression. Une formation intermédiaire d'alpha bore a été observée lors de la synthèse à haute pression et haute température (HPHT) de carbure de bore à partir de bore betarhomboédrique et de carbone amorphe à 5 GPa. La phase alpha-bore a été observée

jusqu'à des températures beaucoup plus élevées (jusqu'à 2073 K) que celles prédites par les diagrammes de phases du bore dans la littérature, et a finalement disparu avec la formation de carbure de bore. Ce travail suggère que la présence de carbone dans le mélange de réactifs pourrait avoir affecté la cinétique de la réaction, stabilisant ainsi l'alpha bore par rapport au bêta bore.

Une idée d'utiliser le silicium comme matériau de renforcement pour le carbure de bore a également été poursuivie. Des outils à haute pression ont été utilisés pour avancer vers la synthèse d'un nouveau composé ternaire de bore, de carbone et de silicium aux propriétés mécaniques améliorées. Pour synthétiser le nouveau matériau ternaire BC-Si, j'ai effectué des calculs théoriques de la théorie fonctionnelle de la densité (DFT) pour établir la structure BC-Si qui aurait l'enthalpie minimale par rapport aux différentes positions de l'atome de silicium dans la cellule unitaire, différents matériaux de départ et l'effet de la pression appliquée sur la stabilité de phase. J'ai suivi ces calculs avec des résultats prometteurs grâce à des synthèses élevées in situ et ex situ.

Appendix A

Application of Wade's rule

Kenneth Wade developed a set of rules in 1971 [182, 183] to understand the structural relationships between a wide range of substituted boranes, carboranes as well as other cluster compounds. The general methodology of these rules, known as Wade's rule or sometimes as Wade-Mingos rule, has been described below.

1. The total number of valence electrons in the structure has to be determined (3 for boron, 4 for carbon, 1 for hydrogen).

2. 2 electrons are to be subtracted for each B-H or C-H bond unit.

3. The remaining electrons is divided by 2 to get the number of skeletal electron pairs (SEP).

4. A cluster with n vertices (*i.e.* n boron atoms) and $n+1$ SEP has a *closo* structure.

5. A cluster with $n-1$ vertices (*i.e.* $n-1$ boron atoms) and $n+1$ SEP has a *nido*

structure.

6. A cluster with *n-2* vertices (*i.e. n-2* boron atoms) and *n+1* SEP has a *arachno* structure.

7. A cluster with *n-3* vertices (*i.e. n-3* boron atoms) and *n+1* SEP has a *hypho* structure.

8. A cluster with *n-4* vertices (*i.e. n-4* boron atoms) and *n+1* SEP has a *klado* structure.

9. If the number of boron atoms is larger than *n+1* SEP, the extra boron atoms occupy capping positions on triangular phases.

Thus, if a vertex atom is removed from the closo structure, one obtains the nido structure. Similarly, if a vertex atom is removed from the *nido* structure, one obtains the *arachno* structure and so on. This has been illustrated in figure A.2.

The summary of the structure of borane clusters with the general formula $B_nH_n{}^{x-}$ has been provided in table A.1.

This is illustrated with an example from the literature. Pentaborane (B_5H_9) is represented in figure. The structure of pentaborane could be found out in the following manner using Wade's rule.

1. Total number of valence electrons = $(5 \times Z_B + 9 \times Z_H) = (5 \times 3 + 9 \times 1) = 24$

2. Number of electrons for each B-H unit in the structure = $5 \times 2 = 10$

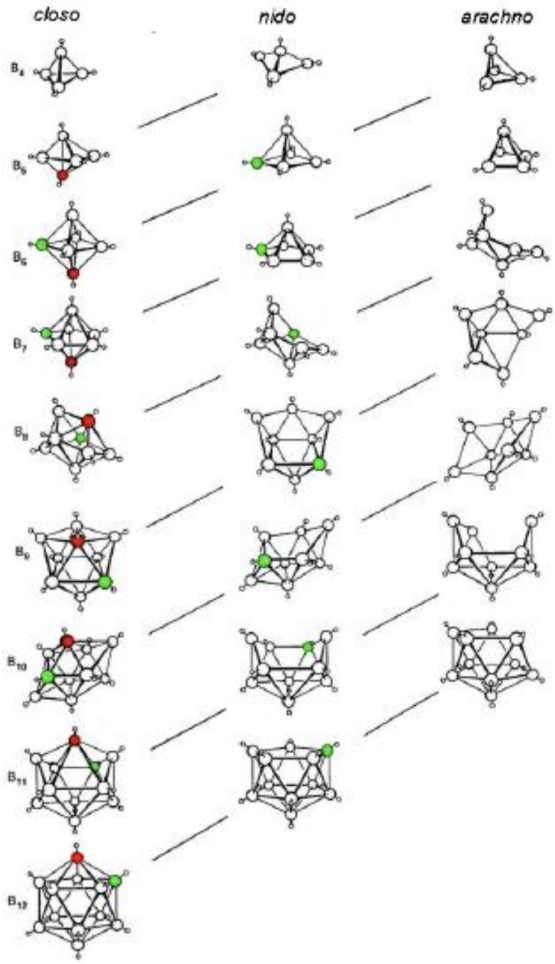

Figure A.1: Structural relationship between closo, nido and arachno boranes. The diagonal lines connect species that have the same number of SEP. The atom shown in red colour would be omitted first, followed by the atom shown in green colour. The picture has been taken from Ref. [184].

3. Number of skeletal electrons = 24 - 10 = 14

4. Number of SEP = *n+1* = 14 / 2 = 7

5. Number of boron atoms = *n-1* = 5

No. of boron atoms	No. of PES	Type of cluster	General formula	Example
n	*n+1*	*closo*	$B_nH_n{}^{2-}$	$B_6H_6{}^{2-}$
n-1	*n+1*	*nido*	$B_nH_n{}^{4-}$	B_5H_9
n-2	*n+1*	*arachno*	$B_nH_n{}^{6-}$	B_4H_10
n-3	*n+1*	*hypho*	$B_nH_n{}^{8-}B_5H_11^{2-}$	
n-4	*n+1*	*klado*	$B_nH_n{}^{10-}$	$B_{10}H_{16}$

Table A.1: Predicted structure of boranes and carboranes using Wade's rule as a function of number of skeletal electron pairs and number of boron atoms.

From table A.1, this gives a *nido* structure. Thus B_5H_9 has an octahedral structure with one apex missing.

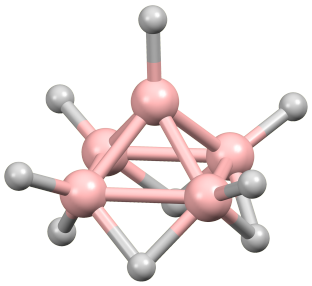

Figure A.2: Ball and stick representation of pentaborane. The picture has been taken from Ref. [185].

Appendix B

DFT calculation and enthalpy of formation equations for silicon incorporation in boron carbide unit cell

In the DFT calculations, the energy of alpha rhombohedral boron and the energy of beta rhombohedral boron are very close. Similarly, the energy of graphite and diamond are also very close. Therefore, alpha rhombohedral boron and diamond were chosen as references for elemental boron and carbon.

Calculation of enthalpy

The enthalpy has been calculated as a function of pressure (P) according to the following equation.

$$H(P) = E(P) + PV(P) \tag{B.1}$$

where E(P) and V(P) are the DFT total energy and the volume of the unit cell respectively.

B.1 DFT-LDA calculations

B.1.1 Insertion of 1 silicon atom in the boron carbide 15-atom unit cell

- **Enthalpy of formation calculated from boron, diamond and silicon**

  The enthalpy of formation of the ternary B_nC_mSi product from an initial mixture of alpha boron, diamond and silicon has been calculated according to the following equation.

$$H_f(B_nC_mSi) = (\frac{1}{n+m})[H(B_nC_mSi) - nH(B) - mH(C) - H(Si)] \tag{B.2}$$

  Here, n = 11 (12) and m = 3 (2) respectively depending on whether the silicon atom replaces a boron site or a carbon site in the 15-atom $(B_{11}C^p)$C-B-C unit cell.

Brute force substitution of silicon atom at 0 GPa When brute force substitution is done at all the 15 positions, it is found that the total enthalpy is minimum for Si in antipodal position with respect to the carbon atom in the icosahedron (CP). It also gives rise to a negative chemical pressure of - 26.7 GPa.

Calculations with relaxed cell parameters at 0 GPa After having replaced the silicon atom in each of the 15 potential positions, there has been only one feasible position for the Si atom, at CP (the position of the polar carbon atom in the icosahedron). The formation enthalpy is -0.0941 eV/atom. Although that is the only position with negative formation enthalpy, there are other positions, namely 1(BP),2(BP),3(BP),4(BP),5(BP),14(BC), where the formation enthalpy when replaced by a Si atom is less than 0.09 eV/atom.

Calculations with relaxed cell parameters at 26.7 GPa There has been just the one feasible position with negative enthalpy of formation again: position 15 (CP) with a formation enthalpy of -0.07333 eV/atom. 5 other positions, namely 1(BP), 2(BP), 3(BP), 4(BP), 5(BP), 14(BC), have formation enthalpy less than 0.09 eV/atom.

Calculations with relaxed cell parameters at 50 GPa Again, Position 15 (CP) has been the only feasible position with a formation enthalpy of -0.055 eV/atom. The other positions, namely 1(BP), 2(BP), 3(BP), 4(BP), 5(BP), 14(BC), with formation enthalpy less than 0.09 eV/atom have also remained the same.

However, the change in formation enthalpy with respect to 26.7 GPa is not uniform. In positions like 1,2,4,5,10,13,14, the formation enthalpy has decreased, but in the other positions, it has increased with increasing pressure.

Calculations with relaxed cell parameters at 75 GPa At 75GPa, position 14 (BC) which is the boron atom position in the chain, becomes feasible as well, with a formation enthalpy of -0.017 eV/atom. The position 15 (CP) has negative formation enthalpy (-0.036 eV/atom) as well. However, it is not possible here to compare the formation enthalpy for Si sunstitution in CP and BC positions, since the resulting product stoichiometry would be different ($B_{12}C_2Si$ and $B_{11}C_3Si$ respectively). The transition of the 14th position as a feasible position for Si insertion occurs between 50 to 55GPa. 5 other positions, namely 1(BP), 2(BP), 4(BP), 5(BP), 13(CC), have formation enthalpy less than 0.09 eV/atom. Positions 3,6,7,9,11,12 have formation enthalpy increasing as pressure increased from 50 to 75GPa. For the rest of the positions, formation enthalpy decreases with this increase in pressure.

Calculations with relaxed cell parameters at 100 GPa At 100GPa, both position 14 (BC) (-0.0338 eV/atom) and position 15th position (-0.018 eV/atom) have negative formation enthalpy. Position 12 (CC) also becomes feasible with a formation enthalpy of -0.0217 eV/atom. This appears odd at first glance since till 75GPa, the formation enthalpy of the 12th position was increasing with pressure. The sudden decrease in formation enthalpy appears due to a drastic decrease in the

volume of the Si embedded boron carbide unit cell, from 629.1636 a.u^3 at 75GPa to 558.421 a.u^3. In comparison, in the 15th position, the volume decreases from 620.8546 a.u^3 to 588.4121 a.u^3.

- **Enthalpy of formation calculated from boron carbide, silicon, and alpha boron**

The enthalpy of formation of the ternary $B_{12}C_2Si$ product from an initial mixture of boron carbide, silicon, and alpha boron has been calculated according to the following equation.

$$H_f(B_{12}C_2Si) = (\frac{1}{15})[H(B_{12}C_2Si) - \frac{2}{3}H(B_{12}C_3) - 4H(B) - H(Si)] \qquad \text{(B.3)}$$

Here the stoichiometry of the final product due to the excess boron in the initial reactants allows the substitution of a Si atom only in the three carbon sites: position 15 (CP) corresponding to the polar atom in the icosahedron and positions 12 and 13 (CC) corresponding to the chain carbon atoms.

Calculations with relaxed cell parameters at 0 GPa Position 15 has been the only one feasible with a formation enthalpy of -0.013 eV/atom. None of the other two positions have a formation enthalpy less than 0.09 eV/atom.

Calculations with relaxed cell parameters at 26.7 GPa Position at 15 (CP) has been the only feasible position with the formation enthalpy of -0.026 eV/atom, which is less than before. This shows that increasing pressure is making the formation more feasible.

Calculations with relaxed cell parameters at 50 GPa Position 15 (CP) has remained the only feasible position with the formation enthalpy of -0.034 eV/atom. The formation enthalpy has decreased from that of 26.7 GPa, which suggests pressure aids Si insertion at this position. The formation enthalpy of position 12, however, increases with increase of pressure.

Calculations with relaxed cell parameters at 75 GPa Position 15 (CP) has remained the only position with feasible formation enthalpy of -0.0403 eV/atom, which is less than that under 50 GPa. Position 13 has a formation enthalpy under 0.09 eV/atom while the formation enthalpy of position 12 increases with the increase of pressure.

Calculations with relaxed cell parameters at 100 GPa Position 15 (CP) has remained feasible (-0.045 eV/atom) while position 12 (CC) has also become feasible with a formation enthalpy of -0.049 eV/atom. Position 13 (0.007 eV/atom) also has shown a small positive formation enthalpy. The formation enthalpy for Si insertion in all the three positions has decreased with increase in pressure from 75 to 100GPa. The drastic change in the formation enthalpy for silicon substitution in the position 12 is again due to a dramatic change in volume at 100 GPa, as was seen during the formation from elements.

- **Enthalpy of formation calculated from boron carbide, silicon, and diamond**

The enthalpy of formation of the ternary B_nC_mSi product from an initial mixture of boron carbide, silicon and diamond has been calculated according to the following equation.

$$H_f(B_{11}C_3Si) = (\frac{1}{15})[H(B_{12}C_2Si) - \frac{11}{12}H(B_{12}C_3) - \frac{1}{4}H(C) - H(Si)] \quad \text{(B.4)}$$

Here the stoichiometry of the final product due to the excess carbon in the initial reactants allows the substitution of a Si atom only in the twelves boron sites of the initial $B_{12}C_3$ unit cell.

Calculations with relaxed cell parameters at 0 and 26.7 GPa There is no feasible position. Moreover, there has not been any position with formation enthalpy less than 0.09 eV/atom.

Calculations with relaxed cell parameters at 50 GPa There has still been no feasible position. However, apart from position 8, the formation enthalpy has decreased with pressure. 5 positions, namely 1 (BP), 2 (BP), 4 (BP), 5 (BP), 14 (BC), have formation enthalpies less than 0.09 eV/atom.

Calculations with relaxed cell parameters at 75 GPa Position 14 (BC), with silicon in place of the chain boron atom, has become feasible at 75 GPa with a formation enthalpy of -0.023 eV/atom. 4 positions, namely 1 (BP), 2 (BP), 4 (BP), 5 (BP), have formation enthalpies less than 0.09 eV/atom. All the 12 positions

have decreasing formation enthalpy as pressure shifts from 50 to 75GPa.

Calculations with relaxed cell parameters at 100 GPa Position 14 (BC) has remained the only feasible position, with the formation enthalpy of -0.071 eV/Atom. All the positions have the formation enthalpies that decrease with increase in pressure. 6 positions, namely 1 (BP), 2 (BP), 3 (BP), 4 (BP), 5 (BP), 10 (BE) have formation enthalpies less than 0.09 eV/atom.

- **Enthalpy of formation calculated from alpha boron, diamond, and cubic silicon carbide**

The enthalpy of formation of the ternary B_nC_mSi product from an initial mixture of alpha boron, diamond, and cubic silicon carbide has been calculated according to the following equation.

$$H_f(B_nC_mSi) = (\frac{1}{n+m})[H(B_nC_mSi) - nH(B) - (m-1)H(C) - H(SiC)] \quad \text{(B.5)}$$

Here, n = 11 (12) and m = 3 (2) respectively depending on whether the silicon atom has replaced a boron site or a carbon site in the 15-atom $(B_{11}C^p)$C-B-C unit cell.

Calculations with relaxed cell parameters at 0 GPa There has been just one feasible position (CP at the position 15) with the formation enthalpy of -0.056 eV/atom. The other positions with formation enthalpy less than 0.09 eV/atom

are 4 (BP) and 5 (BP).

Calculations with relaxed cell parameters at 26.7 GPa Once the pressure of 26.7 GPa is reached, there has not been any feasible position. Position 15 (CP) is the only position with a formation enthalpy less than 0.09 eV/atom (0.006 eV/atom). The formation enthalpy seemed to tip over from negative to positive between 23GPa to 26.7 GPa. Thus in this case, increasing pressure has not helped with Si insertion in the boron carbide unit cell.

Calculations with relaxed cell parameters at 50 GPa There has been no feasible position in this pressure as well, following the trend of 26.7 GPa. The formation enthalpy at position 15 (which was feasible till a pressure of 23GPa) has increased to 0.051 eV/atom at 50 GPa from the 0.006 eV/atom at 26.7 GPa. No other position has a formation enthalpy less than 0.09 eV/atom. Only Si replacement in position 13 (CC) has resulted in a formation enthalpy less than that under 26.7 GPa.

Calculations with relaxed cell parameters at 75 GPa There has been no feasible position, and no position has a formation enthalpy below 0.09 eV/atom. Similar to the case of 50GPa, only position 13 (CC) has a formation enthalpy that decreases from that of the earlier pressure.

Calculations with relaxed cell parameters at 100 GPa Like at earlier pressure, there is no feasible position. There is also not any position with formation

enthalpy less than 0.09 eV/atom. Only positions 12 and 13, which are the chain carbon sites, have formation enthalpies decreasing with increasing pressure. For position 13, the decrease in formation enthalpy is more than 3 times the previous value at 75GPa. Although position 12 is still unfeasible, it follows the general trend of a drastic decrease of formation enthalpy when the pressure increases from 75 to 100GPa.

- **Enthalpy of formation calculated from alpha boron, diamond, and hexagonal silicon carbide**

The enthalpy of formation of the ternary B_nC_mSi product from an initial mixture of alpha boron, diamond, and hexagonal silicon carbide has been calculated according to the following equation.

$$H_f(B_nC_mSi) = (\frac{1}{n+m})[H(B_nC_mSi) - nH(B) - (m-1)H(C) - H(SiC)] \quad \text{(B.6)}$$

Here, n = 11 (12) and m = 3 (2) respectively depending on whether the silicon atom replaced a boron site or a carbon site in the 15-atom $(B_{11}C^p)$C-B-C unit cell.

Calculations with relaxed cell parameters at 0 GPa Similar to the case of cubic silicon carbide, only position 15 (CP) has shown a feasible formation enthalpy of -0.056 eV/atom. No other positions have a formation enthalpy less than 0.09 eV/atom.

Calculations with relaxed cell parameters at 25, 50, 75, 100 GPa Similar to the case of cubic SiC, there has been no more feasible positions and all the formation enthalpies has continued to increase with pressure.

B.1.2 Insertion of 2 silicon atoms in the boron carbide 15-atom unit cell

Next, 2 silicon atoms were replaced in the 15-atom boron carbide unit cell (see table 6.1). Since this would lead to a large number of calculations (105 calculations for each pressure value with each set of reactants), I tried to limit the number of calculations. The first Si atom was held fixed at position 15 (CP) since this is the position that showed feasible formation enthalpies most of the time. The second Si atom was placed in each of the positions ranging from 1 to 14. The calculations were done with only two sets of reactants : i) alpha boron, diamond and silicon, and ii) alpha boron, diamond, and cubic silicon carbide.

- **Enthalpy of formation calculated from alpha boron, diamond, and silicon**

  The enthalpy of formation of the ternary B_nC_mSi product from an initial mixture of alpha boron, diamond, and silicon has been calculated according to the following equation.

$$H_f(B_nC_mSi_2) = (\frac{1}{n+m})[H(B_nC_mSi_2) - nH(B) - mH(C) - 2H(Si)] \quad \text{(B.7)}$$

  Here, n = 11 (12) and m = 2 (1) respectively depending on whether the second

silicon atom has replaced a boron site or a carbon site in the first 14 positions of the 15-atom ($B_{11}C^{p}$)C-B-C unit cell.

Calculations with relaxed cell parameters at 0 GPa None of the positions have shown a feasible formation enthalpy. However, the positions 1 (BP), 2 (BP), 4 (BP), 5 (BP), 9 (BE), 11 (BE), 12 (CC), 13 (CC), 14 (BC) have formation enthalpies less than 0.09 eV/ atom when the second silicon atom takes up these positions.

Calculations with relaxed cell parameters at 26.7 GPa Again, none of the positions have a feasible formation enthalpy. However, the formation enthalpy when the second Si atom has replaced the position 14 (BC) is very small (0.002 eV/atom) which is not greater than the numerical precision of 0.003 eV/atom. The formation enthalpies have decreased with increasing pressure for all the positions in the boron sites. For the carbon sites 12 (CC) and 13 (CC), the formation enthalpies have increased with pressure.

Calculations with relaxed cell parameters at 50 GPa Position 14 (BC) has become feasible with the lowest formation enthalpy of -0.031 eV/atom. Other positions, namely 1 (-0.001 eV/atom), 2 (-0.001 eV/atom), 4 (-0.016 eV/atom), 5 (-0.016 eV/atom) have become feasible too. However the feasible formation enthalpies of position 1 and 2 are not greater than the numerical precision of 0.003 eV/atom. The formation enthalpies have decreased with increasing pressure for

all the positions in the boron sites. For the carbon sites 12 (CC) and 13 (CC), the formation enthalpies have increased with pressure.

Calculations with relaxed cell parameters at 75 GPa Positions 1 (BP), 2 (BP), 4(BP), 5 (BP) and 14 (BC) have remained feasible with formation enthalpies of -0.028 eV/atom, -0.028 eV/atom, -0.037 eV/atom, -0.037 eV/atom and -0.064 eV/atom respectively. Evidently, position 14 has the lowest formation enthalpy. Position 3 (BP) has also become feasible with a formation enthalpy of -0.011 eV/atom. The formation enthalpies have decreased with increasing pressure for all the positions in the boron sites. For the carbon sites 12 (CC) and 13 (CC), the formation enthalpies have increased with pressure.

Calculations with relaxed cell parameters at 100 GPa A number of positions become feasible at this pressure, as shown in table B.1 . However, the most remarkable change is that the position 13 has become feasible at 100 GPa, even though its formation enthalpy had shown a continuous rising trend from 0 GPa to 75 GPa.

- **Enthalpy of formation calculated from alpha boron, diamond, and cubic silicon carbide**

  The enthalpy of formation of the ternary B_nC_mSi product from an initial mixture of alpha boron, diamond, and cubic silicon carbide has been calculated according to the following equation.

Position number for second Si atom	Atom type	Formation enthalpy (eV/atom)
1	BP	-0.067
2	BP	-0.067
3	BP	-0.081
4	BP	-0.056
5	BP	-0.056
9	BE	-0.009
11	BE	-0.009
13	CC	-0.116
14	BC	-0.093

Table B.1: Formation enthalpies at 100 GPa of feasible positions of the second Si atom in the 15-atom $B_{11}C^{p}$ C-B-C unit cell, while the first Si atom is held in the 15th position. The reactants are alpha boron, diamond and silicon. Calculations in DFT-LDA.

$$H_f(B_{11}C_2Si_2) = (\frac{1}{15})[H(B_{11}C_2Si_2) - 11H(B) - H(C) - 2H(SiC)] \qquad \text{(B.8)}$$

Here, the second silicon atom can only replaced a boron site in the first 14 positions of the 15-atom ($B_{11}C^{p}$)C-B-C unit cell because of stoichiometry.

Calculations with relaxed cell parameters at 0 GPa, 26.7 GPa, 50 GPa, and 100 GPa There has been no feasible positions at any of the positions for any pressure ranging from 0 GPa to 100 GPa.

B.2 DFT-GGA calculations

- Enthalpy of formation calculated from alpha boron, diamond and silicon The DFT-GGA was used to calculate the formation enthalpy from the elements and verify whether the results agree with those of DFT-LDA calculations.

  Calculations with relaxed cell parameters at 0 GPa Only position 15 is feasible, same as in the DFT-LDA calculations. Positions 1, 2, 3, 4, 5, 6, 7, 10, 14 have formation enthalpies below 0.09 eV/atom.

  Calculations with relaxed cell parameters at 25 GPa Both positions 14 and 15 become feasible. This is unlike the DFT-LDA calculations, where position 15 remains the only feasible position even at 26.7 GPa. Except for positions 12 and 13, all other positions have formation enthalpies below 0.09 eV/atom.

  Calculations with relaxed cell parameters at 50 and 75 GPa Similar to 25 GPa, both positions 14 and 15 remain feasible. Positions 1, 2, 3, 4, 5, 10, 13 have formation enthalpies below 0.09 eV/atom.

  Calculations with relaxed cell parameters at 100 GPa Both positions 14 and 15 remain feasible. Position 12 becomes feasible as well. This is similar to DFT-LDA calculations, where Position 12 becomes feasible at 100 GPa as well. Positions 1, 2, 3, 4, 5, 10 and 13 have formation enthalpies less than 0.09 eV/atom.

Bibliography

[1] [Online]. Available: http://www.army.mil/-images/2007/04/02/3754/army.mil-2007-04-04-075805.jpg,PublicDomain

[2] [Online]. Available: www.indiamart.com/proddetail/boron-carbide-nozzles-4086622788.html

[3] [Online]. Available: www.irfm.cea.fr

[4] A. K. Suri, C. Subramanian, J. K. Sonber, and T. S. R. C. Murthy, "Synthesis and consolidation of boron carbide: a review," *International Materials Reviews*, vol. 55, pp. 4–40, 2010.

[5] A. Jay, "In silico design of a new phase of boron carbide," Ph.D. dissertation, École Polytechnique, Palaiseau, 2014.

[6] A. Jay, O. Hardouin Duparc, J. Sjakste, and N. Vast, "Theoretical phase diagram of boron carbide from ambient to high pressure and temperature," *Journal of Applied Physics*, vol. 125, p. 185902, 2019.

[7] D. Gosset and M. Colin, "Boron carbides of various compositions: An improved method for x-rays characterisation," *Journal of Nuclear Materials*, vol. 183, 1991.

[8] K. A. Schwetz and P. Karduck, "Investigations in the boron-carbon system with the aid of electron probe microanalysis," *Journal of the Less Common Metals*, vol. 175, pp. 1–11, 1991.

[9] V. Domnich, S. Reynaud, R. A. Haber, and M. Chhowalla, "Boron carbide: Structure, properties, and stability under stress," *Journal of the American Ceramic Society*, vol. 94, pp. 3605–3628, 2011.

[10] M. Bouchacourt and F. Thevenot, "Analytical investigations in the B-C system," *Journal of the Less Common Metals*, vol. 82, pp. 219 – 226, 1981.

[11] H. Werheit, U. Kuhlmann, F. H. Werheit, and G. Krach, "Optical absorption of carbon-doped beta-rhombohedral boron and boron carbide in the absorption edge range," *AIP Conference Proceedings*, vol. 231, pp. 144–147, 1991.

[12] H. K. Clark and J. L. Hoard, "The crystal structure of boron carbide," *Journal of the American Chemical Society*, vol. 65, pp. 2115–2119, 1943.

[13] T. L. Aselage and R. G. Tissot, "Lattice constants of boron carbides," *Journal of the American Ceramic Society*, vol. 75, pp. 2207–2212, 1992.

[14] M. Herrmann, I. Sigalas, M. Thiele, M. Müller, H.-J. Kleebe, and A. Michaelis, "Boron suboxide ultrahard materials," *International Journal of Refractory Metals and Hard Materials*, vol. 39, pp. 53 – 60, 2013.

[15] T. Roy, C. Subramanian, and A. Suri, "Pressureless sintering of boron carbide," *Ceramics International*, vol. 32, pp. 227 – 233, 2006.

[16] S. P. Dodd, G. A. Saunders, and B. James, "Temperature and pressure dependences of the elastic properties of ceramic boron carbide," *Journal of Materials Science*, vol. 37, pp. 2731–2736, 2002.

[17] I. G. Crouch, G. V. Franks, C. Tallon, S. Thomas, M. Naebe, and I. G. Crouch, *The Science of Armour Materials*. Woodhead Publishing, 2017.

[18] F. Thévenot, "Boron carbide—a comprehensive review," *Journal of the European Ceramic Society*, vol. 6, pp. 205–225, 1990.

[19] L. Fitzgerald, "The hardness at high temperatures of some refractory carbides and borides," *Journal of the Less Common Metals*, vol. 5, pp. 356–364, 1963.

[20] J. Lynch, C. Ruderer, and W. Duckworth, *Engineering Properties of Selected Ceramic Materials*. The American Ceramic Society, 1966.

[21] A. Alizadeh, E. Taheri-Nassaj, N. Ehsani, and H. R. Baharvandi, "Production of boron carbide powder by carbothermic reduction from boron oxide and petroleum coke or carbon active," *Advances in Applied Ceramics*, vol. 105, pp. 291–296, 2006.

[22] D. Gosset, *Properties of B_4C*, 2nd ed., R. Konings and R. Stolle, Eds. Elseiver, 2020.

[23] Y. Sunitha and S. Kumar, "^{10} B/^{11} B isotopic ratio and atomic composition of boron carbide: Determination by proton induced γ-ray emission and proton elastic

backscattering spectrometry," *Applied Radiation and Isotopes*, vol. 128, pp. 28–35, 2017.

[24] D. Gosset, P. Herter, and V. Motte, "Evaluation of damage in neutron irradiated boron carbide," *Nuclear Instruments and Methods in Physics Research Section B: Beam Interactions with Materials and Atoms*, vol. 434, pp. 66–72, 2018.

[25] D. Gosset, *Structural Materials for Generation IV Nuclear Reactors*. Woodhead Publishing, 2017.

[26] O. I. Buzhinskij and Y. M. Semenets, "Thick boron carbide coatings for protection of tokamak first wall and divertor," *Fusion Engineering and Design*, vol. 45, pp. 343–360, 1999.

[27] G. B. Gilbert Fantozzi, Jean-Claude Niepce, *Les céramiques industrielles: Propriétés, mise en forme et applications*. Dunod, 2013.

[28] R. Koons and J. Buscaglia, "Forensic significance of bullet lead compositions," *Journal of Forensic Sciences*, vol. 50, pp. JFS2 004 212–11, 2005.

[29] R. Pöllänen, T. K. Ikäheimonen, S. Klemola, V. P. Vartti, K. Vesterbacka, S. Ristonmaa, T. Honkamaa, P. Sipilä, I. Jokelainen, A. Kosunen, R. Zilliacus, M. Kettunen, and M. Hokkanen, "Characterisation of projectiles composed of depleted uranium," *Journal of Environmental Radioactivity*, vol. 64, pp. 133–142, 2003.

[30] V. L. Solozhenko and Y. Le Godec, "A hunt for ultrahard materials," *Journal of Applied Physics*, vol. 126, p. 230401, 2019.

[31] R. H. Wentorf, R. C. DeVries, and F. P. Bundy, "Sintered superhard materials," *Science*, vol. 208, p. 873, 1980.

[32] S. Veprek, A. Zeer, and R. Riedel, *Handbook of ceramic hard materials*, R. Riedel, Ed. Wiley, Weinheim, 2000.

[33] Z. Chen, U. Gandhi, J. Lee, and R. Wagoner, "Variation and consistency of young's modulus in steel," *Journal of Materials Processing Technology*, vol. 227, pp. 227–243, 2016.

[34] J. H. Gieske, T. L. Aselage, and D. Emin, "Elastic properties of boron carbides," *AIP Conference Proceedings*, vol. 231, pp. 376–379, 1991.

[35] M. Beauvy, "Stoichiometric limits of carbon-rich boron carbide phases," *Journal of the Less Common Metals*, vol. 90, pp. 169–175, 1983.

[36] J. M. Wheeler and J. Michler, "Invited article: Indenter materials for high temperature nanoindentation," *Review of Scientific Instruments*, vol. 84, p. 101301, 2013.

[37] N. V. Novikov, Y. V. Sirota, V. I. Mal'nev, and I. A. Petrusha, "Mechanical properties of diamond and cubic bn at different temperatures and deformation rates," *Diamond and Related Materials*, vol. 2, pp. 1253–1256, 1993.

[38] M. M. Balakrishnarajan, P. D. Pancharatna, and R. Hoffmann, "Structure and bonding in boron carbide: The invincibility of imperfections," *New Journal of Chemistry*, vol. 31, pp. 473–485, 2007.

[39] D. E. Grady, "Shock-wave compression of brittle solids," *Mechanics of Materials*, vol. 29, no. 3, pp. 181–203, 1998.

[40] T. J. Vogler, W. D. Reinhart, and L. C. Chhabildas, "Dynamic behavior of boron carbide," *Journal of Applied Physics*, vol. 95, 2004.

[41] M. Chen, J. W. McCauley, and K. J. Hemker, "Shock-induced localized amorphization in boron carbide," *Science*, vol. 299, p. 1563, 2003.

[42] X. Q. Yan, Z. Tang, L. Zhang, J. J. Guo, C. Q. Jin, Y. Zhang, T. Goto, J. W. McCauley, and M. W. Chen, "Depressurization amorphization of single-crystal boron carbide," *Physical Review Letters*, vol. 102, pp. 075 505–, 2009.

[43] D. Ge, V. Domnich, T. Juliano, E. A. Stach, and Y. Gogotsi, "Structural damage in boron carbide under contact loading," *Acta Materialia*, vol. 52, pp. 3921–3927, 2004.

[44] S. Aryal, P. Rulis, and W. Y. Ching, "Mechanism for amorphization of boron carbide B_4C under uniaxial compression," *Physical Review B*, vol. 84, pp. 184 112–, 2011.

[45] E. Betranhandy, N. Vast, and J. Sjakste, "Ab initio study of defective chains in icosahedral boron carbide B4C," *Solid State Sciences*, vol. 14, pp. 1683–1687, 2012.

[46] R. Raucoules, N. Vast, E. Betranhandy, and J. Sjakste, "Mechanical properties of icosahedral boron carbide explained from first principles," *Physical Review B*, vol. 84, p. 014112, 2011.

[47] J. Rabier, L. Pizzagalli, and J. Demenet, *Dislocations in Solids*, J. Hirth and L. Kubin, Eds. Elsevier, 2010.

[48] M. Iyer, V. Gavini, and T. M. Pollock, "Energetics and nucleation of point defects in aluminum under extreme tensile hydrostatic stresses," *Physical Review B*, vol. 89, p. 014108, 01 2014.

[49] B. Morosin, G. H. Kwei, A. C. Lawson, T. L. Aselage, and D. Emin, "Neutron powder diffraction refinement of boron carbides nature of intericosahedral chains," *Journal of Alloys and Compounds*, vol. 226, pp. 121–125, 1995.

[50] A. Ektarawong, S. I. Simak, and B. Alling, "Carbon-rich icosahedral boron carbides beyond B_4C and their thermodynamic stabilities at high temperature and pressure from first principles," *Physical Review B*, vol. 94, p. 054104, 2016.

[51] A. Doucouré, "Rapport d'alternance M2: Synthèse d'un carbure de bore aux propriétés mécaniques renforcées," Master's thesis, Université Paris Sud, 2016.

[52] I. Chuvashova, B. Gasharova, Y.-L. Mathis, L. Dubrovinsky, and N. Dubrovinskaia, "Structural stability of boron carbide under pressure proven by spectroscopic studies up to 73 GPa," *Zeitschrift für anorganische und allgemeine Chemie*, vol. 643, pp. 1357–1363, 2017.

[53] D. W. Bullett, "The electronic origin disorder in boron and boron-rich borides," *AIP Conference Proceedings*, vol. 231, pp. 21–28, 1991.

[54] B. Magnusson and C. Brosset, "The crystal structure of $B_{2.89}Si$," *Acta Chemica Scandinavica*, vol. 16, pp. 449–455, 1962.

[55] A. U. Khan, A. M. Etzold, X. Yang, V. Domnich, K. Y. Xie, C. Hwang, K. D. Behler, M. Chen, Q. An, J. C. LaSalvia, K. J. Hemker, W. A. Goddard, and R. A. Haber, "Locating Si atoms in Si-doped boron carbide: A route to understand amorphization mitigation mechanism," *Acta Materialia*, vol. 157, pp. 106–113, 2018.

[56] B. Morosin, T. L. Aselage, and R. S. Feigelson, "Crystal structure refinements of rhombohedral symmetry materials containing boron-rich icosahedra," in *MRS Proceedings*, vol. 97. Cambridge University Press, 1987, p. 145.

[57] J. E. Proctor, V. Bhakhri, R. Hao, T. J. Prior, T. Scheler, E. Gregoryanz, M. Chhowalla, and F. Giulani, "Stabilization of boron carbide via silicon doping," *Journal of Physics: Condensed Matter*, vol. 27, p. 015401, 2015.

[58] A. Lipp and M. Riöder, "Verbindungen im System B-C-Si bzw. B-Si," *Z. Anorg. Allg. Chem.*, vol. 344, pp. 225–229, 1966.

[59] R. Telle, *Struture and Properties of Si-Doped boron carbide - The Physics and Chemistry of Carbides, Nitrides and Borides*, R. Freer, Ed. Kluwer Academic Publishers, 1990, vol. 185.

[60] R. Lazzari, N. Vast, J. M. Besson, S. Baroni, and A. Dal Corso, "Atomic structure and vibrational properties of icosahedral B_4C boron carbide," *Phys. Rev. Lett.*,

vol. 83, pp. 3230–3233, 1999.

[61] N. Vast, J. Sjakste, and E. Betranhandy, "Boron carbides from first principles," in *Journal of Physics: Conference Series*, vol. 176. IOP Publishing, 2009, p. 012002.

[62] V. L. Solozhenko, O. O. Kurakevych, D. Andrault, Y. Le Godec, and M. Mezouar, "Ultimate metastable solubility of boron in diamond: Synthesis of superhard diamondlike BC_5," *Physical Review Letters*, vol. 102, pp. 015 506–, 2009.

[63] A. Jay, N. Vast, J. Sjakste, and O. H. Duparc, "Carbon-rich icosahedral boron carbide designed from first principles," *Applied Physics Letters*, vol. 105, p. 031914, 2014.

[64] J. S. Schilling, "The use of high pressure in basic and materials science," *Journal of Physics and Chemistry of Solids*, vol. 59, pp. 553–568, 1998.

[65] S. Pandolfi, C. Renero-Lecuna, Y. Le Godec, B. Baptiste, N. Menguy, M. Lazzeri, C. Gervais, K. Spektor, W. A. Crichton, and O. O. Kurakevych, "Nature of hexagonal silicon forming via high-pressure synthesis: Nanostructured hexagonal 4H polytype," *Nano Letters*, vol. 18, pp. 5989–5995, 2018.

[66] P. W. Bridgman, "General survey of certain results in the field of high-pressure physics," *Nobel Lecture*, December 11, 1946.

[67] H. Hubert, L. A. J. Garvie, K. Leinenweber, P. R. Buseck, W. T. Petuskeyt, and P. F. McMillan, "High-pressure, high-temperature synthesis of superhard boron suboxide," *Chemistry of Materials*, vol. 410, p. 191, 1995.

[68] J. Zhao, L. Yang, F. Li, R. Yu, and C. Jin, "Structural evolution in the graphitization process of activated carbon by high-pressure sintering," *Carbon*, vol. 47, pp. 744–751, 2009.

[69] F. Birch, "Equation of state and thermodynamic parameters of nacl to 300 kbar in the high-temperature domain," *Journal of Geophysical Research: Solid Earth*, vol. 91, pp. 4949–4954, 2020/06/14 1986.

[70] D. L. Heinz and R. Jeanloz, "The equation of state of the gold calibration standard," *Journal of Applied Physics*, vol. 55, pp. 885–893, 1984.

[71] Y. L. Godec, D. Martinez-Garcia, M. Mezouar, G. Syfosse, J. P. Itié, and J. M. Besson, "Thermoelastic behaviour of hexagonal graphite-like boron nitride," *High Pressure Research*, vol. 17, pp. 35–46, 2000.

[72] Y. L. Godec, M. T. Dove, S. A. T. Redfern, M. G. Tucker, W. G. Marshall, G. Syfosse, and J.-M. Besson, "A new high P-T cell for neutron diffraction up to 7 GPa and 2000 K with measurement of temperature by neutron radiography," *High Pressure Research*, vol. 21, pp. 263–280, 2001.

[73] Voggenreiter. Laboratory equipment. [Online]. Available: www.voggenreiter-gmbh.de

[74] Z. Jenei, E. F. O'Bannon, S. T. Weir, H. Cynn, M. J. Lipp, and W. J. Evans, "Single crystal toroidal diamond anvils for high pressure experiments beyond 5 megabar," *Nature Communications*, vol. 9, p. 3563, 2018.

[75] L. V. Pamela C. Burnley, University of Nevada. The Diamond Anvil Cell (DAC). [Online]. Available: serc.carleton.edu

[76] J. A. Xu, H. K. Mao, and P. M. Bell, "High-pressure ruby and diamond fluorescence: Observations at 0.21 to 0.55 terapascal," *Science*, vol. 232, p. 1404, 1986.

[77] S. Yamaoka, O. Shimomura, and O. Fukunaga, "Simultaneous measurements of temperature and pressure by the ruby fluorescence line," *Proceedings of the Japan Academy, Series B*, vol. 56, pp. 103–107, 1980.

[78] L. Ming and W. A. Bassett, "Laser heating in the diamond anvil press up to 2000 °c sustained and 3000 °c pulsed at pressures up to 260 kilobars," *Review of Scientific Instruments*, vol. 45, pp. 1115–1118, 1974.

[79] S. Anzellini, A. K. Kleppe, D. Daisenberger, M. T. Wharmby, R. Giampaoli, S. Boccato, M. A. Baron, F. Miozzi, D. S. Keeble, A. Ross, S. Gurney, J. Thompson, G. Knap, M. Booth, L. Hudson, D. Hawkins, M. J. Walter, and H. Wilhelm, "Laser-heating system for high-pressure X-ray diffraction at the Extreme Conditions beamline I15 at Diamond Light Source," *Journal of Synchrotron Radiation*, vol. 25, pp. 1860–1868, 2018.

[80] J. Philippe, Y. Le Godec, M. Mezouar, M. Berg, G. Bromiley, F. Bergame, J. P. Perrillat, M. Alvarez-Murga, M. Morand, R. Atwood, A. King, and S. Régnier, "Rotating tomography Paris-Edinburgh cell: a novel portable press for micro-tomographic 4-D imaging at extreme pressure/temperature/stress conditions," *High Pressure Research*, vol. 36, pp. 512–532, 2016.

[81] M. Eckert, "Max von laue and the discovery of x-ray diffraction in 1912," *Annalen der Physik*, 2012.

[82] J. Jenkin, "A unique partnership: William and lawrence bragg and the 1915 Nobel Prize in Physics," *Minerva*, vol. 39, pp. 373–392, 2001.

[83] K. Cherednichenko, "Boron chalcogenides under extreme conditions," Ph.D. dissertation, Universite Pierre et Marie Curie - Paris VI, 2015.

[84] A. Smekal, "Zur Quantentheorie der Dispersion," *Die Naturwissenschaften*, vol. 11, pp. 873–875, 1923.

[85] C. V. Raman, "The molecular scattering of light," *Nobel Lecture*, 1930.

[86] M. von Ardenne, "Improvements in electron microscopes," British patent GB 511204, 1937.

[87] Y. Wang, T. Uchida, R. Von Dreele, M. L. Rivers, N. Nishiyama, K.-i. Funakoshi, A. Nozawa, and H. Kaneko, "A new technique for angle-dispersive powder diffraction using an energy-dispersive setup and synchrotron radiation," *Journal of Applied Crystallography*, vol. 37, pp. 947–956, 2004.

[88] J. P. Itié, E. Girard, N. Guignot, Y. Le Godec, and M. Mezouar, "Crystallography under high pressure using synchrotron radiation," *Journal of Physics D: Applied Physics*, vol. 48, p. 504007, 2015.

[89] F. Giustino, *Materials modelling using density functional theory : properties and predictions*. Oxford University Press, 2014.

[90] D. M. Ceperley and B. J. Alder, "Ground state of the electron gas by a stochastic method," *Physical Review Letters*, vol. 45, pp. 566–569, 1980.

[91] J. P. Perdew and A. Zunger, "Self-interaction correction to density-functional approximations for many-electron systems," *Physical Review B*, vol. 23, pp. 5048–5079, 1981.

[92] P. Giannozzi, S. Baroni, N. Bonini, M. Calandra, R. Car, C. Cavazzoni, D. Ceresoli, G. L. Chiarotti, M. Cococcioni, I. Dabo, A. Dal Corso, S. de Gironcoli, S. Fabris, G. Fratesi, R. Gebauer, U. Gerstmann, C. Gougoussis, A. Kokalj, M. Lazzeri, L. Martin-Samos, N. Marzari, F. Mauri, R. Mazzarello, S. Paolini, A. Pasquarello, L. Paulatto, C. Sbraccia, S. Scandolo, G. Sclauzero, A. P. Seitsonen, A. Smogunov, P. Umari, and R. M. Wentzcovitch, "QUANTUM ESPRESSO: a modular and open-source software project for quantum simulations of materials," *Journal of Physics: Condensed Matter*, vol. 21, p. 395502, 2009.

[93] P. Giannozzi, O. Andreussi, T. Brumme, O. Bunau, M. B. Nardelli, M. Calandra, R. Car, C. Cavazzoni, D. Ceresoli, M. Cococcioni, N. Colonna, I. Carnimeo, A. D. Corso, S. de Gironcoli, P. Delugas, R. A. D. Jr, A. Ferretti, A. Floris, G. Fratesi, G. Fugallo, R. Gebauer, U. Gerstmann, F. Giustino, T. Gorni, J. Jia, M. Kawamura, H.-Y. Ko, A. Kokalj, E. Küçükbenli, M. Lazzeri, M. Marsili, N. Marzari, F. Mauri, N. L. Nguyen, H.-V. Nguyen, A. O. de-la Roza, L. Paulatto, S. Poncé, D. Rocca, R. Sabatini, B. Santra, M. Schlipf, A. P. Seitsonen, A. Smogunov, I. Timrov, T. Thonhauser, P. Umari, N. Vast, X. Wu, and S. Baroni, "Advanced

capabilities for materials modelling with QUANTUM ESPRESSO," *Journal of Physics: Condensed Matter*, vol. 29, p. 465901, 2017.

[94] T. Fujii, Y. Mori, H. Hyodo, and K. Kimura, "X-ray diffraction study of B_4C under high pressure," *Journal of Physics: Conference Series*, vol. 215, 2010.

[95] V. A. Mukhanov, P. S. Sokolov, and V. L. Solozhenko, "On melting of B_4C boron carbide under pressure," *Journal of Superhard Materials*, vol. 34, pp. 211–213, 2012.

[96] P. Dera, M. H. Manghnani, A. Hushur, Y. Hu, and S. Tkachev, "New insights into the enigma of boron carbide inverse molecular behavior," *Journal of Solid State Chemistry*, vol. 215, pp. 85–93, 2014.

[97] A. Hushur, M. H. Manghnani, H. Werheit, P. Dera, and Q. Williams, "High-pressure phase transition makes $B_{4.3}C$ boron carbide a wide-gap semiconductor," *Journal of Physics: Condensed Matter*, vol. 28, p. 045403, 2016.

[98] S. Mondal, E. Bykova, S. Dey, S. I. Ali, N. Dubrovinskaia, L. Dubrovinsky, G. Parakhonskiy, and S. van Smaalen, "Disorder and defects are not intrinsic to boron carbide," *Scientific Reports*, vol. 6, p. 19330, 2016.

[99] S. Chen, D. Z. Wang, J. Y. Huang, and Z. F. Ren, "Synthesis and characterization of boron carbide nanoparticles," *Applied Physics A*, vol. 79, pp. 1757–1759, 2004.

[100] B. Li-Hong, L. Chen, T. Yuan, T. Ji-Fa, H. Chao, W. Xing-Jun, S. Cheng-Min, and G. Hong-Jun, "Single crystalline boron carbide nanobelts: synthesis and char-

acterization," *Chinese Physics B*, vol. 17, pp. 4247–4252, 2008.

[101] U. Anselmi-Tamburini, Z. A. Munir, Y. Kodera, T. Imai, and M. Ohyanagi, "Influence of synthesis temperature on the defect structure of boron carbide: Experimental and modeling studies," *Journal of the American Ceramic Society*, vol. 88, pp. 1382–1387, 2005.

[102] A. Chakraborti, N. Vast, and Y. Le Godec, "Synthesis of boron carbide from its elements at high pressures and high temperatures," *Solid State Sciences*, vol. 104, p. 106265, 2020.

[103] S. Klotz, G. Hamel, and J. Frelat, "A new type of compact large-capacity press for neutron and x-ray scattering," *High Pressure Research*, vol. 24, pp. 219–223, 2004.

[104] R. Lacomba-Perales, D. Martinez-García, D. Errandonea, Y. Le Godec, J. Philippe, G. Le Marchand, J. C. Chervin, A. Polian, A. Múñoz, and J. López-Solano, "Experimental and theoretical investigation of the stability of the monoclinic $BaWO_4$-II phase at high pressure and high temperature," *Physical Review B*, vol. 81, p. 144117, 2010.

[105] C. B. Wang, S. Zhang, Q. Shen, and L. M. Zhang, "Investigation on reactive sintering process of boron carbide ceramics by xrd," *Materials Science and Technology*, vol. 25, pp. 809–812, 2009.

[106] S. Roszeitis, B. Feng, H.-P. Martin, and A. Michaelis, "Reactive sintering pro-

cess and thermoelectric properties of boron rich boron carbides," *Journal of the European Ceramic Society*, vol. 34, pp. 327–336, 2014.

[107] B. Callmer, "An accurate refinement of the beta-rhombohedral boron structure locality: synthetic," *Acta Crystallographica Section B,*, vol. 33, pp. 1951–1954, 1977.

[108] G. Parakhonskiy, N. Dubrovinskaia, E. Bykova, R. Wirth, and L. Dubrovinsky, "Experimental pressure-temperature phase diagram of boron: resolving the long-standing enigma," *Scientific reports*, vol. 1, pp. 96–96, 2011.

[109] H. Clark and J. Hoard, "The crystal structure of boron carbide," *Journal of the American Chemical Society*, vol. 65, pp. 2115–2119, 1943.

[110] G. Parakhonskiy, N. Dubrovinskaia, L. Dubrovinsky, S. Mondal, and S. van Smaalen, "High pressure synthesis of single crystals of alpha-boron," *Journal of Crystal Growth*, vol. 321, pp. 162–166, 2011.

[111] N. Vast, S. Baroni, G. Zerah, J. M. Besson, A. Polian, M. Grimsditch, and J. C. Chervin, "Lattice dynamics of -boron from ab-initio calculation and raman scattering under high pressure," *physica status solidi (b)*, vol. 198, pp. 115–119, 1996.

[112] K. M. Reddy, P. Liu, A. Hirata, T. Fujita, and M. W. Chen, "Atomic structure of amorphous shear bands in boron carbide," *Nature Communications*, vol. 4, p. 2483, 2013.

[113] J. Kukesh and L. Pauling, "The problem of the graphite structure," *American Mineralogist*, vol. 35, p. 125, 1950.

[114] A. Kouchi, *Amorphous Carbon*. Springer Berlin Heidelberg, 2011, pp. 41–42.

[115] M. A. Caro, A. Aarva, V. L. Deringer, G. Csányi, and T. Laurila, "Reactivity of amorphous carbon surfaces: Rationalizing the role of structural motifs in functionalization using machine learning," *Chemistry of Materials*, vol. 30, pp. 7446–7455, 2018.

[116] J. Robertson, "Amorphous carbon," *Advances in Physics*, vol. 35, pp. 317–374, 1986.

[117] S. Limandri, G. Garbarino, D. Sifre, M. Mezouar, and V. Galván Josa, "Pressure dependence of the silicon carbide synthesis temperature," *Journal of Applied Physics*, vol. 125, p. 165902, 2019.

[118] D. Portehault, G. Gouget, C. G. Stary, and C. Sanchez, "Nanostructured amorphous boron material," Patent WO2016207558A1, 2016.

[119] W. Yang, W. Ao, J. Zhou, J. Liu, K. Cen, and Y. Wang, "Impacts of particle size and pressure on reactivity of boron oxidation," *Journal of Propulsion and Power*, vol. 29, pp. 1207–1213, 2013.

[120] H.-H. Carstensen, A. M. Dean, and R. W. Carr, *Chapter 4 The Kinetics of Pressure-Dependent Reactions*. Elsevier, 2007, vol. 42, pp. 101–184.

[121] A. L. Patterson, "The scherrer formula for x-ray particle size determination," *Physical Review*, vol. 56, pp. 978–982, 1939.

[122] W. Kraus and G. Nolze, "*POWDER CELL* - a program for the representation and manipulation of crystal structures and calculation of the resulting X-ray powder patterns," *Journal of Applied Crystallography*, vol. 29, pp. 301–303, 1996.

[123] K. D. Leinenweber, J. A. Tyburczy, T. G. Sharp, E. Soignard, T. Diedrich, W. B. Petuskey, Y. Wang, and J. L. Mosenfelder, "Cell assemblies for reproducible multi-anvil experiments (the COMPRES assemblies)," *American Mineralogist*, vol. 97, pp. 353–368, 2012.

[124] A. Dewaele, G. Fiquet, D. Andrault, and D. Hausermann, "P-V-T equation of state of periclase from synchrotron radiation measurements," *Journal of Geophysical Research: Solid Earth*, vol. 105, pp. 2869–2877, 2000.

[125] Y. Tange, Y. Nishihara, and T. Tsuchiya, "Unified analyses for P-V-T equation of state of MgO: A solution for pressure-scale problems in high P-T experiments," *Journal of Geophysical Research: Solid Earth*, vol. 114, 2009.

[126] A. R. Oganov, J. Chen, C. Gatti, Y. Ma, Y. Ma, C. W. Glass, Z. Liu, T. Yu, O. O. Kurakevych, and V. L. Solozhenko, "Ionic high-pressure form of elemental boron," *Nature*, vol. 457, pp. 863–867, 2009.

[127] M. Beauvy and M. Guery, "Physical properties of boron carbide," CEA-CONF-6652, France, Tech. Rep., 1983.

[128] C. Barratt, D. Lepore, M. Cherubini, and P. Schwartz, "Computational Models of Thermal Cycling in Chemical Systems , 2: 19-27," *International Journal of Chemistry*, vol. 2, pp. 19–27, 2010.

[129] Y.-K. Lee and C.-S. Choi, "Effects of thermal cycling on the kinetics of the $\gamma \rightarrow \epsilon$ martensitic transformation in an Fe-17 wt pct Mn alloy," *Metallurgical and Materials Transactions A*, vol. 31, pp. 2735–2738, 2000.

[130] O. H. Luk'yanenko, V. S. Pavlyna, A. T. Pichugin, and V. M. Fedirko, "Effect of thermal cycling on high-temperature interaction of titanium with gases," *Materials Science*, vol. 33, pp. 739–750, 1997.

[131] J. Qin, N. Nishiyama, H. Ohfuji, T. Shinmei, L. Lei, D. He, and T. Irifune, "Polycrystalline γ-boron: As hard as polycrystalline cubic boron nitride," *Scripta Materialia*, vol. 67, pp. 257 – 260, 2012.

[132] Y. Akahama and H. Kawamura, "Pressure calibration of diamond anvil raman gauge to 310gpa," *Journal of Applied Physics*, vol. 100, p. 043516, 2006.

[133] G. Fanchini, J. W. McCauley, and M. Chhowalla, "Behavior of disordered boron carbide under stress," *Phys. Rev. Lett.*, vol. 97, p. 035502, 2006.

[134] G. R. Johnson and T. J. Holmquist, "Response of boron carbide subjected to large strains, high strain rates, and high pressures," *Journal of Applied Physics*, vol. 85, pp. 8060–8073, 1999.

[135] R. Flammini, M. Marton, M. Vojs, E. Zdravecká, M. Himmerlich, T. Haensel,

S. Krischok, M. Kotlár, P. Michniak, M. Veselý, and R. Redhammer, "Raman spectroscopy of amorphous carbon prepared by pulsed arc discharge in various gas mixtures," *Journal of Spectroscopy*, vol. 2013, p. 467079, 2013.

[136] S. Xiang, L. Ma, B. Yang, Y. Dieudonne, G. M. Pharr, J. Lu, D. Yadav, C. Hwang, J. C. LaSalvia, R. A. Haber, K. J. Hemker, and K. Y. Xie, "Tuning the deformation mechanisms of boron carbide via silicon doping," *Science Advances*, vol. 5, 2019.

[137] D. Bullett, "Further electronic structure studies of boron and boron rich borides," *The Physics and Chemistry of Carbides, Nitrides and Borides, NATO ASI Series*, vol. 185, pp. 513–524, 1991.

[138] H. J. Monkhorst and J. D. Pack, "Special points for brillouin-zone integrations," *Physical Review B*, vol. 13, pp. 5188–5192, 1976.

[139] J. P. Perdew and Y. Wang, "Accurate and simple analytic representation of the electron-gas correlation energy," *Physical Review B*, vol. 45, pp. 13 244–13 249, 1992.

[140] V. Tyuterev, J. Sjakste, and N. Vast, "Theoretical intrinsic lifetime limit of shallow donor states in silicon," *Physical Review B*, vol. 81, p. 245212, 2010.

[141] F. A. Kröger and N. H. Nachtrieb, "The Chemistry of Imperfect Crystals," *Physics Today*, vol. 17, p. 66, 1964.

[142] R. Carnahan, "Elastic properties of silicon carbide," *Journal of American Chemical Society*, vol. 51, p. 223, 1968.

[143] W. R. L. Lambrecht, B. Segall, M. Methfessel, and M. van Schilfgaarde, "Calculated elastic constants and deformation potentials of cubic sic," *Physical Review B*, vol. 44, pp. 3685–3694, 1991.

[144] F. Aguado and V. G. Baonza, "Prediction of bulk modulus at high temperatures from longitudinal phonon frequencies: Application to diamond, $c-$BN, and $3c-$SiC," *Physical Review B*, vol. 73, p. 024111, 2006.

[145] R. Ramírez, C. P. Herrero, E. R. Hernández, and M. Cardona, "Path-integral molecular dynamics simulation of $3c-$SiC," *Physical Review B*, vol. 77, p. 045210, 2008.

[146] H. J. McSkimin and P. Andreatch, "Elastic moduli of silicon vs hydrostatic pressure at 25.0 °c and 195.8 °c," *Journal of Applied Physics*, vol. 35, pp. 2161–2165, 1964.

[147] O. Madelung, H. Weiss, and M. Schulz, *Landolt-Börnstein, Semiconductors: Physics of Group IV Elements and III-V Compounds.* Berlin: Springer-Verlag, 1982, vol. 17a.

[148] V. Tyuterev and N. Vast, "Murnaghan's equation of state for the electronic ground state energy," *Computational Materials Science*, vol. 38, pp. 350 – 353, 2006.

[149] V. V. Brazhkin, A. G. Lyapin, and R. J. Hemley, "Harder than diamond: Dreams and reality," *Philosophical Magazine A*, vol. 82, pp. 231–253, 2002.

[150] R. J. Nelmes, J. S. Loveday, D. R. Allan, J. M. Besson, G. Hamel, P. Grima, and S. Hull, "Neutron- and x-ray-diffraction measurements of the bulk modulus of

boron," *Physical Review B*, vol. 47, pp. 7668–7673, 1993.

[151] C. Stampfl, W. Mannstadt, R. Asahi, and A. J. Freeman, "Electronic structure and physical properties of early transition metal mononitrides: Density-functional theory lda, gga, and screened-exchange lda flapw calculations," *Physical Review B*, vol. 63, p. 155106, 2001.

[152] R. W. G. Wyckoff, *Crystal Structures.* Interscience Publishers, New York, New York, 1963, vol. 1.

[153] S. Sugiyama and M. Togaya, "Phase relationship between 3c- and 6h-silicon carbide at high pressure and high temperature," *Journal of the American Ceramic Society*, vol. 84, pp. 3013–3016, 2001.

[154] L. V. McCarty, J. S. Kasper, F. H. Horn, B. F. Decker, and A. E. Newkirk, "A new crystalline modification of boron," *Journal of the American Chemical Society*, vol. 80, p. 2592, 1958.

[155] A. Polian, J. C. Chervin, P. Munsch, and M. Gauthier, "Alpha-boron at very high pressure: structural and vibrational properties," in *Journal of Physics: Conference Series*, vol. 121. IOP Publishing, 2008, p. 042017.

[156] K. Shirai, "Phase diagram of boron crystals," *Japanese Journal of Applied Physics*, vol. 56, p. 05FA06, 2017.

[157] A. Masago, K. Shirai, and H. Katayama-Yoshida, "Crystal stability of alpha and beta boron," *Physical Review B*, vol. 73, p. 104102, 2006.

[158] M. J. van Setten, M. A. Uijttewaal, G. A. de Wijs, and R. A. de Groot, "Thermodynamic stability of boron: The role of defects and zero point motion,," *Journal of the American Chemical Society*, vol. 129, pp. 2458–2465, 2007.

[159] S. Shalamberidze, G. Kalandadze, K. D.E., and B. Tsurtsumia, "Production of alpha rhombohedral boron by amorphous boron crystallization," *Solid State Chemistry*, vol. 154, pp. 199–203, 2000.

[160] K. Shirai, H. Dekura, and A. Yanase, "Electronic structure and electrical resistivity of alpha boron under high pressure," *Journal of the Physical Society of Japan*, vol. 78, p. 084714, 2009.

[161] J. Zhao and J. P. Lu, "Pressure-induced metallization in solid boron," *Physical Review B*, vol. 66, p. 092101, 2002.

[162] K. Momma and F. Izumi, "*VESTA3* for three-dimensional visualization of crystal, volumetric and morphology data," *Journal of Applied Crystallography*, vol. 44, pp. 1272–1276, 2011.

[163] E. Amberger and W. Stumpf, *Gmelin Handbook of Inorganic Chemistry.* SpringerVerlag, Berlin, 1981.

[164] F. Horn, "Some electrical and optical properties of simple rhombohedral boron," *Journal of Applied Physics*, vol. 30, p. 1611, 1959.

[165] K.C.Buschbeck, *Gmelin Handbook of Inorganic Chemistry.* Springer-Verlag Berlin, 1982.

[166] F. H. Cocks and W. N. Simmons, "Red boron solid state detector," US Patent US20150060680A1, 2015.

[167] J. R. Srour and J. W. Palko, "Displacement damage effects in irradiated semiconductor devices," *IEEE Transactions on Nuclear Science*, vol. 60, pp. 1740–1766, 2013.

[168] D. Emin, "Unusual properties of icosahedral boron-rich solids," *Journal of Solid State Chemistry*, vol. 179, pp. 2791–2798, 2006.

[169] G. A. Slack and K. E. Morgan, "Some crystallography, chemistry, physics, and thermodynamics of $B_{12}O_2$, $B_{12}P_2$, $B_{12}As_2$, and related alpha-boron type crystals," *Journal of Physics and Chemistry of Solids*, vol. 75, pp. 1054–1074, 2014.

[170] D. Emin, "Bonding and doping of simple icosahedral-boride semiconductors," *Journal of Solid State Chemistry*, vol. 177, pp. 1619–1623, 2004.

[171] R. W. G. Wyckoff, "Second edition. Interscience Publishers, New York, New York," *Crystal Structures*, vol. 1, pp. 7–83, 1963.

[172] Y. Cho, "Density functional theory calculations of alpha-rhombohedral boron with carbon based impurities," Master's thesis, École Polytechnique – Kyung Hee University dual degree master program, 2020.

[173] J. Heyd, G. E. Scuseria, and M. Ernzerhof, "Hybrid functionals based on a screened coulomb potential," *The Journal of Chemical Physics*, vol. 118, pp. 8207–8215, 2003.

[174] S. Gunji and H. Kamimura, "First-principles study on metal-doped icosahedral B_{12} solids," *Physical Review B*, vol. 54, pp. 13 665–13 673, 1996.

[175] H. Dekura, K. Shirai, and A. Yanase, "Efficient method for Li doping of α-rhombohedral boron," *Physical Review B*, vol. 84, p. 094117, 2011.

[176] O. Golikova, "Electrical properties of alpha-rhombohedral boron," *Sov. Phys. Semicond.*, vol. 13, p. 486, 1979.

[177] U. Y. A. Golikova O. A., Solovev N. E. and F. V. A., "Some electrical properties of α rhombohedral boron," *Journal of the Less-Common Metals*, vol. 82, p. 362, 1981.

[178] M. Terauchi, Y. Kawamata, M. Tanaka, M. Takeda, and K. Kimura, "cited by Shirai," *J. Solid State Chem.*, vol. 133, p. 156, 1997.

[179] H. M. Rietveld, "The rietveld method," *Physica Scripta*, vol. 89, p. 098002, 2014.

[180] J. Rodriguez-Carvajal, "FULLPROF: A program for rietveld refinement and pattern matching analysis," in *Abstracts of the Satellite Meeting on Powder Diffraction of the XV Congress of the IUCr, Toulouse, France*, 1990, p. 127.

[181] A. Szent-Györgyi, "II - ELECTRONIC MOBILITY," in *Bioelectronics*, A. Szent-Györgyi, Ed. Academic Press, 1968, pp. 17 – 32.

[182] K. Wade, "The structural significance of the number of skeletal bonding electron-pairs in carboranes, the higher boranes and borane anions, and various transition-

metal carbonyl cluster compounds," *Journal of the Chemical Society D*, pp. 792–793, 1971.

[183] A. J. Welch, "The significance and impact of wade's rules," *Chemical Communications*, vol. 49, pp. 3615–3616, 2013.

[184] R. W. Rudolph, "Boranes and heteroboranes: a paradigm for the electron requirements of clusters?" *Accounts of Chemical Research*, vol. 9, pp. 446–452, 1976.

[185] P. D. By Ben Mills Own work. Pentaborane.

ECOLE
DOCTORALE

Titre : Voies exploratoires pour renforcer les carbures de bore à l'aide de synthèses haute pression

Mots clés : carbure de bore, haute pression haute température, céramique dure, rayonnement synchrotron

Résumé : Le but de ce travail est d'explorer différentes manières de renforcer le carbure de bore en utilisant la synthèse haute pression comme outil. À cette fin, différentes voies de renforcement ont été suivies au cours des trois dernières années.
J'ai utilisé la torsion sous haute pression en utilisant la cellule RoToPEC pour étudier les lacunes développées dans le carbure de bore, ce qui est une raison possible de sa résistance décroissante au-delà de sa limite élastique Hugoniot (HEL).
Des appareils comme la presse Paris-Édimbourg, la presse multi-enclumes et la cellule à enclume de diamant ont été utilisés pour synthétiser de nouvelles phases de carbure de bore. Il avait déjà été prédit que ces phases auraient amélioré la résistance mécanique grâce aux calculs de la théorie de la fonctionnelle de la densité. Les paramètres de synthèse du carbure de bore dans des conditions de haute pression et de température élevée ont été optimisés et de nouvelles techniques de synthèse pour d'autres matériaux comme l'alpha bore ont également été établies.
Une idée d'utiliser le silicium pour renforcement du carbure de bore a été poursuivie. Des outils à haute pression ont été utilisés pour progresser vers la synthèse d'un nouveau composé ternaire de bore, de carbone et de silicium aux propriétés mécaniques améliorées.

Title : Exploratory routes to reinforce boron carbide using high pressure syntheses

Keywords : boron carbide, high pressure high temperature, hard ceramics, synchrotron radiation

Abstract : The goal of this work is to explore different ways to strengthen boron carbide using high pressure synthesis as a tool. To this end, different routes of reinforcement have been followed over the last three years.
I have used torsion under high pressure using the Rotational Tomography Paris-Edinburgh Cell (RoToPEC) to study the vacancies developed in boron carbide, which is a possible reason for its diminishing strength beyond its Hugoniot Elastic Limit (HEL).
High pressure devices like Paris-Edinburgh press, multi-anvil press and diamond anvil cell were used to synthesise new phases of boron carbide. It had already been predicted that these phases would have improved mechanical strength through Density Functional Theory calculations. As part of these experiments, synthesis parameters of boron carbide at high pressure high temperature conditions have been optimised and new synthesis techniques for other industrially relevant materials like alpha boron have also been established.
An idea to use silicon as a reinforcing material for boron carbide has also been pursued. High pressure tools were used to advance towards synthesising a new ternary compound of boron, carbon and silicon with improved mechanical properties.

Institut Polytechnique de Paris
91120 Palaiseau, France